UNIVERSIDADE ESTADUAL DE CAMPINAS

INSTITUTO DE QUÍMICA

JOSÉ CARLOS GERMINO

NEW STRATEGIES FOR THE IMPROVEMENT OF THE PHOTO AND ELECTROLUMINESCENCE PROPERTIES OF Zn(II) AND Pt(II) SALICYLIDENES

NOVAS ESTRATÉGIAS PARA MELHORAMENTO DAS PROPRIEDADES FOTO E ELETROLUMINESCENTES DE SALICILIDENOS DE Zn(II) E DE Pt(II)

CAMPINAS
2018

JOSÉ CARLOS GERMINO

NEW STRATEGIES FOR THE IMPROVEMENT OF THE PHOTO AND ELECTROLUMINESCENCE PROPERTIES OF Zn(II) AND Pt(II) SALICYLIDENES

NOVAS ESTRATÉGIAS PARA MELHORAMENTO DAS PROPRIEDADES FOTO E ELETROLUMINESCENTES DE SALICILIDENOS DE Zn(II) E DE Pt(II)

Tese de Doutorado apresentada ao Instituto de Química da Universidade Estadual de Campinas como parte dos requisitos exigidos para a obtenção do título de Doutor em Ciências

Ph.D's Thesis presented to the Institute of Chemistry of the University of Campinas as part of the requirements to obtain the title of Doctor in Sciences.

Orientadora: Profa. Dra. Teresa Dib Zambon Atvars

O ARQUIVO DIGITAL CORRESPONDE À VERSÃO FINAL DA TESE DEFENDIDA PELO ALUNO JOSÉ CARLOS GERMINO E ORIENTADA PELA PROFA. DRA. TERESA DIB ZABOM ATVARS

CAMPINAS
2018

Agência(s) de fomento e nº(s) de processo(s): CAPES
ORCID: https://orcid.org/0000-0003-2904-127

Ficha catalográfica
Universidade Estadual de Campinas
Biblioteca do Instituto de Química
Camila Barleta Fullin - CRB 8462

Germino, José Carlos, 1990-
G317n New strategies for the improvement of the photo and electroluminescent properties of Zn(II) and Pt(II) Salicylidenes / José Carlos Germino. – Campinas, SP : [s.n.], 2018.

Orientador: Teresa Dib Zambon Atvars.
Tese (doutorado) – Universidade Estadual de Campinas, Instituto de Química.

1. Fotofísica. 2. Fotoquímica. 3. Salicilidenos de zinco(II). 4. Compostos de coordenação. I. Atvars, Teresa Dib Zambon, 1952-. II. Universidade Estadual de Campinas. Instituto de Química. III. Título.

Informações para Biblioteca Digital

Título em outro idioma: Novas estratégias para melhoramento das propriedades foto e eletroluminescentes de Salicilidenos de Zn(II) e Pt(II)
Palavras-chave em inglês:
Photophysical
Photochemistry
Zinc(II) salicylidenes
Coordination compounds
Área de concentração: Físico-Química
Titulação: Doutor em Ciências
Banca examinadora:
Teresa Dib Zambon Atvars [Orientador]
Diego Pereira dos Santos
Paulo Cesar de Sousa Filho
Marian Rosaly Davolos
Francisco Eduardo Gontijo Guimarães
Data de defesa: 05-10-2018
Programa de Pós-Graduação: Química

BANCA EXAMINADORA

Profa. Dra. Teresa Dib Zambon Atvars (Orientadora)

Profa. Dra. Marian Rosaly Davolos (IQ-UNESP/Araraquara)

Prof. Dr. Francisco Eduardo Gontijo Guimarães (IFSC-USP/São Carlos)

Prof. Dr. Diego Pereira dos Santos (IQ-UNICAMP)

Prof. Dr. Paulo Cesar de Sousa Filho (IQ-UNICAMP)

A Ata da defesa com as respectivas assinaturas dos membros encontra-se no processo de vida acadêmica do(a) aluno(a).

Este exemplar corresponde à redação final da Tese de Doutorado defendida pelo(a) aluno(a) **JOSÉ CARLOS GERMINO,** aprovada pela Comissão Julgadora em 05 de outubro de 2018.

I dedicate this Ph.D. thesis to my mother, Maria Gomes Germino, and all the people who contributed to its development.

Acknowledgements

During the Ph.D. period, I thank God who sustained me and who was certainly by my side in difficult times.

I thank my mother and father (in memoriam), Maria Gomes Germino and Carlos Roberto Germino, who always gave support and encouragement to all my choices.

I thank my supervisor, Professor Dr. Teresa Dib Zambon Atvars, for the opportunity to have a master's degree, continuing in the doctorate, for discussions, trust, help in difficult times, by understanding, etc.

I thank my grandfathers and grandparents (in memoriam), Carlos Gomes da Cruz, Lucila Charantola da Cruz, Antônio Germino, Ida Germino, Ulisses Gomes da Cruz and Idalina Alberto Gomes da Cruz.

I thank my sister, Sirlane Naves, who, since we met, has always been at my side, as a friend, teacher, etc., supporting me in all the achievements and difficulties.

I thank CGU secretaries, Kelly Cristina and Danieli Zampieri, for their support, understanding and companionship during this period.

I thank my friend and scientific collaborator Rodrigo Araújo Mendes for his fellowship since graduation and for the direct collaboration of the development of this work and several others.

I thank my friend and collaborator in most of my scientific works, including this one, prof. Dr. Fernando Junior Quites (in memorian) for the friendship and moments of scientific discussion from the first moment I arrived at IQ / UNICAMP, helping with the learning of new techniques, scientific writing, etc.

I thank my friends Guilherme Ferbonink and Shawan Almeida for the company, scientific discussions and moments of fun throughout our academic life.

I thank the friends and scientific collaborators of the Laboratory of Research in Photochemistry and Photophysics Applied to the Science of Materials Luís Duarte, Dr. Marcelo Meira Faleiros, Emmanuel Moraes and Dr. Cristina Barboza for the discussions and collaborations about this work and all the others and for the moments of relaxation.

I thank my friends and scientific collaborators Raquel Domingues, Bruno Zornio, Miguel Galante, Luiz Bonato, Paulo Marchezi, Matheus Holanda, Willian Dantas, Saulo, Jeann for the moments of discussion and relaxation in the laboratory.

I thank the friends Gustavo Leão, David, Pedro Rosseti, Rodrigo Rossi, Rodrigo Martins, Jason, Zé Persil, Antonio Savasi, Richard, Samuel, Carlão, Carlos Fiquer and family, Régis, Selma, Janaína, André, Angelo, Cassiano, "J", Nelson, among other friends I made in this period.

I thank the Information Technology Center (CTI) Renato Archer for the infrastructure provided for the manufacture of electroluminescent devices, especially the researchers Dr. Jilian de Nei Freitas and Dr. Andreia de Morais.

I thank the Prof. Dr. Ana Flávia Nogueira and all her team at the Nanotechnology and Solar Energy Laboratory for technical and scientific support, mainly for the infrastructure for the synthesis of new materials and coordination compounds and for the assembly of OLED devices.

Thank you Prof. Dr. Cleber Renato Mendonça and his team from the Photonics Research Group of the IFSC/USP for the collaboration and infrastructure in the accomplishment of measures of ultrafast spectroscopy and nonlinear optics of our materials and direct collaboration in the discussion of our works in collaboration, including this one.

I thank my friends and teachers Dr. Nirton Cristi, Dr. Edson Fernandes, Dr. Anderson Martinez Santana, Dr. Romildo Jerônimo Ramos and Dr. Marcelo Vivas for the moments of scientific discussion, collaboration and relaxation.

I thank to the professor Dr. Maryan Davolos, Dr. Francisco Eduardo Gontijo Guimarães, Dr. Rossano Lang, Dr. Diego Pereira dos Santos, Dr. Fernando Aparecido Sigoli, Dr. Ana Flávia Nogueira and Dr. Paulo Cesar for the contribution and discussion of the results presented here.

Thank you, CPG-IQ staff and colleagues, prof. Dr. Claudio Tormena, prof. Dr. Fabio Augusto, Janaina, Bel, Isabela and Diego for all support, help and understanding during this period.

This study was financed in part by the Coordenação de Aperfeiçoamento de Pessoal de Nível Superior (CAPES) – Finance Code 001.

I thank to the National Institute of Science and Technology in Organic Electronics (INEO) for the financial support and the opportunity to participate in a network of researchers that directly or indirectly contributed to my training as a researcher. To the Fundação de Amparo à Pesquisa do Estado de São Paulo (FAPESP) (grants: 2013/16245-2 e 2013/07375-0)the Conselho de Desenvolvimento Cientifico e Tecnológico (CNPq) (grants: 470529/2012-1

e 458413/2014-3) and the UNICAMP/FAEPEX for the financial support that allowed the execution of this work.

Finally, I would also like to thank everyone who contributed directly or indirectly to my academic, professional and personal education during this stage of my life. I leave here my sincere acknowledgements.

RESUMO

Esta tese de doutorado apresenta os principais conceitos envolvidos no melhoramento das propriedades óptico-eletrônicas de diodos orgânicos emissores de luz (OLEDs) processados em solução utilizando-se compostos de coordenação de Zn(II) de baixo custo e baixa fluorescência e compostos de coordenação de Pt(II) fosforescentes de alta eficiência sintetizados a partir de novos salicilidenos (salophen, sal-5Cl-py e sal-3,4-ben). Primeiramente, os novos salicilidenos foram sintetizados e caracterizados com sucesso e a ocorrência de seus processos de transferência de próton no estado excitado (ESIPT) foram estudadas por técnicas de espectroscopias eletrônicas no estado estacionário e resolvida no tempo, obtendo-se geração de luz branca a partir de um único cromóforo em solução e em um dispositivo tipo OLED.

Posteriormente, foram estudadas as propriedades foto e eletroluminescentes dos OLEDs processados em solução pela técnica de spin-coating dos compósitos de PVK (host) e dos salicilidenos e de seus compostos de coordenação de Zn(II) (guest) como camada ativa (EML) na proporção de 2.5 % mol/mol. As propriedades eletro-ópticas (Von, brilho ($L_{máx}$) e eficiência de corrente (η_{curr})) dos compostos de coordenação foram melhores que dos ligantes livres e do PVK puro. Esta melhora é explicada pelo aumento da mobilidade de portadores de carga (μ_p) em comparação com o PVK e os compósitos de PVK:salicilidenos, que estão ligados diretamente ao aumento da rigidez e as mudanças da estrutura eletrônica na estrutura dos salicilidenos devido à coordenação do Zn(II). Assim, o diodo PVK:[Zn(sal-3,4-ben)] (V_{on} = 6.5 V; $L_{máx}$ = 131 cd m^{-2}; η_{curr} = 36 mcd A^{-1}) apresentou valores de $L_{máx}$ e η_{curr} três vezes melhores que o PVK:[Zn(salophen)] (V_{on} = 9.5 V; $L_{máx}$ = 52 cd m^{-2}; η_{curr} = 11 mcd A^{-1}) devido ao considerável aumento de sua mobilidade de buracos: μ_p([Zn(sal-3,4-ben)]) ~ $10^2 x \mu_p$([Zn(salophen)]). Além disso, o diodo PVK:[Zn(sal-3,4-ben)] apresentou $L_{máx}$ e η_{curr} comparáveis aos OLEDs dos derivados de 8-hidroxiquinolinato (Alq_3 e Znq_2) preparados da mesma maneira. Depois, estudamos como melhorar suas propriedades óptico-eletrônicas utilizando polímero condutor com uma maior mobilidade de buracos (PFO) como "host" em contraste com o PVK. Comparados aos dispositivos com PVK:Zn(salicilidenos), observou-se uma melhora em torno de vinte e duas vezes da performance dos dispositivos com [Zn(salophen)] e [Zn(sal-3,4-ben)], devido a maiores mobilidades de cargas e rendimento quântico de fotoluminescência. Além disto, a performance dos OLEDs montados a partir do compósito PFO:[Zn(sal-3,4-ben)] (V_{on} = 4.0 V, μ_p = 2.5x10^{-2} cm^2 V^{-1} s^{-1}, L_{max} = 748 cd m^{-2}, η_{curr} = 0.52 cd A^{-1} and η_P = 1.16 lm W^{-1}) mostrou-se melhor que os montados com PFO[Zn(salophen)] (V_{on} = 4.4 V, μ_p = 1.5x10^{-3} cm^2 V^{-1} s^{-1}, L_{max} = 339 cd m^{-2}, η_{curr} = 0.25 cd A^{-1} and η_P = 0.25 lm W^{-1}) e com PFO puro (V_{on} = 4.0 V, μ_p = 1.2x10^{-3} cm^2 V^{-1} s^{-1}, L_{max} = 213 cd m^{-2}, η_{curr} = 0.13 cd A^{-1} and η_P = 0.37 lm W^{-1}), um comportamento em acordo com as mobilidades de cargas calculadas a partir do modelo de corrente limitada por carga de armadilha (TCLC) e suportado por cálculos teóricos de DFT/TD-DTF dos orbitais naturais de transição (NTOs) e das energias de excitação utilizando PBE0/6-311++G(d,p). Diferenças entre as emissões por foto e eletroluminescência foram discutidas em relação aos níveis de energia dos orbitais de fronteira de cada um dos materiais da camada ativa. Em adição, foi estudado o papel da concentração do "guest" no polímero na faixa de 0,1%, 0,5%, 1,0% e 2,5% mol/mol. Melhores performances foram observadas para concentrações menores que 1.0% mol/mol. A agregação das moléculas do "guest" dentro da matriz polimérica diminuí a performance dos diodos.

Finalmente, propusemos dois novos compósitos de PVK e PFO com novos derivados baseados no cátion Pt(II), [Pt(salophen)] e [Pt(sal-3,4-ben)] (emissores vermelhos),

como camada emissiva (EML), com o intuito de combinar-se um polímero de fluorescência azul com um composto de coordenação de Pt(II) de fosforescência vermelha para obter-se uma EML de eletroluminescência branca de alta eficiência para aplicação em WOLEDs. Primeiro, [Pt(salophen)] e [Pt(sal-3,4-ben)] foram sintetizados, purificados e caracterizados estruturalmente por difração de raios-X de monocristal, obtendo-se suas respectivas estruturas moleculares. Suas propriedades fotoluminescentes foram avaliadas em solução por medidas de espectroscopia eletrônica no estado estacionário e transiente em ambiente saturados por ar e N_2(g), observando-se uma forte supressão de fotoluminescência pela presença de moléculas de $^3O_2$(g) nos dois compostos de coordenação devido sua emissão por fosforescência. Nos filmes finos das EMLs com PVK ou PFO foram observados a presença de processos de transferência de energia não-radiativos entre os polímeros condutores e os complexos de Pt(II). OLEDs utilizando os Pt(salicilidenos) dispersos em PVK na concentração de 2.5 % mol/mol foram feitos, obtendo-se dispositivos de emissão vermelha com alta pureza de cor. Entretanto, os dois dispositivos apresentaram valores baixos de eficiência de corrente e energética devido à colheita de estado tripleto dos Pr(salicilidenos) para o estado tripleto do PVK não-emissivo. Com o intuito de melhorar as propriedades de eletroluminescência dos PhOLEDs dos complexos de Pt(II) o PVK foi substituído pelo PFO, utilizando-se das mesmas concentrações que os salicilidenos de Zn(II) e observou-se uma grande melhora de suas propriedades óptico-eletrônicas nos termos de luminância, voltagem, densidade de corrente, eficiência de corrente e energética em comparação aos dispositivos com PVK, PFO puro e PFO:Zn(salicilidenos). Os diodos de PFO:Pt(salicilidenos) exibiram um comportamento de ajuste de cor com o campo elétrico aplicado: primeiro os compostos de coordenação de Pt(II) acenderam em baixas voltagens; e com o aumento da voltagem aplicada o polímero PFO começou a emitir suas componentes verde (agregados e fase-β) e azul (fase-α), que combinados com a emissão fosforescente vermelha dos Pt(salicilidenos) obteve-se WOLEDs de alta eficiência. Os melhores resultados foram obtidos para o PFO:[Pt(sal-3,4-ben)] em 0,1 % mol/mol, sendo V_{on} = 3,4 V, $\mu_P = 1{,}1\text{x}10^{-1}$ cm^2 V^{-1} s^{-1}, L_{max} = 4000 cd m^{-2}, η_{curr} = 5,28 cd A^{-1} e η_P = 26,19 lm W^{-1}. Portanto, nos demonstramos que a combinação de emissor fosforescente vermelho com um polímero condutor azul é uma alternativa fácil, de baixo custo e de economia de energia e material para obtenção de diodos eletroluminescentes de alta eficiência e de cor ajustável, em contraste aos sistemas WLEDs e WOLEDs convencionais evaporados termicamente.

ABSTRACT

This Ph.D. thesis presents the main concepts of the solution-processed organic light-emitting diodes (OLEDs) optical-electronic improvement, using salicylidene derivatives, low-cost and poorly fluorescent Zn(II) and high-efficient Pt(II) coordination compounds synthetized with new salicylidene derivatives (salophen, sal-5Cl-py and sal-3,4-ben). Firstly, the new salicylidene derivatives were successful synthetized and characterized and its ESIPT processes were evaluated by steady-state and time-resolved electronic spectroscopies techniques, obtaining white-light generation with only one emitter in solution and in an OLED device.

After, the photo- and electroluminescence properties of solution-processed OLEDs in composites of PVK as a host with salicylidene derivatives and their Zn(II) coordination compounds as guests were studied in devices containing only single-step spin-coated emissive layer (EML). The electro-optical properties (voltage turn-on (V_{on}), brightness (L_{max}) and current efficiency (η_{curr})) of the coordination compounds were better than the ligands. This improvement is explained by the increase of the charge mobility (μ_p) compared to the PVK and PVK:salicylidenes composites, which are directly linked to the rigidity improvement and the changes of the electronic structure in the salicylidene framework due to Zn(II) coordination. Thereby, L_{max} and η_{curr} were three times higher for the PVK:[Zn(sal-3,4-ben)] (V_{on} = 6.5 V; L_{max} = 131 cd m^{-2}; η_{curr} = 36 mcd A^{-1}) diode than the PVK:[Zn(salophen)] (V_{on} = 9.5 V; L_{max} = 52 cd m^{-2}; η_{curr} = 11 mcd A^{-1}) due to the increase of the hole mobilities: μ_p([Zn(sal-3,4-ben)]) ~ $10^2 x \mu_p$([Zn(salophen)]). Moreover, the PVK:[Zn(sal-3,4-ben)] diode presented L_{max} and η_{curr} comparable to the PVK:8-hydroxyquilinate compounds (Alq_3 and Znq_2) prepared in the same way. After, we study how to improve their optical-electronic properties in solution-processable OLEDs using a higher hole mobility conducting polymer (PFO) as host in contrast with the PVK. Compared to the PVK:Zn(salicylidenes) devices, an improvement about 22 times was noticed in the performances of the [Zn(salophen)] and [Zn(sal-3,4-ben)] diodes due to both the greater charge mobilities and photoluminescence quantum yield. Also, the performance OLEDs assembled with PFO:[Zn(sal-3,4-ben)] (V_{on} = 4.0 V, μ_p = 2.5x10^{-2} cm^2 V^{-1} s^{-1}, L_{max} = 748 cd m^{-2}, η_{curr} = 0.52 cd A^{-1} and η_P = 1.16 lm W^{-1}) showed to be better than that of PFO:[Zn(salophen)] (V_{on} = 4.4 V, μ_p = 1.5x10^{-3} cm^2 V^{-1} s^{-1}, L_{max} = 339 cd m^{-2}, η_{curr} = 0.25 cd A^{-1} and η_P = 0.25 lm W^{-1}) composites and pure PFO (V_{on} = 4.0 V, μ_p = 1.2x10^{-3} cm^2 V^{-1} s^{-1}, L_{max} = 213 cd m^{-2}, η_{curr} = 0.13 cd A^{-1} and η_P = 0.37 lm W^{-1}), a behavior in agreement to the charge mobilities calculated using the trapped-charge limited-current (TCLC) model and supported by the DFT/TD-DFT *Natural Transition Orbitals* (NTO) and vertical excitation calculations at the PBE0/6-311++G(d,p) level. Differences between the photo and electroluminescence emissions were discussed in relation to the energy levels of the frontier orbitals of the active layer materials. In addition, it was also studied the role of the guest concentration in the polymer within the range of 0.1%, 0.5%, 1% and 2.5% mol/mol. Greater performances were observed for concentrations lower than 1% mol/mol. Guest aggregation within the polymer matrices diminishes the diode performance.

Finally, we proposed two new PVK and PFO composite with the salicylidene derivatives based on the Pt(II) cation, [Pt(salophen)] and [Pt(sal-3,4-ben)] (red emitters), as EML in Organic Light-emitting Diodes (OLEDs), in order to combine a blue-fluorescent polymer (PVK and PFO) with a red-phosphorescent emission of Pt(II) coordination complexes to obtain an efficient white electroluminescent EML for WOLEDs application. Firstly, [Pt(salophen)] and [Pt(sal-3,4-ben)] were synthetized, purified and characterized by single-crystal X-ray diffraction, yielding their respective expected molecular structures. The

photoluminescent properties of the devices were evaluated by steady-state and transient measurements in air and N_2(g) saturated environments, observing a strong photoluminescence quenching by the presence of $^3O_2$(g) molecules in the two coordination compounds due to its phosphorescence emission. In the EMLs thin-films with PVK or PFO were observed the presence of non-radiative energy transfer processes between the conducting polymer and the Pt(II) complexes. OLEDs using Pt(salicylidenes) blended with PVK at 2.5 % mol:mol ratio were made, leading to red-emitting devices with high color purity for the two coordination compounds. However, the two devices presented low current and power efficiencies values due to the triplet-harvesting from Pt(salicylidenes) to the PVK non-radiative triplet state. In order to improve the electroluminescence properties of Pt(II) complexes PhOLEDs PVK host was substituted by PFO at same proportions that Zn(II) salicylidenes it was observed a great improvement of their optical-electronic properties in terms of luminance, voltage, current density and current efficiency in comparison to PVK, pure PFO and PFO:Zn(salicylidene) devices. PFO:Pt(salicylidene) diodes exhibited a color tuning behavior with applied electrical field: first the Pt(II) coordination compounds turns-on at lower voltages; and with the increase of the applied voltage PFO polymer starts to emit with its green (aggregates and β-phase) and blue (α-phase) components, which combined to the Pt(salicylidenes) red-phosphorescence emission, achieving high-efficiency WOLEDs. Best results were obtained for the PFO:[Pt(sal-3,4-ben)] at 0.1 % mol/mol, being V_{on} = 3.4 V, $\mu_P = 1.1x10^{-1}$ cm^2 V^{-1} s^{-1}, L_{max} = 4000 cd m^{-2}, η_{curr} = 5.28 cd A^{-1} and η_P = 26.19 lm W^{-1}. Thus, we demonstrated that the combination of a red-phosphorescent emitter with a blue-conducting polymer is as easy, low-cost, energy and material saving alternative to obtain high-efficiency and color-tunable electroluminescent diodes, in contrast to the thermal-evaporated conventional WLEDs and WOLEDs systems.

LIST OF FIGURES

LIST OF TABLES

LIST OF ABBREVIATIONS

ε – molar absorptivity index and dielectric constant
ε – free-space permittivity
π – ”pi” ligand molecular orbital
π^* – ”pi”anti-ligand molecular orbital
μ_p – hole mobility
η_{EL} – External Quantum Efficiency
η_{curr} – Current efficiency
η_P – Power efficiency
λ – wavelength
Φ_L – Luminous flux
χ^2 – chi square
τ – emission lifetime
Abs – Absorbance
Alq_3 – *tris(8-hydroxyquinolinate)aluminum(III)*
CB – conduction band
CCL – Color conversion layer
cd m^{-2} – candela per meter square
cd A^{-1} – candela per ampere
$CDCl_3$ – deuterated chloroform
CIE 1931 – Comission Internationale de L’Eclairage color space
DMSO – dimethyl sulfoxide
DTA – Differential Thermal Analise
E* – Excited state enolic species
EL – Electroluminescence
EBL – Electron Blocking Layer
EML – Emissive Layer
ESIPT – Excited-State Intramolecular Proton Transfer
ETL – Electron Transport Layer
EtOH – Ethanol
F**Ir**pic – *bis[2-(4,6-difluorophenyl)piridinate-C^2,N](picolinate)iridium(III)*
FT-IR – Fourier transform infra-red vibrational spectroscopy
FRET – Förster Resonant Energy Transfer
Gaq_3 – *tris(8-hydroxyquinolinate)gallium(III)*
J – Current density
K* – Excited state keto species
H_2O – water
HBL – Hole Blocking Layer
HOMO – Highest Occupied Molecular Orbital

HPLC – High Performance Liquid Chromatography
HTL – Hole Transport Layer
HRTOF-MS – High-resolution time-of-flight mass spectrometry
ILCT – Intra-ligand Charge Transfer
ISC – Inter-system Crossing
ITO – Indium-tin oxide
LED – Light emitting diode
LUMO – Lowest Unoccupied Molecular Orbital
L – Luminance; brightness
Liq – *lithium 8-hydroxyquinolinato*
LLCT – Ligand-to-Ligand Charge Transfer
MC – Metal centered Charge Transfer
MEH-PPV – *poly[2-methoxy-5-(2-ethylhexyloxy)-1,4-phenylenevinylene]*
MeOH – Methanol
MLCT – Metal to Ligand Charge Transfer
n – non-ligand molecular orbitals
N_t – Total density of trap-states
N_v – Total density of states in the valence band
n_D – refractive index
NMR – Nuclear magnetic resonance
OLED – Organic Light Emitting Diode
OPV – Organic photovoltaic solar cell
PEDOT:PSS – Poly(3,4-ethylenedioxithiophene):Poly(estyrenesulfonate)
PFO – poli(9,9-di-n-octyl-fluorene)
PhOLED – Phosphorescent OLED
Phos – Phosphorescence
PL – Photoluminescence
PLE – Photoluminescence excitation
PLQY – Photoluminescence quantum yield
PPV – poly(phenylenevinylene)
[Pt(salophen)] – *N,N'-bis(salicylidene)-o-phenylenediaminateplatinum(II)*
[Pt(sal-3,4-ben)] – *N,N'-bis(salicylidene)-3,4-diaminebenzophenonateplatinum(II)*
PVK – Poly(N-vinylcarbazole)
RGB – Red-green-blue color system
SC-XDR – Single-crystal X-ray diffraction
SCLC – Space Charge Limited Current
S_n – "nth" singlet state
Salophen – *N,N'-bis(salicylidene)-o-phenylenodiamine*
Sal-3,4-ben – *N,N'-bis(salicylidene)-3,4-diaminebenzophenone*
Sal-5Cl-py – *N-salicylidene-5-Chloroaminopyridine*
SS – Stokes shift
T_1 – Fist triplet excited state
TCLC – Trapped-charge Limited Current

TGA – Thermalgravimetric analysis
THF – Tetrahydrofuran
V_{on} – Turn-on Voltage
$Zn(AcO)_2.2H_2O$ – dihydrate Zinc(II)acetate
Znq_2 – *bis(8-hydroxyquinolinate)zinc(II)*
$[Zn(salophen)(OH_2)]$ – *aquo[N,N'-bis(salicylidene)-o-phenylenediaminate]zinc(II)*
$[Zn(sal\text{-}3,4\text{-}ben)(OH_2)]$ – *aquo[N,N'-bis(salicylidene)-3,4-diaminebenzophenonate]zinc(II)*
WOLED – White-emission OLED

TABLES OF CONTENTS

CHAPTER 1

INTRODUCTION

1.1 Organic Electronic

Organic electronic is a great field of the materials science and engineering, which has several practical applications, such as organic photovoltaic cells (OPVs), sensors and actuators and light-emitting sources and displays (Figure 1.1), mobilizing a large number of researchers from the areas of physics and chemistry in the studies of new materials, processes and theory.[1–3]

Since the Heeger, MacDiarmid and Shirakawa contributions,[4,5] the principal challenges on organic electronic research and technology are the global interest in the development of environmentally friendly, energy and material saving and wide color emissive materials for its applications, which can operate with high efficiency, easy processability and low environmental impact.[6–8]

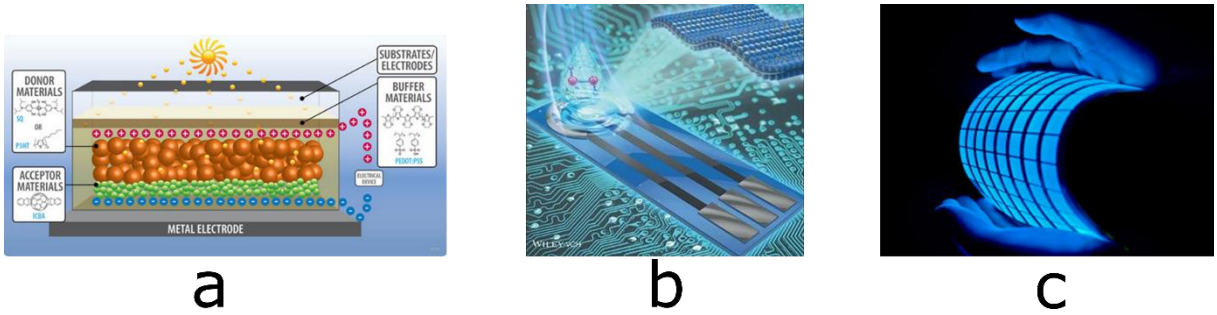

Figure 1.1. Some examples of practical applications of organic electronics: a) OPVs; b) sensors and actuators; and c) flexible light sources.

In the field of display and light-source technologies on organic electronic, the employment of organic small-molecules, organometallic coordination compounds and polymers play an important role on the organic light-emitting diodes (OLEDs) research and technology.[9]

In the following topics it will be presented the principal chemical and physics concepts about OLEDs, such as the materials characteristics, strategies for better devices and the charge injection, transport and recombination mechanisms in this kind of devices.

1.1.1 Organic Light-Emitting Diodes (OLEDs)

Since 80s until the present days, organic light-emitting diodes (OLEDs) play an important role on the organic electronic research, presenting a large number of published

manuscripts in high impact factor journals, showing 4,161 publications between 2017 and 2018, according to Web of Science™.[10]

Among its practical applications, OLEDs comprise versatile materials that may be used in the production of flexible and sustainable technological devices from thin film deposition[11] in contrast to the common paper LEDs technologies. A lot of effort has been put in this field with the development of different device architectures and different materials as active layers[12–15]. In particular, the use of organic materials in displays and light sources is more easily processed and recycled than the inorganic-based conventional systems.[1,6,16]

The evolution in OLEDs systems is clear when we look since the beginning of the its research field (Figure 1.2): Pope and collaborators 1963 report firstly the electroluminescence of an organic material in a diode system using anthracene crystals as emissive layer (EML)[17], however, this device presents a very low efficiency, with a driving voltage of V = 400 V, current density of J = 0.625 A cm^{-2}, consequently, consuming a larger electricity power of P = 250 W cm^{-2}; after twenty years of research and development, polymers were introduced as EML, using the poly(N-vinyl carbazole) (PVK) in OLEDs by Partridge 1983 in its four manuscripts in the *Polymer* journal, nevertheless, the PVK polymer showed very low optical-electronic properties in comparison to illumination conventional systems, but, according to its electrical studies was observed that PVK is good material for hole transport and electron blocking layers (HTL and EBL)[18–21]; in the end of 80s, Tang and VanSlyke, from Kodak research laboratories, they constructed the first high-efficiency OLED using a new architecture, combining the *N,N'-diphenyl-N,N'-bis(3-methylphenyl)-1,1'-biphenyl-4,4'-diamine* (TPD) as HTL and the *tris(8-hydroxyquinolinate)Aluminum(III)* (Alq_3) as EML and electron transport layer (ETL), obtaining brightness L > 1000 cd m^{-2}, with a power efficiency of η_P = 1.5 lm W^{-1} at a driving voltage of V = 10 V.[22]

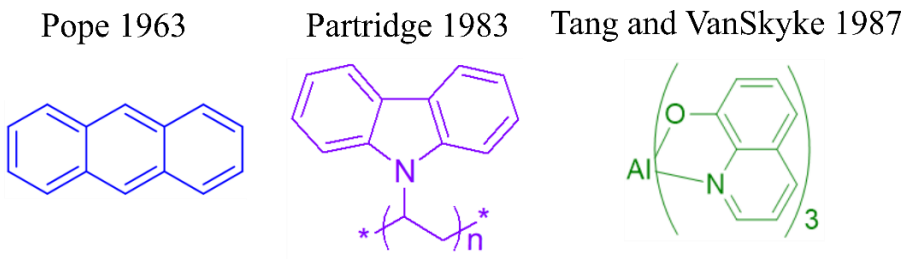

Figure 1.2. Molecular structures of the first OLEDs active layers.

Therefore, the start was given to race in the research of new materials and architectures for OLEDs. After these contributions, OLEDs researches presenting a total of

40,406 published manuscripts, 9,849 only in the last three years, according to Web of Science™ (Figure 1.3).[23]

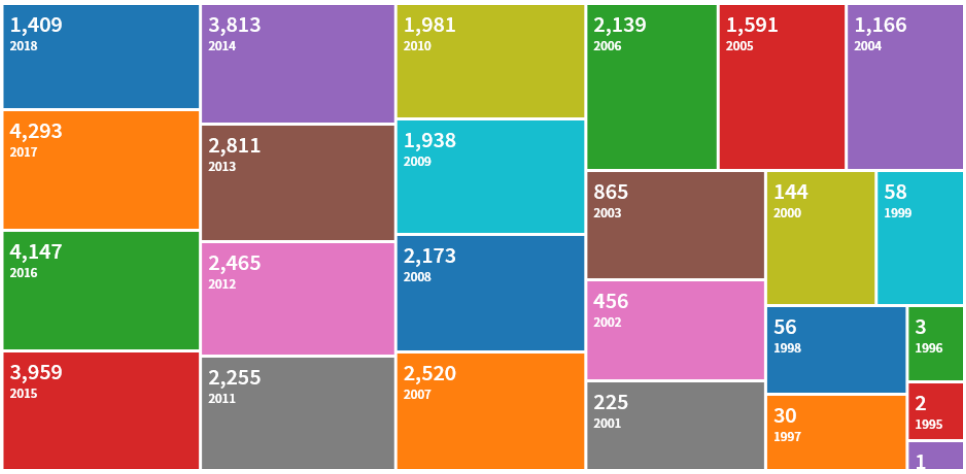

Figure 1.3. Total of published manuscripts containing "OLED" as keyword, according to Web of Science™.[23]

1.1.2 Coordination Compounds on OLEDs

Since Tang and VanSlyke contributions, an enormous effort for development of new electroluminescent coordination compounds is employed by material scientists and engineers. Also, coordination compounds are made up of a group of materials which are often applied in electro-optical devices due to their thermal and chemical stability[24] and variety of color emission with high quantum yields, in comparison to a "pure" organic framework[25–28]. Having said this, electroluminescent coordination compounds can be divided in two great groups, according to their optical properties: fluorescent[29,30] and phosphorescent[31,32] coordination compounds.

According to quantum mechanics statements, the spin-statistics for a fermion particle pair in organic molecules or block "*d*" coordination compounds, such as excitons, one quarter of possible states are singlets (multiplicity of 1, s = 0) and three quarters are triplets (multiplicity of 3, s = 1) in a two particles system. Thus, the nature of coordination compounds fluorescent emitters is limited to radiative relaxations that converse electron spin, resulting on electronic transitions between singlets excited and ground states, while coordination compounds that exhibit phosphorescence emission have spin-forbidden electronic transitions, involving a triplet excited state and a singlet ground state.[33] Some coordination compounds should exhibit phosphorescence emission at room temperature as consequence of spin-orbit coupling due to the presence of electronic transitions between heavy metal atom and ligand

framework.[24,33] Using Dirac notation, equations 1.1 and 1.2 presents the possible states for a singlet and a triplet excitons, respectively.

$$|0,0> = \frac{1}{\sqrt{2}}(|\uparrow\downarrow> - |\downarrow\uparrow>) \equiv 1\ state \tag{1.1}$$

$$\left\{ \begin{matrix} |1,1> = |\uparrow\uparrow> \\ |1,0> = \frac{1}{\sqrt{2}}(|\uparrow\downarrow> + |\downarrow\uparrow>) \\ |1,-1> = |\downarrow\downarrow> \end{matrix} \right\} \equiv 3\ states \tag{1.2}$$

Taking into account those observations, under electrical-field excitation on an OLED device, both singlet (S_n) and triplet (T_n) excitons must be formed in the coordination compound, however, for only-fluorescent OLEDs the maximum quantum efficiency of the diode is limited to 25 %, while 75 % of excitons decays by non-radiative pathways. Already, OLEDs made with room-temperature phosphorescent coordination compounds, due to inter-system crossing (ISC) quantum yield of 100 %, their exciton recombination probability tends to 100 %. Because in addition of 75 % of triplet excitons formation, all 25 % of singlet excitons are converted into triplet states due to efficiency of ISC process. Thus, leading to more efficient OLEDs.[34] Figure 1.4 resumes the spin-statistics of exciton formation in OLEDs made with fluorescent and phosphorescent coordination compounds.

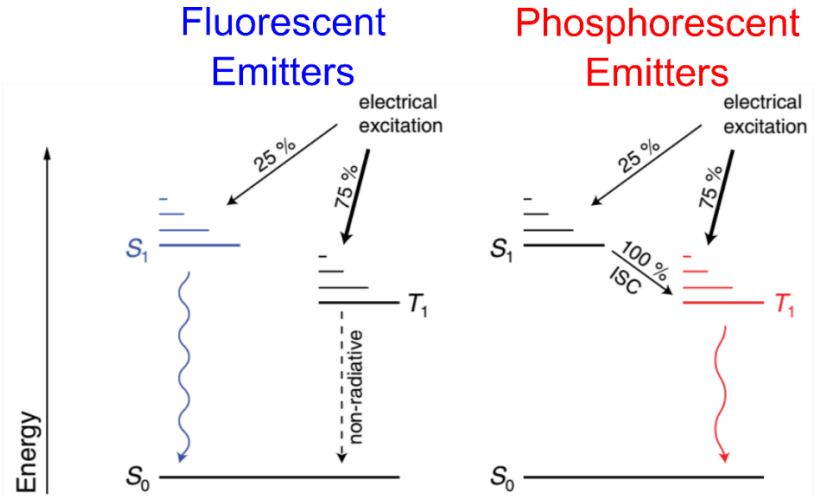

Figure 1.4. Population scheme of singlet and triplet states energy levels of coordination compounds under electrical field excitation. Adapted from Reineke et al., 2013.[34]

In view of these principal concepts on exciton formation allowed by the electrical field, innumerous works about new molecular architectures to obtain phosphorescent coordination compounds for EML applications on OLEDs were noticed and even in present days, it is a hot-topic on organic electronic science and technology.[35–37] In this class of emitting compounds various metal cations may be used to obtain coordination complexes, for example

Osmium(II),[38] Ruthenium(II),[39,40] Rhenium(I),[41] Terbium(III),[42] Europium(III),[43] Gold(III),[44] Cooper(I),[45] among others.[24,25,34,46–48] However, between the phosphorescent coordination compounds that can exhibit electroluminescence, those made from Iridium – Ir(III)[49] and Platinum – Pt(II)[50,51] are highlighted for EML applications on OLEDs. For the Ir(III) and Pt(II) electrophosphorescent materials, the organometallic cyclometalated coordination compounds are highlighted in OLEDs applications. The most efficient and important Ir(III) coordination compounds for EML are the blue-emitter coordination compound *bis[2-(4,6-difluorophenyl)pyridinateC2,N](picolinate)Iridium(III)* (FIrpic),[52,53] the green-emitter *tris[2-phenylpyridinate-C^2,N]Iridium(III)* ($Ir(ppy)_3$)[54–56] and the red-phosphorescent emitter *Tris(1-phenylisoquinoline)iridium(III)* ($Ir(piq)_3$).[56] On the other hand, the principal class of Pt(II) cyclometalated complexes are those contain the N^N^N, C^N, N^C^N and C^N^C tridentate ligands, leading a cruciform structure.[24,57] The mainly electronic transitions on phosphorescent coordination compounds are mixed metal/ligand states,[58] involving *d* orbitals of central cation and p orbitals of the ligand framework, can be: 1) metal-centrated (MC, $d \rightarrow d$); 2) metal-to-ligand-charge-transfer (MLCT, $d \rightarrow \pi^*$); 3) ligand-to-metal-charge-transfer (LMCT, $\pi \rightarrow d$); and 4) intraligand-charge-transfer (ILCT, $\pi \rightarrow \pi^*$). In all cases, emission processes occur via a triplet to singlet state.[24] Figure 1.5 presents the molecular structures of the principal luminescent Ir(III) and Pt(II) organometallic coordination compounds.

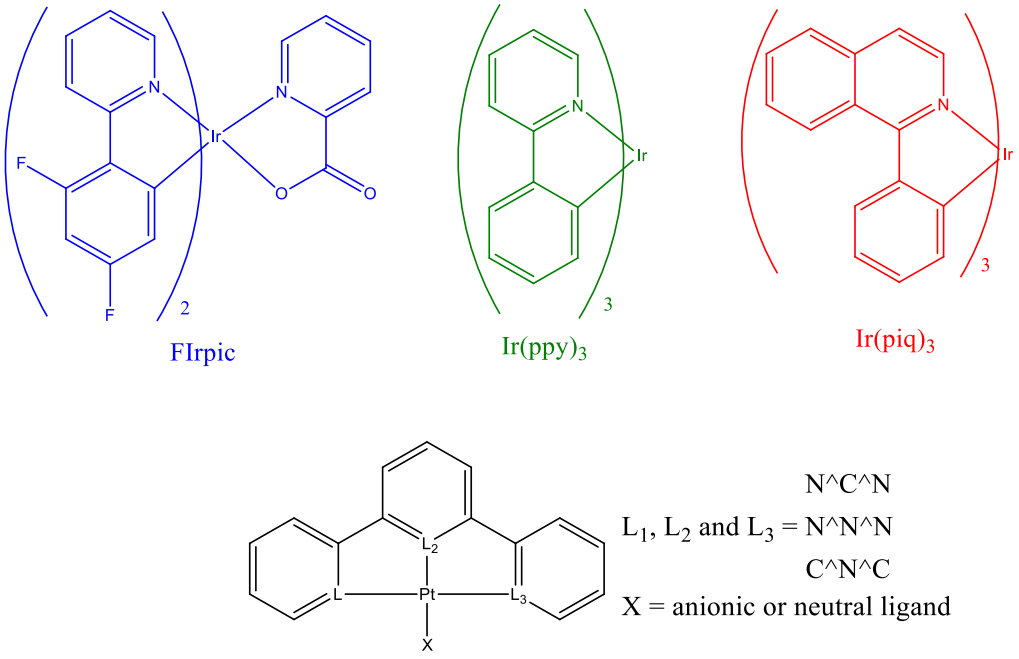

Figure 1.5. Principal Ir(III) and Pt(II) organometallic coordination compounds for OLEDs active layer.

In the class of the fluorescent coordination compounds for OLEDs applications, the 8-hydroxyquinolinate derivatives have shown the most successful molecular systems for EML and generally for ETL, because their energy level arrangement with the metallic cathode.[11,47,59,60] Among that, we can highlight the Alq_3[22,60] and its Zinc(II) (Znq_2),[61,62] Lithium(I) (Liq),[63,64] Beryllium(II) (Beq_2),[60,65] Boron(III) ($LiBq_4$),[66,67] and Gallium(III) (Figure 1.6).[68] Also, various examples of 2-hydroxy(benzothiazoles)[25] and azomethines (Schiff's bases)[69] derivatives coordinates on Zn(II) cations exhibit comparable success in comparison to 8-hydroxyquinolinate derivatives of active layer,[25] charge transport layers[25] and host materials for phosphorescent emitters (Figure 1.6).[68] The main optical-electronic characteristics of fluorescent coordination compounds are: 1) the photophysical properties of these coordination compounds are provide by the ligand optical properties and design, once the central cations on this class of fluorescent emitters are out of the transition-metal series or they are into the d^{10} group (closed shell); 2) however, the presence of metal cation enhance the ligand optical and electrical properties due to the improvement of molecular planarity and rigidity, leading to better charge transport and emission quantum yields; 3) thus, the nature of their electronic transitions are intraligand-charge-transfer (ILCT) and ligand-to-ligand-charge-transfer (LLCT), involving mainly "π" and non-ligand (n) molecular orbitals ($\pi \rightarrow \pi^*$ and $n \rightarrow \pi^*$); 4) as consequence of this, ligands used to obtain fluorescent coordination compounds are the *N,O* and *N,N* electron donors molecules, creating "*N-metal-O*" or "*N-metal-N*" bridges, which improves considerably the optical-electronic properties of these molecular systems.[70–74]

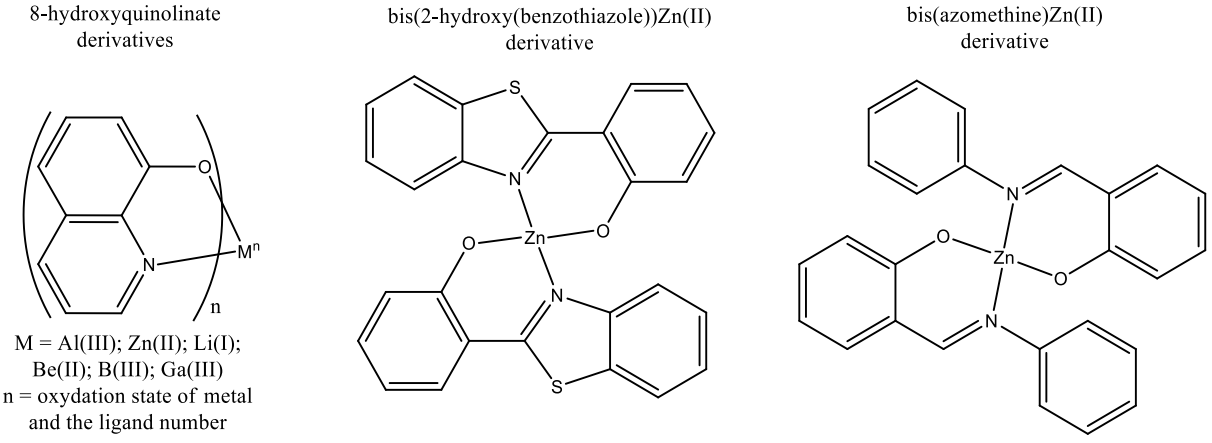

Figure 1.6. Some examples of fluorescent coordination compounds that were successfully applied in OLEDs devices.

Considering these observations, although the high efficiency and chemical stability of the phosphorescent emitters coordination compounds suitable for OLEDs systems, the

scarcity and rarity of their central metal cation makes these materials expensive. It is very important to cite that fluorescent coordination compounds are generally low-cost and environmentally friendly, in contrast to heavy-metal phosphorescent complexes. However, due to their internal quantum efficiency limit (25 %), after the 90s, the research and development of new fluorescent coordination compounds for EML in displays were completely neglected by the material scientist's community. Also, the thermal evaporation in a high vacuum is usually required for the kinds of coordination compounds, consequently, causing the same environmental and energy saving problems and high cost for production of the conventional LEDs sources and displays. Beside this, the low charge mobility and processing difficulty are the most disadvantages to use these class of materials on organic electronic devices applications.

1.1.3 Conducting Polymers on OLEDs (PLEDs)

In order to remedy the disadvantages of electroluminescent coordination compounds, conducting polymers are other class of fluorescent materials for OLEDs applications, leading the polymeric light-emitting diodes (PLEDs).[1,75] Which possess as principal advantage in comparison to the small-molecule systems its processability and mechanical facilities that enable solution-processable protocols (spin-coating, spin-casting, roll-to-roll, silkscreen, inkjet, among others), energy saving, flexible and total transparent devices. Making more environmental friendly and low-cost devices in comparison to common paper OLEDs and LEDs technologies.[1,6,11,75–77]

Our deposition technique approach is the spin-coating that consists on the use of the centrifuge forces for deposit thin-films supported on the substrate via concentrated solutions in the order of tens/hundreds of nanometers (nm) to produce prototype OLEDs: 1) a solution containing the conducting polymer is dropped in the substrate; 2) after this, the solution in the substrate is centrifugated. In this process the material is completely dispersed throughout the substrate from the center to the border of the substrate; 3) subsequently, the solvent excess is removed due to the centripetal force; 4) in the final step a dry film is obtained (Figure 1.7). As consequence of the spin-coating deposition, some parameters of the solvent and the solution must be taken in account: density; wettability; viscosity; vapor pressure; and if the resultant solution is a single solute (a) or a mixture of solutes (blend or composite; b). Also, the rugosity and electrical affinity of the substrate surface are very important. These parameters should influence directly on the thin-film thickness and morphology.[77]

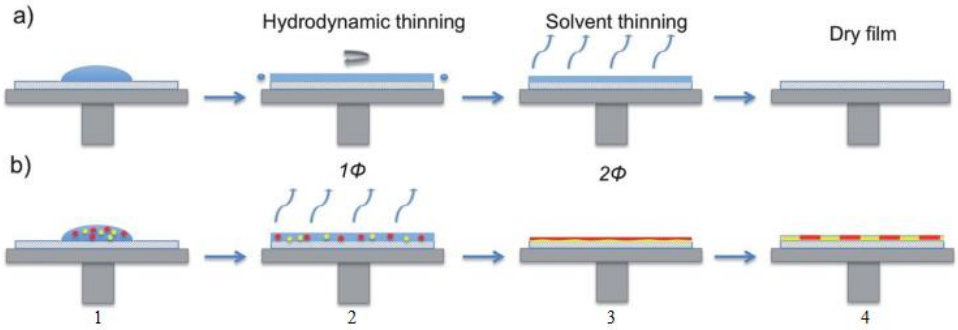

Figure 1.7. Spin-coating deposition technique scheme for a single solute (a) and a ternary mixture of two incompatible solutes (b) solutions. Adapted from Toolan and Howse 2013.[77]

Other important difference between semiconductive fluorescent small-molecules systems and conducting polymers is the exciton formation mechanism due applied field, despite the same nature of their electronic transition (singlet-singlet transitions).[60] Generally, conducting polymers are characterized by a alternance between several single and double molecular bonds into principal chain (conjugated polymer). Thus, the electronic conduction on this class of organic material is given conjugation effect among π bonds along the polymer chain, generating delocalization of the electrons along the polymer chain. In these cases, the emissive excitons formation occurs via injection of charge carries in the polymer: hole (h^+) is injected in the highest energy occupied molecular orbital (HOMO), while electron is injected in the lowest energy unoccupied molecular orbital (LUMO) of the conductive polymer, forming positive ($P^{\cdot+}$) and negative ($P^{\cdot-}$) polarons, respectively. By charge recombination, these polarons may generate a conducting polymer in ground-state (P) and another one in the excited-state (P^*), which decays via radiative (electroluminescence) and non-radiative (trap-states) pathways.[78] Equations 1.3 and 1.4 summarize this mechanism in a simplified way:

$$P^{\cdot+} + P^{\cdot-} \longrightarrow P + P^* \quad (1.3)$$

$$P^* \longrightarrow P + h\nu \quad (1.4)$$

In the most cases, the energy barrier to exciton formation in these systems varies between the visible and ultraviolet (UV) region of the electromagnetic spectrum (1.4 ~ 3.3 eV).[60] In this way, according to these optical-electronic properties, conducting polymer should present better charge mobility in comparison to electroluminescent coordination compounds, what can lead better electroemissive diodes. However, due to their nature of fluorescent material, the external quantum efficiency of a PLED device is limited to 25 %, according to

spin-statistics. Thus, these materials present an intrinsic efficiency barrier as principal drawback.

In this class of polymeric devices, in the begin of the 90s, the first reports that presents PLEDs with competitive optical-electronic properties when compared to common paper OLEDs and LEDs systems were done by the professors Friend, Bradley, Burroughes, and Holmes from Cavendish Laboratories, using *poly(p*-phenylenevinylenes) derivatives (PPVs) which have a yellow-red color-tuning emissions according to their lateral chain substitution. They present the *poly*[2-methoxy-5-(2-ethylhexyloxy)-1,4-phenylenevinylene] (MEH-PPV; Figure 1.8) as the most successful PPV derivative conjugated polymer for PLEDs.[79–85] After these reports, an enormous effort to development of new conjugated polymers systems was done by various researchers on the field of organic electronics and due to their electronic characteristics, conducting polymers are also called as synthetic metals.[86]

Another very important class of conjugated polymers for emitting diodes applications is the polyfluorene derivatives (PFs; Figure 1.8). In the PFs class of conjugated polymers *poly*(9,9-di-*n*-octylfluorenyl-2,7-diyl) (PFO) is the most used and efficient, with electrochemical and optical energy band gap around E_g = 3.70 eV[87] and E_g = 2.95 eV (≈ 380 nm)[88], PFO main electronic absorption (*HOMO* $\rightarrow$ *LUMO*) is on the UV region while its emission band is located at the blue region of the electromagnetic spectrum. Generally, PFO conjugated polymer is used as EML in PLEDs when its blue emission p-charger transport is required, due to great photoluminescence quantum yield (PLQY = 50 ± 10 % in thin-film)[89], higher hole-charge mobility ($\mu_p \approx 1x10^{-3}$ cm^2 V^{-1} s^{-1})[90,91] and low electron-mobility ($\mu_e \approx 1x10^{-7} \sim 1x10^{-5}$ cm^2 V^{-2} s^{-1})[92] of PFO. Also, PFO in thin-film exhibits the photo and electroluminescence spectra (PL and EL, respectively) completely dependent with its morphologically and crystallinity behavior: the amorphous phase (also it called α-phase) presents the maximum absorption band centered at λ_{abs} = 370 ~ 380 nm assigned to exciton delocalization in π orbitals along polymer chain ($\pi \rightarrow \pi^*$ transition) and PL band with a very well resolved vibronic progression at λ_{PL} = 426, 452 and 476 nm, being the zero-phonon band (0-0), 0-1 and 0-2 vibronic coupling, respectively, with a Stokes shift of SS = 2,842 cm^{-1};[60] the crystalline phase (β-phase, also called as green phase) exhibits a maximum absorption band centered at λ_{abs1} = 394 nm and a characteristic shoulder at λ_{abs2} = 437 nm while its emission spectrum profile completely changes to λ_{PL} = 445 (0-0), 468 (0-1) and 499 (0-2) nm with SS = 411 cm^{-1}.[93] Thus, the control of the PFO morphological phase implies directly in its optical-electronic characteristics. Also, PFO polymer may be used for high-efficient blue-PLEDs, as

host conducting polymer material for disperse small-molecules and as blue component in conjugated polymers blends and coordination compounds composites for obtaining white light generation OLEDs (WOLEDs).[94]

In order to obtain wide range visible-light emission polymers with PFO electrical properties, fluorene monomers are used to obtain wide types of conjugated copolymers, as the *poly[(9,9-dioctylfluorenyl-2,7-divinylene-fluorene)-co-alt-{2-methoxy-5-(2-ethylhexyloxy)-1,4-phenylene}]* (PFO-MEHPV)[95], and the classical donor-acceptor *poly[(9,9-di-n-octylfluorenyl-2,7-diyl)-alt-(benzo[2,1,3]thiadiazol-4,8-diyl)]* (F8BT; Figure 1.8)[96]. As PFO, F8BT exhibits p-type charge transport characteristic, with μ_P in the same order of magnitude of PFO ($\approx 5x10^{-3}$ cm^{-2} V^{-1} s^{-1}) and absorption and emission spectra at the visible range, allowing its application as active layer in high-efficiency PLEDs displays[97] and in bulk-heterojunction polymeric solar cells (PSCs)[98].

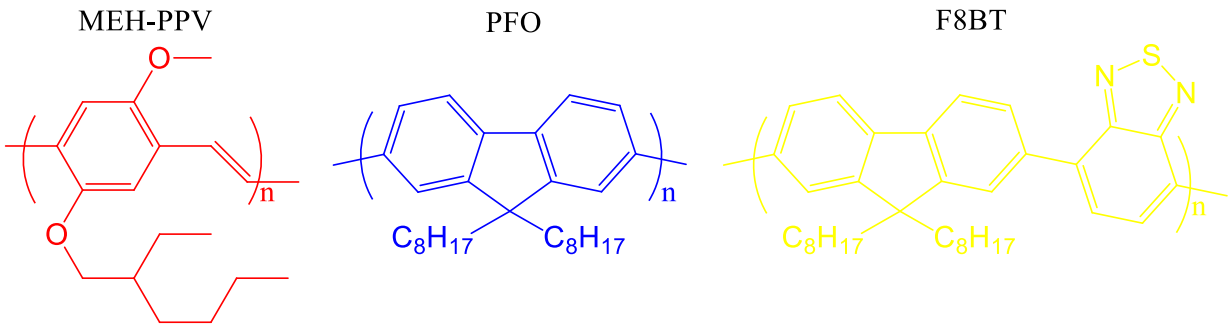

Figure 1.8. Main conjugated polymers applied as EML on PLEDs devices: MEH-PPV, PFO and F8BT.

1.1.4 OLEDs Charge Injection, Transport and Recombination

Having presented the principal fluorescent and phosphorescent coordination compounds and conjugated polymers semiconductor materials for EML on light-emitting devices, in this topic, the main concepts involved in the operation (charge injection, transport and recombination) in OLEDs will be presented.

The mechanism of the charge injection and transport on a simple OLED device (Figure 1.9a; Anode|EML|Cathode) is well established: in the first step the electrons (e^-) are injected in conduction band (CB; LUMO) while the hole (h^+) charge carriers are injected in the valence band (VB; HOMO) of the active matrix by the cathode and the anode, respectively; after this, the charge carriers are transported in the organic semiconductor frontier molecular orbitals; and in the last step the e^-:h^+ pair (exciton) is formed on the EML, being able to decay via radiative (electroluminescence process) or non-radiative (trap-states) pathways after reaching the turn-on voltage (V_{on}) and at the OLED driving voltage.[60,99]

Nevertheless, other OLED's architectures may be used in order to improve the devices charge balance (Figure 1.9b).[100] Since Pope (one organic layer), going through Tang and VanSlyke works (HTL|EML) until nowadays (multilayer devices and doped EMLs) great advances were given in the OLEDs architecture engineering, and these additional layers are added for improvement of the exciton confinement on the EML, doing that the h^+ and e^- charge carriers pair recombination processes occur only, or preferably, into the constituents of the active layer, and as consequence of these processes, it is expected an improvement of the emissive diode efficiency, charge balance and stability.[101] However, the production cost of the OLEDs increases with the addition of several layers, due to the use of high-vacuum thermal evaporation and the quantities of materials to produce the devices, which contrasts directly to the OLEDs processability, flexible technology, energy and material saving concepts involved into electronic organics field.

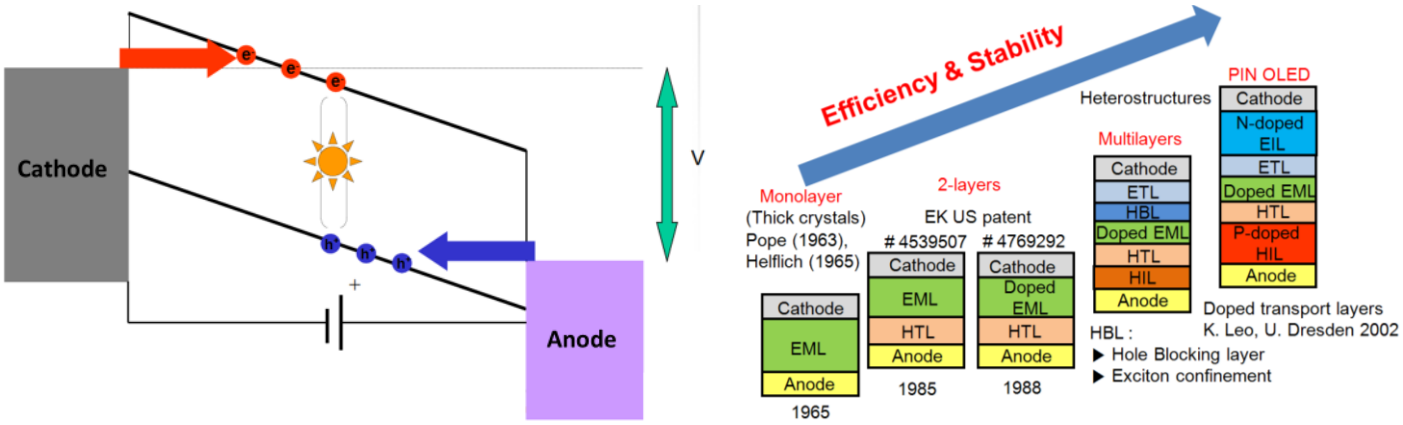

(a) **(b)**

Figure 1. 9. Simplified charge carrier injection, transport and recombination mechanism; and b) evolution of the OLEDs architecture[100].

One fundamental parameter for the charge carrier transport evaluation is the charge mobility (μ) on the OLEDs/PLEDs that may be evaluated by transient electroluminescence techniques (time-of-flight[90] and photo-induced charge carrier extraction by linearly increase voltage – Photo-CELIV[102]) and by steady-state one-carrier model using the current density (J) *versus* Voltage (V) curves (JxV), according to the Child's power law[103]:

$$J \propto V^m \tag{1.3}$$

where the J is directly proportional with V raised to m power and m is directly related to the trap energy parameter according to the following equations:

$$m = l + 1 \tag{1.4}$$

$$l = \frac{E_t}{kT} \tag{1.5}$$

being E_t energy of trap states (defects), k is the Boltzmann constant and T is the system temperature.[104]

Considering a p-type semiconductor organic material, such as PEDOT:PSS, PVK and PFO, the JxV curves of an OLED device may be exhibit different domains due to magnitude of the applied electrical field (Figure 1.10),[104,105] thus they must be considerate as a Schottky diode. Accordingly, at low voltages, organic materials that consists the OLED architecture exhibit insulator characteristics, presenting an ohmic behavior ($m = 1$; $J \propto V^1$) with free-charges along the organic insulator, which must be describe by equation 1.6:

$$J_{ohmic} = q\mu_p \eta \frac{V}{L} \tag{1.6}$$

where q is the elemental charge, μ_p is the free-charge mobility, η is the free-charge density and L is the active layer thickness.[104]

With the increment of the applied electrical-field intensity into the organic diode, the charge transport on the organic semiconductor should be follow two different mechanisms, according to the trap-density parameter of the material on the kind of device. First, due to the capacitive characteristic of an organic insulator diode, space-charges must be generated into the active matrix of the OLED. In this case, the current density dependence with the applied voltage is raised at second power ($J \propto V^2$, with m = 2) and in a free-trap case this behavior is described by the space-charge limited current (SCLC) model:

$$J_{SCLC} = \frac{9}{8} \varepsilon \varepsilon_0 \mu_p \frac{V^2}{L^3} \tag{1.7}$$

this equation is also known as Mott-Gurney law[103] and ε is the organic semiconductor dielectric constant and ε_0 is the free-space permittivity. The principal problem with this model is the free-trap generalization which is opposite with randomly distribution of the active layers of solution-processable OLEDs, with pure semiconductor polymer or a polymer:small-molecule composite, that may be generate high density of trap states, due to various trap types, such as

structural and morphological defects, energy and charge transfer aggregates, as well as commonly non-radiative pathways. In these cases, as consequence of the materials characteristics and the deposition techniques (spin-coating or spin-casting), it is observed a high density of trap-states ($m > 2$), causing most of the injected holes must be localized and it do not contribute to the current flow into the OLED. Thus, the Child's power law assumes the trapped-charge limited current (TCLC) model, as equation 1.8 describes:

$$J_{TCLC} = q^{1-l}\mu_p N_V \left(\frac{2l+1}{l+1}\right)^{l+1} \left(\frac{l}{l+1}\frac{\varepsilon\varepsilon_0}{N_t}\right)^{l} \frac{V^{l+1}}{L^{2l+1}} \quad (1.8)$$

where N_V is total valence band density of states and N_t is the total density of hole-traps in the valence band.[106,107]

The most part of polymeric emissive diodes and host-guest OLEDs exhibit TCLC domain of charge transport at driving voltage.[108] After these regions in the JxV curve a trap-free SCLC behavior is observed, however, the most part of the organic diodes must be passed by non-reversible processes (oxidation, reduction and chemical modifications of the device layers) in this step, thus, leading the degradation of the device.[109]

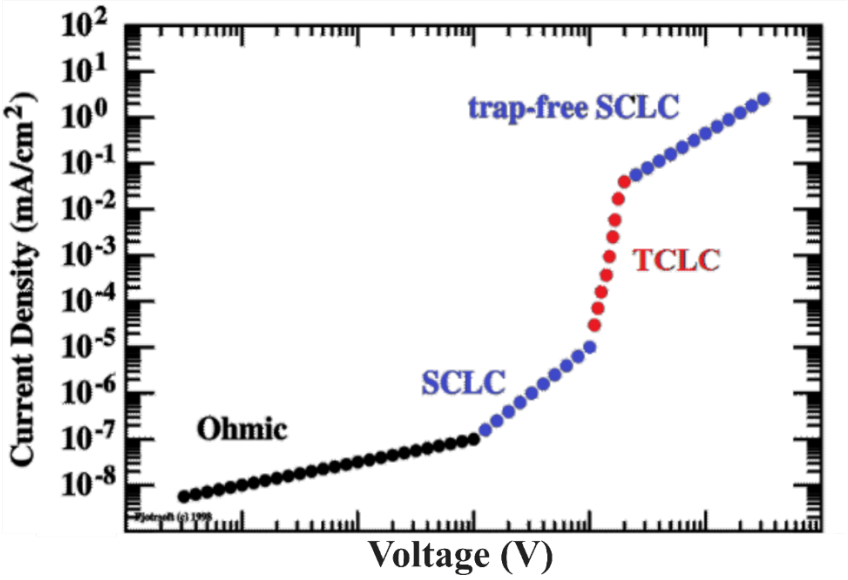

Figure 1.10. OLED typical current density versus voltage curve (JxV) containing the main mechanisms of charge mobility. Adapted from Stallinga 2009[109].

In addition, to measure and to interpret the main physical quantities for optical-electronic characterization of OLEDs systems are utilized the luminous flux (**Φ**), the luminous

intensity (I), the luminance (L), current density (J), the applied electrical field (V), the luminous efficiency (η_{curr}), the power efficiency (η_W) and the external quantum efficiency (η_{EL}).[110,111]

The Φ is a fundamental quantity of illumination that can be define the total emitted radiation of an illumination source in all directions which may produce light on the visible region of the electromagnetic spectrum (380 ~ 780 nm). Its unit on the International System (IS) of the lumen (lm). To measure this quantity in laboratory is necessary the use of Ulbricht type integrated sphere.[110,111]

Already, the luminous intensity (I) is defined as the luminous flux quantity emitted by a light-source in one direction. Its "IS" unit is the candela (cd), which was directly linked to the concept of quantity of light emitted by one candle. The "I" may be measured in a laboratory using a photodiode, diode array or photomultipliers (PMTs), being express by the follow equation:

$$I = \frac{\Phi}{4\pi} \tag{1.9}$$

where Φ is the luminous flux and 4π is the solid angle correction factor for the emitted light in all directions.

The luminance (L) is the measure of the light-emitted density in an only-one direction by a light-source. L describes the quantity of light emitted by a device surface (area) and it decays according to a solid angle and the L unit in the "IS" is the cd m^{-2}. If the solid angle between the light-meter and the OLED was 90º, L must be obtained from equation 1.10:

$$L = \frac{I}{A} \tag{1.10}$$

being I the luminous intensity emitted by the device and A is the area of the diode.

Current density (J) is the quantity that measure how much electrical current (*i*) pass by a determined area (A) due to the applied electrical field (V), being Ampère m^{-2} (A m^{-2}) its "IS" unit.[112]

$$J = \frac{i}{A} \tag{1.11}$$

Thus, the luminous efficiency (also called as current efficiency; η_{curr}) is obtained combining equations 1.10 and 1.11 and its "IS" unit is cd A^{-1}, as the follow equation:

$$\eta_{curr} = \frac{L}{J} \tag{1.12}$$

with L and J as the luminance and the current density of the OLED, respectively.

Another important parameter for the characterization of EL devices is the power efficiency (η_W), that express the energy expended (Watts – W) to generate a luminous flux in an area (Φ_A – lm m^{-2}). To measure the η_W is necessary the use of an integrated sphere, employing the follow equation:

$$\eta_W = \frac{\Phi_A}{J.V} \tag{1.13}$$

where Φ_A is the luminous flux by the OLED area, J is the current density and V is the applied voltage. η_W unit is lm W^{-1}.[110]

The external quantum efficiency of an OLED device (η_{EL}) should be estimated by the equation 1.14:

$$\eta_{EL} = \gamma\, \eta_{S/T}\, PLQY\, \xi_{out} \tag{1.14}$$

where: γ is the ratio of the exciton formation as function of the electron flowing in the external circuit, basically the e^-:h^+ pair recombination efficiency; $\eta_{S/T}$ is the ratio of emissive singlet/triplet excitons formed on the active layer ($\eta_{S/T}$ = 0.25 for fluorescent materials and $\eta_{S/T}$ = 1 for room-temperature phosphorescent materials); PLQY is the photoluminescence quantum yield of the active layer; and ξ_{out} is the out-coupling efficiency, also defined as the loss of EL photons by the surface of the OLED.[60]

Nevertheless, η_{EL} should be determined experimentally using an integrated sphere by ratio of the OLED's luminous power (W m^{-2}) with the applied electrical power (J.V ≡ W m^{-2}):

$$\eta_{EL} = \frac{Luminous\ Power\ (W\ m^{-2})}{J.V\ (W\ m^{-2})} \tag{1.15}$$

1.1.5 Strategies to achieve White OLEDs (WOLEDs)

A special kind of organic light-emitting sources is the White Organic Light-Emitting Diodes (WOLEDs) that consist on the combination of primary colors of the electromagnetic visible spectrum (blue, green and red) in order to obtain a broad electroluminescence band. As principal applications it can be cite commercial displays illumination back-light (such as cellphone, television and PC monitors displays) and room lightning technologies, for the last case, in contrast to common paper room-illumination systems, such as incandescent bulbs, fluorescent tubes and inorganic LEDs.[113] In comparison to commercial illumination systems, WOLEDs exhibit competitive characteristics in terms of white emission color, power efficiency, manufacturing cost, processability and environmental key-parameters. However, inorganic LEDs lamps present approximately 130 % more operation durability in comparison to organic systems, as consequence of the nature of the active matrix materials, being of utmost importance the research and development new stable organic materials, as well as, new efficient encapsulation processes for this king of electronic devices (Figure 1.11).[47]

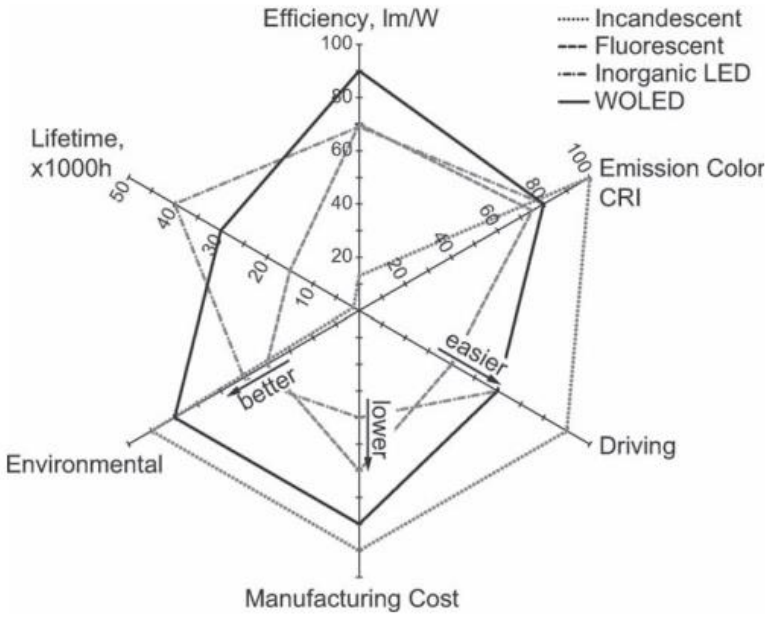

Figure 1. 11. Comparison of the key parameters of WOLEDs with common paper illumination devices. Adapted from Gather et al 2011.[47]

To obtain white-light electroluminescent devices some strategies may be done (Figure 1.12): a) three-independent red, green and blue OLED in vertical arrangement; b) three-independent red, green and blue OLED in horizontal arrangement; c) a single-component organic white-light emitter (conducting polymer or dye); d) a blue-greenish OLED with a

external color conversion layer (CCL) on the device outcoupling; e) conducting polymer blend or composite with small-molecules or coordination compounds, combining the EL color of each component at a given composition to generate a WOLED in a single-emissive layer; and f) a tandem WOLED consists in the combination of three emitters layers in the same device – blue, green and red emitters as OLED active layers.[34]

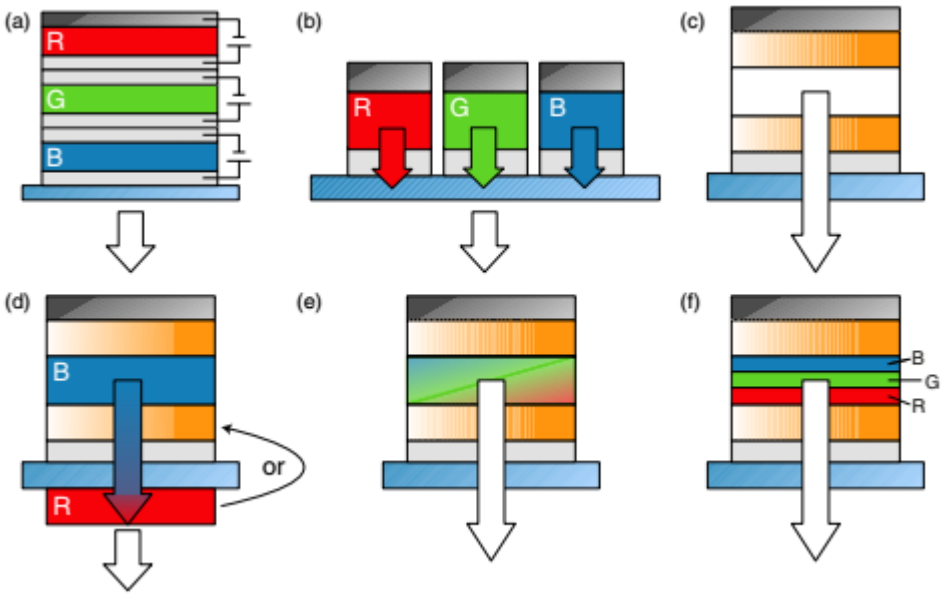

Figure 1. 12. Principal strategies for achieve WOLEDs devices. Adapted from Reineke et al 2013.[34]

Thus, all kind of WOLEDs architecture has your specifics advantages, drawbacks and challenges, which should be considered for obtaining white-light diodes. In specific, this thesis we use (e) kind of device in order to construct our OLED system, combining a blue-fluorescent (PVK or PFO) conducting polymer with a yellowish-fluorescent Zn(II) coordination compound or a red-phosphorescent Pt(II) coordination compound, leading host-guest composite that were spin-coated as active matrix. Also, this is an easiest way to obtain a WOLED and the most interesting in terms of the device physics and chemistry. In this approach, some considerations must be taken into account: 1) the complementarity of the EL emission color of the host and the guest to lead wide emission spectra; 2) complementarity of the energy levels against vacuum and spectral overlap between the host emission spectra and the guest electronic absorption spectra of the composite, enabling energy and charge transfer between the active layer components; 3) energy and charge transfer process should be occur from the host to the guest molecules, in order to the exciton formation in the guest molecules; 4) ideally, host and guest must be exhibit great optical properties – high PLQY and molar absorption coefficients (who it is directly linked to the linear cross-section of the molecular system); 5) a

balance between the injected charge carriers must be respected, to favor the exciton formation and recombination processes into the active layer; and 6) inherently, the presence of non-radiative energy transfer processes (such as Förster and Dexter mechanism) and randomly dispersion of the guest molecules into conducting polymer matrix will occur, changing completely the charge transport and morphology/crystallinity of the conducting host, producing a high density of emissive and non-emissive trap-states.

Taking into account such observations, the next topic will explain the mainly concepts of photophysical processes in semiconductor organic molecules in an isolated chromophore system and in bimolecular aggregates (radiative and non-radiative energy transfer processes).

1.2 Photophysical Process on Organic Semiconductors

With the absorption of electromagnetic radiation, an organic aromatic molecular system returns to ground electronic state through dissipation of the acquired energy[114]. This return is not always simple, it can involve different deactivation pathways[115], divided into photophysical and photochemical processes. A photochemical process differs from the photophysical once promotes molecular alterations due to a chemical reaction triggered by light absorption.

Condensed matter presents several deactivation paths from electronic excited states, some of them constitute intrinsic properties (unimolecular processes), others are derived from external perturbations (bimolecular processes)[116]. All of them respect the basic principles regarding the Jablonski Diagram (Figure 1.13).

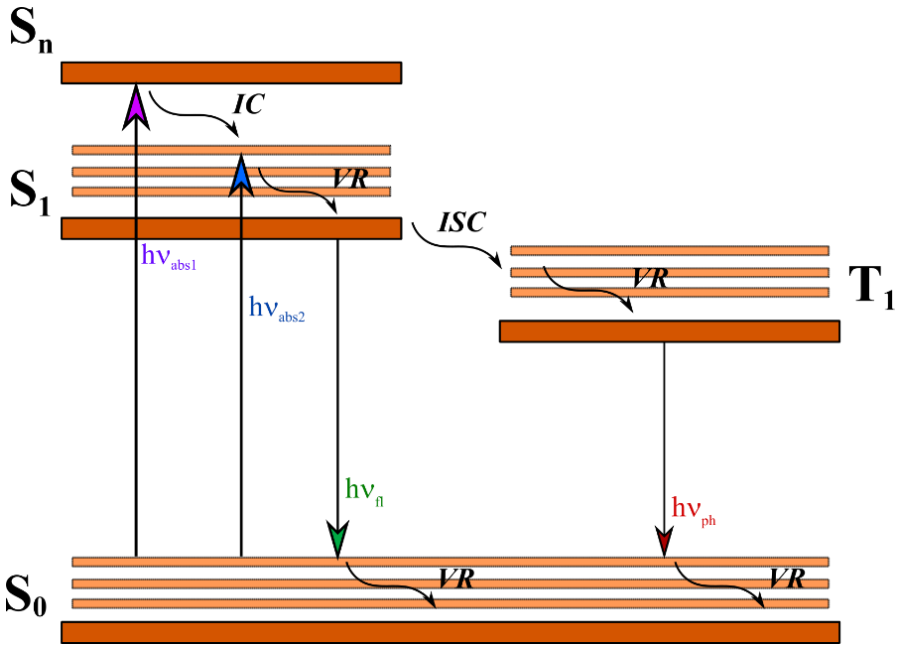

Figure 1. 13. The Jablonski diagram for photon-excitation of an organic semiconductor, where: $h\nu_{abs1}$ and $h\nu_{abs2}$ are the photon absorption energies to promote the molecular excitation from the ground-state (S_0) to the *n* singlet and first singlet excited-states (S_1), respectively; IC is the internal conversion processes; VR is the vibrational relaxations; ISC is the inter-system crossing process; and $h\nu_{abs1}$ and $h\nu_{abs2}$ are the photon emission energies via fluorescence and phosphorescence processes, respectively.

The diagram contains all relative energies of typical photophysical steps. Starting from ground state electronic configuration, an organic aromatic molecular system undergoes to excited state electronic configuration due to momentum transfer from light, which must contain a specific energy that resonates with the electronic density of the molecule. This characterizes an electronic transition and the probability of this event follows Franck-Condon Principle, mathematically expressed by:

$$F = |\langle \psi_i | \mu | \psi_j \rangle|^2 |\langle \chi_a | \chi_b \rangle|^2 \tag{1.9}$$

where, ψ_i and ψ_j are the electronic wavefunctions of two states, with χ_a and χ_b being the vibrational wavefunctions and μ is the transition dipole moment operator, and acts just on the electronic package[114]. Rotational energies can be neglected since do not imply significant energy changes. In fact, equation (1.9) is responsible for spectral bands intensities because allows the verification of the electronic transition probability related with wavefunctions overlap. Thus, the physical meaning of a spectral band is a distribution of states[117].

Once on the excited electronic state, our generic molecular system is ready to dissipate that accumulated energy from excitation. It will happen by the emission of heat or radiation.

The first one is named Vibrational Relaxation (VR), if comes from the deactivation of vibrational levels on the same electronic level, or Internal Conversion (IC), if comes from different electronic levels – hence the energy difference from $h\nu_{abs1}$ to $h\nu_{abs2}$ on Figure 1.11. Those are non-radiative paths of excited states deactivation, which are typically evaluated by the Stokes Shift (SS): the difference between the absorption and emission energies.

The second one receives other two distinct names, both assigned as luminescence, radiative paths to deactivate an excited state, and start solely from the first excited electronic state (S_1) for further electronic states are very close in energy, deactivating by IC. These paths depend on molecular orbital symmetry between ground and excited electronic states. Besides, if the electronic transition does not promote spin change, after VR and/or IC, the return to S_0 radiatively is named fluorescence. In other hand, the electronic transition from S_0 to S_1 may result in spin multiplicity change (inter-system Crossing – ISC), then the Triplet state (T_1), an intermediate excited state, is originated, also deactivating radiatively by a process named phophorescence[118].

1.2.1 Steady-state and Photodynamic Conditions

Continuing our description of unimolecular processes of excited electronic states deactivation, another photophysical parameter of great importance is the photoluminescence quantum yield (PLQY), the ratio between the number of emitted and absorbed photons. Considering a generic system ^{1}M on the excited state, with k_F as the emission rate and k_{nr} the sum of all non-radiative deactivation rates of the organic semiconductor chromophore ^{1}M* (equations 1.10 and 1.11) assigned by the Jablonski Diagram, one can write its formation rate through the following kinetic equation:

$$\frac{d[\,{}^1M^*]}{dt} = I_0 - (k_{FM} + k_{nrM})[\,{}^1M^*] \tag{1.10}$$

$$k_{nr} = k_{IC} + k_{ISC} \tag{1.11}$$

where $\frac{d[\,{}^1M^*]}{dt}$ is the formation rate of ^{1}M*; I_0 is the intensity of the absorbed photons by ^{1}M; k_{IC} and k_{ISC} are the internal conversion and the inter-system crossing rates constants, respectively.

To photostacionary conditions, $\frac{d[\ ^1M^*]}{dt} = 0$, so:

$$I_0 = (k_F + k_{nr})[\ ^1M^*] \tag{1.12}$$

Taking equation 1.12, the PLQY of ^{1}M* is described by

$$\text{PLQY} = \int_0^\infty F(\nu)d\nu = \frac{\#\ emitted\ photons}{\#\ absorbed\ photons} = \frac{k_F[\ ^1M^*]}{I_0} = \frac{k_F}{k_F + k_{nr}} \tag{1.13}$$

where $F(\nu)$ is the normalized photoluminescence spectrum for ^{1}M*. This equation represents the ratio between radiative and the sum of radiative and non-radiative processes that might take place with ^{1}M*.[116]

The same idea is used to photodynamic (or transient) conditions, depending on the emission lifetime. Considering the process after formation of ^{1}M*, and that the intensity of transient emission $I(t)$ is proporcional to ^{1}M* concentration ($I(t) \propto [^1M^*]$), the deactivation rate of ^{1}M* becomes:

$$\frac{d[\ ^1M^*]}{dt} = \frac{dI(t)}{dt} = -(k_F + k_{nr})I_M \tag{1.14}$$

$$\frac{dI(t)}{I} = -(k_{FM} + k_{nr})dt \tag{1.15}$$

Integrating equation 1.15 e applying the exponential function in both sides gives:

$$I(t) = I_0 e^{-(k_{FM}+k_{nr})t} \tag{1.16}$$

From equation 1.10, for photodynamic conditions is known that: $k_F + k_{nr} = k_M = \frac{1}{\tau_M}$. Replacing this statement on equation 1.16:

$$I(t) = I_0 e^{-\frac{t}{\tau_M}} \tag{1.17}$$

Equation 1.17 represents the photoluminescence decay to the chromophore ^{1}M* as a monoexponential decay, where τ_M is the fluorescence lifetime, t is the time and I_0 the normalized intensity at decay beginning.[116,118]

Now, equation 1.17 also stands for the emission profile of a single species on excited electronic state. However, once on the excited state, several processes may occur, including conformational variations, aggregation processes or even photoreactions. In the occurrence of such events, the same chromophore may exhibit a multiexponential decay. Thus, equation 1.17 becomes to:

$$I(t) = \sum_{i=1}^{n} B_i e^{-\frac{t}{\tau_i}} \quad (1.18)$$

where τ_i is the fluorescence lifetime and B_i is the amplitude of each species on excited-state at t = 0 (relative percentage of each of the components)[116].

1.2.2 Kinetics of Bimolecular Energy Transfer Processes in Organic Semiconductors

Bimolecular processes on excited state are related to quenching processes. Photoluminescence quenching depends on the presence of an energy quencher "Q" (also called as acceptor "A"), which can be an impurity on the organic semiconductor, or dye added as guest on purpose in a host-guest systems (conducting polymer blends or conducting polymer:coordination compound composite) . Herein, it will be present the main concepts about energy transfer processes that may be occur in the OLEDs devices.

1.2.3.1 Energy Transfer

The understanding of energy transfer mechanisms is of great interest to many scientific fields. Among them we can cite: materials science, where energy and charge transfer processes play an relevant role on optoelectronic properties and efficiency of organic and polymeric light emitting diodes (OLEDs and PLEDs)[9,119] and photovoltaic cells, for which those events are used to explain their operation[88]; biology, where there are many studies about non-radiative energy transfer in biochemical systems[2,120]; chemistry, where through energy transfer one may obtain the actual distance between molecules and estimate its efficiency as a

function of the distance and emission lifetimes from host to guest;[118,121] physics, which developed the main models to the comprehension of radiative and non-radiative energy, whereupon we highlight Förster model (1946), described from quantum mechanical and classical physics[122,123]. Also, here the chromophores involved in energy transfer processes were called "A" (acceptor) and "D" (donor).

1.2.3.2 Radiative Energy Transfer

The radiative energy transfer process is also designated as the trivial model due to the simplicity of the physical process involved on the energy transfer from donor (D*) to acceptor (A*). Its mechanism is considered simple since the donor (a species on the excited state) deactivates radiatively through fluorescence ($^1D^*$) or phosphorescence ($^3D^*$), the acceptor (a species on the singlet ground, ^1A) absorbs this energy coming from the donor, goes to the excited state ($^1A^*$), and finally deceives too – radiatively or not.

Therefore, this process demands spectral overlap between the emission electronic spectrum of D* and the absorption electronic spectrum of ^1A. Figure 1.14 presents the proposed mechanism, which is relevant to diluted solutions or solid systems with two independent layers.[116]

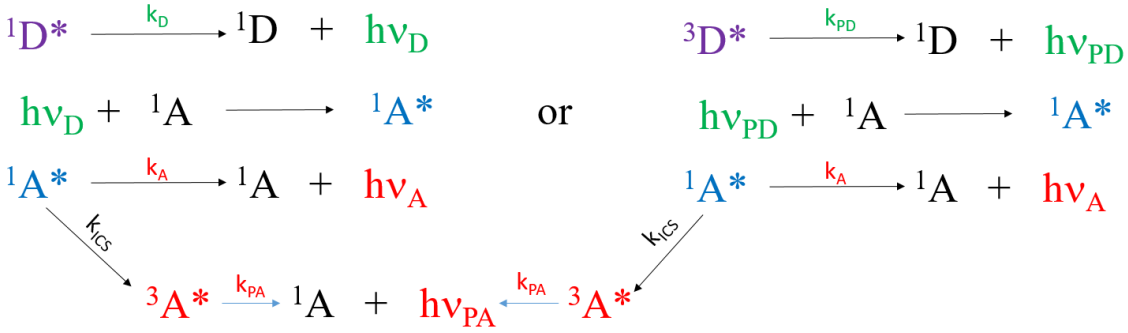

Figure 1.14. Radiative Energy Transfer mechanism between $^1D^*$ or $^3D^*$ as donor, and ^1A as the acceptor. Where: k_D and k_A are the fluorescent rate constants to deactivation of $^1D^*$ and $^1A^*$; $h\nu_D$ and $h\nu_A$ represent the emitted light by $^1D^*$ and $^1A^*$; k_{PD} and k_{PA} are the phosphorescent rate constants to deactivation of $^3D^*$ e $^3A^*$; $h\nu_{PD}$ and $h\nu_{PA}$ represent the emitted light by $^3D^*$ and $^3A^*$. Adapted from Birks 1970.[116]

It is important to emphasize that for low intensity transitions as $S_0 \rightarrow T_1$ and $T_0 \rightarrow T_1$, the probability a_{AD} of trivial energy transfer to triplet ground state ^3A is close to zero. At the same time, if the chromophore ^1A has a high intersystem crossing rate constant, the excited species $^1A^*$ will become $^3A^*$, being that the last one maybe phosphorescent.[116]

Also, trivial energy transfer processes from PLEDs to environmental-friendly dyes CCLs might be used to obtain multicolor emission diodes, as Azevedo et al 2016[16] presented in his manuscript. The authors presented the use of PFO and F8BT PLEDs EL emission with Erythrosin B (ERB) and Rose Bengal (RB) environment-friendly composites with poly(vinyl alcohol) (PVA) at (0.01 % mol/mol ratios) CCLs (Figure 1.15). ERB and RB electronic absorption spectra did not exhibit spectral overlap with PFO EL spectrum, while they exhibited a higher spectral overlap with F8BT EL spectrum. Thus, combining the red-dyes PL color with yellow color of the PLED device, tuning the result color from yellow to red emission, increasing the PVA:dye film thickness. However, an efficiency loss was observed with the addition of the CCL layers.[16]

1.2.3.3 Non-radiative Energy Transfer

In this section, theoretical and experimental concept regarding a specific mechanism of non-radiative energy transfer related to photophysical and photochemical processes, the Förster Resonance Energy Transfer (FRET) mechanism. A model developed by Theodore Förster during the 1940s[10].

The kinetic mechanism to Förster model is of pseudo-first order. In spite of not depending on collisions, FRET is treated as a bimolecular process between ^{1}D* and ^{1}A (Figure 1.15).

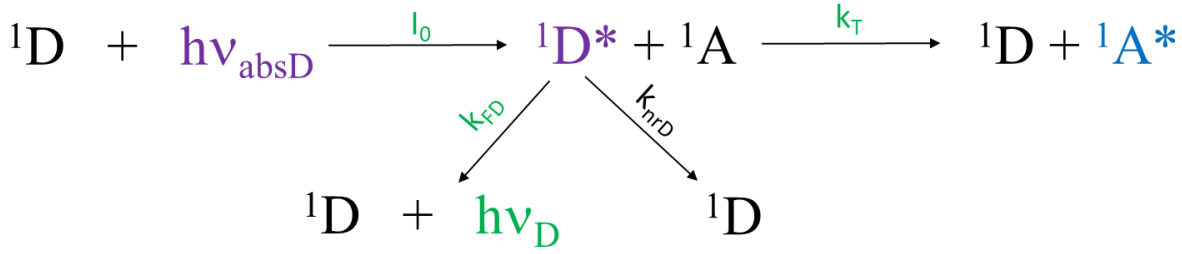

Figure 1.15. FRET kinetics mechanism between donor ^{1}D* and acceptor ^{1}A. With $\boldsymbol{k_T}$ as the FRET rate constant.

Having said that, we can write the kinetic equation that describes the deactivation rate of ^{1}D* as a bimolecular process follows:

$$\frac{d[\,^1D^*]}{dt} = I_0 - (k_{FD} + k_{nrD})[\,^1D^*] - k_T[\,^1A][\,^1D^*] \qquad (1.20)$$

Considering the pseudo-first order approximation:

$$\frac{d[\,{}^1D^*]}{dt} = I_0 - \left(k_{FD} + k_{nrD} + k_T[\,{}^1A]\right)[\,{}^1D^*] \tag{1.21}$$

Again, in photodynamic case, $[\,{}^1D^*] \propto I_D(t)$:

$$\frac{dI_D(t)}{dt} = -\left(k_{FD} + k_{nrD} + k_T[\,{}^1A]\right)I_D \tag{1.22}$$

Integration and subsequent application of the exponential function on equation 1.22, it results in the equation 1.23:

$$I_D(t) = I_{D0}e^{-(k_{FD}+k_{nrD}+k_T[\,{}^1A])t} \tag{1.23}$$

It is known that $k_{FD} + k_{nrD} = k_D = \frac{1}{\tau_D}$, thus:

$$k_{FD} + k_{nrD} + k_T[\,{}^1A] = \frac{1}{\tau_{AD}} \tag{1.24}$$

This is an indicative that when species ^{1}D* are in the presence of acceptor ^{1}A, the fluorescence lifetime of ^{1}D* (τ_D) will be decrease to τ_{AD}, the fluorescence lifetime of ^{1}D* in the presence of ^{1}A, as a consequence of FRET.

In other words, replacing equation 1.24 on 1.23 giving:

$$I_{DA}(t) = I_{DA0}e^{\frac{t}{\tau_{AD}}} \tag{1.25}$$

Further algebraic modifications in the equation 1.24 it offers the photodynamic experimental FRET efficiency (E_{FRET}) relation:

$$k_{FD} + k_{nrD} + k_T[\,{}^1A] = \frac{1}{\tau_{AD}}$$

$$k_D + k_T[\,{}^1A] = \frac{1}{\tau_{AD}}$$

$$k_T[\,{}^1A] = \frac{1}{\tau_{AD}} - k_D$$

$$k_T\left[\,^1A\right] = \frac{1}{\tau_{AD}} - \frac{1}{\tau_D}$$

$$k_T\left[\,^1A\right] = \frac{\tau_D - \tau_{AD}}{\tau_D \tau_{AD}}$$

$$\tau_{AD} k_T\left[\,^1A\right] = \frac{\tau_D - \tau_{AD}}{\tau_D}$$

$$E_{FRET} = \tau_{AD} k_T\left[\,^1A\right] = 1 - \frac{\tau_{AD}}{\tau_D} \qquad (1.26)$$

Until now, the mechanism[124] to FRET was described on kinetic terms. However, the real meaning of the FRET rate k_T is not fully explained. To do so, Förster theory to non-radiative energy transfer makes use of quantum and classical mechanics[125]. Considering a system with ^{1}D* in a certain distance *r* from ^{1}A in a rigid and inert solvent, the electronic energy of the donor will be greater than the one of the acceptors ($E_D > E_A$). Thus, intramolecular non-radiative energy transfer is a resonance phenomenon, which involves transitions on isoenergetic levels of donor and acceptor (Figure 1.16)[15,126]. In this point, it is relevant to mention that non-radiative energy transfer to such system can happen by Coulombic interactions (FRET) or by a redox reaction with electron exchange (Dexter model[124]) between ^{1}D* and ^{1}A.

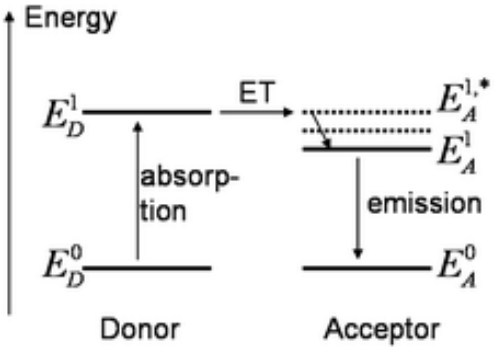

Figure 1. 16. Schematic view of FRET process with the energy levels of donor and acceptor (E and E_A)[126].

Thereby, the electronic transitions ^{1}D* → ^{1}D e ^{1}A → ^{1}A*, schematic depicted on Figure 1.9, correspond to the fluorescence spectrum of ^{1}D* ($F_D(\lambda)$) and the absorption spectrum of ^{1}A ($\varepsilon_A(\lambda)$). Furthermore, in terms of the energetic evolution of the process, FRET works as an adiabatic reaction[127], and the energy difference $E_D - E_A$ can be partitioned on vibrational levels of the two species[1].

Besides, FRET rate constant is expressed as:

$$k_T = \frac{4\pi p_E}{h} \beta_{el}^2 F \qquad (1.27)$$

where p_E is the density of vibronic state, β_{el} is the element of matrix to electrostatic interaction between initial and final states, h is the Planck constant, and F the Franck-Condon factor (as giving by equation 1.9), given by the sum:

Coulombic interaction originated on excited state between ^{1}D* and ^{1}A can be divided in two terms: one from the pure electrostatic interaction (defined by Förster)[122] and another from electron exchange (defined by Dexter in 1951)[124]. These interactions are the result of multipole-multipole expansion of charge interaction, with the major contribution from the dipole-dipole interaction. This "dipole-dipole" force comes from the transaction dipole moments of both species, μ_D and μ_A, and express the term β_{el} from equation 1.27:

$$\beta_{el}\ \alpha\ \frac{\mu_D \mu_A}{r^3} \tag{1.27}$$

With this result, Förster also derived a relation to obtain k_T only expressed by experimental parameters, now as a function of the distance r:

$$k_T(r) = \frac{(9000ln10)\kappa^2}{128\pi^5 n^4 N \tau_D r^6} \int_0^\infty F_D(\lambda)\varepsilon_A(\lambda)\lambda^4 d\lambda \tag{1.28}$$

where, n is the medium refractive index, τ_D is the emission lifetime of ^{1}D* in the absence of ^{1}A; N is the Avogadro constant, $\int_0^\infty F_D(\lambda)\varepsilon_A(\lambda)\lambda^4 d\lambda$ integral is the spectral overlap integral between the donor fluorescence ($F_D(\lambda)$) and acceptor absorption ($\varepsilon_A(\lambda)$) spectra, κ is the orientation factor of the transition dipole moments from ^{1}D* and ^{1}A, which varies from 0 to 4, the values to perpendicular and parallel transitions, and mathematically expressed by:

$$\kappa = cos\theta_{AD} - 3cos\theta_D cos\theta_A \tag{1.29}$$

where, θ_{AD} is the angle between μ_D and μ_A, θ_D and θ_A are the angles formed between the transiction dipole moments and their resulting vector. κ is experimentally obtained bt transient anisotropy measurements, but, commonly, it is assumed to be equal to 2/3 for randomly distribution of donor and acceptor species.

Furthermore, equation 48 can be rewritten to a most useful way, as follows:

$$k_T(r) = \frac{1}{\tau_D}\left(\frac{R_0}{r}\right)^6 \tag{1.30}$$

where R_0 is a critical distance to non-radiative energy transfer, also it is known as the "Förster radius". It is the distance to an efficiency of resonant energy transfer equal to 50%.

$$R_0^6 = \frac{(9000ln10)\kappa^2}{128\pi^5 n^4 N} \int_0^\infty F_D(\lambda)\varepsilon_A(\lambda)\lambda^4 d\lambda \quad (1.31)$$

Finally, FRET efficiency E_{FRET} can also be written as a function of the distance between donor and acceptor single pair:

$$E_{FRET}(r) = \frac{{R_0}^6}{{R_0}^6 + r^6} \quad (1.32)$$

Taking into account the FRET mathematical formalism, this kind of energy transfer is also studied in conducting polymers frameworks, in order to understand the true role of ET processes on organic electronic devices. Nome et al., in 2011[128], described energy transfer from PFO (blue emitter) to MEH-PPV (orange emitter) in solution and solid-state (thin-film) (Figure 1.14), a classical polymer blend to white-light generation, using steady-state and time-resolved fluorescence measurements. In this manuscript, it was observed that the ET process in this system was composed by two mechanisms: the trivial and FRET. It was possible to separate and quantify these two mechanisms, using the total energy transfer calculation from the steady-state fluorescence spectra and the suppression of the PFO (donor) fluorescence life-times in the presence of MEH-PPV (acceptor), quantifying only the FRET mechanism.

Also, de Azevedo and his contributors 2017[129] presenting in their manuscript the separation between the contributions of PFO and F8BT emissions in two kinds of device: blend and layer PLEDs as function of its concentration. Also, the authors identified the contribution of FRET-like energy transfer process in these diodes, with the bi-layer device exhibiting a highest FRET efficiency than the blend PLED, using the classical Förster equations for resonant energy transfer phenomena. This behavior is possible due the interpenetration between PFO and F8BT layers, leading a high contact among the polymers in comparison to its polymer blend, according to the authors. Thus, the steady-state and transient photophysical properties are fundamental to understand these processes.

The use of the photoluminescence techniques is fundamental to comprehend the devices work as well as which polymer phase, organization and chromophore favors the radiative pathways in the PLED. Thus, Ma et al 2010 (PL with temperature)[130] and Bonon et al

2012 (steady-state measurements with Stern-Volmmer equation)[95] described the three species of PVK on excited state, leading to an multiexponential fluorescence decay, using steady-state and transient techniques. According to these authors observations and measurements, PVK polymer presents an multiexponential decay composed by three species: the isolated carbazole (PVK), the partially overlapped (p-PVK) and the fully overlapped (f-PVK) species. According to the authors observations, the fastest fluorescence lifetime was attributed to isolated carbazole, the intermediary to the p-PVK and the slowest to the f-PVK.

1.3 Objectives

This Ph.D. thesis has as principal objective to present novel simple strategies for improvement of the optical-electronic properties of the salicylidenes (*N,N'-bis(salicylidene)-o-phenylenediamine* (salophen), *N,N'-bis(salicylidene)-3,4-diaminebenzophenone* (sal-3,4-ben) and *N-salicylidene-5-chloroaminopyridine* (sal-5Cl-py)) and their Zn(II) (*aquo[N,N'-bis(salicylidene)-o-phenylenediamine]zinc(II)* ([Zn(salophen)] and *aquo[N,N'-bis(salicylidene)-3,4-diaminebenzophenone]zinc(II)* ([Zn(sal-3,4-ben)]) and Pt(II) coordination compounds (*N,N'-bis(salicylidene)-o-phenylenediamineplatinum(II)* [Pt(salophen)] and *N,N'-bis(salicylidene)-3,4-diaminebenzophenoneplatinum(II)* ([Pt(sal-3,4-ben)]); Figure 1.17) as guests for active-matrix all-solution-processable OLEDs, manipulating the polymer-host charge mobilities and PLQY, small and easy chemical modifications on the salicylidene ligand framework as simple and low-cost alternatives, energy and material saving principles in contrast to multilayer devices, by combining firstly a blue-fluorescent polymer (PVK and PFO) with a yellowish-fluorescent Zn(salicylidenes) coordination compounds and then blue-fluorescent polymer with red-phosphorescent Pt(salicylidenes) coordination compounds in order to achieve high performance WOLEDs.

1.3.1 Specific Objectives

To synthetize and to characterize structurally new salicylidene derivatives and their Zn(II) and Pt(II) coordination compounds by ^{1}H and ^{13}C nuclear magnetic resonance (NMR) and Fourier-transform infra-red (FT-IR) spectroscopies, high-resolution mass spectrometer (HR-MS), thermogravimetric analyses, CHN elemental analyses and single-crystal X-ray diffraction (SC-XDR);

To evaluate photophysics of photochemical processes of salicylidene derivatives and their Zn(II) and Pt(II) coordination complexes in solution and solid-state by steady-state

and time-resolved electronic spectroscopies techniques. To study the role of photoacidity on the excited-state intramolecular proton transfer reactions on a simple salicylidene system;

To determine the presence and efficiencies of the energy transfer processes (trivial and/or FRET-like) between the host conducting polymers (PVK or PFO) and the salicylidene derivatives by steady-state and transient fluorescence measurements, according to FRET kinetics equation model (equation 1.32);

To obtain the optimized molecular, electronic structures and calculated vertical excitations of the salicylidene derivatives and their Zn(II) and Pt(II) coordination compounds under density functional theory and time-dependent density functional theory (DFT and TD-DFT) framework;

To assemble all-solution-processable organic layers OLEDs with a conducting polymer-salicylidene derivative host-guest composite as EML, using PVK or PFO as polymer matrix and to evaluate their optical-electronic properties in terms of current density, luminance, chromaticity, EL spectra and current efficiencies *versus* voltage curves;

To evaluate morphological changes on PFO polymer host due to the addition of the Zn(salicylidenes) as function of the coordination compounds concentration by fluorescence confocal measurements;

To improve optical-electronic properties of Zn(II) and Pt(II) salicylidenes by modifying the host-conducting-polymer charge mobility (μ) and PLQY (from PVK to PFO devices);

To determine the key-role of the hole-charge mobility and singlet and triplet-harvesting on the PVK and PFO pure devices and in their composites with the salicylidene derivatives, according to the TCLC at the OLEDs driving voltage region and the influence of the salicylidene derivative electronic structure in ground and excited states to OLEDs performances.

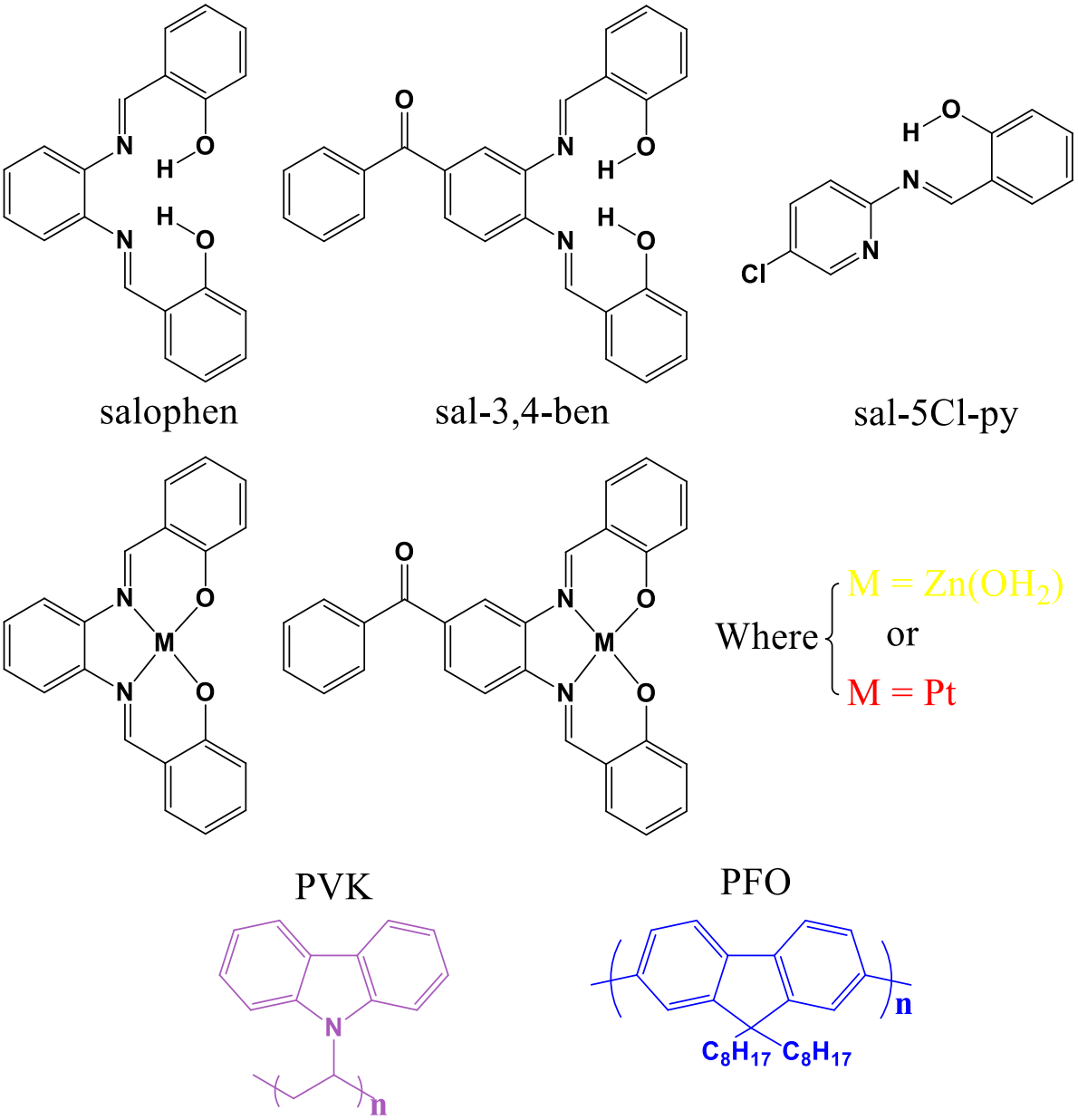

Figure 1. 17. Molecular structures that was used in this Ph.D. thesis: salicylidene derivatives, their aquo-Zn(II) and Pt(II) coordination compounds and PVK and PFO conducting polymers-host.

CHAPTER 2

PHOTOPHYSICS OF NEW SALICYLIDENE DERIVATIVES AND REACTIVITY OF EXCITED-STATE INTRAMOLECULAR PROTON TRANSFERS (ESIPT)

2.1 Motivation

Recently, a series of new materials that are potentially useful in the field of organic electronics as photonics,[131,132] sensors and actuators,[133,134] photovoltaic cells,[135,136] organic light-emitting diodes,[9,137] and photoswitching systems[138] have been synthesized.[2] Some of them are π-conjugated molecules,[9,139,34] such as the salicylidenes, which have interesting applications in material sciences,[140] coordination chemistry,[141,142] catalysis,[143,144] supramolecular chemistry,[143,145,146] optical chemosensors,[147] photonics and in OLEDs as active layers and electron transport layers.[148–152] Salicylidenes have been widely used in coordination chemistry as ligands[153,154] that coordinate with certain metal atoms, including Al(III),[150] Zn(II),[155,156] Ru(II),[157,158] Pt(II),[151] Ni(II),[159] and Cu(II).[160,161]

Salicylidenes are particularly interesting molecules because they might exhibit intramolecular proton transfer in the electronic excited state and also they can be obtained from a easy and inexpensive chemical reaction between salicylaldehyde and a primary amine, called Schiff's condensation.[152,162] This process involves a hydrogen transfer from the nitrogen to the oxygen atoms of the iminic group, leading to a balance between the enol (E^*) and keto (K^*) species and, consequently, dual fluorescence decays.[163] The keto form emits at a lower energy than the enol tautomer. Experimentally, the occurrence of the ESIPT process is evidenced by the dual fluorescence decay profile and large Stokes shifts (*SS*).[152,163,164] Because the ESIPT is a very fast process (50 ~ 400 fs)[165], two emission bands are observed with a constant ratio under stationary conditions. Also, because the ESIPT process is influenced by the solvent-solute interactions, the intensity ratio between the two emission bands can be modified by the solvent. If these two emission bands are not overlapped, the final emission color is completely different of every individual emission. Depending on the balance between the emissions of these two species, white light emission can be obtained. This combination would be potentially useful for white emitting OLEDs (WOLEDs).[163,167] Thus, for OLEDs application with white emission one should looking for molecules undergoing ESIPT with the following characteristics: emissions with two different colors, non-expensive and abundant materials, easily synthetic process with good yields and well known ESIPT process.[44,60]

In a previous work we studied the ESIPT mechanism of two salicylidene derivatives in solutions and in solid state.[152] One molecule was the *N,N'-bis*(salicylidene)-1,2-phenylenediamine (salophen) and the other was the *N,N'-bis*(salicylidene)-4,5-diaminopyrimidine (sal-4,5-pym). These two molecules are differentiated only by the presence of the 4,5-diaminopyrimidine moiety. That results suggest the occurrence of ESIPT only in the

case of sal-4,5-pym in solutions. The emissions from the E^* and K^* species of this molecule were observed at 425 and 545 nm, respectively, whereas for the parent compound, salophen, only emission from the E^* species is observed at approximately 460 nm. In addition, theoretical calculations at the time-dependent density functional theory (TD-DFT) level showed that the distance between the nitrogen and the proton was controlling the ESIPT process. Also, radiative decay for the K^* specie can occur through two different deactivation channels: (i) intersystem crossing (ISC), which leads to the triplet excited state of the K^*- tautomer and (ii) tautomerization generating the *keto* form, which is a faster process. Such processes can be mapped by time-resolved transient absorption spectroscopy.[165]

In this way, herein we synthetized two new salicylidene derivatives: *N,N'-bis*(salicylidene)-3,4-benzophenone (sal-3,4-ben) and *N-salicylidene-5-chloroaminopyridine* (sal-5Cl-py). In the two systems, the structural characterizations were done by ^{1}H and ^{13}C 1D NMR and FT-IR spectroscopies, ESI-MS at positive mode, CHN elemental analyses and single-crystal X-ray diffraction using Mo-α source. The mechanism ESIPT occurrence of the sal-3,4-ben was evaluated by steady-state (electronic absorption and emission spectroscopies) and transient (ultrafast white-light pump-probe transient absorption, time-correlated single-photon counting (TCSPC) and time resolved emission spectroscopies (TRES)) techniques and with DFT and TD-DFT calculation. In the case of sal-5Cl-py, in contrast to the previously studied rigid bis-salicylidenes structures, might undergo rotation around the C-N bond, leading to *cis* - *trans* isomerism that may influence on ESIPT processes, which was employed under DFT and TD-DFT framework. In the two ESIPT reactive molecular structures two separated emission bands in DMSO solutions: an emission band centered around the blue and other around the red regions of the visible electromagnetic spectrum; each of the emission bands present different fluorescence dynamics with two exponential behavior, containing two fluorescence rates, which corroborates to the presence of E K balance on the excited-state; and in the two cases, an ultrafast ESIPT processes was observed. Thus, generating white-light emission from a single chromophore, which is essential for development WOLEDs devices.

2.2 Materials and Experimental Details

2.2.1 Materials

3,4-diaminobenzophenone, 5-chloroaminopyridine, salicylaldehyde, ethylene glycol, DMSO-d_6 and $CDCl_3$ were purchased from Sigma-Aldrich, São Paulo, Brazil. DMSO solvent in HPLC/Spectrum grades was purchased from Tédia, Brazil.

2.2.2 Experimental Details

^{1}H (Figure A1) and ^{13}C (Figure A2) NMR 1D spectra of sal-3,4-ben in DMSO-d_6 solution (33 mg mL^{-1}) were measured in a Varian Mercury 300 MHz spectrometer. ^{1}H (Figure A5) and ^{13}C (Figure A6) NMR 1D spectra of the sal-5Cl-py in $CDCl_3$ (33 mg mL^{-1}) were acquired in a Bruker Avance 400 MHz spectrometer. FTIR spectra of sal-3,4ben (Figure A3) and sal-5Cl-py (A7) were recorded in an Agilent Technologies Cary 630 spectrometer in attenuated total reflectance (ATR) mode. Elemental analysis (%) of the C, H and N atoms was performed using a Perkin-Elmer microanalyzer model PE 2400.

Electrospray mass spectroscopy (ESI-MS) of sal-3,4-ben (Figure A4) and sal-5Cl-py (Figure A8) were measured on a Bruker HCT Ultra spectrometer in Ultra-Scan with a mass work range of 50−400 m/z. ESI acquit with mist flow of 10 μL min^{-1}, capillary voltage of 3,000 V, nebulizer gas pressure of 10 psi, drying gas flow rate of 5 L min^{-1} and dry temperature of 300 °C at ESI+ mode sampler was used for salophen at 10 ppm ($3.16x10^{-5}$ mol L^{-1}) in acetonitrile (ACN) with 0.5 % (V/V) of formic acid to protonate the salophen molecules.

Crystal structure of sal-3,4-ben (Table A1) and sal-5Cl-py (Table A2) were determined by single-crystal X-ray diffraction in a Bruker Apex Duo X-ray diffractometer using Mo (Ka = 0.71073 Å) radiation with the following software for cell refinement: APEX2[168] for data collection, SAINT[168] for cell refinement and data reduction, SHELXS97[169] to solve structure and SHELXL2014/7[170] for refine structure and Mercury[171] for molecular graphics.

2.2.2.1 Synthesis of sal-3,4-ben

Sal-3,4-ben was obtained by dissolving the 3,4-diaminobenzophenone (1 mmol; 212 mg) in ethyleneglycol (15 mL) by sonication (Figure 2.1). After 5 minutes, the salicylaldehyde (244 mg; 211 μL; 2 mmol) was slowly dropped into this solution, and the mixture was then sonicated for 1 hour. The precipitate was filtered, recrystallized in hot ethanol, it kept in refrigerator (10 °C) for two days to furnish plate-like yellow single crystals and washed with cold ethanol. The reaction yield was 71 %. Sal-3,4-ben was a yellow crystalline solid with the following elemental analysis (%): C 77.13, H 4.79, N 6.66 and O 11.42. MS (ESI+): m\z 421.20 (calcd for M+ 421.16). m.p.: 111 °C. ¹H NMR (300 MHz, DMSO-d_6) δ (ppm): 6,95 (*m*, 2H), 7.41 (*m*, 4H), 7.57 (*t*, *J* = 9.0 Hz, 2H), 7.69 (*m*, 6H), 7.79 (*d*, *J* = 6.6 Hz, 2H) 8,96 (*s*, 1H) and 8.97 (*s*, 1H).^{13}C NMR (75 MHz, DMSO-d_6) δ (ppm): 117.37, 117.46, 119.86, 119.90, 120.13, 120.21, 120.70, 121.40, 129,37, 129.99, 130.39, 133.09, 133.22, 133.54, 134.42, 134.72, 136.60, 137.60, 142.93, 146.76, 161.05, 161.05, 165,54, 165.65 and 195.44. The main infrared

bands at ATR mode are (cm^{-1}) $\nu_{C=N}$ = 1610, ν_{O-H} = 3337 and 3460, $\nu_{C=O}$ = 1648, ν_{C-O} = 1277 and 1270, $\nu_{Ar(C-H)}$ = 3053, and ν_{Ar} = 747 and 706.

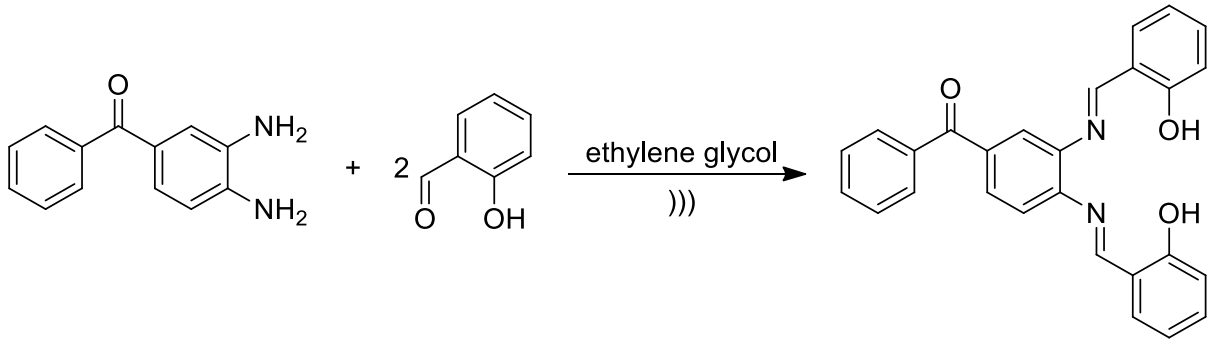

Figure 2. 1. Scheme for the synthesis of sal-3,4-ben in ethylene glycol.

2.2.2.2 Synthesis of sal-5Cl-py

Sal-5Cl-py was obtained by dissolving 5-chloroaminopyridine (1 mmol; 128 mg) in ethanol (15 mL) under sonication (Scheme in Figure 2.2). After 5 minutes, salicylaldehyde (1 mmol; 106 μL) was slowly dropped into this solution, and the mixture was sonicated for 1 hour. Then, the reaction mixture was refrigerated, yielding yellow crystals that were filtered under vacuum, recrystallized from hot ethanol and washed with cold ethanol, leading yellow single-crystals. The reaction yield was 95%. Elemental analysis (%): Calculated: C 61.95, H 3.90 and N 12.04; found: C 61.90, H 3.92 and N 12.05. ^{1}H NMR (400 MHz, $CDCl_3$) δ 13.23 (s, 1H), 9.40 (s, 1H), 8.45 (s, 1H), 7.74 (d, *J* = 8.4 Hz, 1H), 7.50 (d, *J* = 7.7 Hz, 1H), 7.43 (t, *J* = 7.0 Hz, 1H), 7.27 (d, *J* = 8.4 Hz, 1H), 7.04 (d, *J* = 8.3 Hz, 1H) and 6.97 (t, *J* = 7.5 Hz, 1H); ^{13}C NMR (101 MHz, $CDCl_3$) δ 165.21, 161.87, 155.90, 147.78, 138.09, 134.16, 133.63, 130.42, 121.17, 119.37, 118.87 and 117.33. MS (ESI+): *m/z* 233.00 (calcd for M^+: 233.04). The characteristic infrared bands from ATR are (cm^{-1}) $\nu_{C=N}$ = 1606, ν_{C-O} = 1279, ν_{C-Cl} = 522, ν_{C-H} = 3050, and ν_{Ar} = 771.

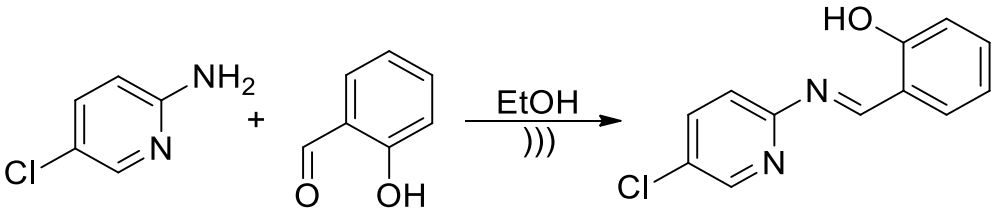

Figure 2. 2. Scheme for the synthesis of sal-5Cl-py in EtOH.

2.2.2.3 Steady-state Photophysical Measurements

Electronic absorption spectrum in solution and solid-state were measured using a *Hewlett-Packard* 8452A diode array spectrophotometer.

Steady-state fluorescence spectra in diluted solutions (C = 10 μmol L^{-1} in a 1 cm quartz cuvette was used) and solid-state were obtained using an ISS-PC1 spectrofluorometer using the following excitation wavelengths: λ_{exc} = 335 nm (sal-5Cl-py) and λ_{exc} = 375 nm (sal-3,4-ben and sal-5Cl-py).

2.2.2.4 Time-resolved Photophysical Measurements

Fluorescence decays were recorded using time-correlated single photon counting and an Edinburgh Analytical Instruments FL 900 spectrofluorimeter with an MCP-PMT detector (Hamamatsu R3809U-50), using a pulsed diode laser with λ_{exc} = 375 nm (Edinburg model EPL-375, with a 10 nm bandwidth, 77.0 ps) for sal-3,4-ben and sal-5Cl-py in DMSO solutions and solid-state and a pulsed diode with λ_{exc} = 335 nm (Edinburg pulsed diode model EPLED-340, with a 14.4 nm bandwidth, 815 ps) for sal-5Cl-py in DMSO, MeOH and mixtures with CF_3COOH (10 μL of concentrated CF_3COOH in 2000 μL of solution).

Sal-3,4-ben fluorescence decays signals in DMSO solution were collected at λ_{PL} = 430 and 575 nm (E^* and K^* species, respectively) and at the solid-state was collected at λ_{PL} = 560 nm. While fluorescence decays signals for the sal-5Cl-py samples were collected at λ_{em} = 376, 395, 425, 545 and 550 nm for MeOH, MeOH + CF_3COOH, DMSO + CF_3COOH and DMSO solutions and solid-state, respectively. The instrument response was recorded using Ludox samples. At least 10.000 counts in the peak channel were accumulated for lifetime measurements. The emission decays were analyzed using exponential functions.[152,65,66]

Time resolved emission spectra (TRES) of the sal-3,4-ben in DMSO solution (λ_{exc} = 375 nm; λ_{PL} = 400 to 700 nm) was recorded using the same TCSPC setup. And TRES of the sal-5Cl-py in DMSO (λ_{exc} = 375 nm; λ_{PL} = 400 to 700 nm), MeOH (λ_{exc} = 335 nm; λ_{PL} = 355 to 620 nm), DMSO + CF_3COOH (λ_{exc} = 335 nm; λ_{PL} = 350 to 550 nm) and MeOH + CF_3COOH (λ_{exc} = 335 nm; λ_{PL} = 350 to 550 nm) were recorded. The intervals between emission wavelengths were 5 nm. Delays between 0 to 2.880 ns and 0 a 15 ns were used to generate the TRES plots for the sal-3,4-ben and sal-5Cl-py samples, respectively.[137,152]

Femtosecond time-resolved excited state absorption (ESA) spectra of the sal-3,4-ben in DMSO solution (C = 10 μmol L^{-1}) were recorded using 150 fs pulses from a Ti:sapphire

chirped pulse amplified system operating at 1 kHz repetition rate (λ_{exc} = 775 nm). This beam was divided in two using a beam splitter (90% - 10%). The stronger beam was doubled (λ_{exc} = 387.5 nm) using a BBO crystal and employed as the pump pulse. A small portion of the weaker beam was used to generate the white-light continuum (WLC) probe, using a sapphire window (2 mm of thickness). The time delay between pump and probe pulses was carefully varied by a computer-controlled translation stage, providing a maximum resolution of 37.5 fs. The intensity of the relative spectral components of WLC probe pulse, at each specific time, that characterize the time-resolved transient absorption (ΔA), was monitored by means of a spectrometer. The chirp of WLC probe pulse was measured to be < 1 ps in the 400-700 nm spectral region. Pump and probe pulses with energy smaller than 1 μJ and 1nJ, respectively, were used.

2.2.2.5 Computational Details

Sal-3,4-ben calculations were done under the DFT and TD-DFT framework using the density functional PBE0[39-41] and the basis set cc-pVTZ.[42] Ligand X-ray structure was used for excited state calculations. Molecular structures, corresponding to the ground and first active singlet states (S_0 and S_1), were optimized. Calculations were done using the Orca 3.0 software.[43-45] In order to evaluate the migration of the proton in the excited state, relaxed scans were done, following the path from the phenolic oxygen to the iminic nitrogen. The solvent medium was considered through the COSMO approach.[46] Frequencies were calculated in order to assure that the optimized structures correspond to a minimum and to obtain the emission wavelength through energy differences S_1-S_0.

As sal-5Cl-py is a small-molecule in comparison to sal-3,4-ben derivative, a better DFT model (CAM-B3LYP) with a better wavefunction base (aug-cc-pVDZ) was chosen for describe its theoretical predictions. Sal-5Cl-py isolated molecules were calculated using DFT and TD-DFT as implemented in the Gaussian 09[67] and DALTON[68] software, respectively. The hybrid exchange-correlation functional CAM-B3LYP[69] and the basis set aug-cc-pVDZ[70-72] were chosen for these calculations. Solvent effects were considered using the Polarizable Continuum Model - PCM.[73-76] This calculation level has been proven to be useful in the study of the electronic ground and excited states of aromatic molecules.[77,78]

2.3 Results and Discussion

2.3.1 Sal-3,4-ben

Sal-3,4-ben was successfully synthetized by Schiff's condensation via sonication method and it characterized by ^{1}H and ^{13}C, FT-IR, ESI-MS, elemental analyses and single-crystal X-ray diffraction, analogous to salophen and sal-4,5-pym.[173] Figure 2.3 (a) illustrates the molecular structure of the sal-3,4-ben using (a) 50% probability displacement ellipsoids, while (b) show the ones obtained by X-ray diffraction of the *cis*-sal-3,4-benand optimized geometries at ground (S_0) and first singlet excited state (S_1), at the PBE0/cc-pVTZ level.

The structure of the sal-3,4-ben determined by X-ray diffraction indicates that the C-N-C-C torsion angles involving the fragments that contain the imine groups are very close (C1-N1-C14-C15 = -179.49 (18)° and C2-N2-C21-C22 = -179.84 (18)°), while those for C-C-C-O are slightly different from each other (C14-C15-C20-O2 = 0.3 (3)° and C21-C22-C23-O3 = 1.5 (3)°). Both C14=N1 and C21=N2 of the imine groups assume an (*E*) configuration that favors the O2H2A···N1 and O3H3A···N2 intramolecular hydrogen bonds (Table 2.1). These intramolecular interactions are also present in the structure of salophen,[47] whose geometric parameters are similar to those of the title compound: *D*···*A* distances of 2.613 (1) Å and 2.564 (1) Å (for the title compound: 2.667 (2) Å and 2.546 (2) Å, respectively) and *D*-H···*A* angles of 147.0° and 150.0° (for the title compound: 143 (2)° and 158 (2)°, respectively).

Table 2. 1. Structure data for the hydrogen-bond interactions of the sal-3,4-ben molecule.

D—H···*A*	*D*—H	H···*A*	*D*···*A*	*D*—H···*A*
O3—H3*A*···N2	0.92 (3)	1.67 (3)	2.546 (2)	158 (2)
O2—H2*A*···N1	0.89 (2)	1.91 (3)	2.667 (2)	143 (2)
C14—H14···O3^{i}	0.93	2.40	3.219 (3)	147
Symmetry code: (i) *x*, *y*+1, *z*.				

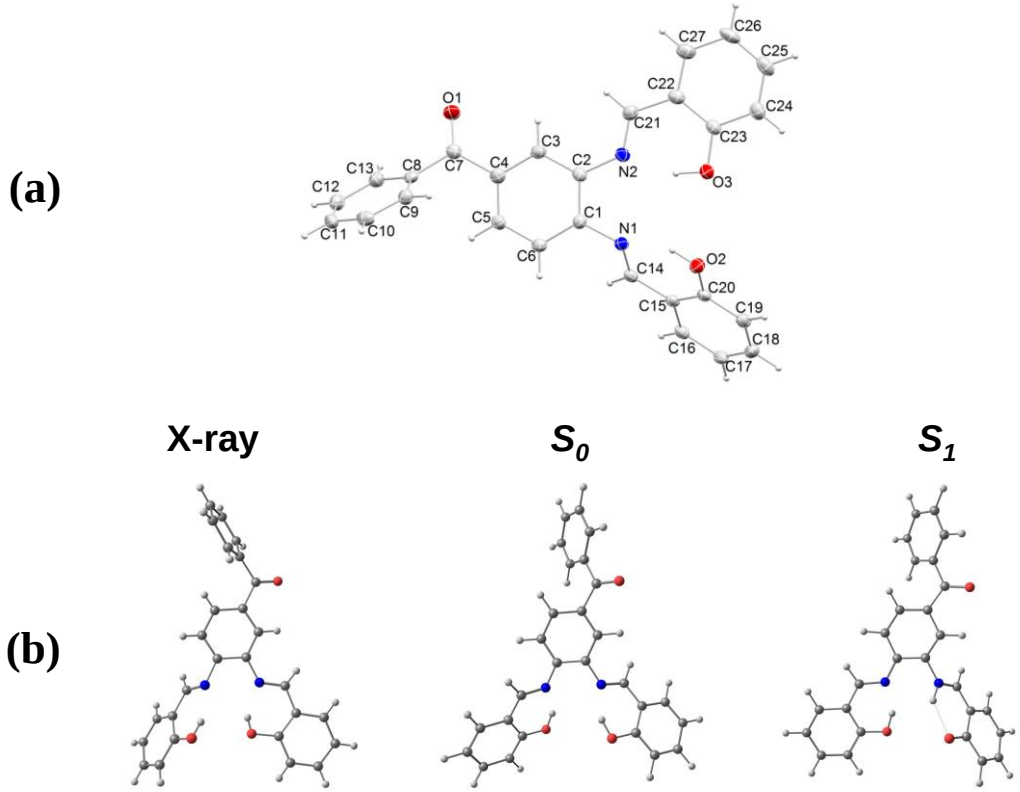

Figure 2. 3. (a) Molecular structure of the sal-3,4-ben using 50% probability displacement ellipsoids. (b) Molecular structures obtained by X-ray diffraction of the cis-sal-3,4-ben, and optimized at ground (S0) and first singlet excited state (S1) at the PBE0/cc-pVTZ level

Figure 2.4 shows the ground-state absorption (solid lines – left axis) and fluorescence spectra (diamonds – right axis) for the sal-3,4-ben dissolved in DMSO (dimethyl sulfoxide). It is observed that the sal-3,4-ben present strong absorption band at 338 nm with high molar absorptivity (2.16×10^4 L mol^{-1} cm^{-1}) and two shoulders at 375 ($1.58x10^4$ L mol^{-1} cm^{-1}) and 470 nm.

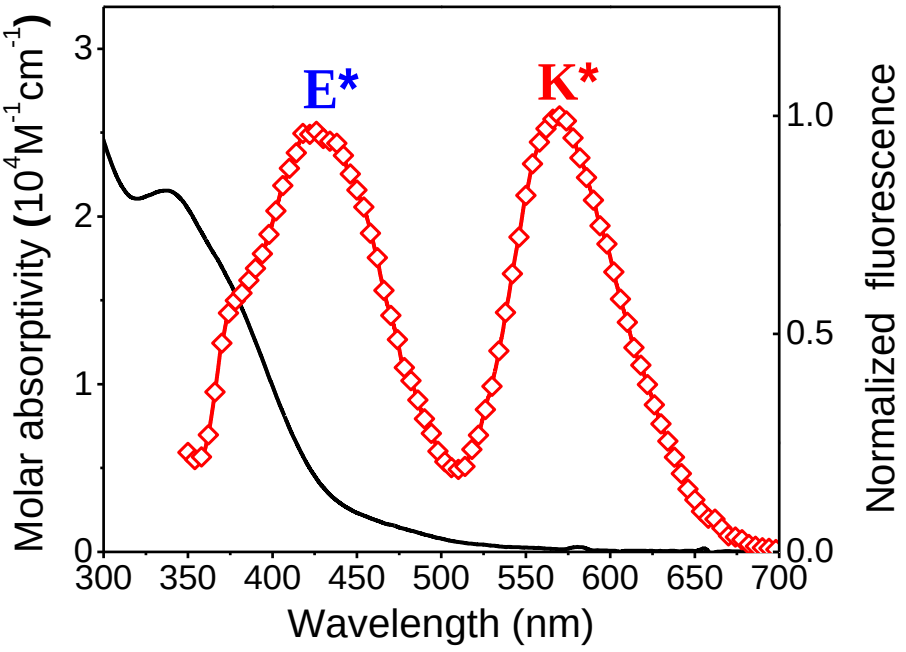

Figure 2. 4. Electronic absorption (black curve) and normalized photoluminescence spectra (red curve with open-diamonds) of sal-3,4-ben in DMSO solutions (C = 10 μmol L^{-1}; λ_{exc} = 375 nm).

According to our calculations, performed using PBE0/cc-pVTZ and considering DMSO as solvent, the band located at 375 nm presents π-π^* character (λ = 371 nm and f = 0.40), involving HOMO → LUMO transition with the molecular orbitals located on the conjugated backbone (data shown in Figure 2.5). The presence of the benzophenone increases macrocycle electron delocalization, red shifting the ligand absorption bands in respect to the parent salophen compound,[30] while the shoulder, that was also observed in the salophen DMSO solution absorption spectra, can be assigned to a vibronic transition.[30]

According to our data, the sal-3,4-ben crystalline structure corresponds to the *cis* isomer with a non-symmetric conformation. Selected structural parameters are given in Table 2, whose labels are shown in Figure 2.3 (a). Neither ground state or crystal structures are planar, however, as previously observed for this type of ligand, the planarity of the ligand framework increases upon excitation, [26,31] favoring the appearing of the absorption bands in the 400 nm region, observed in the absorption spectrum. In addition, as shown in Ref. [30] for relative ligands salophen and sal-4,5-pym, the ground state N-H bond distance of the sal-3,4-benis short enough (~0.7 Å) to allow proton transfer upon excitation.

Table 2. 2. Selected bond lengths (Å) and dihedral angles (degrees) for the ground and first singlet state structures of the ligand calculated at the PBE0/cc-pVTZ level.

	S_0	S_1
C_2-N_2	1.394	1.439
N_2-$_{21}$	1.284	1.276
C_{21}-C_{22}	1.438	1.440
C_{22}-C_{27}	1.400	1.374
C_{27}-C_{26}	1.375	1.404
C_{26}-C_{25}	1.395	1.395
C_{25}-C_{24}	1.380	1.372
C_{24}-C_{23}	1.396	1.446
C_{23}-O_3	1.328	1.238
O_3-H	0.993	1.895
O_2-N_1-N_2-O_3	41.7	29.0

The possibility of the ESIPT was evaluated through a structure relaxed scan, performed by optimizing the structure corresponding to the ground and first excited singlet states (S_0 and S_1), varying the O-H distance, as shown in Figure 2.5. As it can be seen, in the ground state the enol conformation is more stable than keto by ~ 5 kcal mol^{-1}. The opposite trend is observed for S_1, suggesting the occurrence of the proton transfer from the phenolic oxygen to the iminic nitrogen upon excitation. The small energy barrier observed between enol* and keto* species in the S_1 state (~10 kcal mol^{-1}) suggests that the single proton transfer process can occur in this state. This data suggests that the cis-keto tautomer is significantly more stable than cis-enol in the first active singlet state, in agreement with the large Stokes shift and dual fluorescence decay profile observed experimentally, supporting ESIPT process for the sal-3,4-ben. In addition, calculated emission energy for the $S_1 \rightarrow S_0$ transition (524 nm) suggests that the experimentally observed emission band around 575 nm is due to the decay from the longer lived cis-keto* to the ground state cis-enol.

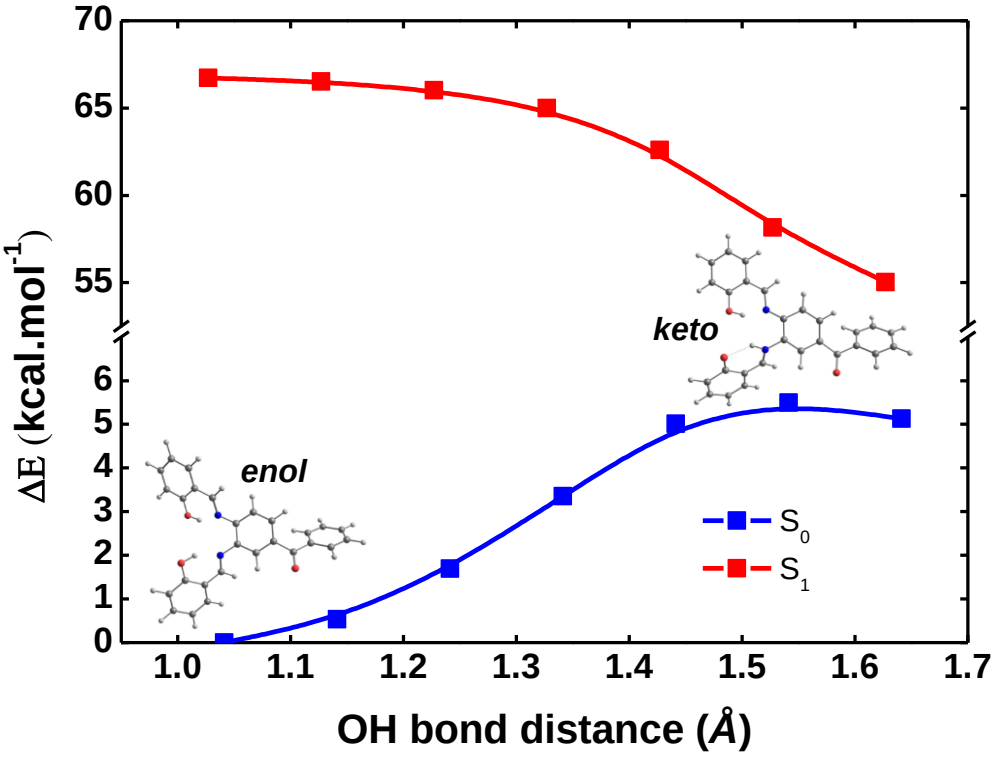

Figure 2. 5. Relative energy profiles along the O-H on ESIPT reaction coordinate for both the electronic ground state and the lower-lying excited state of the cis-sal-3,4-ben obtained at the PBE0/cc-pVTZ level.

The fluorescence spectrum (red diamonds in Figure 2.6) displays two bands centered at 430 nm and 575 nm which are related, respectively, to the emission from the excited *cis-enol** form (E^*) and *cis*-keto tautomer (K^*), indicating that this molecule present ESIPT. The fluorescence quantum yield for this molecule is about 5 % in DMSO. The fluorescence lifetimes for the two fluorescent bands corresponding to the E^* and K^* tautomeric forms were measured through time-correlated single photon counting with excitation at 375 nm.

Fluorescence decay curves collected at 430 nm (E^*) and 575 nm (K^*) are in the Figure 2.7. The results interpretation was made by using the global analysis method from the photon counting software. To obtain the better fit to experimental data, it was necessary to take into account three independent decay rates. In addition, the analysis was also performed through the convolution of the theoretical decays with the impulse response function (IRF) from the photon counting system. For the band at 430 nm (Figure 2.7a), it was found the following decay times: τ_1 = 0.08 ± 0.30 ns (23 %), τ_2 = 0.89 ± 0.01 ns (57 %) and τ_3 = 2.46 ± 0.01 ns (20 %), while for the band at 575 nm (Figure 2.7b) τ_1 = 0.18 ± 0.22 ns (7 %), τ_2 =1.14 ± 0.03 ns (32 %) and τ_3 = 2.17 ± 0.01 ns (61 %). The faster component is attributed to the nonradiative de-

excitation pathways of the *enol** and *keto** tautomer. However, these times are in the order of the instrument response time and, therefore, presenting a high standard deviation.

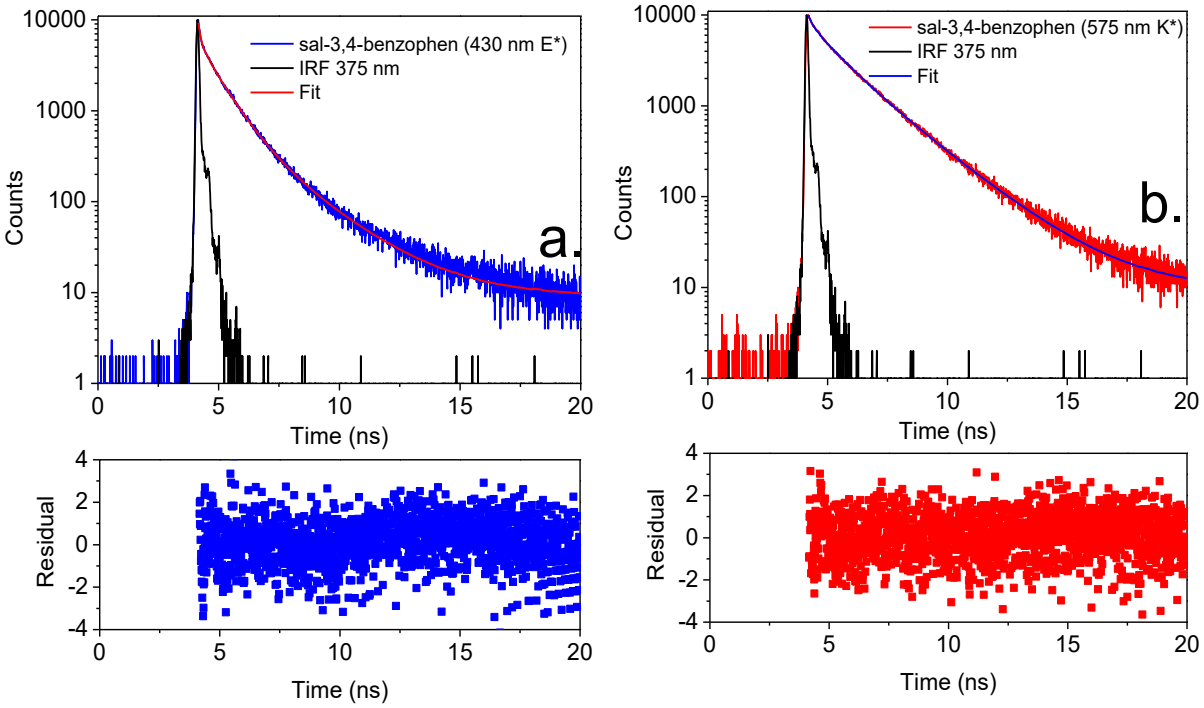

Figure 2. 6. Time-resolved fluorescence for the sal-3,4-ben dissolved in DMSO (C = 10 μmol L^{-1}; λ_{exc} = 375 nm and λ_{PL} = 430 nm (a) and 575 nm (b)).

Consequently, TCSPC measurement does not describe accurately the faster components of the $E^* \rightleftharpoons K^*$ equilibrium. On the other hand, the TCSPC results explain adequately the photophysical dynamics after the ESIPT process, exhibiting two longer fluorescence decays, which are related with the *enol** and *keto** forms lifetimes. This outcome is in accordance with the overlap between the two fluorescent bands at around 500 nm (see Figure 2.4). Therefore, for the band at 430 nm there is a contribution from the band at 575 nm and vice versa. Hence, we attributed the *enol** and *keto** lifetimes as τ (E*) = 0.89 ± 0.01 ns and τ (K*) = 2.17 ± 0.01 ns for the bands located at 430 nm and 575 nm, respectively. This behavior is confirmed by the time resolved emission spectra (TRES) showed in Figure 2.8 and it is in agreement with others excited state reactions in equilibrium.[48,49] As seen in Figure 2.8, the TRES for the sal-3,4-ben exhibits a time-dependent behavior for the band at 430 nm, while for the one at 575 nm there is no changes during the first 3 ns. Such results suggest that the decay of the *enol** form is faster than the *keto* tautomer. These processes are associated with the excited state molecular geometry assumed by the chromophore after excitation.

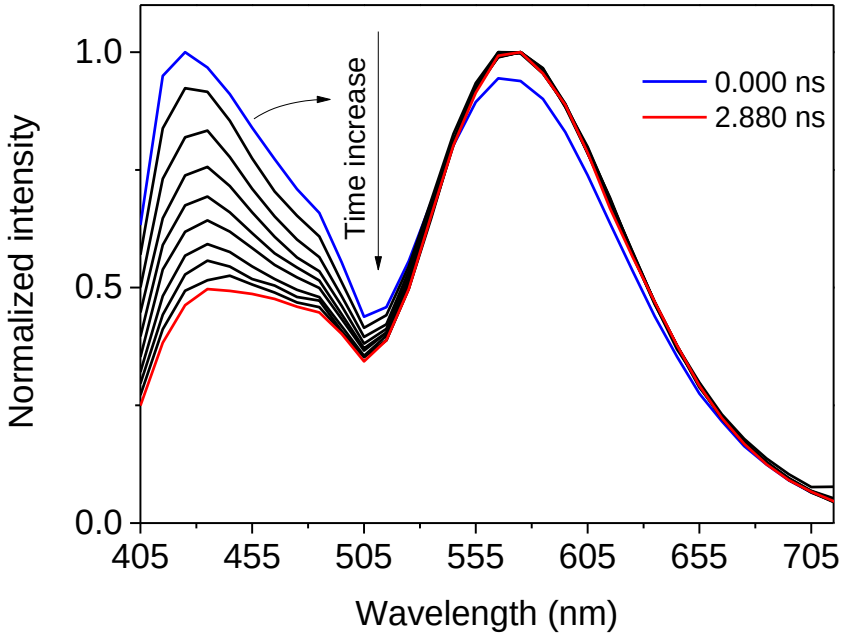

Figure 2. 7. Normalized time resolved emission spectra (TRES) of sal-3,4-ben in DMSO solution: λ_{exc} = 375 nm, delay: 0 to 2.880 ns (step between the spectra was of 320 ps). Concentration: 10 μmol L^{-1}.

To shed more light on the ESIPT and its dynamics, we have measured the excited-state absorption spectrum for sal-3,4-ben in DMSO by using the white-light femtosecond pump-probe technique. Figure 2.9a shows the colormap representing the time- and wavelength-resolved dynamics of the transient absorption spectrum. The excited state absorption (ESA) spectra for different times are displayed in Figure 2.9b, while Figure 2.9c illustrates a decay curve for probe pulse at the peak of ESA band. This band presents $\Delta A > 0$ and is associated with the transient absorption of hot *cis-keto** state. Another ESA band also is observed between 550 nm and 680 nm, with $\Delta A < 0$ (saturable absorption). This negative part of the ESA spectrum (for wavelength greater than 550 nm) is due to the stimulated emission of *cis-keto** state.[16] As we compare this part of the ESA spectrum with the *cis-keto** emission spectrum (Figure 2.4), we observed that the shape and the maximum are quite different. Such aspect can be explained by the strong attenuation in WLC intensity for wavelengths longer than 620 nm, caused by the broadband filter used to remove the pump pulse (775 nm) from the WLC. Adding to the fact that the stimulated emission signal is low, we obtained a poor signal/noise rate for the stimulated emission (> 620 nm). However, this drawback does not affect the interpretation of the ESIPT dynamics.[50]

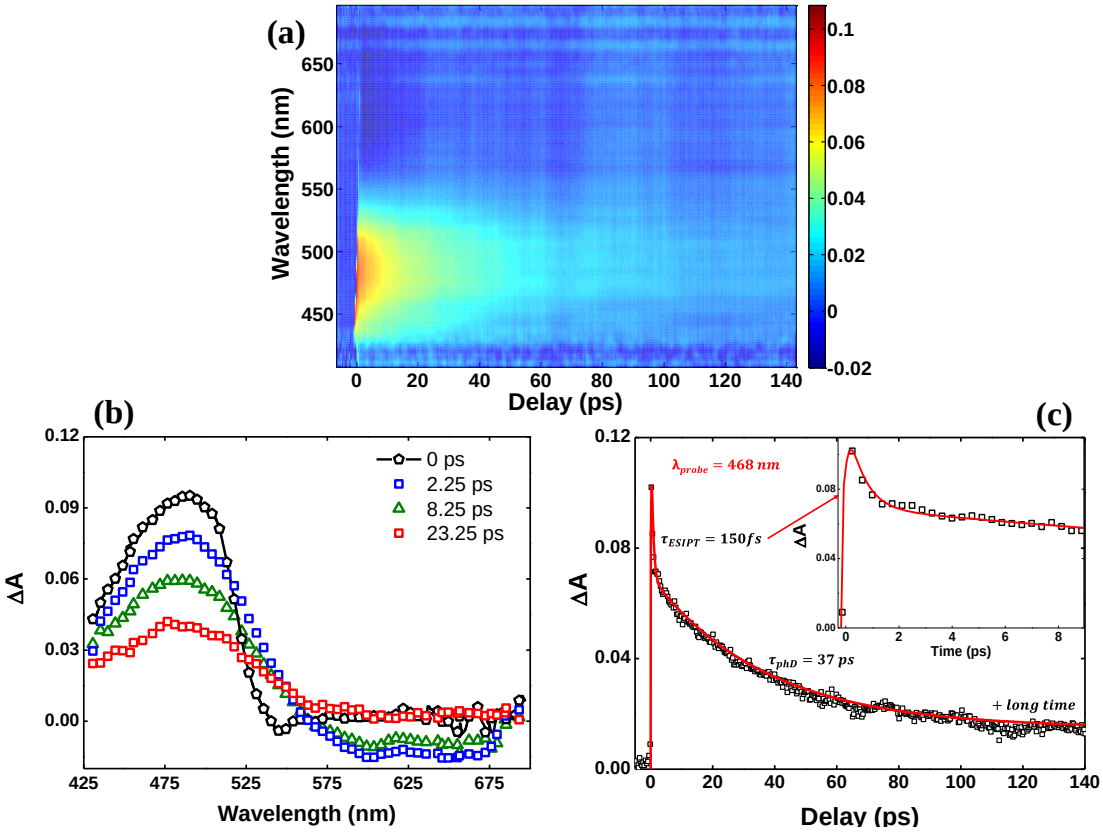

Figure 2. 8. (a) ESA colormap representing the time- and wavelength-resolved dynamics of transient absorption spectrum. (b) ESA spectra for different times (0 ps, 2.25 ps, 8.25 ps and 50 ps). (c) Decay curves for probe pulse tuning at 468 nm.

Based on these results, we proposed a kinetic model to the ESA dynamics of sal-3,4-ben illustrated by the energy-diagram presented in the Figure 2.9. In such model, electrons are promoted from ground-state (*cis-enol* form, S_0) to the first excited state (*cis-enol**, S_1) by the pump pulse (390 nm). After that, the *cis*-enol* form is quickly converted to the hot *cis-keto** (hK*) form due to the fast ESIPT process (τ_{ESIPT}), which is stabilized by the intramolecular hydrogen bond. Subsequently, there is a cooling process from the hot *cis-keto** (hK*) to cold *cis-keto** (cK*) state ($\tau_{hK^* \rightarrow cK^*}$), which has a characteristic time constant from hundreds of femtoseconds to picoseconds, and, then, there is the ($\tau_{cK^* \rightarrow K}$) fluorescence relaxation time from the *cis-keto** tautomer to the ground *cis-keto* state with a maximum emission at 575 nm (measured by time-resolved fluorescence spectroscopy - see Figure 2.7 - $\tau_{cK^* \rightarrow K} = 2.17\ ns$).

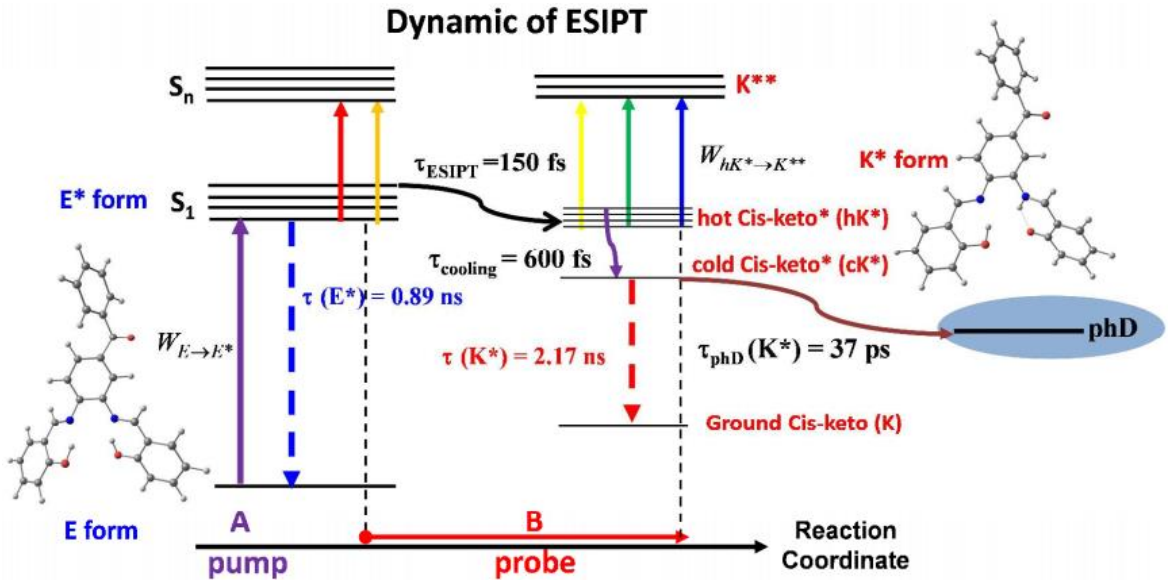

Figure 2. 9. Representative mechanism of the ESIPT dynamics for the sal-3,4-ben molecular system.

This simplified kinetic model can be described through the following rate equations:

$$\frac{dn_E(t)}{dt} = -n_E(t)W_{E\to E^*} + \frac{1}{\left(\tau_{E^*\to E}\right)} n_{E^*}(t) \tag{2.1}$$

$$\frac{dn_{E^*}(t)}{dt} = +n_E(t)W_{E\to E^*} - \frac{n_{E^*}(t)}{\tau_{ESIPT}} - \frac{1}{\left(\tau_{E^*\to E}\right)} n_{E^*}(t), \tag{2.2}$$

$$\frac{dn_{hK^*}(t)}{dt} = +\frac{n_{E^*}(t)}{\tau_{ESIPT}} - \frac{n_{hK^*}(t)}{\tau_{hK^*\to cK^*}} - n_{hK^*}(t)W_{hK^*\to K^{**}}, \tag{2.3}$$

$$\frac{dn_{K^{**}}(t)}{dt} = +n_{hK^*}(t)W_{hK^*\to K^{**}} \tag{2.4}$$

$$\frac{dn_{cK^*}(t)}{dt} = +\frac{n_{hK^*}(t)}{\tau_{hK^*\to cK^*}} - \frac{n_{cK^*}(t)}{\tau_{cK^*\to K}} - \frac{n_{cK^*}(t)}{\left(\tau_{cK^*\to phD}\right)}, \tag{2.5}$$

$$\frac{dn_{phD}(t)}{dt} = +\frac{n_{cK^*}(t)}{\left(\tau_{cK^*\to phD}\right)}, \tag{2.6}$$

$$\frac{dn_K(t)}{dt} = +\frac{n_{cK^*}(t)}{\tau_{cK^*\to K}}, \tag{2.7}$$

in which, $n(t)$ describe the population in each state. The transition rate is given by $W_{01} = \sigma_{E\to E^*} I_{pump} / \left(h\nu_{pump}\right)$ and $W_{1n} = \sigma_{K^*\to K^{**}} I_{probe} / \left(h\nu_{probe}\right)$. Here, $\sigma_{E\to E^*}$ corresponds to the one-photon absorption cross-section obtained through the linear absorption data ($\sigma_{E\to E^*} = 4.8\times10^{-17}\,cm^2$ at 390 nm) and $\sigma_{K^*\to K^{**}} = 7.0\times10^{-17}\,cm^2$ is the cross-section between the

first and the n_{th} excited state in *cis*-keto form, which is associated with the amplitude of pump-probe signal. I_{pump} and I_{probe} are the irradiance for the pump and probe pulses, *h* is the Planck constant, and *v* is the photon frequency. $\tau_{E^*\to E} = 0.89\ ns$ is the fluorescence decay lifetime from the *cis-enol** form. In this approach, $\Delta A(t) = N_0 \log(e) L \left\{ n_{S_0}(t)\sigma_{E\to E^*} + \left[n_{S_1}(t) + n_{S_{hK^*}}(t) + n_{S_{cK^*}}(t) \right] \sigma_{K^*\to K^{**}} \right\}$ describes the transient absorption change, in which N_0 is the concentration and L is the optical path length.

The solid line in Figure 2.8c corresponds to the fit obtained using the kinetic model described by Eqs. (1) to (7). The faster components of 150 fs and 600 fs were assigned to ESIPT (τ_{ESIPT}) and cooling ($\tau_{hK^*\to cK^*}$) times respectively. It is worth mentioning that the ESIPT time of about 150 fs is related with the DMSO solvent used in our measurements. DMSO is a polar aprotic solvent with high viscosity and, therefore, it is expected longer times for the excited state dynamics for the chromophore in solution. The slow decay, 37 ± 3 ps, is assigned to photodynamic from sal-3,4-ben ($\left(\tau_{cK^*\to phD}\right)$). It is known that the benzophenone group, present in sal-3,4-ben, have a very efficient intersystem crossing with lifetime $S_1 \rightarrow T_1$ of about 10-20 ps (depending of the solvent) at 530 nm (ESA spectrum) with the peak of ESA spectrum at 530 nm.[51] The hot *cis-keto** state for the sal-3,4-ben is located at 475 nm in the ESA spectrum, favoring the ISC process. Therefore, we associated the decay time of 37 ps with a non-emissive state (n_{phD}) related with the photodynamic from sal-3,4-bendue to the occurrence of the *cis*→*trans* photo-isomerization (iso) and ISC mechanisms, after the cooling process ($\left(\tau_{cK^*\to phD}\right) = \frac{1}{k_{iso} + k_{ISC}}$ in the rate equation model). The longer decay time, on the scale of nanoseconds, is the lifetime of the keto* tautomer.

2.3.2 Sal-5Cl-py

The molecular structure of *N*-salicylidene-5-chloroaminepyridine was determined using solid-state X-ray diffraction. According to the crystalline structure, in the solid state, the isomer corresponds to the *trans*-conformation with a planar structure and C_s symmetry. Nevertheless, *cis- trans* isomerization might be possible in solutions via rotation around the exocyclic N=C double bond. The structural parameters are given in Table 2.3, and the labels are shown in Figure 2.10. From these structural parameters, we can assume that an

intramolecular hydrogen bond between the iminic nitrogen atom and the OH groups is possible, and thus, both the keto (*K*) and enolic (*E*) species are possible (Figure 3).

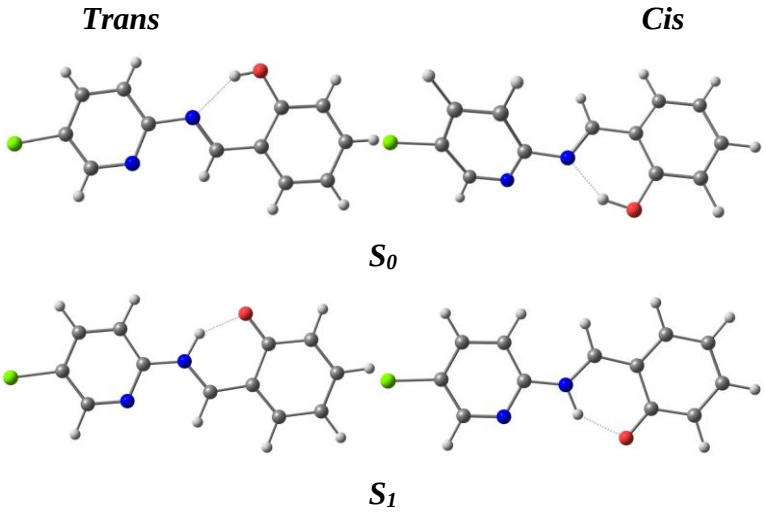

Figure 2. 10. Molecular structures obtained by X-ray diffraction of the trans isomer, and the cis isomer optimized at ground (S0) and first singlet excited state (S1) of the CAMB3LYP/aug-cc-pVDZ level. Dotted lines indicate hydrogen bonding.

Table 2. 3. Selected bond lengths (Å) and dihedral angles (degrees) for the ground and first singlet state structures of the ligand calculated at the CAMB3LYP/aug-cc-pVDZ level.

	Cis		*Trans*	
	S_0	S_1	S_0*	S_1
H_1-O_2	1.001	1.766	0.840	1.677
O_2-C_3	1.337	1.263	1.352	1.267
C_3-C_4	1.417	1.480	1.410	1.467
C_4-C_5	1.451	1.427	1.444	1.435
C_5-N_6	1.287	1.344	1.293	1.336
N_6-C_7	1.406	1.371	1.416	1.378
C_7-N_8	1.336	1.346	1.339	1.340
N_8-C_9	1.330	1.325	1.334	1.328
C_9-C_{10}	1.391	1.395	1.387	1.391
C_{10}-Cl_{11}	1.744	1.743	1.736	1.742
C_5-N_6-C_7-N_8	145.3	179.9	11.8	0.0

*Crystallographic structure.

The geometric parameters for the S_0 and S_1 states for both the *cis* and *trans*-conformations of sal-5Cl-py in DMSO were obtained at the CAMB3LYP/aug-cc-pVDZ level and are given in Table 2.3. The potential energy surfaces for both the electronic ground (S_0) and first singlet excited (S_1) states were built using two strategies: The strategy shown in Figure 2.11 changes the dihedral angle N_6-C_7-N_8-C_9 for both *E* and *K*. The strategy shown in Figure 2.12 was obtained using a relaxed scan of the distance between the hydrogen atom and the oxygen atom for both states.

According to our results (Figure 2.11), the *trans* isomer is the most stable structure in the ground state by ~2.9 kcal mol^{-1}, whereas in the electronic excited state, the *cis* and *trans* conformations are almost isoenergetic. These results suggest that sal-5Cl-py in DMSO solution might present a *trans-cis* balance in the electronic ground state, and when excited either *trans* or *cis* isomers of each *keto* and *enol* species might be formed.

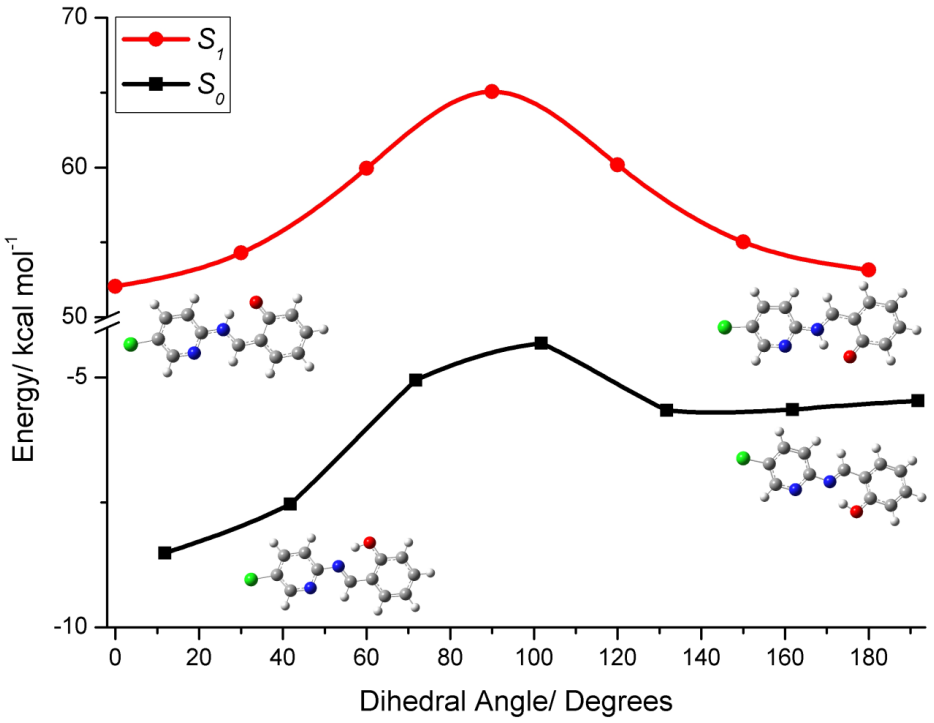

Figure 2. 11. Relative potential energy surfaces of sal-5Cl-py in DMSO as a function of the rotation of the N6-C7-N8-C9 dihedral angle in both the electronic ground state (S0) and the low-lying electronic excited state (S1), simulated at the CAMB3LYP/aug-cc-pVDZ level.

The occurrence of ESIPT in this molecule was postulated based on the X-ray diffraction data, which show that the hydrogen atom and the iminic nitrogen have a suitable separation. Additionally, the theoretical calculations performed by optimizing the structures of the S_0 and S_1 states (Figure 2.12) indicate that both E and K structures are planar; the main

differences between them are in the ligand site and the O-H distance. The K^* tautomer is more stable than E^* by ~ 5 kcal mol^{-1}. In addition, the emission bands for K^* calculated in DMSO (Table 2.4) using the S_1 optimized structures assuming a vertical excitation and emission is 100 nm lower in energy than E*. This result is consistent with the emission spectra shown below.

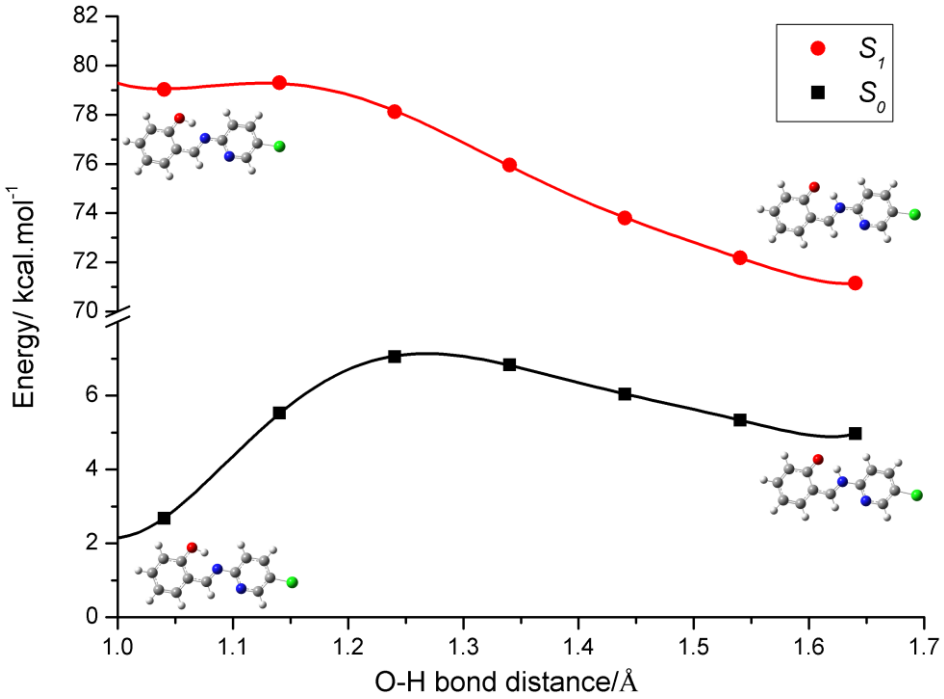

Figure 2. 12. Relative energy profiles along the O-H coordinate for both the electronic ground state and the lower-lying excited state of sal-5Cl-py obtained at the CAMB3LYP/aug-cc-pVDZ level in DMSO.

Based on our calculations, the photochemical mechanism of sal-5Cl-py in DMSO is proposed in Figure 2.13. According to our calculations, *trans-E* is the most stable species in the electronic ground state. When excited, this molecule forms *trans-E**, which can undergo ESIPT, leading to a balance between *trans-E** and *trans-K**. Once formed, *trans-K** can undergo a rotation along the iminic bridge leading to the *cis*-isomer, which is almost isoenergetic with *trans-K** (step 4) or can decay to the electronic ground state (step 5). In this scheme, step 1 corresponds to the electronic absorption of *trans-E*, leading to the formation of the *trans-E** tautomer. The *trans-E** form may undergo radiative decay (step 2) or ESIPT (step 3), generating the *trans-K** species. Step 4 describes the formation of the *cis-K** tautomer (step 4). Finally, reverse ESIPT (RESIPT) can occur causing *cis-K** or *trans-K** to return to the ground state *trans-E* (step 6). Based on this hypothesis, we searched for experimental evidence using optical spectroscopic techniques and sal-5Cl-py in solutions of both DMSO and MeOH.

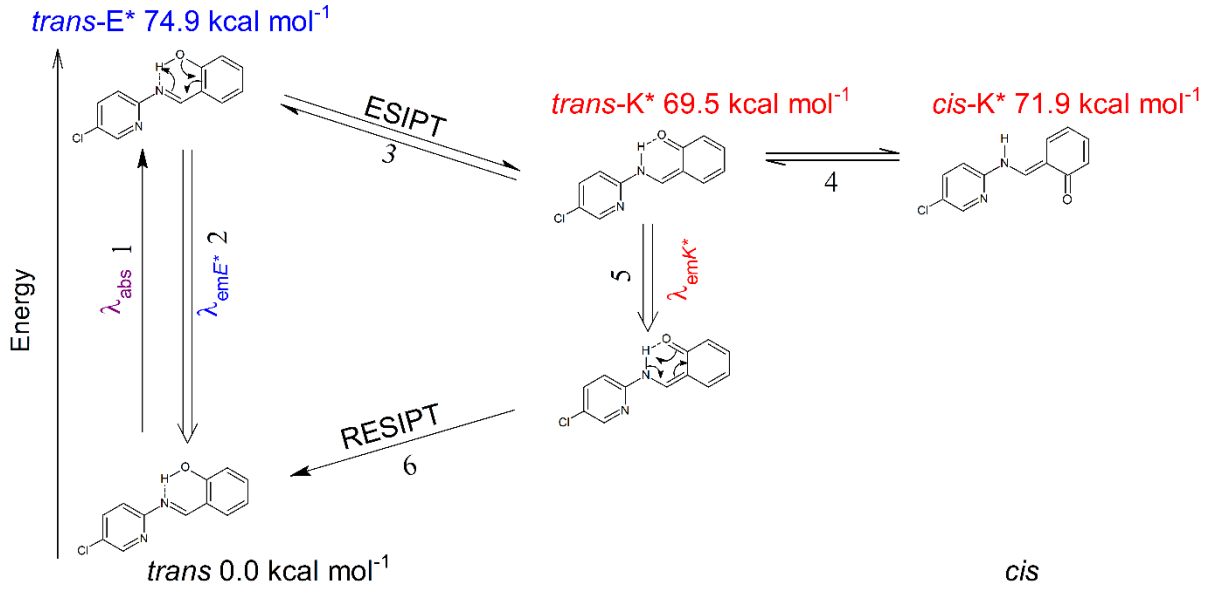

Figure 2. 13. Scheme showing the processes that occur in sal-5Cl-py after photoexcitation. The respective energies for each species were obtained at CAMB3LYP/aug-cc-pVDZ level.

The electronic absorption spectra of sal-5Cl-py measured in DMSO and MeOH (10 μmol L^{-1}) are given in Figure 2.14. They show two bands at 354 and 350 nm ($\varepsilon = 1.64 \times 10^4$ and 1.14×10^4 L mol^{-1} cm^{-1}) and 316 and 314 nm ($\varepsilon = 1.59 \times 10^4$ and 1.33×10^4 L mol^{-1} cm^{-1}) in DMSO and MeOH solutions, respectively. These bands were assigned as HOMO → LUMO ($S_0 \rightarrow S_1$) and ($S_0 \rightarrow S_2$) transitions based on our theoretical calculations (Table 2). The intensity of the low-lying band (λ = 350 - 354 nm) compared with that of the higher energy band (λ = 316 - 314 nm) is higher in DMSO than in MeOH, suggesting that the hydrogen bonding between the protic solvent and the sal-5Cl-py molecule modifies the transition dipole moment associated with the S_1 state more significantly.

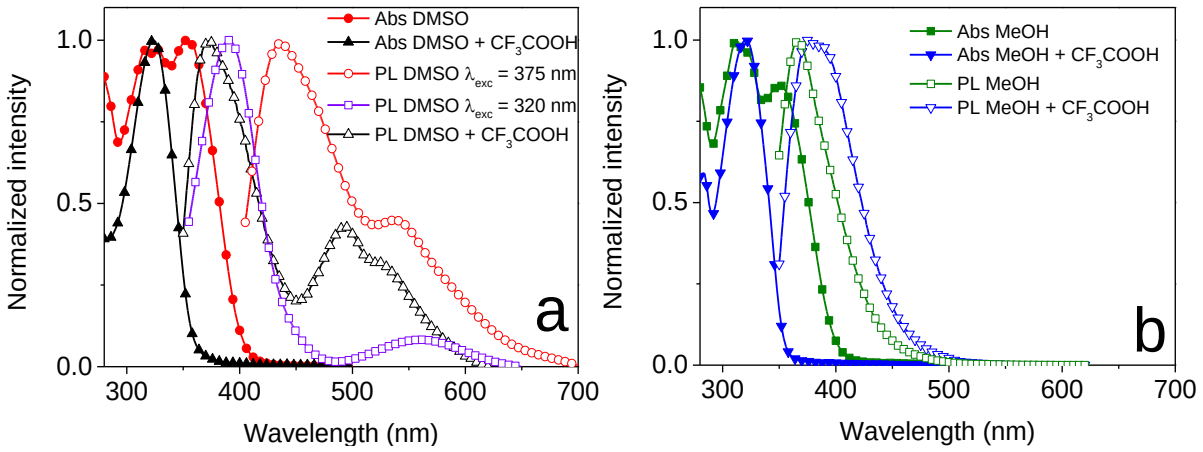

Figure 2. 14. Normalized electronic absorption and steady state fluorescence spectra of sal-5Cl-py in a. DMSO (λ_{exc} = 375 nm and λ_{exc} = 320 nm) and b. MeOH (λ_{exc} = 320 nm) in the presence and absence of CF_3COOH (λ_{exc} = 320 nm). Concentration: 10 μmol L^{-1}.

To obtain more information about the nature of the electronic transitions that appear in the absorption spectrum of sal-5Cl-py, calculations were performed at the TD-DFT level. Table 2.4 lists the main vertical excitation energies calculated at the aug-cc-pVDZ/CAMB3LYP level in DMSO. The calculated energies are in close agreement and reproduce the experimentally observed low-lying transitions with a deviation of less than 12%. The E_{HOMO} obtained from cyclic voltammetry is -5.93 eV. Due to the impossibility of obtaining the E_{LUMO} directly, the solid-state optical band gap (E_{gap} = 3.40 eV) was used to obtain its value: -2.53 eV (Figure A9). These electronic transitions mainly involve frontier molecular orbitals, particularly of the HOMO → LUMO type. Frontier molecular orbital densities are given in Figure 2.15 and can be used to qualitatively describe the main orbitals participating in low-lying transitions.

For both the HOMO and the LUMO, the electron density is spread out over the entire ligand, while HOMO-1 has important contributions from the chlorine atomic orbitals and LUMO+1 (S_1) is mainly located over the pyridine fragment. This result supports the experimental observation that, under protonation, the S_1 state is more affected.

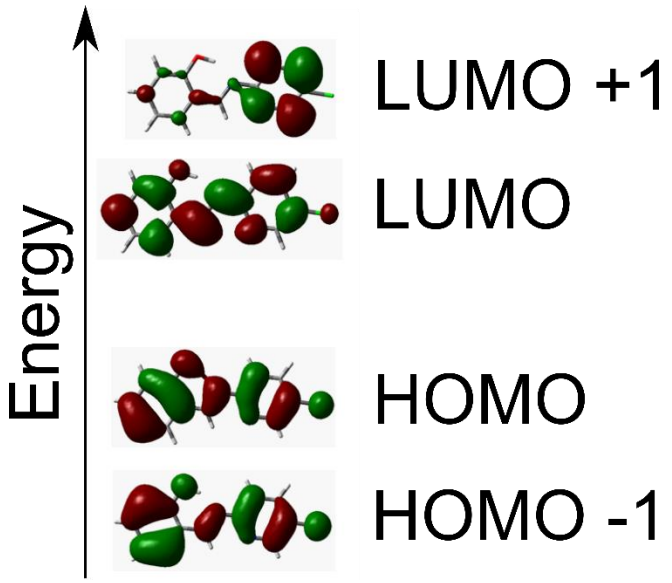

Figure 2. 15. Main frontier molecular orbitals in the ground state of the sal-5Cl-py obtained at the CAMB3LYP/aug-cc-pVDZ level using DMSO as the solvent involved in the electronic transitions.

Table 2. 4. Excitation energies obtained experimentally and calculated at the CAMB3LYP/aug-cc-pVDZ level using DMSO as the solvent. The composition of the electronic transitions is given in %.

CAMB3LYP/aug-cc-pVDZ				***Experimental***			
E/eV	**λ/nm**	***f***	**Assignment**	**λ/nm**	E_{HOMO}**/eV**	E_{LUMO}^{*}**/eV**	E_{gap}**/eV**
3.81	326	0.70	94% H → L	354	-5.93	-2.53	3.40
4.41	281	0.36	84% H-1 → L; 5% H → L+1	326			

*The E_{LUMO} energy was obtained from the optical band gap energy of sal-5Cl-py in the solid-state.

When trifluoroacetic acid (10 μL in 2000 μL) is added to the solutions of sal-5Cl-py in both solvents, the low-lying absorption band is not observed in the spectra, which shows only a band at approximately 320 nm for both solvents. This observation supports the occurrence of protonation of the ligand by CF_3COOH.

The steady-state fluorescence spectra (λ_{exc} = 320 nm) of sal-5Cl-py in the DMSO solution (10 μmol L^{-1}) showed two emissions centered at λ_{em} = 395 and λ_{PL} = 550 nm (Figure 2.14a, Table 2.5), which is assigned to the E^* and K^* species, respectively. The Stokes shifts of these two bands are equal to 3033 and 10067 cm^{-1} due to decays of the enol* and keto* species,

respectively (pathways 2 and 5 in Figure 2.13). When this molecule is excited at λ_{exc} = 375 nm (Figure 2.14a), two emission bands are observed: The higher energy band observed at 395 nm shifts towards λ_{PL} = 425 nm, and the lower energy band peaks at 490 nm. Taking the corresponding bands from the absorption spectra, we determined smaller Stokes shifts of 4720 and 9900 cm^{-1}, respectively (Table 2.5).

The emission (λ_{exc} = 320 nm) of sal-5Cl-py in MeOH solution showed only one band centered at λ_{PL} = 367 nm (Figure 2.4b) (Table 2.5). No emission could be detected when the excitation wavelength is λ_{exc} = 375 nm. A very small Stokes shift was obtained of SS = 1323 cm^{-1} for the emission band at 367 nm. These results indicate that, although the absorption spectra are very similar for both solvents, which means that the species in the electronic ground state were the same (step 1 in Figure 2.13), the dynamics of this molecule in the electronic excited state are different in the different solvents. These observations are consistent with the occurrence of the ESIPT process from the E* to K* species (step 3 in Figure 2.13) in DMSO with an $E^* \rightleftharpoons K^*$ balance (steps 2, 3 and 4 in Figure 2.13), whereas in MeOH, only the E^* species is emissive. This steady-state photoluminescence study suggested that there was a hydrogen bond between the enol species (E^*) and the solvent that inhibited the formation of the keto (K^*) species.

Based on this hypothesis, we added CF_3COOH to both DMSO and MeOH solutions. This acid protonates the sal-5Cl-py molecules in both solvents and inhibits the formation of the K^* form. Based on this strategy, we recorded the emission spectra (λ_{exc} = 320 nm) of sal-5Cl-py in both DMSO (Figure 2.14a) and MeOH (Figure 2.14b) solutions with CF_3COOH. Two emission bands were observed for sal-5Cl-py in the DMSO solution with different band profiles compared with the solution in absence of the acid. The higher energy emission band appears at λ_{PL} = 376 nm (λ_{PL} = 425 nm in DMSO) and has a higher intensity. The absorption band at λ_{abs} = 316 nm has a Stokes shift of 4268 cm^{-1}. The lower energy band is a broad band and has a very low intensity at λ_{PL} = 493 nm (λ_{PL} = 550 nm in DMSO). When trifluoroacetic acid was added to the MeOH solution (Figure 2.14b), only one emission band (λ_{exc} = 335 nm) centered at λ_{PL} = 376 nm was observed, which is the same as observed in MeOH. The emission band is narrow and redshifted compared with the MeOH solutions, and the SS is 4654 cm^{-1} (Table 2.5), which is greater than in MeOH. All of these spectral changes confirm the hypothesis that sal-5Cl-py is protonated in the presence of acid.

The fluorescence decay of sal-5Cl-py in DMSO using λ_{exc} = 335 nm and collecting the emission at λ_{em} = 395 nm (E^* species) was also recorded. This decay is monoexponential

with a fluorescence lifetime of τ_{FL} = 2.36 ± 0.01 ns (Figure 2.16a). When CF_3COOH is added to this solution, the decay of the sal-5Cl-py (λ_{exc} = 335 nm; λ_{PL} = 376 nm) (Figure 2.169c) becomes biexponential with τ_{FL1} = 0.18 ± 0.01 ns (B_1 = 63%) and τ_{FL1} = 2.18 ± 0.01 ns (B_2 = 37%). These data suggest that the protonation of sal-5Cl-py by the solvent disturbs the E^* emission and some molecules still emit with a characteristic lifetime of approximately 2 ns (similar to the solution in the absence of acid), while others are quenched and have faster decays.

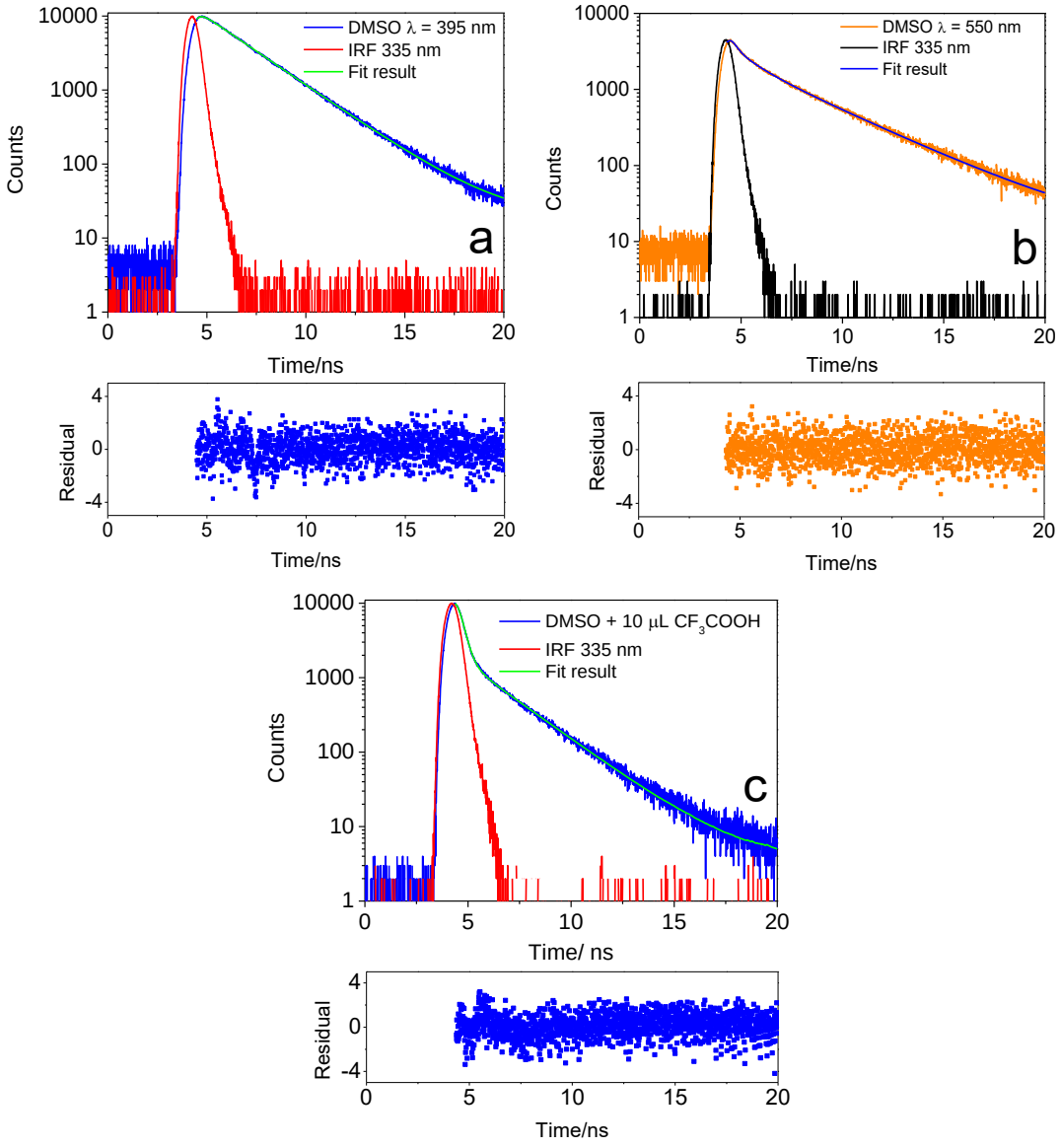

Figure 2. 16. Fluorescence decays of sal-5Cl-py in DMSO solution (λ_{exc} = 335 nm): a. λ_{PL} = 395 nm; b. λ_{PL} = 550 nm, c. with CF_3COOH, λ_{PL} = 395 nm. Concentration: 10 μmol L^{-1}.

The fluorescence decay was produced by the excitation at λ_{exc} = 375 nm and monitored at λ_{PL} = 550 nm where the K^* species preferentially emits. The decay is biexponential

with a shorter τ_{FL1} = 1.03 ± 0.08 ns (15 %) and a longer τ_{FL2} = 3.54 ± 0.04 ns (85 %) (Figure 2.17b). This biexponential decay was also obtained with excitation at λ_{exc} = 375 nm, either when the signal was collected at λ_{PL} = 425 nm (Figure 2.17a) (emission due to the E^* species) (τ_{FL1} = 1.24 ± 0.01 ns, B_1 = 39% and a longer lifetime τ_{FL2} = 5.29 ± 0.03 ns, B_2 = 61%) (Table 2.5) or when it was collected at λ_{PL} = 545 nm (Figure 2.17b) (emission preferentially due to the K^* species) (τ_{FL1} = 1.50 ± 0.13 ns, B_1 = 88% and τ_{FL2} = 7.14 ± 0.07 ns, B_2 = 12%).

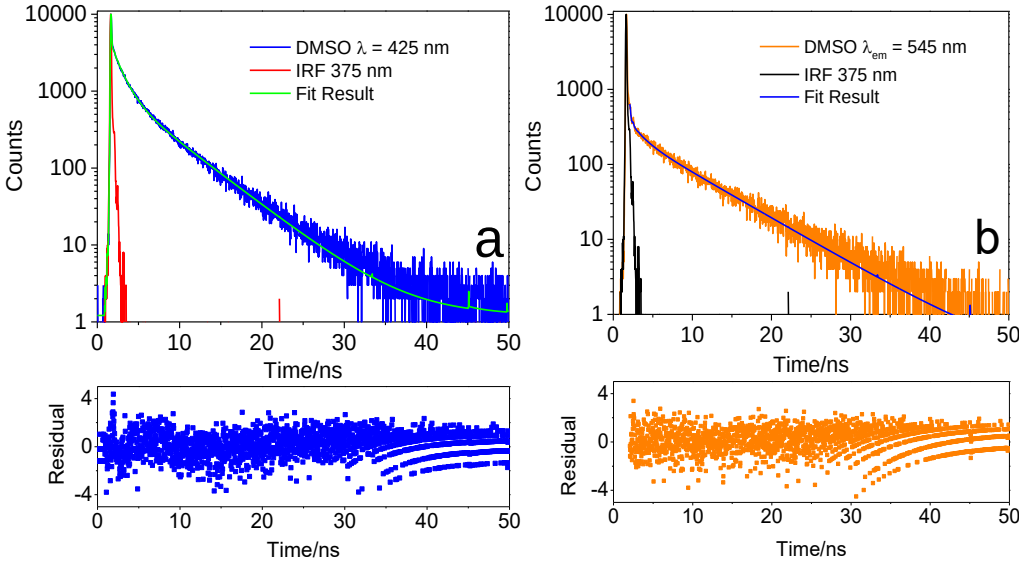

Figure 2. 17. Fluorescence decays of sal-5Cl-py in solutions of DMSO (λ_{exc} = 375 nm) a. λ_{PL} (E*) = 425 nm and b. λ_{PL} (K*) = 545 nm. Concentration: 10 μmol L^{-1}.

The fluorescence decay of sal-5Cl-py in MeOH solution (λ_{exc} = 335 nm; λ_{PL} = 367 nm) (Figure 2.18a, Table 2.5) is biexponential with τ_{FL1} = 1.77 ± 0.03 ns, B_1 = 66% and τ_{FL2} = 3.13 ± 0.16 ns. In addition, B_2 = 34%, which also indicates that hydrogen bonding occurs with the solute. Regardless, the decay is monoexponential in DMSO, while the emission profile measured in MeOH is biexponential and faster than in DMSO, indicating that some quenching process might be involved in this system, where the solute-solvent interactions are stronger. When CF_3COOH is added to the MeOH solution, the decay (λ_{exc} = 335 and λ_{PL} = 376 nm) (Figure 2.18b) becomes monoexponential with a lifetime of τ_{FL} = 8.28 ± 0.01 ns. The biexponential decay obtained for DMSO+CF_3COOH is consistent with the two emission bands observed in Figure 2.14a, and the monoexponential decay for the MeOH+CF_3COOH is also consistent with both the absorption and the emission spectra in Figure 2.14b.

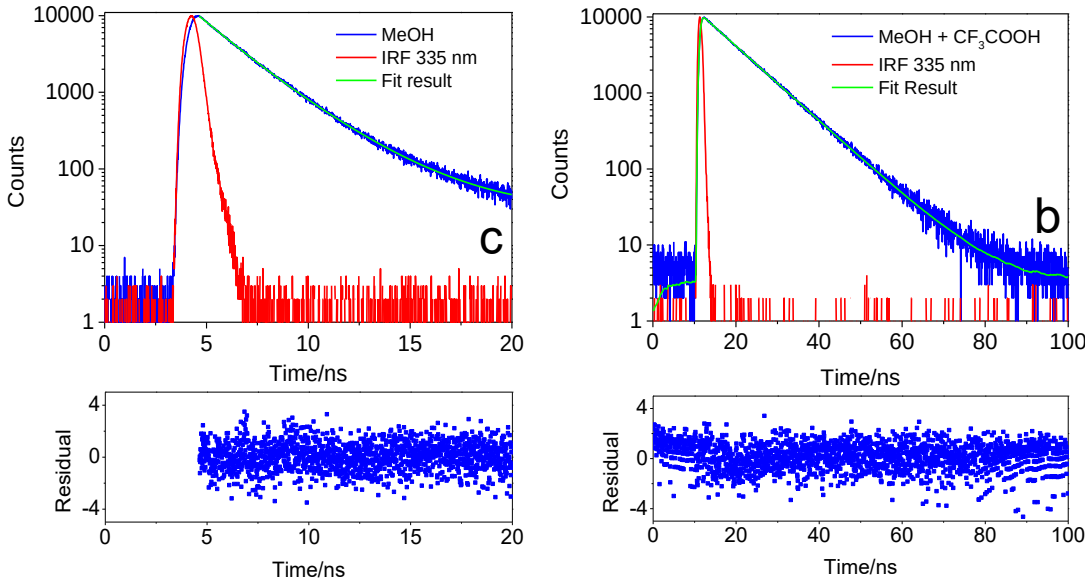

Figure 2. 18. Fluorescence decays of sal-5Cl-py in MeOH solutions without (a) and with (b) CF_3COOH. λ_{exc} = 335 nm, λ_{PL} = 376 nm. Concentration: 10 μmol L^{-1}.

In summary, considering the obtained results, we can concluded that 1. there are two electronic excited states accessible by photoexcitation in the UV spectral range for sal-5Cl-py in both solvents (DMSO and MeOH), which are characterized by the presence of two bands in the electronic absorption spectra; 2. two emission bands are observed in the DMSO solution (a solvent with weak solvent-solute interactions) regardless of the excitation wavelength (375 nm and 335 nm), indicating that there is an equilibrium between the E^* and K^* forms and both species decay radiatively. In MeOH (a protic solvent in which H-bonding between the solute and a methanol molecule is possible, which inhibits ESIPT), only E^* is formed and emissive. 3. Trifluoroacetic acid added to both solutions protonates sal-5Cl-py, leading to the disappearance of the absorption band at 350 - 360 nm due to the prevention of the formation of the K^* tautomer. 4. The protonation of the lower-lying emission spectrum in DMSO significantly decreases the intensity and redshifts the low-lying emission band.

Table 2. 5. Optical properties of sal-5Cl-py in DMSO and MeOH solutions (10 μmol L-1) in the absence and presence of CF3COOH.

DMSO				**MeOH**			
λ_{PL}/nm	**SS/cm^{-1}**	**τ_1/ns (B%)**	**τ_2/ns (B%)**	**λ_{PL}/nm**	**SS/cm^{-1}**	**τ_1/ns (B%)**	**τ_2/ns (B%)**
λ_{exc} = 320 nm		**λ_{exc} = 335 nm**		**λ_{exc} = 320 nm**		**λ_{exc} = 335 nm**	
395 (E*)	3033	2.36±0.01 (100)		367 (E*)	1323	1.77±0.03 (66)	3.13±0.16 (34)
550 (K*)	10067	1.03±0.08 (15)	3.54±0.04 (85)				
DMSO + CF_3COOH				**MeOH + CF_3COOH**			
λ_{exc} = 335 nm				**λ_{exc} = 335 nm**			
376 (E*)	4268	0.18±0.01 (63)	2.18±0.01 (37)	376 (E*)	4654	8.28±0.01 (100)	
493 (K*)	10580						

To obtain information about the dynamics of the emission decays, the time-resolved emission spectra - TRES of sal-5Cl-py in solutions of both DMSO and MeOH were evaluated. The TRES of sal-5Cl-py in DMSO solution at λ_{exc} = 335 nm (Figure 2.19a) showed a strong emission band at λ_{PL} = 395 nm (E^*) and a lower intensity band at λ_{PL} = 550 nm (K^*). Both bands arise immediately after the pulse, indicating that the ESIPT process is faster than the experimental time scale. For longer delays, the K^* emission band completely disappeared. When the excitation was performed with λ_{exc} = 375 (Figure 2.19b), the emission at λ_{PL} = 555 nm (K^*) is stronger than the higher energy emission band (E^*), and for longer delays, the relative intensity of the K^* emission also decreases substantially.

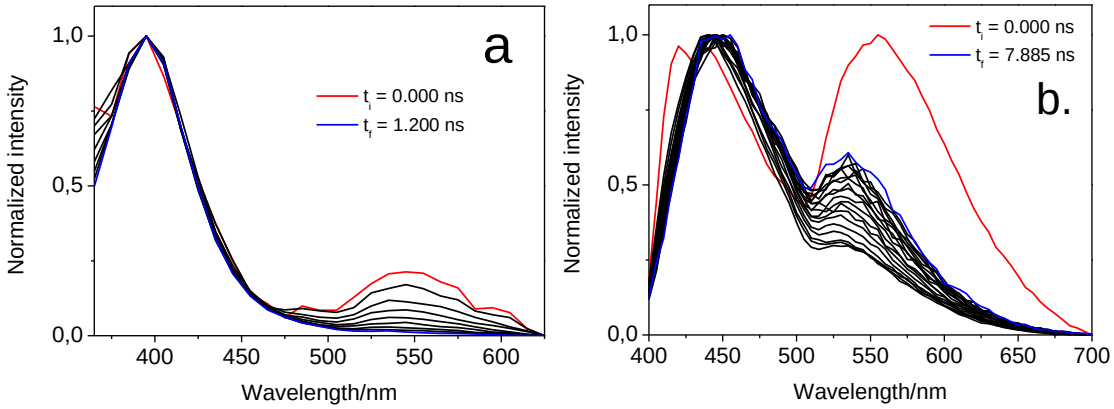

Figure 2. 19. Normalized time resolved emission spectra (TRES) of sal-5Cl-py in DMSO solution: a. λ_{exc} = 335 nm, delay: 0 to 1.200 ns, b. λ_{exc} = 375 nm, delay: 0 to 7.885 ns. Concentration: 10 μmol L^{-1}.

The TRES of sal-5Cl-py in MeOH (Appemdix) is time independent and has an emission band centered at λ_{PL} = 367 nm, as observed in the steady-state experiments. When trifluoroacetic acid is added to the DMSO solution, the TRES (λ_{exc} = 335 nm) of sal-5Cl-py had the following properties: i. for shorter delays, the spectra showed a broad emission band centered at λ_{PL} = 380 nm with the same spectral range as the steady-state fluorescence spectra (Figure 7a) without the low-lying emission band (λ_{PL} = 490 nm) (Figure 2.20). ii. For longer delays, this band predominates. This pattern is similar to that obtained under steady-state conditions (Figure 7a). Hence, in the presence of CF_3COOH, the TRES reflect a balance between E^* (emission at 380 nm) and the protonated species (emission at 490 nm). The TRES (λ_{exc} = 335 nm) of sal-5Cl-py in MeOH solutions containing CF_3COOH (Figure A13) are also time independent with an emission band centered at λ_{PL} = 384 nm; only the E^* protonated form is emissive.

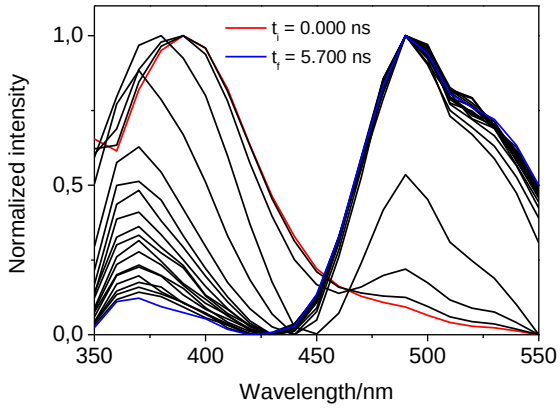

Figure 2. 20. Normalized time resolved emission spectra (TRES) (λ_{exc} = 335 nm) of sal-5Cl-py in DMSO solutions containing CF_3COOH. Concentration: 10 μmol L^{-1}.

As proof of concept, an all-solution-processable WOLED of the sal-5Cl-py was made using PVK as host material (2.5 % mol/mol of salicylidene derivative), as the following diode architecture: ITO|PEDOT:PSS|PVK:sal-5Cl-py 2.5 % (mol/mol ratio)|Ca|Al (Figure 2.21). Its electroluminescence spectrum presented clearly the presence of the emission of the two species generate on the excited-state, with the maxima centered at λ_{EL} = 399 nm and 553 nm, which were attributed to the E* and K* species, respectively. Thus, combining the deep-blue EL emission of the E* species with the orange emission color of the K* species for white-light emission generation device (Inset Figure 2.21a) with CIE = 0.35, 0.45 (Figure 2.21b). However, due to the prototype characteristic of the device it presented a very low luminance and efficiency values, enabling the measure of their parameters, according our experimental setup resolution.

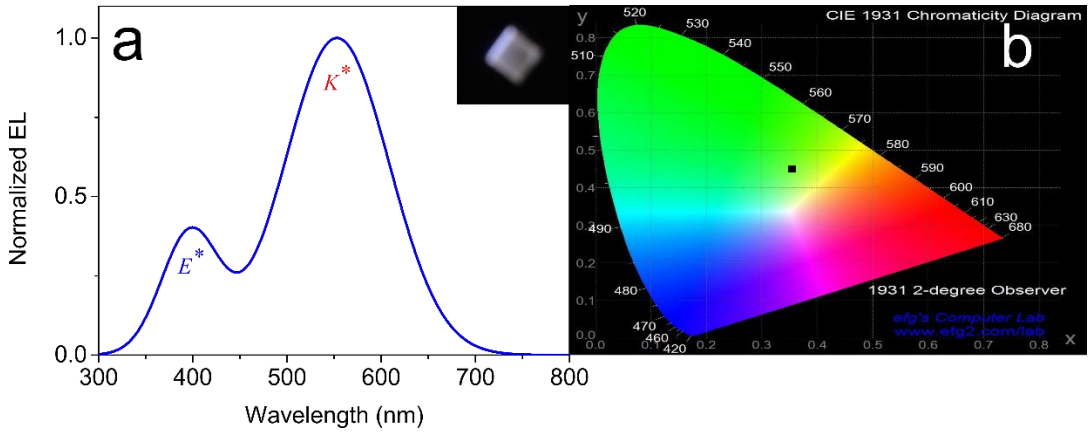

Figure 2. 21. (a) Normalized electroluminescence spectrum and device photography and (b) CIE 1931 chromaticity color diagram of the ITO|PEDOT:PSS|PVK:sal-5Cl-py 2.5 % (mol/mol ratio)|Ca|Al WOLED.

2.4 Conclusions

The synthesis and structural characterization of the new salicylidene derivatives (sal-3,4-ben and sal-5Cl-py) were successfully performed via Schiff's condensation under ultrasonic bath and by ^{1}H and ^{13}C NMR, FTIR, ESI-MS+, elemental analysis and single-crystal X-ray diffraction, respectively.

In summary, the entire excited state dynamics of a novel salicylidene ligand sal-3,4-ben were evaluated. Upon excitation of the sal-3,4-ben chromophore (in the *enol* form) to the *cis-enol** form (pump at 390 nm), a fast conversion to the hot *cis-keto** (hK*) form occurs due to the ESIPT process (τ_{ESIPT} = 150 fs), which is stabilized by the intramolecular hydrogen

bond, as can be seen in the optimized structures for the first excited state obtained at PBE0/cc-pVTZ level.

Also, the steady state and transient properties of these salicylidenes in DMSO revealed the $E^* \rightleftharpoons K^*$ balance. In the case of sal-5Cl-py, hydrogen bonds between MeOH and chromophore inhibited the formation of the K^* species, and the only emission component in MeOH is attributed to E^*. In agreement with the DFT and TD-DFT theoretical calculations at the CAM-B3LYP/aug-cc-pVDZ level, ESIPT may occur due to the proximity of the hydrogen and the iminic group. When trifluoroacetic acid was added to both DMSO and MeOH, there is a protonation of the dye, and thus, the emission from the K^* species is absent. The ESIPT process is very fast, as demonstrated by the time evolution of the E^* and K^* species in DMSO. The occurrence of ESIPT leads to an $E^* \leftrightharpoons K^*$ balance in the excited state, hence a broader emission range spectrum is obtained, allowing its applications in photonics and organic electronics devices such as white OLEDs, as the proposed prototype diode using the sal-5Cl-py as active layer to achieve white-light generation.

CHAPTER 3

HOW TO IMPROVE Zn(SALICYLIDENES) OPTICAL-ELECTRONIC PROPERTIES?

3.1 **Motivation**

Among the practical applications of organic electronics, Organic Light Emitting Diodes (OLEDs) comprise versatile materials that may be used in the production of flexible and sustainable technological devices from thin film deposition[11] in contrast to the common paper LEDs technologies. Since the 80s, a lot of effort has been put in this field with the development of different device architectures and different materials as active layers[12–15].

Coordination compounds are made up of a group of materials which are often applied in electro-optical devices due to their thermal and chemical stability[24] and variety of color emission with high quantum yields either by fluorescence[29,30] or phosphorescence,[174,175] in comparison to a "pure" organic framework[25,26]. Among the coordination compounds, those with Zinc(II) are of interest due to their low cost compared to others metal ions as consequence of its natural abundance (70 % of production)[176,69], ease recycling process (30 % of production)[177] and it possesses a great industrial interest. [178] Moreover, Zn(II) plays an important role in biological systems, being fundamental for life-maintenance,[179] which favors the production of sustainable-materials for technological applications, such as OLEDs.[69,112] Figure 3.1 displays the Zn(II) abundance in the Earth's crust in comparison to other chemical elements.

Also, Zn(II) can be coordinated into salicylidene derivatives ligands frameworks, disturbing the salicylidene electronic structures principally by the increase of the ligand rigidity and planarity and the block of the ESIPT processes on the excited-state, which must be directly linked to the improvement of the ligand optical-electronic properties, for example the molar absorption coefficient (ε),[180] photoluminescence quantum yields (PLQY) and non-linear two-photon absorption properties.[27] Even impacting directly on the salicylidene optical properties, Zn(II) $3d^{10}$ orbitals contribute minimally into the molecular electronic structure ($IP_{Zn(II)(3d^{10})}$ = 40 eV), principally in the frontier orbitals (HOMO and LUMO). Therefore, the principal electronic transition involving frontier orbitals in Zn(II) coordination compounds are of $\pi \rightarrow \pi^*$ character: intra-ligand charge transfer (ILCT); and for a non-symmetric ligand-to-ligand charge transfer (LLCT).[24]

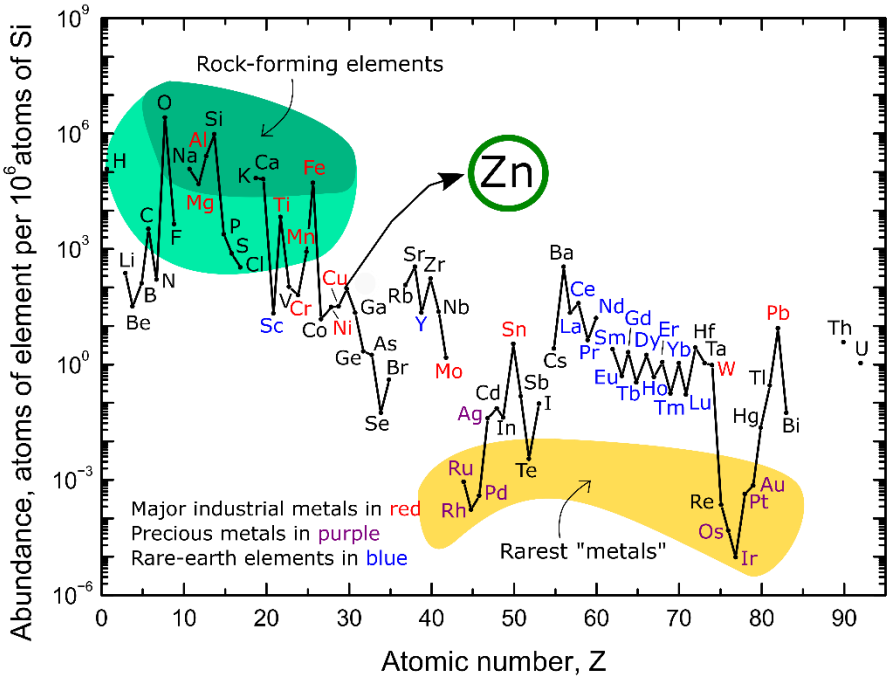

Figure 3.1. Abundance of the chemical elements in Earth's crust as with their atomic number relative to Silicon (Si) atoms (Zinc in highlight).[178]

The disadvantage of these materials is the low charge mobility and the necessity of using the vapor deposition process for the device's construction. On the other hand, polymeric materials have been used as active layer especially when blue emission is required[1,64,181,182]. Also, these materials are very useful for the construction of solution-processable devices with the advantage of being an energy saving process, enabling the production of flexible and large-area devices[183,184]. Due to the particular limitations of each material, the combination of conjugated polymers with coordination compounds might be a convenient strategy to produce environmental-friendly solution-processable devices with a variety of colors, with better charge transport and greater performance.

Previously, we demonstrated that PVK can be used as hole transport and electron blocking material[185] for the improvement of PLEDs optical-electronic properties.[88] Also, the active layer charge mobility was improved considerably by the addition of the Zn(II)salicylidenes into PVK host due their electron acceptor characteristic and polymer/dye heterojunction formation, as it were reported elsewhere for another similar systems.[186–188] However, the diodes with PVK have very poor both electron and hole mobilities. To attempt of the these observations, herein we present how to improve the performance of the diodes using the salicylidenes and their Zn(II) coordination compounds in a composite with polyfluorene (PFO) in contrast to PVK as

host conducting polymer, which has greater charge mobility compared to PVK ($10^3 \sim 10^4$ times higher than μ_{PVK}).[99,189]

The diodes were fabricated with the two following architectures: a) ITO|PEDOT:PSS|PVK:***X***|Ca|Al, where X = salophen, sal-3,4-ben, [Zn(salophen)] or [Zn(sal-3,4-ben)] (Figure 3.2a); and b) ITO|PEDOT:PSS|PVK|PFO:***X***|Ca|Al, where X = [Zn(salophen)] or [Zn(sal-3,4-ben)] (Figure3. 2b) and their optical and electrooptical properties were determined. The performances of the diodes were analyzed and interpreted using the *trap-charge limited-current* (TCLC) model.[103,107,190] We also theoretically analyzed the charge density of the HOMO and LUMO and the ground-state (S_0) and first singlet excited-state (S_1) dipole moments for both molecules for a better understanding of the charge changes upon electronic excitation. For this theoretical analysis we used DFT and TD-DFT natural transition orbitals (NTO) and calculated the electronic transitions at the PBE0/6-311++G(d,p) level. Thereby, we demonstrate that the charge mobility of the active layer, as well as of the host polymer, is one of the most important parameters to the Zn(II)salicylidenes solution-processable OLEDs optical-electronic properties, being a simple tool to improve their optical-electronic properties in comparison to multilayer diodes. We also prepared the active layers with different molar concentrations of the coordination compounds (0.1, 0.5, 1.0 and 2.5 mol/mol%) to optimize the diode efficiency.

3.2 Materials and Experimental Details

3.2.1 Materials

Poly(9-vinylcarbazole) (PVK) (M_W = 1,100,000 g mol^{-1}), Alq_3 and Znq_2 were purchased from Sigma-Aldrich, São Paulo, Brazil. Zinc acetate was purchased from Fisher Scientific Company (Brazil). THF solvent was purchased from Sigma-Aldrich, São Paulo, Brazil as anhydrous and inhibitor-free grade. Poly(ethylene dioxythiophene):poly(4-styrenesulfonate) (PEDOT:PSS) was purchased from Baytron P CH 8000, Bayer AG, Germany. [Zn(sal-3,4-ben)] coordination compound were synthesized and characterized according to the literature.[180]

3.2.2 Experimental Details

3.2.2.1 Synthesis of the [Zn(sal-3,4-ben)]

[Zn(sal-3,4-ben)] was produced by dissolving 133 mg (0.316 mmol) of sal-3,4-ben in 20 mL of methanol under constant stirring. A methanolic solution of zinc(II) acetate dihydrate (69 mg; 0.316 mmol) was slowly dropped into the ligand mixture. The

precipitate was filtered and washed with hot deionized water and ethanol. The product was an orange polycrystalline powder, which was obtained with 83 % yield. Elemental analysis: calculated, C 64.62, H 4.02 and N 5.58; found, C 64.60, H 4.05 and N 5.56. ^{1}H NMR (300 MHz, DMSO-d_6) δ (ppm): 6.50 (*m*, 2H), 6.69 (*dd*, *J* = 8.55 Hz, 2H), 7.25 (*m*, 2H), 7.42 (*d*, *J* = 8.4 Hz, 2H), 7.63 (*m*, 2H), 7.80 (*m*, 2H), 8.00 (*d*, *J* = 8.7 Hz, 2H), 8.22 (*d*, *J* = 1.5 Hz, 2H), 9.03 (*s*, 1H) and 9.06 (*s*, 1H) (Figure A14); ^{13}C NMR (75 MHz, DMSO-d_6) δ (ppm): 113.83, 114.01, 117.22, 118.19, 120.07, 120.11, 123.81, 124.02, 129.42, 130.43, 133.60, 135.37, 135.79, 136.00, 137.19, 137.26, 137.62, 140.15, 143.59, 164.53, 165.07, 173.10, 173.60 and 195.63 (Figure A15). The infrared bands were (cm^{-1}) $\nu_{Zn\text{-}N}$ = 492, $\nu_{Zn\text{-}O}$ = 542, $\nu_{C=N}$ = 1614, $\nu_{(O\text{-}H)Zn}$ = 3429, $\nu_{C\text{-}O}$ = 1271, $\nu_{C\text{-}H}$ = 3047 and ν_{Ar} = 756 and 710 (Figure A16). TGA weight loss ($m_{\%}$, calculated values in parenthesis) was 3.82 (3.59) (150-220 °C) – coordination water and 0.23 % of hydration water, 77.52 (80.28) (300-600 °C) ligand pyrolysis and residual 18.66 (16.13) – ZnO (Figure A17).

. Elemental analysis (%) of the C, H and N atoms was performed using a Perkin-Elmer microanalyzer model PE 2400. ^{1}H and ^{13}C NMR 1D spectra were measured using a DMSO-d_6 solution (33 mg mL^{-1}) in a Varian Mercury 300 MHz spectrometer. FTIR spectra were recorded in an Agilent Technologies Cary 630 spectrometer in attenuated total reflectance (ATR) mode. Thermal stability was evaluated using a Shimadzu model DTG 60H thermobalance. TG/DTA curves were recorded from T = 25 °C to 1000 °C with a heating rate of 25 °C min^{-1} in an oxidant atmosphere.

3.2.2.2 Steady-state Photophysical Measurements

Electronic absorption spectra of the [Zn(sal-3,4-ben)] in solution and solid-state, PVK: and PFO:guest films were acquired with a *Hewlett-Packard* 8452A diode array spectrophotometer.

Steady-state photoluminescence (PL) and excitation (PLE) spectra were recorded with a Cary Eclipse Varian spectrofluorimeter using λ_{exc} = 290, 375, 400 and 420 nm to excite preferably the PVK of the PVK:*X* composites, the PFO into PFO:*X* thin-films composites, [Zn(salophen)] and [Zn(sal-3,4-ben)] in solution and solid-state, respectively. The emission ranges were recorded from 320 nm to 700 nm. The films were oriented in a back-face configuration at 45º and solutions measurements were done in a 1 cm quartz cuvette.

Relative PLQYs of the [Zn(salophen)] and [Zn(sal-3,4-ben)] in solution were obtained using the relative method, according to equation 3.1, using coumarin 153-C153

(λ_{exc} = 418 nm; $PLQY_S$ = 0.38) diluted to the same concentration in ethanol as standard, following the IUPAC recommendations.[191–193]

$$PLQY_{obs} = \frac{F_i}{F_s}\frac{\varepsilon_s}{\varepsilon_i}\frac{n_i^2}{n_s^2}PLQY_s \quad (3.1)$$

where: F_i and F_S are the integrated emission spectra of the sample and of the standard, ε_i and ε_s their absorbances at the excitation wavelength of the measurement, n_i and n_s the refractive indexes of the solvents on which the compounds where diluted.

Solid-state PLQYs of the salicylidenes and Zn(II)salicylidenes were obtained in a Quanta-ϕ (Horiba-Jobin-Yvon F-309) integrating sphere equipped with an optical fiber bundle (NA = 0.22-Horiba-FL-3000/FM4-3000) according to the methodology outlined by de Mello et al. 1997[194].

The redox potentials of sal-3,4-ben and of [Zn(sal-3,4-ben)] were determined by cyclic voltammetry using a model PAR 273A potentiostat with platinum working and counter electrodes and an Ag/AgCl reference electrode in an acetonitrile/tetrabutylammonium hexafluorophosphate solution (0.1 mol L^{-1}) (Figure A18). The scan rate for the cyclic voltammograms was 20 mV s^{-1}. The formal standard potential of the Fc^+/Fc redox couple in acetonitrile is approximately -5.1 eV. The HOMO (E_{HOMO}) and LUMO (E_{LUMO}) energies were determined using the following equations[195]:

$$E_{HOMO} = -\left(E_{\left[onset,ox\ vs.\ {}^{Fc+}/_{Fc}\right]} + 5.1\right) \quad (3.2)$$

$$E_{LUMO} = -\left(E_{\left[onset,red\ vs.\ {}^{Fc+}/_{Fc}\right]} + 5.1\right) \quad (3.3)$$

Only for sal-3,4-ben free ligand the solid-state optical E_{gap} was used in order to obtain the E_{LUMO} value (where $E_{gap} = E_{LUMO} - E_{HOMO}$). The redox potentials for the other compounds are from the literature.

3.2.2.3 Time-resolved Photophysical Measurements

Fluorescence decays of the PVK composites were recorded using time-correlated single-photon counting (TCSPC) in an Edinburg Analytical Instruments FL 900 spectrofluorimeter with an MCP-PMT (Hamamatsu R3809U-50) with a pulsed diode operating at λ_{exc} = 290 nm (model EPLED-290, with a band width of 5 nm, 815 ps) and

a pulsed diode laser at λ_{exc} = 375 nm (model EPL-370, with a band width of 5 nm, 77 ps) were used for excite PVK and PFO matrix preferably, respectively. The decay signal was collected at λ_{PL} = 405 nm (PVK emission). The instrument response was recorded using Ludox samples. At least 10,000 counts in the peak channel were accumulated for the lifetime determination. The emission decays were analyzed using exponential functions as previously described[95,196].

3.2.2.4 OLEDs Assembly

Initially, ITO substrates (25 Ω/cm^2 from Delta Technologies, USA) were washed with deionized water, 2-propanol and acetone in an ultrasonic bath for 15 min each. Substrates were dried on a hot plate at 130 °C for 10 min and, subsequently, treated with UV ozone for 30 min. Over this substrate, a 30-nm-thick layer of PEDOT:PSS was spin-coated (5000 rpm, 60 s) and annealed for 30 min at 110 °C. Next, 80 nm of the PVK:**X** (2.5 % mol/mol) THF solution (2.591x10^{-2} mol L^{-1}) was spin-coated under a controlled atmosphere environment. After this deposition, the film was annealed for 30 min at 90 °C. Finally, layers of calcium (30 nm) and aluminum (100 nm) were deposited by thermal evaporation under a vacuum of 10^{-6} mbar within an mBraun Evaporator. Diodes were fabricated in a glove box (H_2O, O_2 < 1 ppm) with a simple OLED configuration of glass|ITO|PEDOT:PSS|PVK:***X*** (2.5 % mol/mol)|Ca|Al with ***X*** = Alq_3, Znq_2, salophen, [Zn(salophen)], sal-3,4-ben or [Zn(sal-3,4-ben)] (Figure 3. 2a).

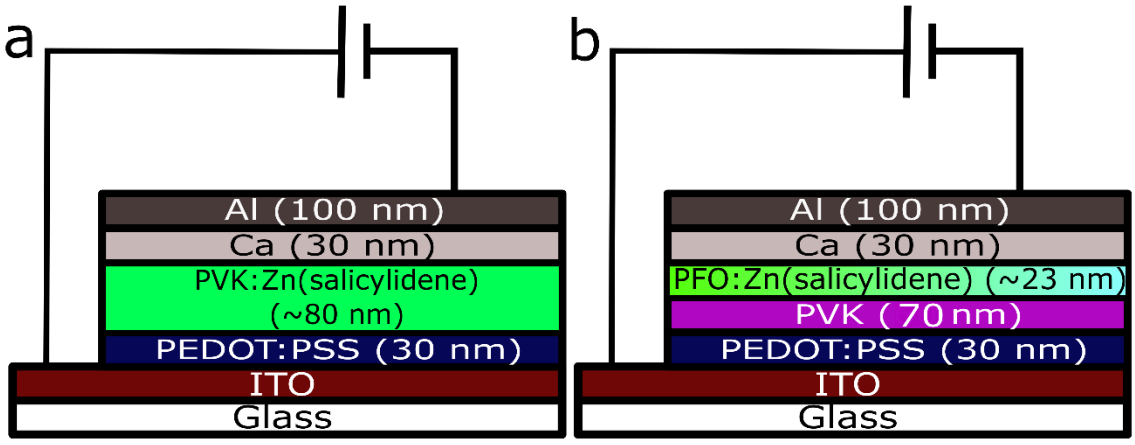

Figure 3. 2. Solution-processed OLEDs architecture: a) ITO|PEDOT:PSS|PVK:dye|Ca|Al, where dye = Alq3, Znq2, salophen, sal-3,4-ben, [Zn(salophen)] or [Zn(sal-3,4-ben)]; and b) ITO|PEDOT:PSS|PVK|PFO:Zn(salicylidene)|Ca|Al, where Zn(salicylidene) is [Zn(salophen)] or [Zn(sal-3,4-ben)].

Diodes with the configuration: glass|ITO|PEDOT:PSS (30 nm)|PVK (70 nm)|PFO:Zn(salicylidene) (≈23 nm)|Ca (30 nm)|Al (100 nm) (Figure 3. 2b) were prepared in similar way: ITO substrates (25 Ω/cm^2 from Delta Technologies, USA) were washed with Extran® neutral detergent, deionized water, isopropanol and acetone in an ultrasonic bath for 15 min each. Substrates were dried on a hot plate at 130 °C for 10 min they treated with UV ozone for 30 min. Subsequently, a 30-nm-thick layer of PEDOT:PSS (hole injection layer) was spin-coated (5000 rpm, 60 s) and annealed for 30 min at 110 °C. Next, 70 nm of the HTL/EBL (PVK) followed by the active layers with ≈ 23 nm of thickness composed by PFO:Zn(salicylidene) in a THF solution ($2.591x10^{-2}$ mol L^{-1}) were spin-coated under a controlled atmosphere ($Ar_{(g)}$). Finally, calcium (30 nm) and aluminum (100 nm) layers were deposited by thermal evaporation under a vacuum of 10^{-6} mbar within an mBraun Evaporator. The concentration of [Zn(salophen)] and [Zn(sal-3,4-ben)] were 0.1, 0.5, 1.0 and 2.5 % mol/mol ratio.

Optical-electrical properties of the OLEDs were measured in an oxygen-free sample holder. The diodes were analyzed in terms of current vs. voltage measurements (IxV) using a 2400 Keithley SourceMeter. Electroluminescence (EL) spectra were acquired using a USB2000+ Ocean Optics diode array spectrometer. The luminance-voltage curves (LxV) and the CIE 1931 chromaticity coordinates were measured using a Konica Minolta CS-100A luminancimeter using a close-up lens No. 110, ø = 40.5 mm, 10 to 20 cm. All data were collected simultaneously using a homemade LabView® interface. Current and power efficiencies vs. voltage curves (η_{curr}xV and η_PxV) were obtained applying equations 1.12 and 1.13, respectively.

Confocal fluorescence microscopies were performed in a Leica SP5 confocal laser scanning, using an HCX PL APO CS 10x0.4 DRY objective. Argonium laser line (λ_{exc} = 458 nm) were used for exciting preferably the Zn(salicylidene) derivatives in the composite.

Thickness of the active layer was estimated by field emission gun scanning electron microscopy (FEG-SEM) cross-section image (Figures A23 and A31) in a Thermo Fischer Scientific Quanta^{TM} 250 FEG at 10 kV, under high vacuum ($1.24x10^{-4}$ Pa), magnitude of 10^5x and with an Everhart-Thornley Detector (ETD). The addition of a small amount of the dye (0.1 % → 2.5 % mol/mol) in the PVK and PFO matrix does not disturb substantially the thickness of the layer.

3.2.3 Theoretical Approach

Considering the success of the DFT framework to describe the excited states of salicylidene chromophores,[27,152,197–199] our calculations were done under the DFT/TD-DFT framework using the density-functional PBE0[200] with the triple-ζ basis set 6-311++G(d,p).[201,202] Ligand X-ray structure was used for the initial structure of the aquo-Zn(II) coordination compounds. Molecular structures and dipole moments, corresponding to the ground and first excited singlet states (S_0 and S_1), were optimized both in the gas phase. The solvent medium was considered through the PCM approach,[203] using the PFO parameters (n_{PFO} = 1.725 and ε_{PFO} = 3)[204], thus obtaining the vertical excitation energies and natural transition orbitals (NTOs) for [Zn(salophen)] and [Zn(sal-3,4-ben)]. All calculations were done using the Gaussian 09 software.[205]

3.3 Results and Discussion

3.3.1 Photophysics of [Zn(salophen)] and [Zn(sal-3,4-ben)] in Solution and Solid-state

Firstly, the steady-state and time-resolved photophysical properties of the salicylidene derivatives ([Zn(salophen)] and [Zn(sal-3,4-ben)]) were evaluated in terms of electronic absorption and photoluminescence spectra and fluorescence decays in THF solution (10 μmol L^{-1}), as well as, in solid-state (Figure 3.3). The salophen[206] and sal-3,4-ben[207] free-ligands were characterized in the previous chapter. Table 3.1 summarizes the [Zn(salophen)] and [Zn(sal-3,4-ben)] photophysical properties.

In THF solution, [Zn(salophen)] (green curves on Figure 3.3a) presented in the electronic absorption spectra two maxima wavelengths centered at λ_{abs1} = 405 nm and λ_{abs2} = 295 nm, exhibiting a red-shift and improvement of its molar attenuation coefficients in comparison to the salophen free-ligand (ε_1 = 1.8x10^4 L mol^{-1} cm^{-1} and ε_2 = 1.8x10^4 L mol^{-1} cm^{-1}), which were attributed to ILCT-$\pi \rightarrow \pi^*$ type electronic transitions, involving the singlet-state orbitals: lowest and highest energies to the $S_0 \rightarrow S_1$ (HOMO-LUMO) and $S_0 \rightarrow S_2$. PL spectra exhibited an emission profile with a well-resolved vibronic progression centered at λ_{PL} = 500 (0-0) and 527 nm (0-1) with a PLQY = 1.7 % and Stokes shift of SS = 4691 cm^{-1}, a behavior similar to its steady-state and time-resolved spectra in DMSO solution at the same conditions. Electronic absorption and PL spectra on the solid-state of the [Zn(salophen)] (green curves on Figure 3.3b) a significative red-shift was observed, presenting λ_{abs1} = 420 nm and λ_{abs2} = 300 nm, a loses in its PL vibronic progression with zero-phonon band centered at λ_{PL} = 515 nm. Also, [Zn(salophen)]

PLQY and SS diminished on the solid-state (PLQY = 0.7 % and SS = 4124 cm^{-1}), as expected for some solid-state samples due to inner-filter and aggregation effects.

The electronic absorption spectra of [Zn(sal-3,4-ben)] in THF solution (blue curves in the Figure 3.3a) showed an analogous spectral profile to the [Zn(salophen)] with a smallest red-shift in its maxima absorption wavelengths (λ_{abs1} = 418 nm and λ_{abs2} = 302 nm), however, a considerably improvement of their molar attenuation coefficients (ε_1 = $5.1x10^4$ L mol^{-1} cm^{-1} and ε_2 = $5.5x10^4$ L mol^{-1} cm^{-1}). In a different way of the [Zn(salophen)], PL spectra of [Zn(sal-3,4-ben)] in THF did not present a well-defined vibronic progression resolution and the maximum emission centered at λ_{PL} = 542 nm, which exhibited a PLQY 11 times higher in comparison to the [Zn(salophen)] (PLQY = 19.0 %), approximately, with SS = 5473 cm^{-1}. As for the [Zn(salophen)], absorption and PL spectra of the [Zn(sal-3,4-ben)] in solid-state (blue curves in Figure 3.3b) noticed a red-shift of the maxima wavelengths with the same spectral profile: λ_{abs1} = 428 nm and λ_{abs2} = 310 nm; λ_{PL} = 560 nm; PLQY = 1.1; and SS = 5507 cm^{-1}. In summary, the nature of the [Zn(sal-3,4-ben)] is quite similar to the [Zn(salophen)] coordination compounds, being mainly of ILCT electronic transitions. However, the inclusion of the benzophenone moiety on the salophen organic framework disturbs considerably its electronic structure, promoting an enhancement of the optical properties of the [Zn(sal-3,4-ben)] coordination compound in THF solution, as well as, in solid-state, which will be discussed better with DFT and TD-DFT calculations in the PFO devices section.

Also, a spectral overlap between PVK (violet curves) and PFO (black curves) PL spectra with Zn(II) salicylidene derivatives is presented in the Figure 3.3b. The two conducting polymers PL spectra exhibited a larger spectral complementary with [Zn(salophen)] and [Zn(sal-3,4-ben)] electronic absorption spectra in solid-state, as well as in THF solution. Thus, energy transfer and charge recombination processes will be observed from the conducting polymers to the Zn(II) coordination compounds. Spectral overlap between the free salicylidene ligands and Zn(II) salicylidenes with the PVK are in the appendix (Figure A21).

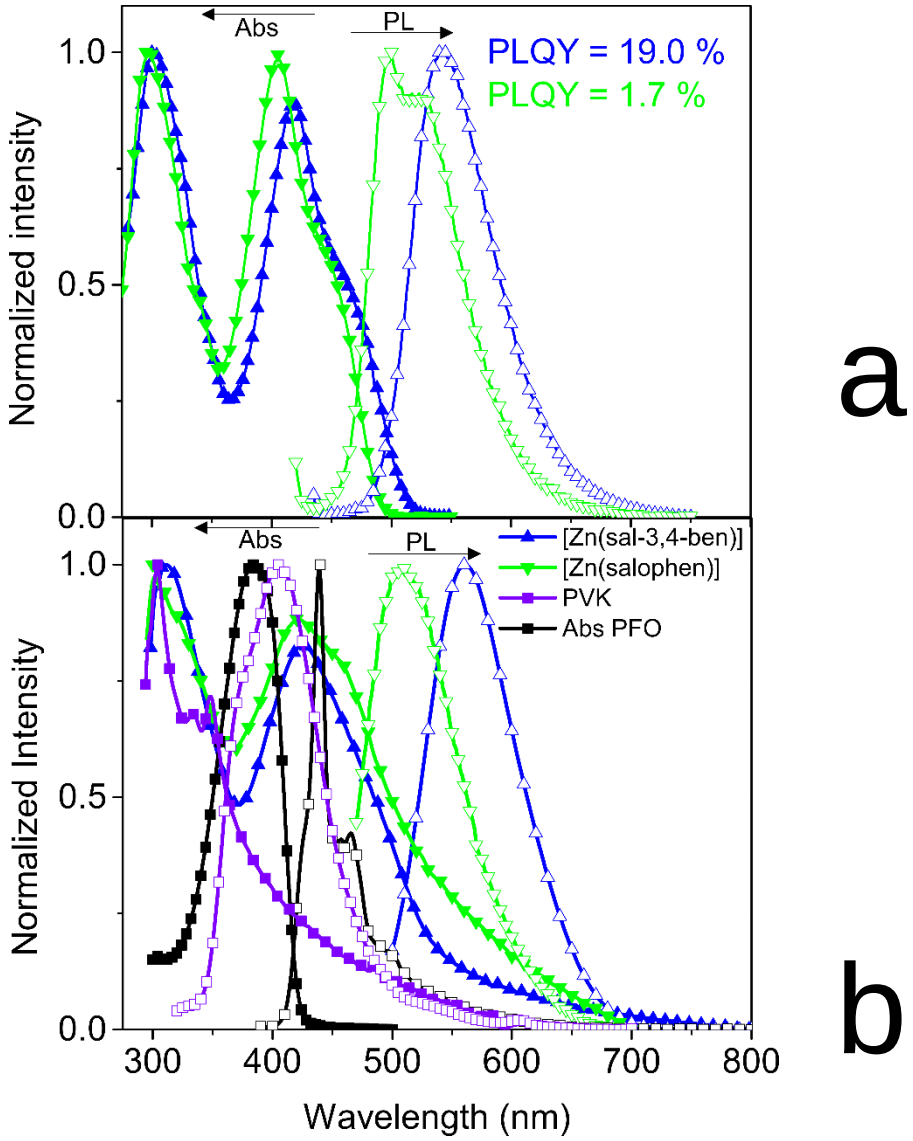

Figure 3. 3. Normalized electronic absorption and PL spectra of the [Zn(salophen)] (green curves) and [Zn(sal-3,4-ben)] (blue curves) in THF solution (a) and solid-state (b). Spectral overlap between PVK (violet curves) and PFO (black curves) thin-films PL spectra with Zn(salicylidenes) absorption spectra in solid-state (b).

Table 3. 1. Resume of photophysical parameters of [Zn(salophen)] and [Zn(sal-3,4-ben)] in THF solutions (10 μmol L^{-1}) and solid-state. Where λ_{abs} (nm) and λ_{PL} (nm) are the experimental absorption and emission maximum, ε (x10^4 L mol^{-1} cm^{-1}) is the molar extinction coefficient, PLQY (%) is the quantum yield of fluorescence and SS (cm^{-1}) is the Stokes Shift.

		λ_{abs}	ε	λ_{PL}	PLQY	SS
[Zn(Salophen)]	THF solution	405 295	1.8 1.8	500 527	1.7	4691
	Solid-state	420 300	-	515	0.7	4124
[Zn(Sal-3,4-ben)]	THF solution	418 302	5.1 5.5	542	19	5473
	Solid-state	428 310	-	560	1.1	5507

3.3.2 Poly(N-vinylcarbazole) Devices

3.3.2.1 Optical Properties of the PVK/Composite Films

PL quantum yield (PLQY) of the [Zn(sal-3,4-ben)] in the solid-state was PLQY = 1.1 % with small increase in comparison to [Zn(salophen)] (PLQY = 0.7 %). However, the [Zn(sal-3,4-ben)] solid-state PL quantum yield is very low in comparison to the 8-hydroxyquinolinate derivatives ($PLQY_{Alq_3}$ = 22 % [208] and $PLQY_{Znq_2}$ = 45 %[62]).

Optical properties of the films prepared by the spin-coated were investigated by electronic absorption and by steady-state (PL) and dynamic photoluminescence spectroscopy. The electronic absorption spectra of PVK and its composites showed peaks of the PVK (λ_{abs1} = 346 ~ 348 nm, λ_{abs2} = 332 nm and λ_{abs3} = 300 ~ 304 nm) in addition to the peaks of the guests (Table 3.2, Figure A20).

The PL spectra of PVK and its composites (λ_{exc} = 290 nm) with Alq_3, Znq_2, salophen, [Zn(salophen)], sal-3,4-ben or [Zn(sal-3,4-ben)] are in Figure 3. 3. All of the PL spectra presented the emission of the PVK (λ_{PL} = 405)[95] and the emission of the guests: λ_{PL} (Alq_3) = 511 nm, λ_{PL} (Znq_2) = 522 nm, λ_{PL} (salophen) = 460 nm and 530 nm, λ_{PL} ([Zn(salophen)]) = 495 nm, λ_{PL} (sal-3,4-ben) = 538 nm, and λ_{PL} ([Zn(sal-3,4-ben)]) = 532 nm (Table 3.2). The emission band at 460 nm observed for PVK:salophen was attributed to the enol species[173]. The second band observed at 538 nm for this system is

absent in dilute DMSO solutions, although it has been observed in acetonitrile at $9x10^{-5}$ mol L^{-1}.[209] Although the assignment is still controversial, we are suggesting that it is due to aggregates, according to our work in progress[210].

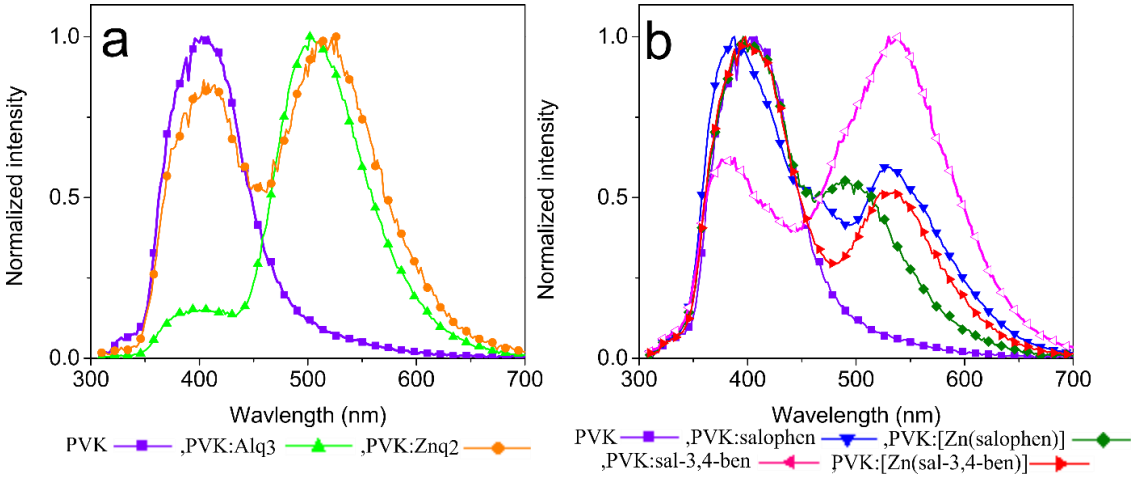

Figure 3. 4. Normalized PL spectra (λ_{exc} = 290 nm) of the PVK and its composites (2.5 % mol/mol).

The fluorescence decays of the PVK and its composites (2.5 % mol/mol) are in Figure 3. 4. These decays were obtained using λ_{exc} = 290 nm where the PVK host was preferentially excited and collected at λ_{PL} = 405 nm (PVK emission). The resonant nonradiative energy transfer (FRET) according to the Förster mechanism from the PVK (donor) to the guests (acceptor) leads to a decrease in the donor lifetime (PVK) in the presence of the acceptors (guests) [123]. Fluorescence decays and their fittings using exponential functions are in the appendix (Figures A22a-A22g).

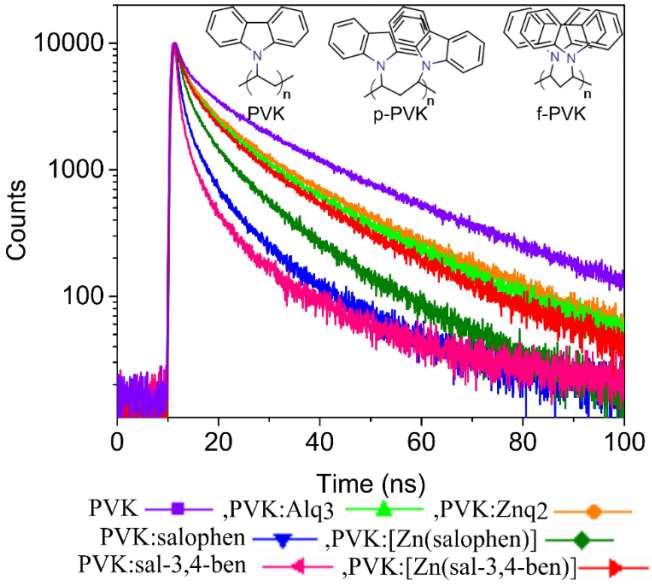

Figure 3. 5. Fluorescence decays of the PVK:X composites (2.5 % mol/mol, X = guests) λ_{exc} = 290 nm; λ_{PL} = 405 nm.

The fluorescence decay of PVK is very complex, and a reasonable fitting can be obtained using triexponential functions[95]. The nature of this complexity is the presence of excimer emissions in addition to the emission of isolated chain segments.[211] The presence of excimers requires proximity between two polymeric segments in a specific conformation, which can result in partially (p-PVK) or completely (f-PVK) overlapped carbazole moieties (inset on Figure 3.4)[130]. From the fittings, the lifetimes of the PVK were obtained as: τ_{FL1} = 1.076 ± 0.033 ns (B_1 = 6 %), τ_{FL2} = 6.524 ± 0.166 ns (B_2 = 20 %) and a longer component with a higher contribution τ_{FL3} = 24.256 ± 0.246 ns (B_3 = 74 %) due to the completely overlapped excimers (Table 1), where B_i is the relative contribution of every lifetime. Considering PVK as a donor, the presence of the acceptors might change both the lifetimes and their relative contributions if FRET processes are involved.

Additionally, the decay of the PVK in the PVK:Alq_3 composite can be fitted using a triexponential function. All of the lifetimes of this composite were faster than in the absence of this guest. Furthermore, the relative contributions of the faster decays increased from B_1 = 6 % and B_2 = 20 % in PVK to B_1 = 11 % and B_2 = 29 % in the PVK:Alq_3 composite, whereas B_3 decreased from 74 % to 60 % (Table 3.2). A similar behavior is also observed for both coordination compounds, PVK:Znq_2, PVK:[Zn(salophen)] and PVK:[Zn(sal-3,4-ben)]. For these composites (PVK:Alq_3, PVK:Znq_2 and PVK:[Zn(sal-3,4-ben)]), there was a decrease in lifetimes and a decrease in the contribution of B_3 compared to PVK alone. The PVK:[Zn(sal-3,4-ben)] composite followed a trend similar to that of PVK:Alq_3. Considering that the longer emission decay is attributed to excimers with a coplanar interaction between the carbazole moieties, the decrease in the B_3 contribution can be explained by partial inhibition of this excimeric conformation. Hence, we propose that the guest molecules are interposed between the chain segments, and consequently, the carbazole interchain or intersegmental interactions become inhibited. Therefore, we may assume that the dissolution of these three guest molecules in the PVK host inhibits the approach of the two carbazole moieties at a suitable distance and orientation required for the formation of the completely overlapped excimer.

However, the PVK composites with the salophen and sal-3,4-ben ligands showed a remarkable decrease in both the τ_{FL1} and τ_{FL2} lifetimes and in the B_3 contribution compared to the host and compared to the respective coordination compounds (Table 3.1).

These results suggest that the free ligands are more soluble in the polymer matrix than the respective metal coordination complexes undergoing a greater intercalation in the polymer chains. This higher solubility favors the FRET and decreases the efficiency of the excimer formation.

As a general trend, the relative contribution of the excimer emission decreases in the following order: PVK > PVK:Alq_3 = PVK:[Zn(sal-3,4-ben)] > PVK:Znq_2 > PVK:[Zn(salophen)], accompanied by a decrease in the respective emission lifetimes.

The lifetime decrease was explained by the FRET process via the Förster mechanism. Two conditions are required for an efficient FRET process: a substantial spectral overlap between the absorption band of the acceptor (guests) and a particular distance and orientation between the donor and the acceptors[123]. The decrease in the lifetimes demonstrates that the FRET process is present. The efficiency of the FRET can be calculated using the spectral overlap between the donor and the acceptor spectra or using the fluorescence lifetimes of the donor in the presence and absence of the acceptor. Considering that the emission decay of the PVK is very complex and that each component of the triexponential functions undergoes changes in both the lifetimes (τ_i) and the relative contributions (B_i) of each individual component of the lifetimes, a facile interpretation of the FRET efficiency is quite difficult. Therefore, in a very simplified and approximate approach, we estimated the FRET efficiency of the guests using the weighted arithmetic average lifetime $< \tau >$, defined as

$$< \tau > = \frac{\int_0^\infty t \sum B_i e^{-\frac{t}{\tau_i}} dt}{\int_0^\infty \sum B_i e^{-\frac{t}{\tau_i}} dt} = \frac{\sum B_i \tau_i^2}{\sum B_i \tau_i} \qquad (3.3)$$

where τ_i is the fluorescence lifetime and B_i is the relative contribution of each component[212]. According to this approach, we estimated the average FRET efficiency using the average lifetimes of the donor in the absence, $< \tau_D >$, and in the presence, $< \tau_{DA} >$, of the acceptor:

$$< E_{FRET} > = \left(1 - \frac{<\tau_{DA}>}{<\tau_D>}\right) . 100\ \% \qquad (3.4)$$

where $< \tau_D >$ = 22.981 ns for the PVK.

Using the data showed in Table 3.2, and combining the equations 3.3 and 3.4, the obtained average FRET efficiency decreases in the following order: PVK:sal-3,4-ben > PVK:salophen > PVK:[Zn(salophen)] > PVK:[Zn(sal-3,4-ben)] > PVK:Alq_3 > PVK:Znq_2. As a general trend, the FRET efficiency is higher for the free ligands than for the Zn(II) coordination compounds. Additionally, the FRET average efficiencies of Alq_3 and Znq_2 are lower than those of the Zn(II) compounds (Figure 3.6). This result can be explained partially by the smaller spectral overlap between the emission of the PVK (donor) and the absorption spectra of the compounds (acceptor) (Figure A21); for the Zn compounds, the overlap is smaller than for the free ligands. Although the spectral overlap (Figure 3.3b and Figure A21) between the PVK PL and the absorption of the Alq_3 and the Znq_2 are greater, the FRET is not high probably because of the longer distance between the donor and acceptor species.

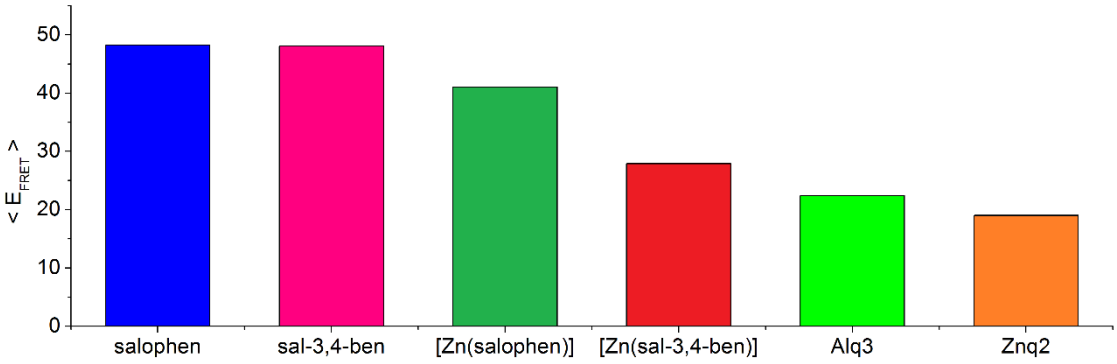

Figure 3. 6. Average FRET efficiencies of the PVK emission by the guests according to equation 4.

The major conclusion from the optical data is that there is a substantial FRET process of the PVK excitons by the ligands, which are greater than that of the coordination compounds. The probable impact of the quenching process is not only proportional to the spectral overlap between the donor emission and the acceptor absorption but also dependent on the guest interaction with the host. The free ligands are better acceptors than the coordination compounds.

Table 3. 2. Steady-state PL, fluorescence decays and average FRET efficiency percentages (<EFRET>) of PVK:X (2.5 % mol/mol; λ_{exc} = 290 nm; λ_{PL} = 405 nm) composites.

X	λ_{PL} (nm)	τ_1 (ns)	B_1 (%)	τ_2 (ns)	B_2 (%)	τ_3 (ns)	B_3 (%)	<τ> (ns)	<E_{FRET}> (%)
PVK	405	1.076 ± 0.033	6	6.524 ± 0.166	20	24.256 ± 0.246	74	22.981	-
PVK:Alq_3	405, 511	0.988 ± 0.023	11	5.389 ± 0.103	29	19.632 ± 0.173	60	17.826	22
PVK:Znq_2	405, 522	1.051 ± 0.026	10	5.573 ± 0.114	27	20.293 ± 0.293	63	18.614	19
PVK:[Zn(sal-3,4-ben)]	405, 532	0.991 ± 0.024	11	5.176 ± 0.098	30	18.358 ± 0.157	59	16.568	30
PVK:[Zn(salophen)]	405, 495	0.939 ± 0.019	19	4.611 ± 0.080	36	15.942 ± 0.150	45	13.558	41
PVK:sal-3,4-ben	405, 538	0.538 ± 0.009	41	3.161 ± 0.050	33	14.936 ± 0.205	26	11.932	48
PVK:salophen	405, 460, 530	0.657 ± 0.011	31	3.643 ± 0.055	37	14.750 ± 0.169	32	11.905	48

Considering that the efficiency of the diode emission is proportional to the quantum efficiency of the PL emission, we might expect that the quenching process of the PVK will impact the diode efficiency in the spectral range of the PVK emission. In contrast, the efficiency of the spectral emission of the guests might be positively impacted by the FRET process from the donor to the acceptors.

3.3.2.2 Electroluminescence of the Diodes with PVK

The OLEDs using the PVK:***X*** composites as an active layer were fabricated by spin-coating of THF solutions, giving a diode with an architecture of ITO|PEDOT:PSS|PVK:***X***(2.5 % mol/mol)|Ca|Al, where ***X*** is Alq_3, Znq_2, salophen, [Zn(salophen)], sal-3,4-ben or [Zn(sal-3,4-ben)]. The electroluminescence (EL) spectra, chromaticity coordinates (x, y, CIE 1931) and luminances (L) of these diodes are summarized in Table 3.2. For comparison, we also measured the electrical properties of a diode with PVK only.

The PVK EL spectrum (Figure 3.6a – violet color, Table 3.2) presents a band centered at λ_{EL} = 414 nm at a voltage of 14 V, with CIE coordinates of 0.19, 0.10 (Figure 3.7, very similar to the profile of the PVK PL emission (Figure 3.3). Comparing the EL to the PL suggests that this emission may be attributed to an excimer with the carbazole groups overlapped in a sandwich conformation. Furthermore, differing from the PL, a broad and weak band centered at approximately 550 nm is observed. Some authors suggest that this band can be attributed to the carbazole electromers[130].

The EL emissions of the diodes with PVK:Alq_3 at V = 12.0 V and with PVK:Znq_2 (Figure 3.6a) at V = 10.0 V are centered at λ_{EL} = 508 nm (CIE 0.23, 0.47, Figure 3.7) and λ_{EL} = 532 nm (CIE 0.33, 0.58, Figure 3.7), respectively. These spectral data are similar to those reported in the literature for these coordination compounds[61,213]. Almost no difference between the EL and PL (Figure 3.3) emissions of these compounds in PVK was observed. Nevertheless, in Figure 3. 3, we observed the PVK emission, which is absent in the EL spectrum.

The EL spectrum of the PVK:salophen composite (V = 17.5 V) (Figure 3.6b) shows remarkable differences compared to the PL (Figure 3.3), with the appearance of a low-lying broad band that can be deconvoluted into three peaks at $\lambda_{EL(1)}$ = 468 nm, $\lambda_{EL(2)}$ = 536 nm and $\lambda_{EL(3)}$ = 606 nm (see inset Figure 3.6b). No emission at 606 nm was observed in the PL. The emission centered at 460 nm is attributed to the enol emission[173] and the emission at 536 nm can be attributed to the salophen aggregates[210]. The EL broad

peak at 606 nm has been assigned by some authors to the carbazole electromer.[130] The CIE coordinates of this diode are (0.29, 0.33) (Figure 3.7), close to the white emission region.

The EL emission of the diode with PVK:[Zn(salophen)] (V = 16.0 V) showed a band with a maximum at λ_{EL} = 516 nm (CIE coordinates of 0.32,0.60, Figure 3.7), which is similar to the EL of this compound in a diode with polyfluorene as a host[196]. The EL spectrum of this diode is similar to the solid-state PL of the [Zn(salophen)] complex[173]. This spectrum differs from the PL emission (Figure 3.3), in which two bands have been observed: a higher intensity band at 400 nm due to the PVK and another at 492 nm attributed to the [Zn(salophen)] coordination compound. For the other composites, the EL emission of the PVK is absent.

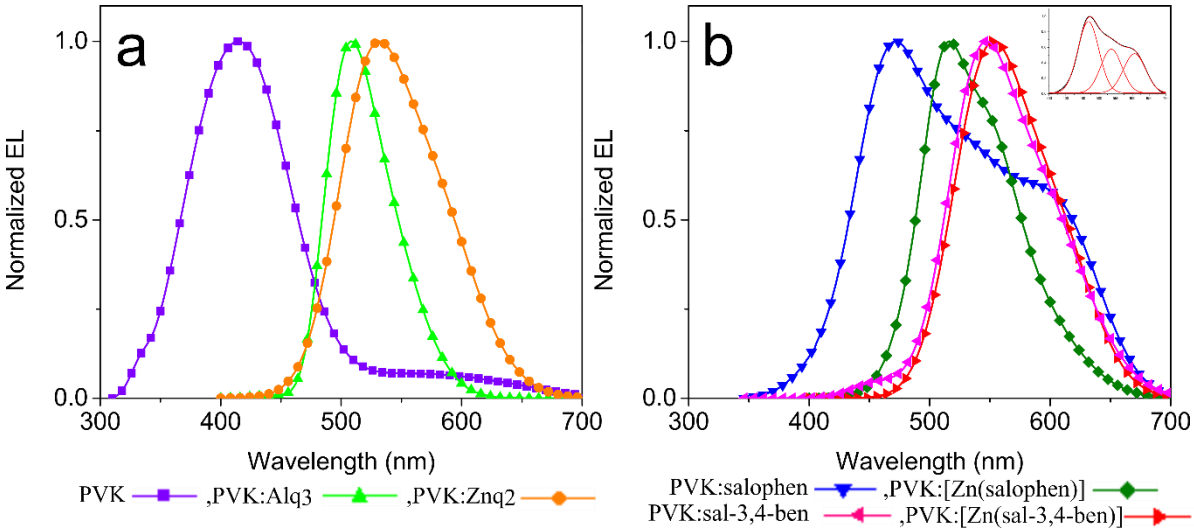

Figure 3.7. Normalized EL spectra of the diodes ITO|PEDOT:PSS|PVK:X(2.5 % mol/mol)|Ca|Al, (2.5 % mol/mol).

A yellowish EL emission (CIE 0.41,0.54, Figure 3.7) was observed for the PVK:sal-3,4-ben composite (Figure 3.6b), which is similar to the PL spectrum (Figure 3.3b), with a peak at λ_{EL} = 552 nm. The EL spectrum of PVK:[Zn(sal-3,4-ben)] diode (Figure 3. 6b) is present as the yellowish band (CIE 0.43,0.56, Figure 3.7) centered at λ_{EL} = 554 nm, with a small blue shift in comparison to the PL spectrum of the [Zn(sal-3,4-ben)] in solid state (λ_{PL} = 560 nm).

Some conclusions arise from the EL spectra, notably the absence of the PVK emission in all of the diodes, and with the exception of the salophen, the PL and the EL spectra of all the compounds are similar in terms of spectral range. The absence of the

PVK emission cannot be explained by the quenching process, which is only partial, as shown by the FRET processes.

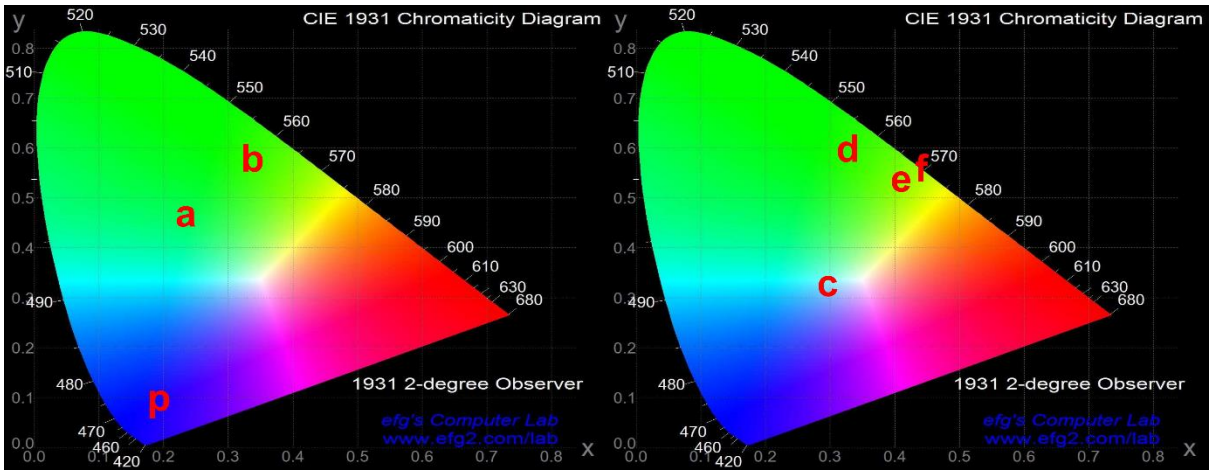

Figure 3.8. Chromaticity coordinates (x,y CIE 1931) of the diodes ITO|PEDOT:PSS|PVK:X(2.5 % mol/mol)|Ca|Al diodes with X = Alq3 (a), Znq2 (b), PVK (p), salophen (c), [Zn(salophen)] (d), sal-3,4-ben (e) and [Zn(sal-3,4-ben)] (f).

The current density, luminance and current efficiency (Figure 3.8a-c, respectively) curves were obtained as a function of the applied voltage. The electronic properties extracted from these measurements are summarized in Table 3.2. The luminous intensities for the diodes containing the PVK:salophen and PVK:sal-3,4-ben composites were very low, and no luminance and current efficiency for these OLEDs could be recorded under our experimental apparatus.

The diodes with PVK:Alq_3 and PVK:Znq_2 presented the same turn-on voltages of V_{on} = 8.5 V, current densities of J = 0.19 and 0.34 A cm^{-2}, luminance maxima of L_{max} = 364 cd m^{-2} (16.0 V) and 126 cd m^{-2} (13.0 V) and current efficiencies of η_{curr} = 0.049 cd A^{-1} (13.0 V) and 0.031 cd A^{-1} (13.5 V), respectively.[213]

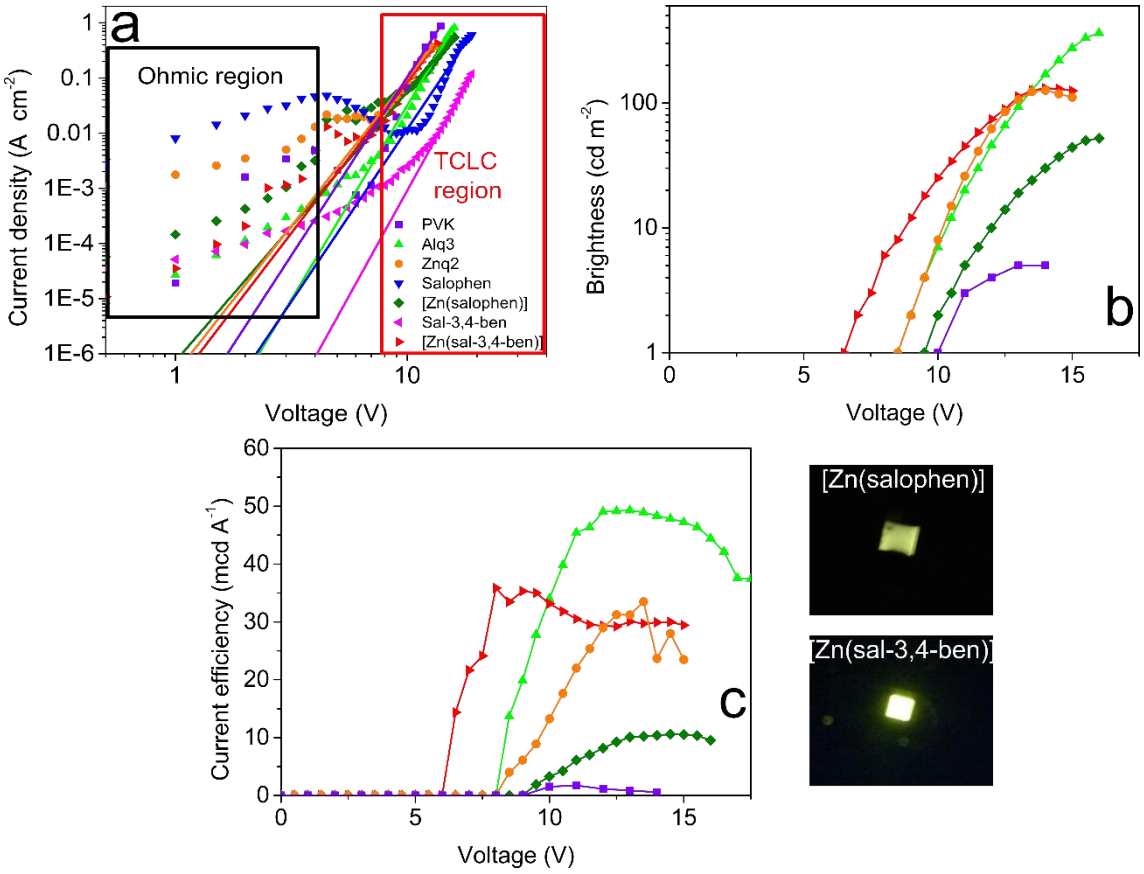

Figure 3.9. a. log-log Current density vs. voltage; b. brightness vs. voltage, c. current efficiency vs. voltage curves of the diodes ITO|PEDOT:PSS|PVK:X|Ca|Al. Picture of [Zn(salophen)] and [Zn(sal-3,4-ben)] devices work at L_{max}.

The diode PVK:[Zn(salophen)] presented poorer optical-electronic properties compared to the Alq_3 and Znq_2 complexes but better properties compared to the PVK:salophen, with a turn-on voltage of V_{on} = 9.5 V, a current density of J = 0.35 A cm^{-2}, a maximum luminance of L_{max} = 52 cd m^{-2} (16 V) and a current efficiency of η_{curr} = 0.011 cd A^{-1} (14.5 V) (Figure 3. 8). However, the optical-electronic properties of the diode PVK:[Zn(sal-3,4-ben)] were remarkable enhanced in comparison to both the PVK:sal-3,4-ben free ligand and the PVK:[Zn(salophen)], and were comparable to the PVK:Alq_3 and PVK:Znq_2 diodes. In addition, both the turn-on voltage (V_{on} = 6.5 V) and the density current (J = 0.02 A cm^{-2}) were lower than all the other compounds whereas the luminance and current efficiency were greater, with L_{max} = 131 cd m^{-2} (14 V) and a current efficiency of η_{curr} = 0.036 cd A^{-1}. The current efficiency is three times higher than the PVK:[Zn(salophen)] diode.

The other explanation is related to the charge injection, charge transport and exciton formation processes in the diode, which partially depend on the relative energy

levels of the frontier orbitals. The energies of the frontier orbitals are shown in Figure 3. 9 (Table 2). The energy levels of Al[214], Ca[214], ITO[214], PEDOT:PSS[215], PVK[216], Alq_3[217], Znq_2[61], salophen[173] and [Zn(salophen)][173] were obtained from the literature. The energies of the HOMO and LUMO orbitals of sal-3,4-ben and [Zn(sal-3,4-ben)] as determined by cyclic voltammetry[195] were E_{HOMO} = -5.70 eV/E_{LUMO} = -2.59 eV and E_{HOMO} = -5.52 eV/E_{LUMO} = -3.26 eV, respectively (Figure 3. S5). As a general trend, the band gap of the ligand coordinated to Zn(II) is lower than the free ligand. The decrease of LUMO and of the band gap caused by Zn(II) is related to the electronic coupling between the metal and the ligand[27,173]. This decrease might improve the charge injection processes from the electrodes to the active layers of the diodes. As we can see, the band gap and the frontier orbitals of salophen are higher than those of the other compounds; thus, we might expect a poorer performance of the diode with PVK:salophen, as we observed experimentally. Moreover, the diode performances follow the same trend of the band gaps for the [Zn(salophen)] and [Zn(sal-3,4-ben)] compounds. [Zn(sal-3,4-ben)] has a greater performance compared with the other Zn(II) compounds having a similar behavior of the Alq_3 device.

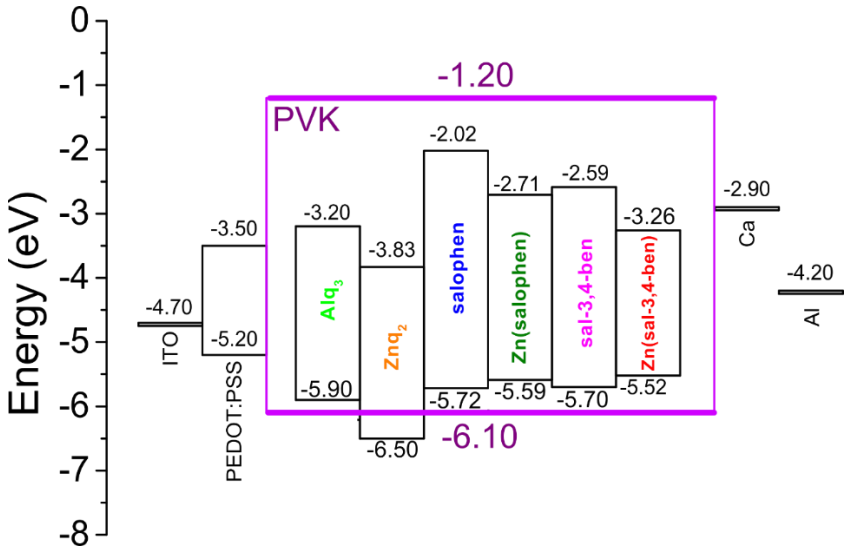

Figure 3. 10. Diagram with the frontier energy levels of Al[214], Ca[214], ITO[214], PEDOT:PSS[215], PVK[216], Znq_2[61], Alq_3[217], salophen, [Zn(salophen)], sal-3,4-ben and [Zn(sal-3,4-ben)].

Thus, although the diagram with the frontier energy levels provides some insights that might explain the electrical performance of the diodes, it is insufficient to explain all of our observations. For example, this diagram can not explain the differences between the PL and the EL profiles and, in particular, the complete absence of the PVK

EL emission. The explanation for this absence in all these diodes might be twofold: one is the complete quenching of the PVK emission by the guests. This hypothesis was considered unlikely because the maximum quenching efficiency was determined previously to be 73 % for the PVK:sal-3,4-ben. We did not observe complete quenching in any systems. Therefore, we should expect some PVK EL emission. The other explanation might be related to the charge transport processes.

It is well known that PVK is a poor EL emitter[130]. Therefore, the absence of the PVK emission in the diodes is probably much more related to this poor electrical property than to the quenching of the guest acceptors. Nevertheless, it is also known that PVK is a good hole injector[34], which favors better diode performance. Thus, we are considering that these guests and PVK host were involved in a cascade mechanism after the charge injection producing the excitons inside the lower energy traps, and these are the emissive states. In addition, one possible reason for the greater performance of the Zn(II) compounds ([Zn(salophen)] and [Zn(sal-3,4-ben)]) than the free ligands (salophen and sal-3,4-ben) is related to the charge mobility being favored by the metal ion. To explore that possibility, we analyzed the log-log plots of the JxV curves using two models: the SCLC according to Mott-Gurney law (eq. 1.7) and the TCLC (1.8).

As we can see in Figure 3.8a an ohmic behavior was observed for all devices at low voltages. The fit of the experimental data using the SCLC model was not good, probably due to the high density of trap states (m > 2) as consequence of both the heterogeneity of the polymer chain conformations and the randomly dispersion of the dyes into the PVK matrix. Differently, the fit of the experimental curves using the TCLC model was very good, giving values for PVK device of: m = 6.464, l = 5.464 (E_t = 0.140 eV) and hole mobility $\mu_p = 1.7x10^{-7}$ cm^2 V^{-1} s^{-1}. Values of hole mobility of PVK is within the range of 10^{-6} to 10^{-7} cm^2 V^{-1} s^{-1}.[99] For example, Khalifa et al. reported values of μ_p (PVK) = $2x10^{-7}$ cm^2 V^{-1} s^{-1} for L = 36 nm [218]. Using the same model, we determined the charge mobility for all the diodes containing the ligands and the metal complexes (values are in Table 2). According to those data, the charge mobilities followed the trend: $\mu_{Zn(sal-3,4-ben)} = 7.7x10^{-5}$ cm^2 V^{-1} s^{-1} > $\mu_{Znq_2} = 6.4x10^{-7}$ cm^2 V^{-1} s^{-1} > $\mu_{Alq_3} = 5.9x10^{-7}$ cm^2 V^{-1} s^{-1} > $\mu_{Zn(salophen)} = 4.2x10^{-7}$ cm^2 V^{-1} s^{-1} > $\mu_{PVK} = 1.7x10^{-7}$ cm^2 V^{-1} s^{-1} > $\mu_{sal-3,4-ben} = 1.8x10^{-8}$ cm^2 V^{-1} s^{-1} > $\mu_{salophen} = 1.7x10^{-9}$ cm^2 V^{-1} s^{-1} with is the opposite trend of the turn-on voltage of the diodes. Thus, the charge mobility values are in accordance to the HOMO/LUMO energies barriers for these molecules. Furthermore, from these results we might conclude:

1) higher exponential values obtained of $J \alpha V^m$ power law (m > 2) indicate that an elevated density of trap states are present on the PVK diodes; 2) the charge carrier mobility and voltage turn-on are strongly correlated in the diodes; 3) the improvement of the diode performance by the benzophenone moiety is probably due to the greater acceptor ability of this ligand electron transfer from the carbazole moieties; 4) the Zn(II) metal center improves both the current efficiency as well as the charge mobility: $\eta_{Zn(sal-3,4-ben)} > \eta_{Zn(salophen)} > \eta_{sal-3,4-ben} > \eta_{salophen}$. 5). The charge mobility of the diode assembled with [Zn(sal-3,4-ben)] is higher than the Alq_3 and Znq_2 by two orders of magnitude.

Although the charge mobility of the PVK:[Zn(sal-3,4-ben)] suggests a greater performance than the diodes with PVK:Alq_3 and PVK:Znq_2. However, its current efficiencies are of the same magnitude. Probably, the reason for this contradictory behavior is due to the lower PLQY, which is an important parameter for the OLEDs efficiency[189]. Therefore, in spite of $PLQY_{Alq_3}$ and $PLQY_{Znq_2} >> PLQY_{[Zn(sal-3,4-ben)]}$, the higher charge mobility of [Zn(sal-3,4-ben)] compensates the device current efficiency in comparison to the 8-hydroxyquinolinate derivatives ($\eta_{Zn(sal-3,4-ben)} \approx \eta_{Znq_2} \approx \eta_{Alq_3}$).

Table 3. 3. Optical-electronic properties of the solution-processed PVK:X diodes (2.5 % mol/mol).

	E_L (eV)	E_H (eV)	E_{gap} (eV)	λ_{EL} (nm)	V_{on}	J (A cm^{-2})[a]	μ_p (cm^2 V^{-1} s^{-1})[b]	L_{max} (cd m^{-2})	η_{curr} (cd A^{-1})	CIE1931 (x,y)
PVK	-1.20	-6.10	4.90	414	10.0	0.17	$1.7x10^{-7}$	5	0.002	0.19, 0.10
Alq_3	-3.20	-5.90	2.70	508	8.5	0.19	$5.9x10^{-7}$	363	0.049	0.23, 0.47
Znq_2	-3.83	-6.50	2.67	532	8.5	0.34	$6.4x10^{-7}$	126	0.031	0.33, 0.58
[Zn(sal-3,4-ben)]	-3.26	-5.52	2.26	554	6.5	0.02	$7.7x10^{-5}$	131	0.036	0.43, 0.56
[Zn(salophen)]	-2.71	-5.59	2.88	516	9.5	0.35	$4.2x10^{-7}$	52	0.011	0.32, 0.60
salophen	-2.02	-5.72	3.70	472, 532, 600	16.0	0.42	$1.7x10^{-9}$	-	-	0.34, 0.39
sal-3,4-ben	-2.58	-5.70	3.11	450, 558	13.0	0.04	$1.8x10^{-8}$	-	-	0.41, 0.54

[a]Values of current density were obtained at the maximum current efficiency; [b]Hole mobility were obtained from TCLC model.

3.3.3 Polyfluorene Devices

3.3.3.1 Optical properties of the PFO:Zn(salicylidenes) composites

Optical properties of [Zn(salophen)] and [Zn(sal-3,4-ben)] in PFO composites as well as theoretical calculations were summarized in the Table 3.3. Devices containing the free salicylidene ligands were not made because them did not exhibited spectral overlap with PL spectra and energy level complementarity with PFO.

Normalized electronic absorption spectra of both PFO:[Zn(salophen)] and PFO:[Zn(sal-3,4-ben)] (Figure Ax) show a maximum absorption band centered at λ_{abs} = 384 nm attributed to the electronic absorption of the delocalized π orbitals along the PFO principal chain, independently of the relative concentration of the guest molecules in the polymer (0.1 to 2.5 % mol/mol).[60,90] The optical absorption of the Zn(II) coordination compounds can be detected only for concentrations higher than 2.5 % at the red-edge of the PFO band: λ_{abs} = 405 nm and λ_{abs} = 418 nm for PFO:[Zn(salophen)] and PFO:[Zn(sal-3,4-ben)], respectively (Figure A24). These bands were attributed to the HOMO/LUMO intra-ligand charge transfer (ILCT) with minimal contribution of the Zn(II) $3d^{10}$ orbitals, as we can see in the HOMO/LUMO frontier orbitals and NTOs hole:particle pairs (h:p) densities at the PBE0/6-311++G(d,p) level (Figure 3.10). Although the Zn(II) *d* orbitals are not contributing significantly to the $S_0 \rightarrow S_1$ electronic transitions in both cases, the metallic center plays an important role in the electronic density of the salicylidene framework, as it improves the ligands planarity and stiffness and enhances charge delocalization on the ligands. However, a small contribution of Zn(II) *d* orbitals were noticed for high energy states, principally for the [Zn(sal-3,4-ben)] coordination compound (Figure 3.11).

In contrast to [Zn(salophen)], the presence of the benzophenone moiety in the Zn coordination compound, [Zn(sal-3,4-ben)], it changes charge density completely, leading a charge transfer (ILCT) between the salophen rings towards benzophenone, improving the [Zn(sal-3,4-ben)] optical properties ($\varepsilon_{[Zn(sal\text{-}3,4\text{-}ben)]} > \varepsilon_{[Zn(salophen)]}$) (Figure A19).

The calculated transitions are in agreement to the experimental data (Figure A26) for the two coordination compounds as summarized on Table 1. Moreover, the [Zn(salophen)] and [Zn(sal-3,4-ben)] experimental data are supported by the TD-DFT calculations at the PBE0/6-311++G(d,p) level, using the PCM solvation method with the PFO solvation parameters in order to understand the host/guest interactions in the electronic ground and excited states (Figure 3.10, Table 3.3).

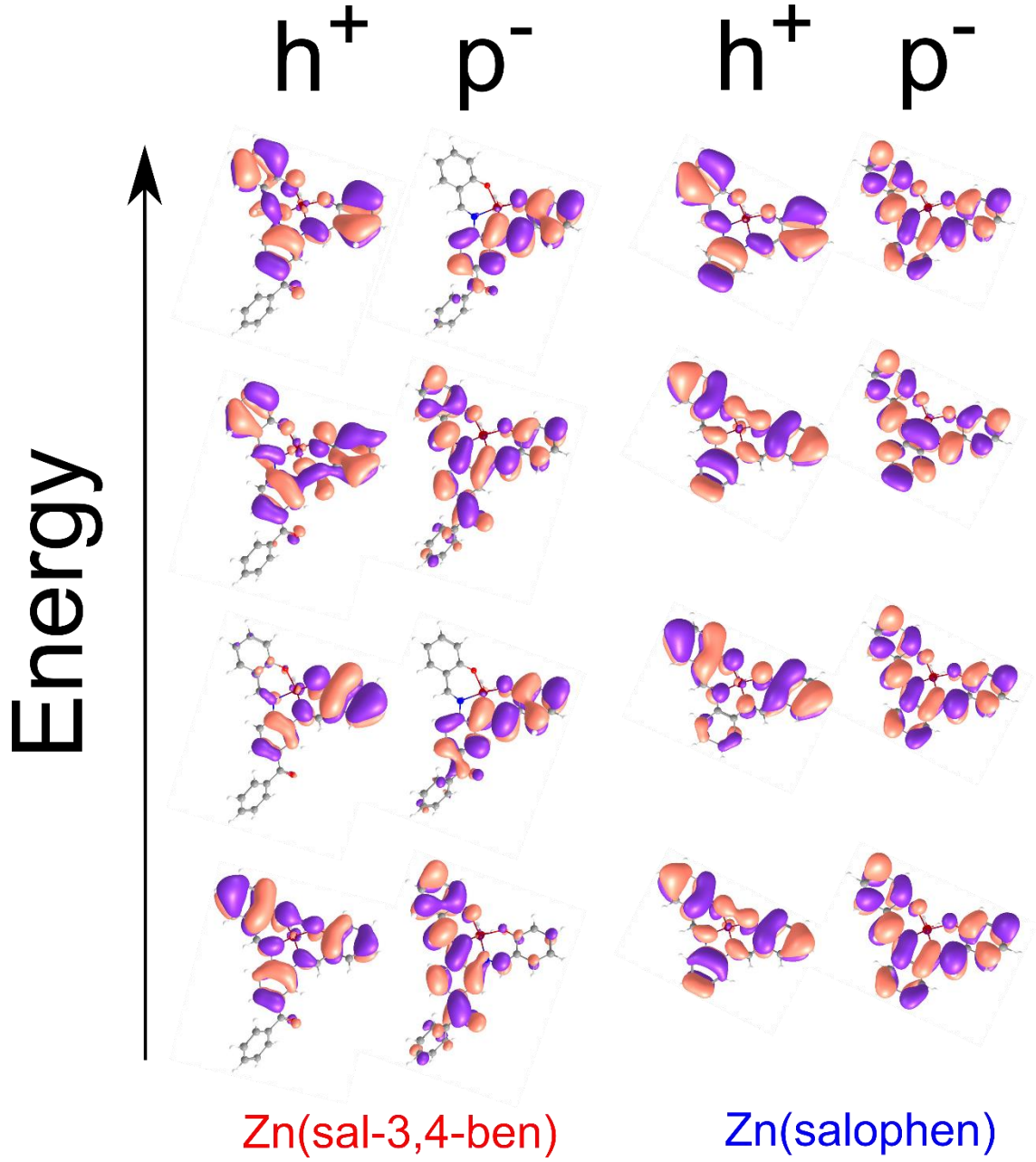

Figure 3.11. Calculated NTOs hole/particle pairs densities for the first four singlet excited states of [Zn(sal-3,4-ben)] and [Zn(salophen)] considering the PFO solvation with the PCM model at the PBE0/6-311++G(d,p) level.

The photoluminescence (PL) spectra of PFO:Zn(salicylidene) composites (Figure 3.11) were obtained using λ_{exc} = 375 nm, where the PFO host is preferably excited. The emission spectrum is composed of vibronic progression centered at λ_{PL} = 425 (shoulder), 440 (0-0), 466 (0-1) and 495 nm (0-2), attributed to the a mixture of the PFO crystalline (β-phase) and amorphous (α-phase) phases[93,172]. A shoulder with low intensity between 500 and 600 nm of the PFO aggregates was observed[137].

In addition to the emission of the PFO, we observe a band of the [Zn(salophen)] at λ_{PL} = 515 nm with lower PL quantum yield (PLQY = 0.7 %) in comparison to the PFO (PLQY = 50 %). The peak positions are independent of the relative concentration of the salophen complex. For the PFO:[Zn(sal-3,4-ben)] composites, we observe a blue shift of the PFO emission spectrum (λ_{PL} = 434 nm) and the emission of [Zn(sal-3,4-ben)] ($PLQY_{solid}$ = 1.1 %) appears at λ_{PL} = 520 nm for the 0.5 and 1.0 % mol/mol ratios and at λ_{PL} = 530 nm for 2.5 %. Interestingly, there is higher vibronic resolution of the PFO bands when Zn(II) compounds were added to the matrix, probably due to the increase of the PFO crystallinity. This observation was proved by the PLE spectra of PFO:[Zn(salophen)] and PFO:[Zn(sal-3,4-ben)] (Figure 3. S2) using λ_{PL} = 440, 515 and 530 nm, which shows an excitation band centered around 430 nm. Also, when the PLE spectra were monitored at the Zn(II)salicylidene emission bands, the PFO excitation band was observed, indicating the presence of resonant electronic states between the PFO and salicylidene derivatives. This enables radiative and non-radiative resonance (FRET) energy transfer processes from the PFO excited electronically as a donor towards the coordination compounds as the acceptor.

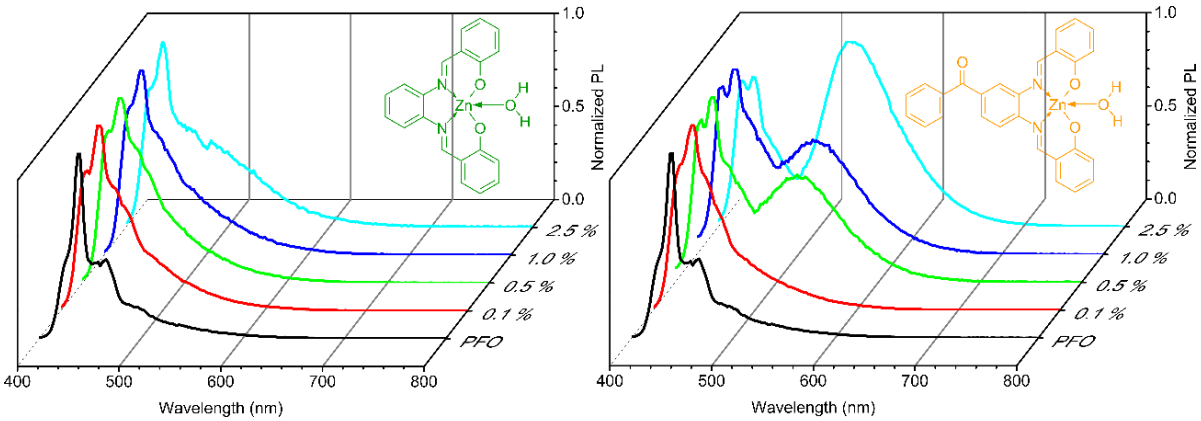

Figure 3.12. Normalized photoluminescence spectra of the PVK|PFO:Zn(salicylidene) composites films (λ_{exc} = 375 nm).

Table 3. 4. Resume of optical parameters of [Zn(salophen)] and [Zn(sal-3,4-ben)] in PFO composites and theoretical predictions at the PBE0/6-311++G(d,p) level in PFO, where λ_{abs} (nm) and λ_{PL} (nm) are the experimental absorption and emission maximum, SS (cm^{-1}) is the Stokes Shift, λ (nm) is the calculated excitation energies with oscillator strength *f*.

Experimental				
	Media	**λ_{abs}**	**λ_{PL}**	**SS**
[Zn(salophen)]	**PFO**	405 316	515	5274
[Zn(sal-3,4-ben)]	**PFO**	418 316	530	5055
Theory				
		λ (*f*)	**Assignment**	
PFO:Zn(Salophen)		396 (0.22)	86% H→ L, 14% H-1→L+1	
		374 (0.13)	100% H-1→ L	
		362 (0.35)	100% H→ L+1	
		305 (0.39)	73.30% H-2 → L, 18.28% H-3 → L+1, 8.42% others	
PFO:Zn(Sal-3,4-ben)		418 (0.29)	56.45% H → L, 33.75% H-1 → L	
		380 (0.49)	87.22% H → L+1, 12.78% H-1 → L	
		327 (0.14)	51%H-2→L, 34.82% H-3→L+1, 14.18 % others	
		304 (0.21)	56.45%H-2→L+1, 25.52% H-4→L	

3.3.3.2 Electro-optical properties of the PFO:Zn(salicylidenes) composites

EL spectra (Figure 3.13) of ITO|PEDOT:PSS|PVK|PFO|Ca|Al and ITO|PEDOT:PSS|PVK|PFO:Zn(II) salicylidene|Ca|Al diodes, which exhibit two sets of bands: at the higher energy attributed to the PFO (λ_{EL} = 425 - 440 nm) and at the low-lying energies assigned to the [Zn(salophen)] ($\lambda_{EL} \approx$ 515 nm) and the [Zn(sal-3,4-ben)] ($\lambda_{EL} \approx$ 540 nm) compounds, respectively. As a general trend, the EL spectra of both the Zn(salophen) and the [Zn(sal-3,4-ben)] redshifts with the increase of the concentration due to the aggregation process. Also, the PFO crystalline phases change with the increase of coordination compounds concentration from the dominant β-phase with the zero phonon band at λ_{EL} = 440 nm to the α-phase with the zero phonon band at λ_{EL} = 425 nm (see I_β/I_α in Table 2). For the PFO:[Zn(sal-3,4-ben)] composites with 1.0 and 2.5 %, the

vibronic progression at the blue region is similar to the pristine α-phase PFO OLED (λ_{0-0} = 425 and λ_{0-1} = 454 nm) with $I_{0-1}/I_{0-0} < 1$.

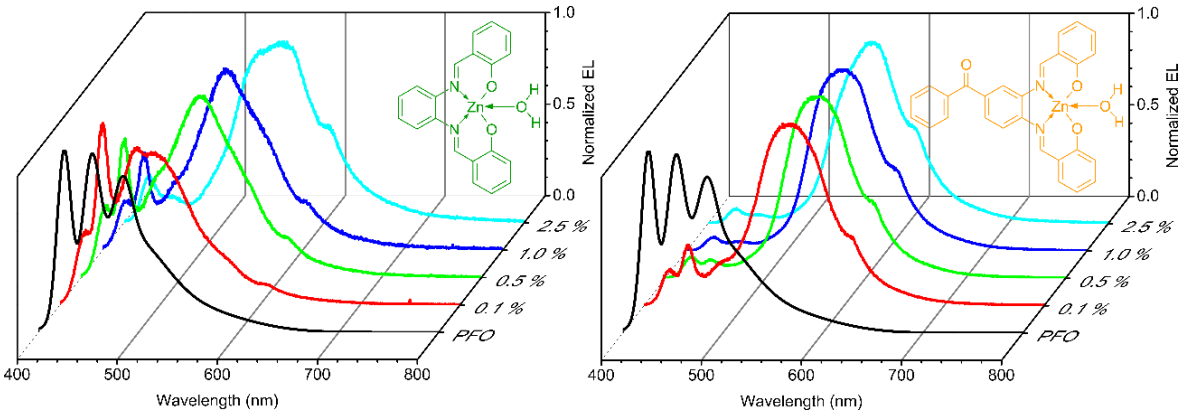

Figure 3.13. Normalized EL spectra of ITO|PEDOT:PSS|PVK|PFO:Zn(II) salicylidene|Ca|Al diodes, where Left = [Zn(salophen)] and Right = [Zn(sal-3,4-ben)] at the following molar ratios: PFO (V = 8 V), 0.1 % (V = 8 V); 0.5 % (V = 8 V); 1.0 (V = 8 V); and 2.5 % (V = 20 V).

CIE1931 chromaticity diagrams of both the PFO:[Zn(salophen)] (Figure 3.14) and the PFO:[Zn(sal-3,4-ben)] (Figure 3.15) OLEDs with concentrations of 0.1, 0.5 and 1.0 % mol/mol showed a tunable EL emission shifting to higher energy with the increase of the applied voltage. Nevertheless, only a minor spectral dependence with the applied electric field was noticed for the sample with the highest concentration (2.5 % mol/mol). The relative intensity of the greenish emission increases with dye concentration.

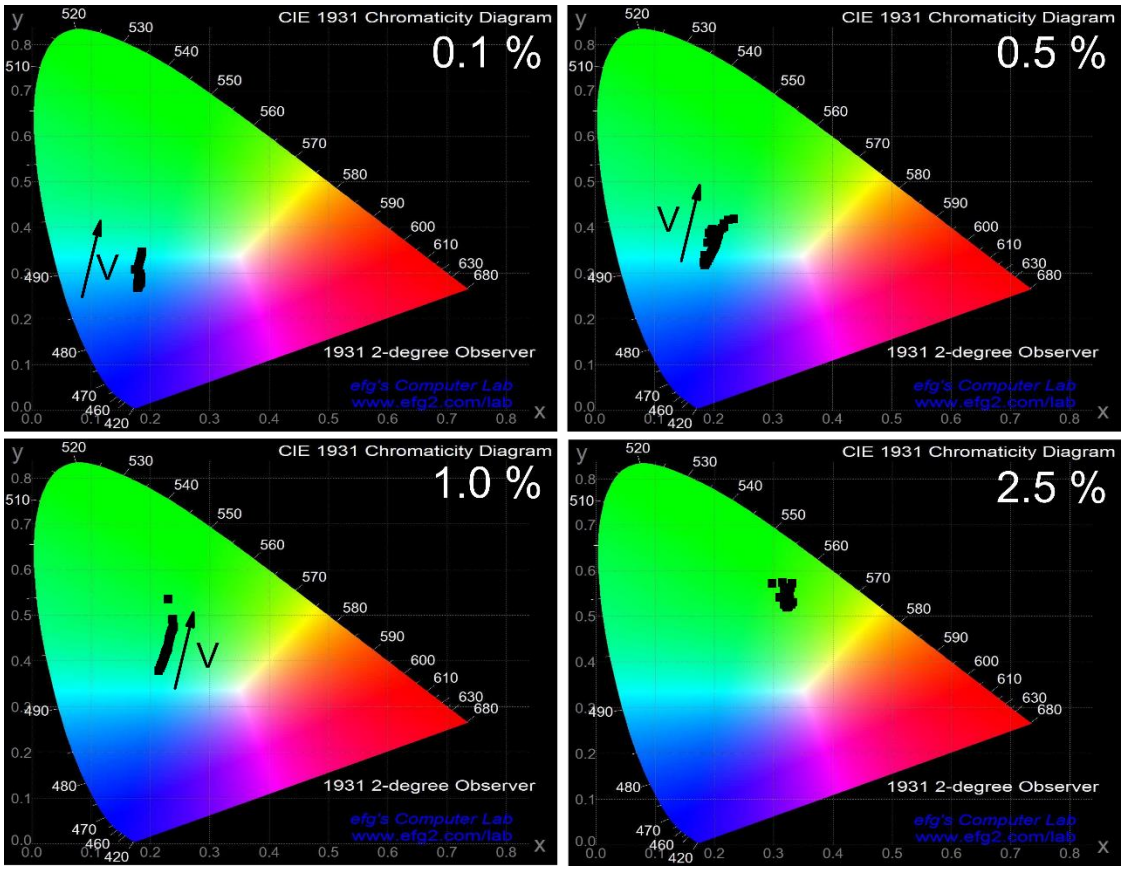

Figure 3.14. The CIE 1931 Chromaticity coordinates diagram of the ITO|PEDOT:PSS|PVK|PFO:[Zn(salophen)]|Ca|Al diodes with molar ratios: 0.1, 0.5, 1.0 and 2.5 % (mol/mol).

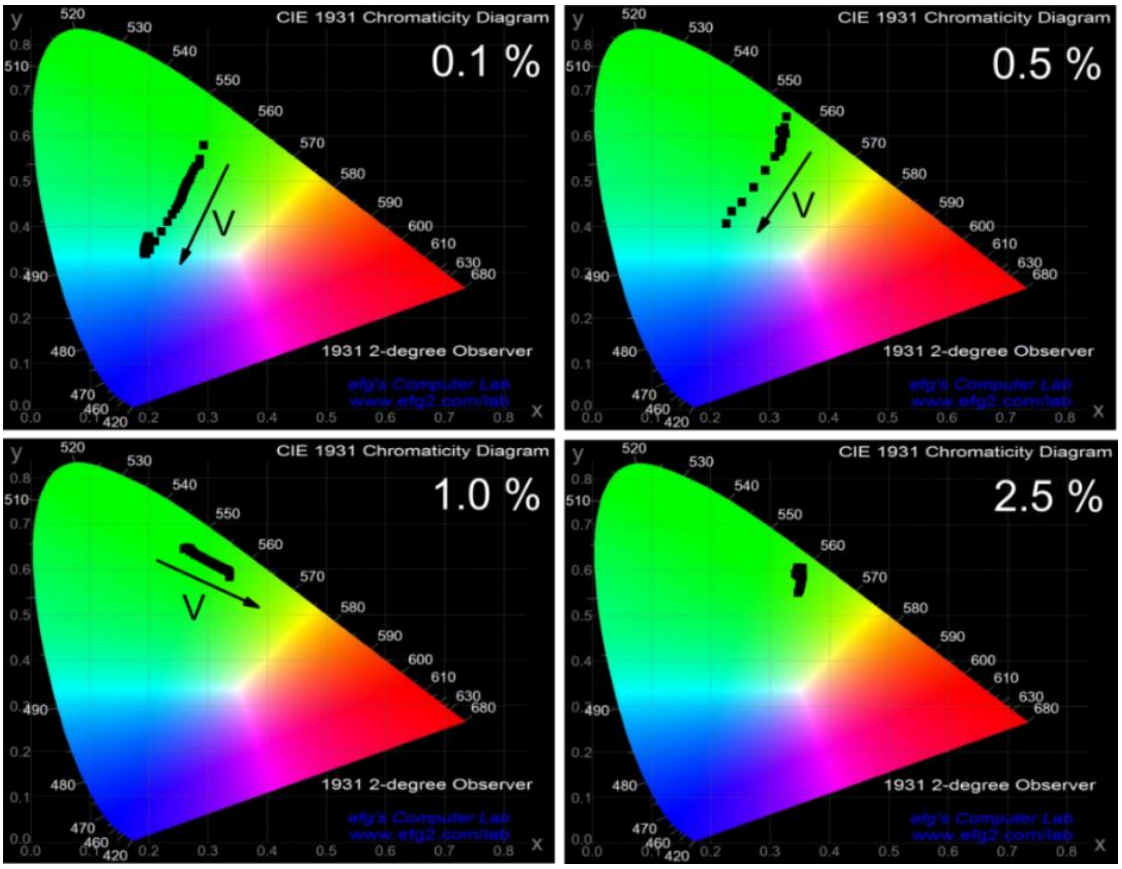

Figure 3.15. The CIE 1931 Chromaticity coordinates diagram of the ITO|PEDOT:PSS|PVK|PFO:[Zn(sal-3,4-ben)]|Ca|Al diodes with molar ratios: 0.1, 0.5, 1.0 and 2.5 % (mol/mol).

As a general trend, the color of the PFO:[Zn(salophen)] diodes changes with the BIAS, from blue (PFO) (lower voltages) to greenish ([Zn(salophen)]) (higher voltages). On the contrary, for PFO:[Zn(sal-3,4-ben)] the emission of PFO is turned on at higher voltages. This means that the emission color changes from yellow-greenish to blue-greenish. The active layer of the composites exhibits a combination of the HTL (PFO and PVK) and an electron transport material (salicylidene derivative), both processes playing an important role in charge balance. Based on these, we should expect a cascade-type charge transport from PVK towards the PFO and Zn(II)salicylidenes, where the [Zn(sal-3,4-ben)] is the material with lower energy band gap (E_g). Thus, the components with higher energy gap should emit at higher bias, as observed in Figure 3.16. Whereas for the LUMO of [Zn(sal-3,4-ben)] is energetically below the LUMO of β-phase (λ_{em} = 440 nm) of the PFO, for the E_{LUMO} of [Zn(salophen)] has higher energy and hence it turns on at higher bias (Figure 3.15).

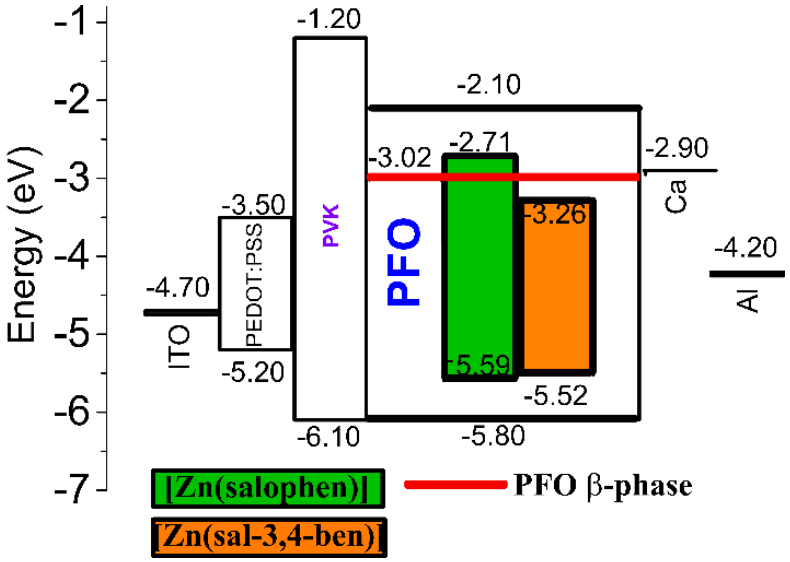

Figure 3. 16. Diagram of HOMO/LUMO frontier orbitals energy level diagram of Al[214], Ca[214], ITO[214], PEDOT:PSS[215], PVK[216], PFO,[196] PFO β-phase, [Zn(salophen)] and [Zn(sal-3,4-ben)].

Additionally, the turn-on voltage (V_{on}) of both the PFO:[Zn(salophen)] and the PFO:[Zn(sal-3,4-ben)] diodes increases with the increase of the concentration of the guest (Table 3.4). As a trend, the V_{on} of the composites is higher than for the PFO (V_{on} = 4.0 V) and their values increase with the concentration of the Zn(II) coordination compounds, except for PFO:[Zn(sal-3,4-ben)] at 0.1 % mol/mol concentration. This behavior is probably associated with both the lower charge mobility of the coordination compounds, and with the morphological changes of the polymer films with higher concentration of the Zn(II) guests. However, the V_{on} values are lower in comparison to the PVK:Zn(II)salicylidene electroluminescent devices ($V_{on[Zn(salophen)]}$ = 9.0 V and $V_{on[Zn(sal-3,4-ben)]}$ = 6.0 V) because the charge mobility of the PFO is higher than that of the PVK.[28]

The current density (JxV), luminance (LxV), current efficiency (η_{curr}xV) and power efficiency (η_PxV) versus Voltage curves of the diodes are displayed in Figure 3.16. As a general trend (data are summarized in Table 3.5), except for the 2.5% mol/mol concentrated samples, the PFO:Zn(II)salicylidenes diodes exhibit luminance and current efficiencies greater than the pure PFO (Figure 3.17). Moreover, the diodes with PFO:[Zn(sal-3,4-ben)] have greater performances (2 times increase in terms of L_{max} and η_{curr}) than the diodes with PFO:[Zn(salophen)] . All of them have also greater performances than the diodes with PVK:Zn(II)salicylidenes composites; they are at least 6 times better in terms of luminance, and 22 and 14 times better in terms of current efficiency for [Zn(salophen)] and [Zn(sal-3,4-ben)], respectively.[28] These greater

performances are associated to both the greater optical property ($PLQY_{PFO}$ >> $PLQY_{PVK}$) and the higher charge carrier mobility ($\mu_{PFO} \approx 10^4 \times \mu_{PVK}$).[94,189]

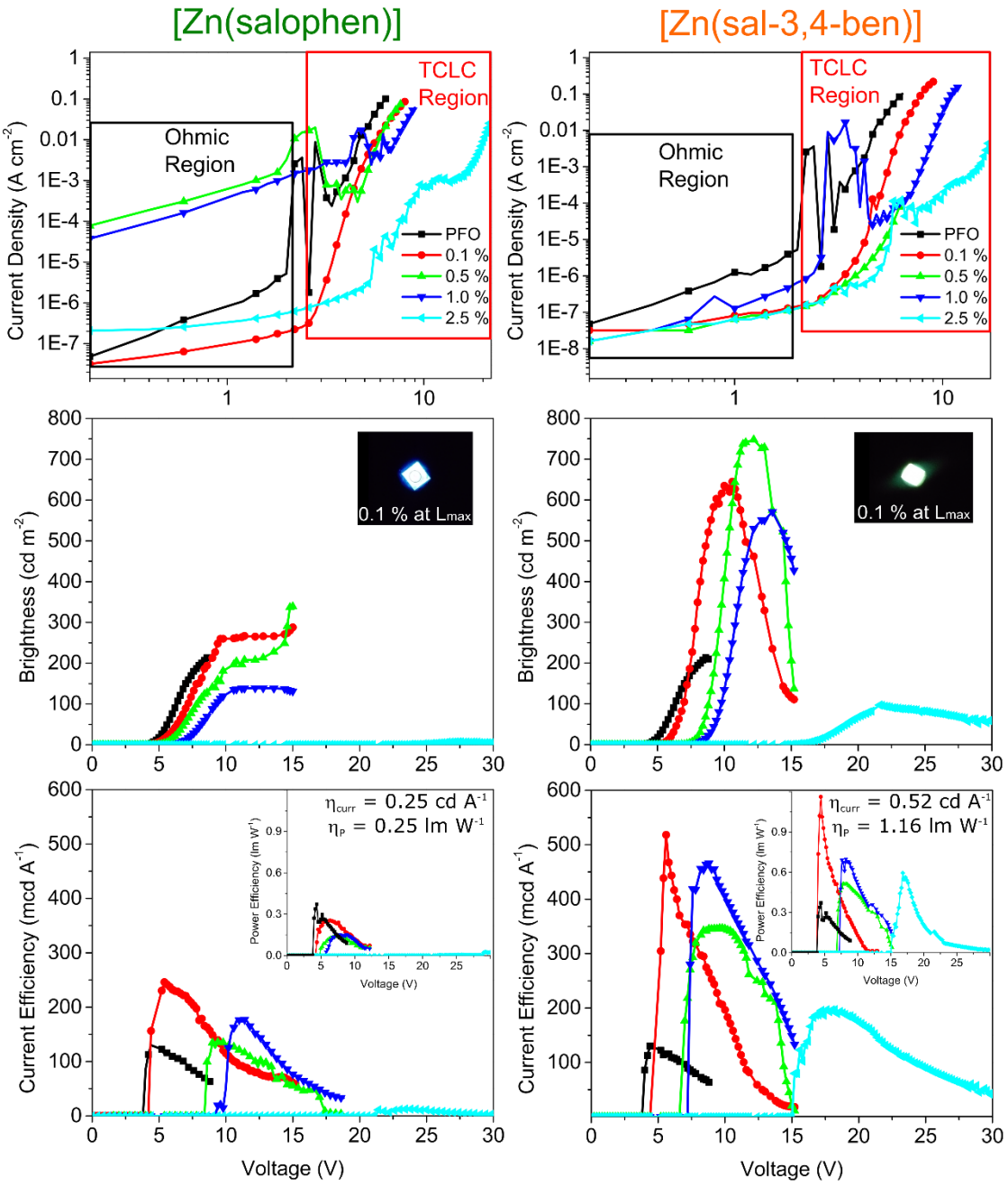

Figure 3.17. Optical-electronic properties of the diodes ITO|PEDOT:PSS|PVK|PFO:Zn(salicylidenes)|Ca|Al: Log-log Current density vs. voltage, brightness vs. voltage, current efficiency vs. voltage curves and power efficiency vs. voltage curves (inset).

Also, TCLC model was applied to understand the charge transport characteristics in PFO:Zn(Salicylidenes) OLEDs. The TCLC model is required because of the presence of a high trap level (m > 2) in the polymeric LEDs (PLEDs), especially

when there is an irregular dispersion of the small dye molecules forming its composites.[103,107,190] For instance, the device ITO|PEDOT:PSS|PVK|PFO|Ca|Al (black curves on Figure 3.16) exhibits $\mu_p = 1.2x10^{-3}$ cm^2 V^{-1} s^{-1} with a high trap level (m = 7.322; l = 6.322; E_t = 0.16 eV), and the hole mobility value was in agreement to the time-of-flight (TOF) measurements reported by Redecker et al.[90,91]

For the PFO:[Zn(salophen)] diodes, we observed a decrease of the μ_p values in comparison to the pure PFO, being $\mu_p = 3.7x10^{-4}$, $1.5x10^{-3}$, $2.4x10^{-4}$ and $6.6x10^{-5}$ cm^2 V^{-1} s^{-1} for the diodes containing 0.1, 0.5, 1.0 and 2.5 % (mol/mol) of the complex, respectively. Nevertheless, they are 3 orders of magnitude higher than the PVK:[Zn(salophen)] diode ($\mu_p = 4.2x10^{-7}$ cm^2 V^{-1} s^{-1})[28], which explains the greater performances of the diodes with PFO as host. Furthermore, the hole mobilities of the PFO:[Zn(sal-3,4-ben)] diodes are still greater by 2 orders of magnitude in comparison to PFO:[Zn(salophen)], 10 times greater than the pure PFO device and around 300 times greater than the diodes with a PVK host ($\mu_p = 7.7x10^{-5}$ cm^2 V^{-1} s^{-1}).[28] However, with the increase of the concentration, the performance and the mobilities decreased: $\mu_{p(0.1\ \%)} = 2.4x10^{-2}$, $\mu_{p(0.5\ \%)} = 2.1x10^{-3}$, $\mu_{p(1.0\ \%)} = 1.6x10^{-3}$ and $\mu_{p(2.5\ \%)} = 1.7x10^{-6}$ cm^2 V^{-1} s^{-1}.

As expected, the higher concentrated Zn(II)salicylidene samples (2.5 % mol/mol) exhibited the lowest charge carrier mobility and lowest luminance and current efficiencies among the composite OLEDs, probably due to the guest aggregation within the host, demonstrating that there is a limit in the concentration of the solution-processable diodes that must be considered. These achievements are corroborated by the images of confocal fluorescence microscopy of the PVK|PFO:[Zn(salicylidenes)] films by exciting emissive compounds [Zn(salophen)] (Figure 3.18) and [Zn(sal-3,4-ben)] (Figure 3.19) (λ_{exc} = 458 nm). These images showed a uniform dye emission in the PFO matrix, in addition to emissive domains of crystal of the coordination compounds. These nucleated crystals create defects in the OLED's active layer. Thereby, with the increase of the Zn(II)salicylidenes concentration, there are morphological changes according to the increase of these crystals either in terms of relative amount or in terms of size: more irregular is the distribution, consequently, leading poorer optical-electronic properties at their devices. Therefore, for the present systems, this concentration threshold is around 1% mol/mol.

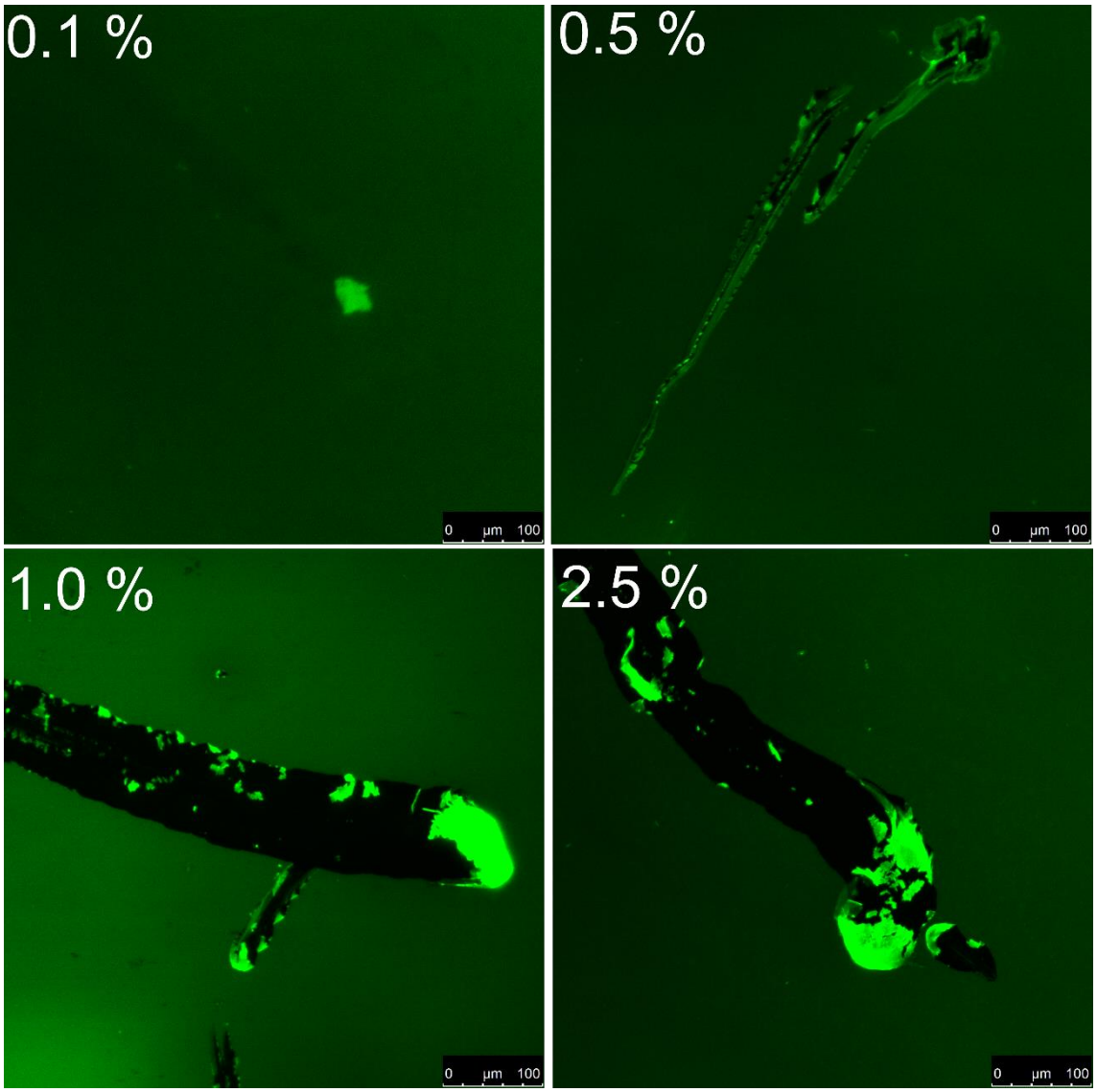

Figure 3.18. Fluorescence confocal images of the PFO:[Zn(salophen)] active layers (λ_{exc} = 458 nm).

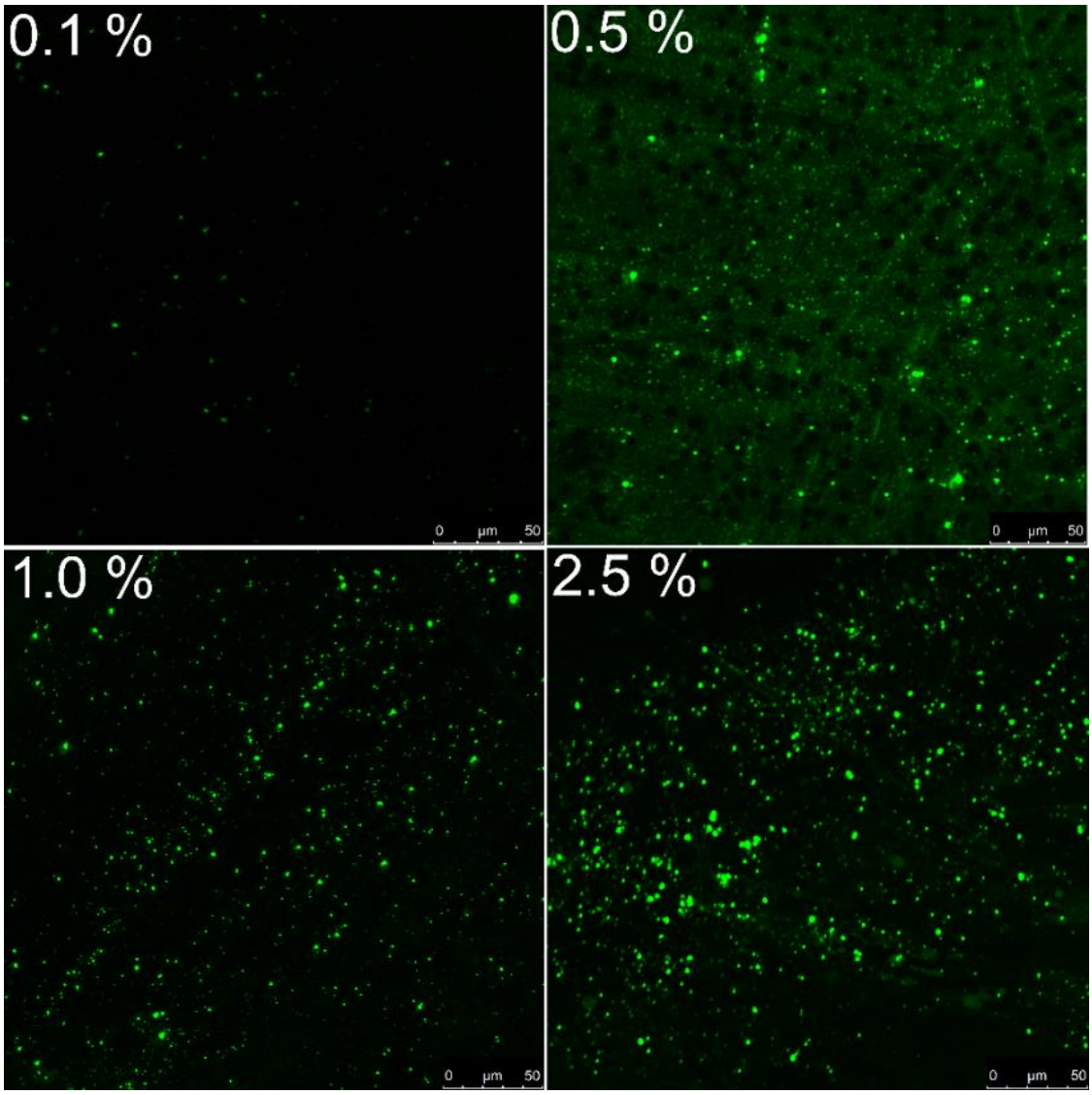

Figure 3.19. Fluorescence confocal images of the PFO:[Zn(sal-3,4-ben)] active layers (λ_{exc} = 458 nm).

Table 3.5. Optical-electronic properties of the solution-processed OLEDs of the PFO-Zn(II)salicylidenes composites OLEDs.

	%	λ_{EL} (nm)	I_β/I_α	V_{on}	J (A cm^{-2})[§]	μ_p (cm^2 V^{-1} s^{-1})	L_{max} (cd m^{-2})	η_{curr} (cd A^{-1})	η_P (lm W^{-1})	CIE 1931 (x,y)[§]
PFO		425	0.98[a]	4.0	$3.0x10^{-3}$	$1.2x10^{-3}$	213	0.13	0.370	0.17, 0.21
[Zn(salophen)]	**0.1**	440	2.44	4.4	$6.1x10^{-3}$	$3.7x10^{-4}$	288	0.25	0.25	0.18, 0.28
	0.5	507	1.96	5.0	0.18	$1.5x10^{-3}$	339	0.14	0.14	0.21, 0.39
	1.0	514	1.89	5.8	0.16	$2.4x10^{-4}$	139	0.18	0.15	0.23, 0.46
	2.5	539	0.59	23.8	$6.0x10^{-2}$	$6.6x10^{-5}$	7	0.02	0.01	0.32, 0.53
[Zn(sal-3,4-ben)]	**0.1**	531	1.71	4.0	$8.3x10^{-3}$	$2.5x10^{-2}$	645	0.52	1.16	0.28, 0.53
	0.5	538	0.87	7.0	0.18	$2.1x10^{-3}$	748	0.35	0.51	0.31, 0.57
	1.0	541	0.62[a]	7.4	$5.3x10^{-2}$	$1.6x10^{-3}$	571	0.47	0.70	0.27, 0.63
	2.5	551	0.60[a]	16.8	$2.0x10^{-3}$	$1.7x10^{-6}$	97	0.20	0.590	0.35, 0.58

[a]Values of $I_{0\text{-}1}/I_{0\text{-}0}$ ratio. [§]Values of current density and CIE 1931 were obtained at the maximum current efficiency.

3.4 Conclusions

This part of the Ph.D. thesis, we synthetized and characterized structurally and optically a new Zn(II)salicylidene coordination compound, the [Zn(sal-3,4-ben)], which exhibited better optical properties in comparison to [Zn(salophen)] in solution and in solid-state.

It was studied that PVK and organic molecules or coordination compounds are suitable systems for solution-processable diodes by a single spin-coating step deposition. However, there have been some concerns when organic molecules or coordination compounds have been used, which are related to the charge mobility, energy transfer processes and PL quantum yield emission. There is no sprightful correlation between the energy diagram of the frontier orbitals and the efficiency of the diode emission. In this study, we showed that [Zn(salophen)], sal-3,4-ben and [Zn(sal-3,4-ben)] have very similar energy levels, but their diode performances are quite different. Additionally, the FRET process observed in the PL might quench the donor excitons, but in the case of PVK, the most important parameter for the absence of the EL emission is probably the lower efficiency of the exciton formation in the diodes. The free ligands presented poorer EL efficiencies than the Zn(II) coordination compounds, showing that the metallic ion plays an important role in the charge transport properties. The hole mobility obtained from JxV power law ($\mu_{Zn(salicylidenes)} >> \mu_{salicylidenes}$) is an important parameter for the diode performance. [Zn(sal-3,4-ben)] was a successful guest for PVK, whose diode had a greater performance than the Znq_2, which was similar to that of the Alq_3. We also have shown that coordination compounds with metal ions of greater natural abundances might be explored as materials for light-emitting diodes.

Already, when PVK host was substituted by PFO conducting polymer, the performance of these diodes is much better than those with PVK, due to both higher charge mobility and PLQY of the PFO matrix. The charge mobility was obtained successfully by the TCLC model, which was required because of the presence of a high trap level ($m > 2$) on this kind of device, exhibiting high μ_p values for [Zn(sal-3,4-ben)] OLEDs in comparison to the ones made with [Zn(salophen)] and of pure PFO, which are in agreement to the energy level diagram, optical properties and theoretical calculations evaluated at the PBE0/6-311G(d,p) level to the Zn(II)salicylidene derivatives. We also demonstrated that the molar ratio of the Zn(II)salicylidene into the PFO host is limited to 1% mol/mol. Concentrations bigger than that impairs the diodes charge transport and performances due to morphological changes in the PFO film. In this sense, the manipulation of the charge mobility and PLQY are easy tools to

assemble high-efficient all-solution-processable OLEDs with low-cost fluorescent coordination compounds as active layers, in contrast to multilayer devices, which corroborates directly to energy saving concepts on technological applications.

CHAPTER 4

COLOR-TUNABLE AND HIGH-EFFICIENCY WOLEDs: FROM RED-PHOSPHORESCENT Pt(II)SALICYLIDENES TO BLUE-FLUORESCENT POLYMER

4.1 Motivation

Photo and electroluminescent transition metal complexes continue to represent an important branch of the chemistry,[219] mainly due to the diversity of applications in organic electronics, such as OLEDs to the development of high efficient, low-cost, material and energy saving, full color and flat panel displays,[25] solar cells[220] and sensors.[221] In this context, coordination compounds containing heavy atoms are particularly interesting, primarily due to the large spin-orbit coupling in transition metal complexes, which gives rise to fast ISC process, and consequently strong phosphorescence at room-temperature.[222] Unlike fluorescent organic materials that can only use singlet excitons, having maximum efficiencies around 25%, complexes containing heavy metals such as Ru(II), Os(II), Pt(II) and Ir(III) are capable of harvesting both singlet and triplet states, hence they could reach an internal quantum efficiency near to 100%.[223]

In these kinds of phosphorescent emitters, Pt(II) coordination compounds with salicylidenes ligands are versatile building blocks for the construction of materials for a wide range of applications,[224] due to the easy modification in the ligand framework, allowing the modulation of its optical and electrical properties.[225,226] Recently, Pt(salicylidenes) derivatives have been shown to be highly promising candidates for technological applications, because they present high phosphorescent PLQY due to its electronic-transitions with mixed MLCT/ILCT character ([Pt(5*d*) $\rightarrow \pi^*$]) between HOMO and LUMO orbitals,[227] and its thermal and chemical stability afforded by the chelate effect make them particularly attractive as electro-emissive materials.[57,151,224,228–230]

In this way, a successful strategy is the combination of a blue-fluorescent organic molecules with a yellow/orange/red-phosphorescent coordination compound electroluminescent emitters to the achievement of white organic light-emitting diodes (WOLEDs), which can be applied as room lightning apparatus and/or displays back-light illumination.[34] The principal mechanisms involved in the charge recombination in this kind of WOLEDs is governed singlet and triplet-harvesting, according to the Förster and Dexter theories, respectively. Basically, the energy levels of the S_1 and T_1 of the blue-fluorescent (donor species) must be higher energy than the red-phosphorescent (acceptor species). Thus, all formed excitons and the charge carriers will be harvested by the acceptor molecules, leading a high-efficiency WOLEDs.[231] In the other hand, even though the donor-acceptor pairs have shown complementarity on its S_1 energy levels, if the T_1 (non-radiative pathway) energy of the blue-emitter is higher than the acceptor, the emissive triplet exciton of the phosphorescent

material must be harvested by the host material, putting an end on the diode efficiency, once fluorescent emitters do not present a radiative triplet state at room-temperature.[232]

Therefore, the choice of the materials combination must be done with careful of their singlet and triplet energy levels.[233] Also, conducting polymers may be applied as blue-fluorescent polymer in host-guest systems, which combined with the phosphorescent coordination compounds and the polymer charge transport characteristic, yielding solution-processable WOLEDs via triplet and singlet harvesting mechanism.[9] Furthermore, a system using PVK as host-material, PFO as the blue-emitter and two another Ir(III) coordination compounds as green and red phosphorescent emitters has presented efficient solution-processable WOLED by triplet-harvesting mechanism,[234] but in this work the authors used a thermal-evaporated charge transport layer, which runs counter the energy saving principle.

Taking into account these considerations, herein we present the synthesis, structural and optical characterization of a new Pt(II)salicylidene derivative, the *platinum(II)[N,N'-bis(salicylidene)-3,4-diaminobenzophenone)]* ([Pt(sal-3,4-ben)]) and its precursor *platinum(II)[N.N'-bis(salicylidene)-o-phenylenediamino]* ([Pt(salophen)]) which were characterized by ^{1}H and ^{13}C NMR and FT-IR spectra, high-resolution time-of-flight mass spectrometry (HRTOF-MS), elemental analyses and single-crystal X-ray diffraction (SC-XDR) and steady-state and time-resolved photophysical measurements (electronic absorption and photoluminescence spectra and emission decays) at THF, DMSO (10 μmol L^{-1}) and EPA (1 μmol L^{-1}) solutions. [Pt(sal-3,4-ben)] were successful synthetized and exhibited a strong phosphorescence emission (PLQY = 76 %) even at room-temperature which were proved by its photophysical data and its supported by the calculated vertical excitations and natural transition orbitals (NTOs) under relativistic DFT/TD-DFT at the PBE0/(ZORA-def2-TVZP(C,N,O,H) and SARC-Pt(II)) level, exhibiting mixed MLCT/ILCT/MC electronic transitions between the frontier orbital ([π + Pt($5d_{x-y}$) $\rightarrow$ π^{*} + Pt($5d_{x^2-y^2}$)]) with a small deviation among the experimental excitation (δ = 0.08 eV). Also, as expected for phosphorescent emitters, [Pt(salophen)] and [Pt(sal-3,4-ben)] have shown a strong and reversible $^{3}O_2$(g) sensitization.

After the photophysical characterization, [Pt(salophen)] and [Pt(sal-3,4-ben)] coordination compounds were used into PVK and PFO composites as active-matrix in phosphorescent OLEDs with architectures: ITO|PEDOT:PSS|PVK:Pt(salicylidenes) 2.5 % mol/mol|Ca|Al; and ITO|PEDOT:PSS|PVK|PFO:Pt(salicylidenes) **X** % mol/mol|Ca|Al, where **X** = 0.1, 0.5, 1.0 and 2.5. In the first case, two red-phosphorescent OLEDs with the [Pt(sal-3,4-

ben)] presented better performance. However, their PVK's OLEDs exhibited very poorly performances in terms of all optical-electronic parameters, even in comparison to the [Zn(salophen)] and [Zn(sal-3,4-ben)] devices assembled at the same conditions. This behavior was due to the lower energy of T_1 state of PVK compared to the Pt(salicylidenes) compounds and a cascade mechanism of PVK towards the coordination compounds is subsequently followed by a non-radiative triplet state has harvested the emissive triplet state of the [Pt(salophen)] and [Pt(sal-3,4-ben)] via Dexter mechanism, which affects directly the efficiency of the OLEDs, leading inefficient devices. As for PFO:Pt(salicylidenes) solution-processed diodes was observed a completely different behavior. A color-tunable with the concentration of the Pt(salicylidene) and principally with the applied electrical field from red-phosphorescent of the Pt(salicylidenes) to the blue-greenish-fluorescent emission of the conducting polymer, passing by the true white color EL emission (CIE 1931 x = 0.33, y = 0.33). These devices exhibited high performance parameters at the 0.1 % mol/mol ratio of the Pt(II) coordination compounds into the PFO conducting polymer, and the best results were obtained from the ITO|PEDOT:PSS|PVK|PFO:[Pt(sal-3,4-ben) 0.1 % mol/mol|Ca|Al – V_{on} = 3.4 V, μ_P = 1.1x10^{-1} cm^2 V^{-1} s^{-1}, L_{max} = 4000 cd m^{-2}, η_{curr} = 5.28 cd A^{-1} and η_P = 26.19 lm W^{-1}. In comparison to the PFO:[Zn(sal-3,4-ben)] OLED assembled at same conditions an improvement about 22 times in terms of the diode performances. The main reason to its WOLEDs successful was the complete singlet and triplet-harvesting from the PFO polymer to the [Pt(sal-3,4-ben)] molecules, once the S_1 and T_1 levels of PFO is higher than the two Pt(salicylidenes), which turned-on at low-voltages while PFO at high-voltages and it was restricted by the Pt(salicylidene) concentration (1.0 % mol/mol). Therefore, we demonstrated that the combination of a red-phosphorescent emitter with a blue conducting polymer is an easy, low-cost and energy saving alternative to obtain high-efficiency and color-tunable electroluminescent diodes, in contrast to the thermal-evaporated conventional systems.

4.2 Materials and Experimental Details

4.2.1 Materials

PVK (M_W = 1,100,000 g mol^{-1}), potassium tetrachloroplatinate(II) (K_2PtCl_4), dimethyl formamide (DMF), DMSO-d_6 and THF (anhydrous inhibitor-free grade) were purchased from Sigma-Aldrich, São Paulo, Brazil. Dimethyl sulfoxide (DMSO) was supplied by Tédia, Brazil in a HPLC/spectrum grade. Sodium acetate trihydrate was purchased from Synth, Brazil–SP. PFO (ADS129BE; M_w = 40,000 ~ 150,000 g mol^{-1}) was supplied by

American Dye Source, Inc., Quebec, Canada. PEDOT:PSS was purchased from Clevios P VP Al 4083, H.C. Starck, Germany. Salophen and sal-3,4-ben salicylidene ligands were synthetized and characterized elsewhere.

4.2.2 Experimental Details

^{1}H and ^{13}C NMR spectra of [Pt(salophen)] and [Pt(sal-3,4-ben)] in DMSO-d_6 solution (33 mg mL^{-1}) were measured in a Bruker Avance 500 MHz spectrometer.

FTIR spectra were recorded in an Agilent Technologies Cary 630 spectrometer in attenuated total reflectance (ATR) mode. Elemental analysis (%) of the C, H and N atoms was performed using a Perkin-Elmer microanalyzer model PE 2400.

High-resolution time-of-flight mass spectrometry was acquired on a Xevo G2 QTof spectrometer with *m/z* work range of 460-572 coupled on a WATERS ultra-performance liquid chromatograph (UPLC). HRTOF-MS was obtained from an acetonitrile solution (1% of formic acid), mist flow of 100 L h^{-1}, using the ES+ mode.

Crystal structure of the [Pt(salophen)] (Table A3) and [Pt(sal-3,4-ben)] (Table A4) were determined by single-crystal X-ray diffraction in a Bruker Apex Duo X-ray diffractometer using Mo ($K\alpha$ = 0.71073 Å) radiation with the following software for cell refinement: APEX2[168] for data collection, SAINT[168] for cell refinement and data reduction, SHELXS97[169] to solve structure and SHELXL2014/7[170] for refine structure and Mercury[171] for molecular graphics.

4.2.2.1 Synthesis of Pt(Salicylidenes)

Pt(II)salicylidene synthesis procedure was adapted from Zhou et al. 2014[230] and Che at al. 2010[227] (Figure 4.1). In a 25 mL three-neck round-bottom flask, a DMF (15 mL) solution of salicylidene ligand (0.5 mmol) and sodium acetate trihydrate (1 mmol; 82 mg) were stirring under N_2(g) atmosphere at 70 ºC for 20 min. A DMSO (3 mL) solution of K_2PtCl_4 (0.5 mmol; 207 mg) was added with dropwise and the reactional mixture was stirred under 12h. Upon cooling, deionized water (50 mL) was added to the mixture and the red precipitate was filtrated, dried and purified by recrystallization in the DMF:THF solvent mixture, giving dark-red crystals.

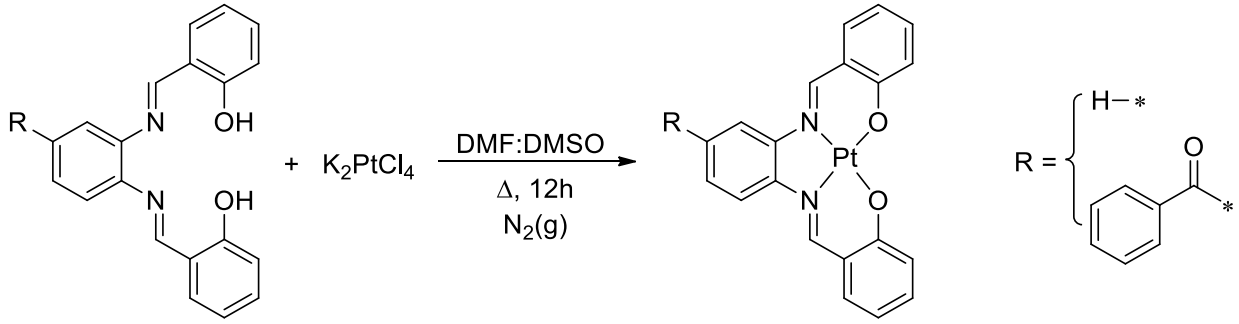

Figure 4. 1. Reactional scheme for the Pt(salicylidenes) synthesis.

[Pt(salophen)]: yield 219 mg, 86 %. ^{1}H NMR (500 MHz, DMSO-d_6) δ (ppm): 9.53 (s, 2H), 8.46 (dd, J = 6.2, 3.4 Hz, 2H), 7.88 (d, J = 8.0 Hz, 2H), 7.58 (t, J = 7.7 Hz, 2H), 7.46 (dd, J = 6.3, 3.1 Hz, 2H), 7.13 (d, J = 8.6 Hz, 2H), 6.80 (t, J = 7.3 Hz, 2H) (Figure A32); ^{13}C NMR (126 MHz, DMSO-d_6) δ (ppm): 164.97, 151.82, 145.13, 136.17, 135.99, 128.49, 122.42, 121.70, 117.26, 116.80 (Figure A33). The main infrared bands in the ATR mode were (cm^{-1}): ν_{Pt-N} = 466, ν_{Pt-O} = 543, $\nu_{C=N}$ = 1601, ν_{C-O} = 1327, $\nu_{(C-H)Ar}$ = 3012 - 3086 and ν_{Ar} = 844 and 749 (Figure A38). HRTOF-MS ES+ (*m/z*): 510.0717 (Figure A36), calcd for [M-H]$^{+}$: 510.0776. Elemental analysis calcd (%) for $C_{20}H_{14}N_2O_2Pt$: C 47.15, H 2.77, N 5.50; found (%): C 47.16, H 2.86, N 5.44.

[Pt(sal-3,4-ben)]: yield 257 mg, 84 %. ^{1}H NMR (500 MHz, DMSO-d_6): 9.55 (s, 1H), 9.54 (s, 1H), 8.56 (d, J = 8.7 Hz, 1H), 7.88 (m, 5H), 7.72 (m, 2H), 7.60 (m, 5H), 7.16 (t, J = 8.5 Hz, 2H), 6.80 (dt, J = 17.8, 6.9 Hz, 2H) (Figure A34); ^{13}C NMR (126 MHz, DMSO-d_6) δ 194.96, 165.51, 165.16, 152.92, 152.77, 147.86, 145.08, 137.20, 136.73, 136.49, 136.44, 136.36, 136.22, 133.71, 130.47, 129.52, 129.29, 122.53, 122.43, 121.95, 121.69, 118.13, 117.10, 117.07, 116.85 (Figure A35). The principal infrared bands in the ATR mode were (cm^{-1}): ν_{Pt-N} = 460, ν_{Pt-O} = 555, ν_{Ar} = 751 and 824, $\nu_{C=N}$ = 1603 and 1592, $\nu_{C=O}$ = 1661, ν_{C-O} = 1329 and $\nu_{(C-H)Ar}$ = 3031 – 3049 (Figure A38). TOF-MS (*m/z*): 614.0939 (Figure A37), calcd for [M-H]$^{+}$: 614.1038. Elemental analysis calcd (%) for $C_{27}H_{18}N_2O_3Pt$: C 52.86, H 2.96, N 4.57; found (%): C 52.75, H 3.09, N 4.53.

4.2.2.2 Steady-state Photophysical Measurements

Electronic absorption spectra of the Pt(salicylidene) coordination compounds in solution and PVK: and PFO:guest films were acquired with a *Hewlett-Packard* 8452A diode array spectrophotometer.

Steady-state photoluminescence (PL) and excitation (PLE) spectra were recorded with a Cary Eclipse Varian spectrofluorimeter using λ_{exc} = 290, 375, 400 and 450 nm to excite

preferably the PVK of the PVK:*X* composites, the PFO into PFO:*X* thin-films composites, and the [Pt(salophen)] and [Pt(sal-3,4-ben)] in solutions, respectively. The emission ranges were recorded from 320 nm to 800 nm. The films were oriented in a back-face configuration at 45º and solutions measurements were done in a 1 cm quartz cuvette.

Relative phosphorescence PLQYs of the [Pt(salophen)] and [Pt(sal-3,4-ben)] in solutions were obtained using the relative method, according to the equation 3.1, using *tris(bypyridine)ruthenium(II) chloride* ($[Ru(bipy)_3]Cl_2$) coordination compound (λ_{exc} = 450 nm; $PLQY_S$ = 0.094) diluted to the same concentration in acetonitrile as standard, following the IUPAC recommendations.[191–193] Solid-state PLQYs of the Pt(salicylidenes) were not measured due to their high aggregation on the solid-state.

The redox potentials of Pt(salicylidenes) were determined by cyclic voltammetry using a model PAR 273A potentiostat with platinum working and counter electrodes and an Ag/AgCl reference electrode in an acetonitrile/tetrabutylammonium hexafluorophosphate solution (0.1 mol L^{-1}) (Figure A41). The scan rate for the cyclic voltammograms was 20 mV s^{-1}. The formal standard potential of the Fc^+/Fc redox couple in acetonitrile is approximately -5.1 eV. The HOMO (E_{HOMO}) and LUMO (E_{LUMO}) energies were also determined using equation 3.2 and 3.3[195].

4.2.2.3 Time-resolved Photophysical Measurements

Phosphorescence decays of the Pt(salicylidenes) in solution ($1x10^{-5}$ mol L^{-1}) were recorded using time-correlated single-photon counting (TCSPC) in an Edinburg Analytical Instruments FL 900 spectrofluorimeter with an MCP-PMT (Hamamatsu R3809U-50) with a pulsed diode laser operating at λ_{exc} = 375 nm (model EPL-370, with a band width of 5 nm, 77 ps). The decay signals of [Pt(salophen)] were collected at λ_{PL} = 613, 621 and 625 nm for DMSO, THF and EPA solutions, respectively, while [Pt(sal-3,4-ben)] decay signals were measured at λ_{PL} = 626, 637 and 641 nm for DMSO, THF and EPA solutions, respectively. The instrument response was recorded using Ludox samples. At least 1,000 counts in the peak channel were accumulated for the lifetime determination. The emission decays were analyzed using exponential functions as previously described[95,196].

4.2.2.4 OLEDs Assembly

ITO substrates (25 Ω/cm^2 from Delta Technologies, USA) were washed with deionized water, 2-propanol and acetone in an ultrasonic bath for 15 min each. Substrates were dried on a hot plate at 130 °C for 10 min and, subsequently, treated with UV ozone for 30 min. Over this substrate, a 30-nm-thick layer of PEDOT:PSS was spin-coated (5000 rpm, 60 s) and

annealed for 30 min at 110 °C. Next, 80 nm of the PVK:Pt(salicylidene) (2.5 % mol/mol) THF solution ($2.591x10^{-2}$ mol L^{-1}) was spin-coated under a controlled atmosphere environment. Finally, layers of calcium (30 nm) and aluminum (100 nm) were deposited by thermal evaporation under a vacuum of 10^{-6} mbar within an mBraun Evaporator. Diodes were fabricated in a glove box (H_2O, O_2 < 1 ppm) with a simple OLED configuration of glass|ITO|PEDOT:PSS|PVK:Pt(salicylidene) (2.5 % mol/mol)|Ca|Al with Pt(II) coordination compounds = [Pt(salophen)] or [Pt(sal-3,4-ben)] (Figure 4.2a).

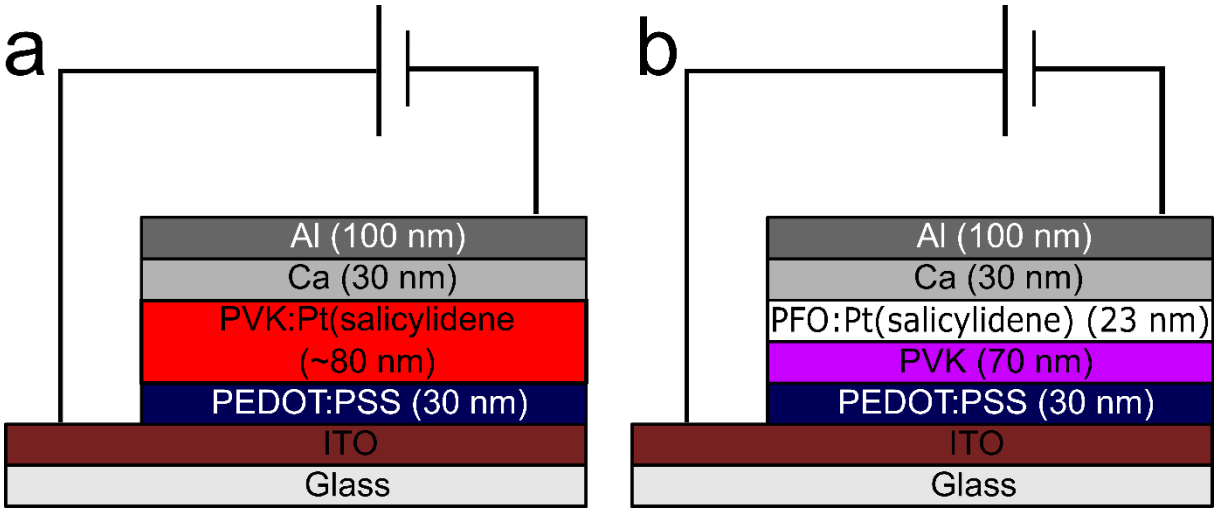

Figure 4. 2. Solution-processed OLEDs architecture: a) ITO|PEDOT:PSS|PVK:Pt(salicylidene) 2.5 % (mol/mol)|Ca|Al; and b) ITO|PEDOT:PSS|PVK|PFO:Pt(salicylidene)|Ca|Al.

Furthermore, diodes with the configuration: glass|ITO|PEDOT:PSS (30 nm)|PVK (70 nm)|PFO:Pt(salicylidene) (≈23 nm)|Ca (30 nm)|Al (100 nm) (Figure 4.2b) were prepared in similar way: ITO substrates (25 Ω/cm^2 from Delta Technologies, USA) were washed with Extran® neutral detergent, deionized water, isopropanol and acetone in an ultrasonic bath for 15 min each. Substrates were dried on a hot plate at 130 °C for 10 min they treated with UV ozone for 30 min. Subsequently, a 30-nm-thick layer of PEDOT:PSS (hole injection layer) was spin-coated (5000 rpm, 60 s) and annealed for 30 min at 110 °C. Next, 70 nm of the HTL/EBL (PVK) followed by the active layers with ≈ 23 nm of thickness composed by PFO:Pt(salicylidene) in a THF solution ($2.591x10^{-2}$ mol L^{-1}) were spin-coated under Ar(g) atmosphere. Finally, calcium (30 nm) and aluminum (100 nm) layers were deposited by thermal evaporation under a vacuum of 10^{-6} mbar within an mBraun Evaporator. The concentration of the Pt(salicylidenes) were 0.1, 0.5, 1.0 and 2.5 % mol/mol ratio.

Optical-electrical properties of the OLEDs were measured in an oxygen-free sample holder. The diodes were analyzed in terms of current density vs. voltage measurements (JxV) using a 2400 Keithley SourceMeter. Electroluminescence (EL) spectra were acquired using a USB2000+ Ocean Optics diode array spectrometer. The luminance-voltage curves (LxV) and the CIE 1931 chromaticity coordinates were measured using a Konica Minolta CS-100A luminancimeter using a close-up lens No. 110, ø = 40.5 mm, 10 to 20 cm. All data were collected simultaneously using a homemade LabView® interface. Current and power efficiencies vs. voltage curves (η_{curr}xV and η_PxV) were obtained applying equations 1.12 and 1.13, respectively.

4.2.3 Theoretical Approach

Considering the considerably relativistic effect due the presence of the Pt(II) heavy atom, theoretical calculations of [Pt(salophen)] and [Pt(sal-3,4-ben)] were done under the DFT/TD-DFT framework using the density-functional PBE0[200] with the relativistic effects within the zeroth-order regular approximation (ZORA). This approaches were employed using relativistic all-electron gaussian basis ZORA-def2-TZVP to O, N, C and H atoms[235] and segmented all-electron relativistic contracted (SARC) Gaussian-type basis sets are assigned to Pt.[236,237] Pt(II) salicylidene X-ray single-crystal structures were used for the initial structure. Molecular structures corresponding to the ground, first excited singlet and first excited triplet states (S_0, S_1 and T_1) were optimized in gas phase. Vertical electronic excitations and the first natural transition orbitals (NTOs) pair were obtained also in the gas phase. All calculations were done using the ORCA 4.0.1 software.[238]

4.3 Results and Discussion

4.3.1 Structural Characterization

Pt(II) coordination compounds were isolated from reactional mixture by the addition of the deionized water and they were dried and purified by recrystallization process in a DMF:THF solvent mixture, leading dark-red single-crystals which were successfully characterized via 1D ^{1}H and ^{13}C NMR, FT-IR, HRTOF-MS, elemental analysis and single-crystal X-ray diffraction (SC-XRD) (Figure 4.3). The coordination bonds parameters and 3D cartesian parameters are summarized in the Tables 4.1 and 4.2, respectively. The complete characterization data are supplied on thesis Appendix at Tables A3 and A4.

After the Pt(II) metal coordination into salophen framework, an considerably improvement of the molecular planarity, conferring a structure close to the C_{2v} point group, as

previously described elsewhere for Zn(II) coordination.[27,206] In the case of the sal-3,4-ben ligand despite the increase of the planarity of the salophen moiety after Pt(II) coordination, its molecular structure exhibits a non-symmetric system (C_1 point group) due the presence of the benzophenone. However, into benzene ring of benzophenone group, a C_{2v} point group symmetry should be noticed (Figure 4.3). Also, a THF solvent molecule was inserted in the [Pt(sal-3,4-ben)] crystal structure during the crystallization process, changing the crystal system from orthorhombic (space group $P2_12_12_1$) of the [Pt(salophen)] to monoclinic crystal system with space group $P2_1$ (Figures A39 and A40).

Angles of the coordination site are very closed to 90° and the angles O3-Pt1-N4/O2-Pt1-N5 are 179.009°/178.100° and 179.730°/177.730° for the [Pt(salophen)] and [Pt(sal-3,4-ben)] coordination compounds, respectively, which confers a planar square molecular geometry on the Pt(II) cation coordination site (Table 4.1).

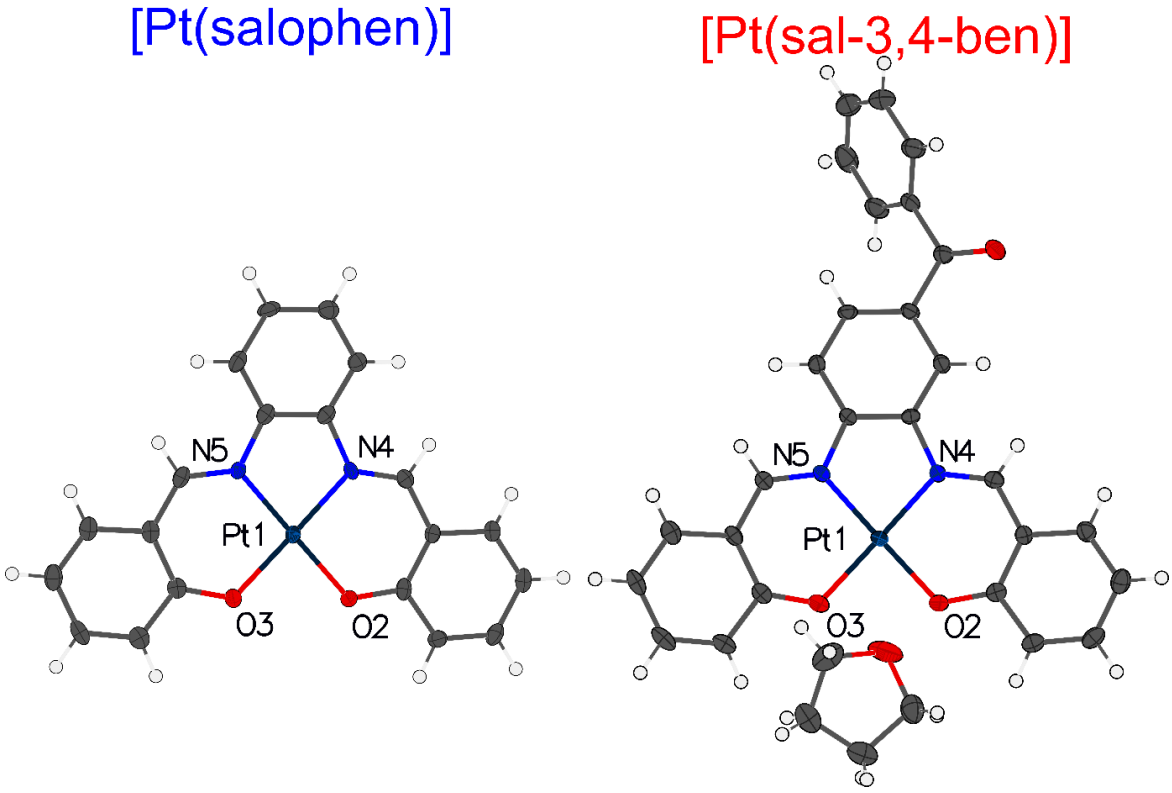

Figure 4. 3. Molecular crystal structure of the [Pt(salophen)] and [Pt(sal-3,4-ben)] coordination compounds ellipsoids with 50 % probability.

Table 4. 1. Selected chemical bonds parameters into the coordination site from single-crystal X-ray data of the [Pt(salophen)] and [Pt(sal-3,4-ben)] parameters.

Bonds	[Pt(salophen)]	[Pt(sal-3,4-ben)]
Pt1–O2	1.983(4) Å	1.984(2) Å
Pt1–O3	1.991(4) Å	1.994(2) Å
Pt1–N4	1.965(5) Å	1.959(2) Å
Pt1–N5	1.955(4) Å	1.953(2) Å
N–Pt1–N	83.830°	83.727°
O–Pt1–O	85.258°	86.380°
N5–Pt1–O3	95.509°	95.437°
N4–Pt1–O2	95.587°	95.440°
O3–Pt1–N4	179.003°	179.730°
O2–Pt1–N5	178.100°	177.730°

Table 4. 2. Main [Pt(salophen)] and [Pt(sal-3,4-ben)] cartesian coordinates (x,y,z) of the O-Pt-N atoms coordination site according to the experimental single-crystal X-ray refinement.

		[Pt(salophen)]	
Atom	***x***	***y***	***z***
Pt1	0.34259 (4)	0.28306 (2)	0.69175 (2)
O2	0.3515 (8)	0.3876 (2)	0.6395 (2)
O3	0.0437 (8)	0.3266 (2)	0.7469 (2)
N4	0.6391 (9)	0.2390 (3)	0.6389 (2)
N5	0.3447 (10)	0.1809 (3)	0.7449 (2)
		[Pt(sal-3,4-ben)]	
Pt1	−0.15330 (2)	0.77547 (2)	0.59169 (2)
O2	−0.1503 (4)	0.7888 (2)	0.72457 (15)
O3	−0.4382 (4)	0.70176 (15)	0.59538 (16)
N4	−0.1513 (4)	0.7629 (3)	0.46139 (16)
N5	0.1332 (5)	0.84343 (17)	0.58692 (18)

4.3.2 Photophysical Properties of Pt(salicylidenes)

Steady-state electronic absorption and photoluminescence spectra of [Pt(salophen)] and [Pt(sal-3,4-ben)] coordination compounds in THF and DMSO solutions (10 μmol L^{-1}) were

displayed in the Figures 4.4 and 4.5 and the data were summarized in the Table 4.4. The electronic spectra of the salophen and sal-3,4-ben free-ligands were detailed in our previous works in the references 18 and 20, respectively. Upon coordination of the Pt(II) cation, absorption spectra profile was significantly disturbed in the two coordination compounds, increasing the molar absorptive index for absorption bands in comparison to the free-ligands and creating a new electronic structure on the coordination compounds, presenting a rich electronic absorption spectra with a several absorption band at the UV-Vis region of the electromagnetic spectrum. For the [Pt(salophen)], the following absorption bands λ_{abs} (nm) and ε (L mol^{-1} cm^{-1}; in parenthesis) were observed: THF – 544 ($1.87x10^4$), 515 ($1.72x10^4$), 462 ($1.81x10^4$), 385 ($7.90x10^4$), 364 ($7.75x10^4$) and 316 ($4.70x10^4$); DMSO – 524, ($2.12x10^4$), 494 ($1.83x10^4$), 452 ($2.00x10^4$), 380 ($9.03x10^4$), 362 ($9.01x10^4$) and 318 ($5.81x10^4$). And for its benzophenone derivative [Pt(sal-3,4-ben)]: THF – 554 ($2.45x10^4$), 524 ($2.11x10^4$), 470 ($1.96x10^4$), 389 ($8.21x10^4$), 374 ($7.68x10^4$) and 322 ($6.26x10^4$); DMSO – 536 ($2.88x10^4$), 510 ($2.51x10^4$), 460 ($2.29x10^4$), 386 ($1.00x10^5$), 370 ($9.5x10^4$) and 322 ($8.01x10^4$). According to these data we can observe that when benzophenone moiety was inserted in the [Pt(salophen)] a red-shift (≈10 nm) at the absorption maxima wavelengths was noticed and when a high polarity solvent was used (DMSO) a blue-shift (≈20 nm) was observed for [Pt(salophen)] and [Pt(sal-3,4-ben)], except for the high energy electronic transition.

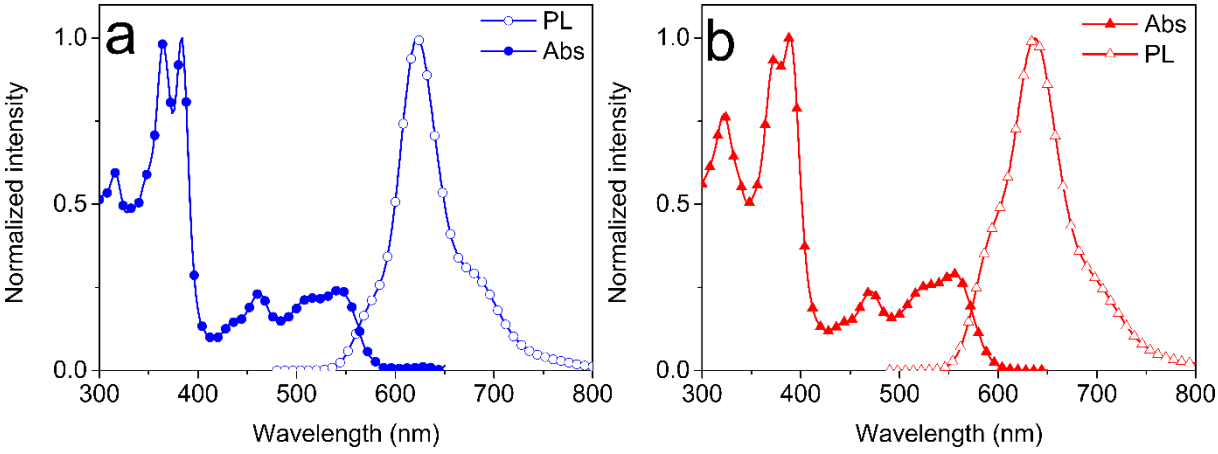

Figure 4. 4. Normalized electronic absorption and phosphorescence spectra of [Pt(salophen)] (a; λ_{exc} = 385 nm) and [Pt(sal-3,4-ben)] (b; λ_{exc} = 389 nm) in THF solutions (10 μmol L^{-1}).

In order to explore the electronic structures of the Pt(salicylidene) derivatives, [Pt(salophen)] and [Pt(sal-3,4-ben)] electronic vertical excitation and NTOs hole/particle pairs for the first singlet excited state (Figure 4.7) were done under relativistic DFT/TD-DFT framework at PBE0/(ZORA-def2-TVZP(C,N,O,H) and SARC-Pt(II) atom) level. Molecular

structures of the Pt(II) coordination compounds were obtained through SC-XDR and they were used for the optimization of the S_0 structures of each Pt(II) complex in vacuum. All vertical excitation energies (E/eV), oscillator strength (*f*) and their molecular orbitals assignment for [Pt(salophen)] and [Pt(sal-3,4-ben)] are summarized in the Table 4.4.

For the [Pt(salophen)] the energy calculated of the first singlet electronic transition ($S_0 \rightarrow S_1$) was 2.47 eV (501.3 nm; f = 0.079) assigning only to the frontier molecular orbitals (*HOMO* $\rightarrow$ *LUMO*), in agreement to the [Pt(salophen)] experimental data (E = 2.37 eV; 524 nm), with a small difference of $\delta \approx 0.10$ eV. Also, according to the [Pt(salophen)] NTOs densities (Figure 4.7), this electronic transition must be assigning a mixed character of MLCT/ILCT $\rightarrow$ ILCT (hole $\rightarrow$ particle), combining the salophen ligand π framework with Pt(II) cation $5d_{x-y}$ and π^* on the ground and excited states, respectively.

[Pt(sal-3,4-ben)] exhibited an energy calculated of the first singlet electronic transition of 2.39 eV (519.1 nm; f = 0.047), assigned to *HOMO* $\rightarrow$ *LUMO* electronic transition with a well correlation to its experimental value of the first electronic transition (E = 2.31 eV; 536 nm), presenting a very small variation of $\delta \approx 0.08$ eV in contrast to the experimental electronic absorption transition data. NTOs hole/particle pairs densities (Figure 4.7) for this electronic transition showed a similar electronic density distribution of [Pt(salophen)] in the ground-state (HOMO), having a minimal contribution of benzophenone moiety. However, on the particle electronic density (LUMO) the presence of benzophenone disturbs its electronic structure, considerably, causing unoccupied $5d_{x^2-y^2}$ orbital of Pt(II) takes part on the S_1 density delocalized along π^* framework. Therefore, [Pt(sal-3,4-ben)] frontier orbitals electronic transition exhibits a mixed character of MLCT/ILCT $\rightarrow$ MLCT/ILCT, being a minimal contribution of the metal-centered charge transfer (MC).

Table 4. 3. [Pt(salophen)] and [Pt(sal-3,4-bem)] energy excitations calculated at DFT/TD-DFT framework at PBE0/(ZORA-def2-TVZP(C,N,O,H) and SARC-Pt(II) atom) level in vacuum.

E (eV)	λ (nm)	*f*	Assignment*
	[Pt(salophen)]		
2.47	501.3	0.079	H→L
3.02	410.7	0.045	H-1→L
3.60	344.5	0.750	H-2→L
3.69	336.5	0.250	H-1→L+1
4.08	303.6	0.079	H-2→L+1
1.97**	629.4		
	[Pt(sal-3,4-ben)]		
2.39	519.1	0.047	H→L
2.81	441.0	0.034	H→L+1
2.95	420.7	0.019	H-1→L
3.46	358.9	0.650	H-2→L
3.55	349.3	0.180	H→L+2
3.64	341.0	0.001	H-6→L
1.91**	647.7		

*Greatest contributions, ** First triplet state

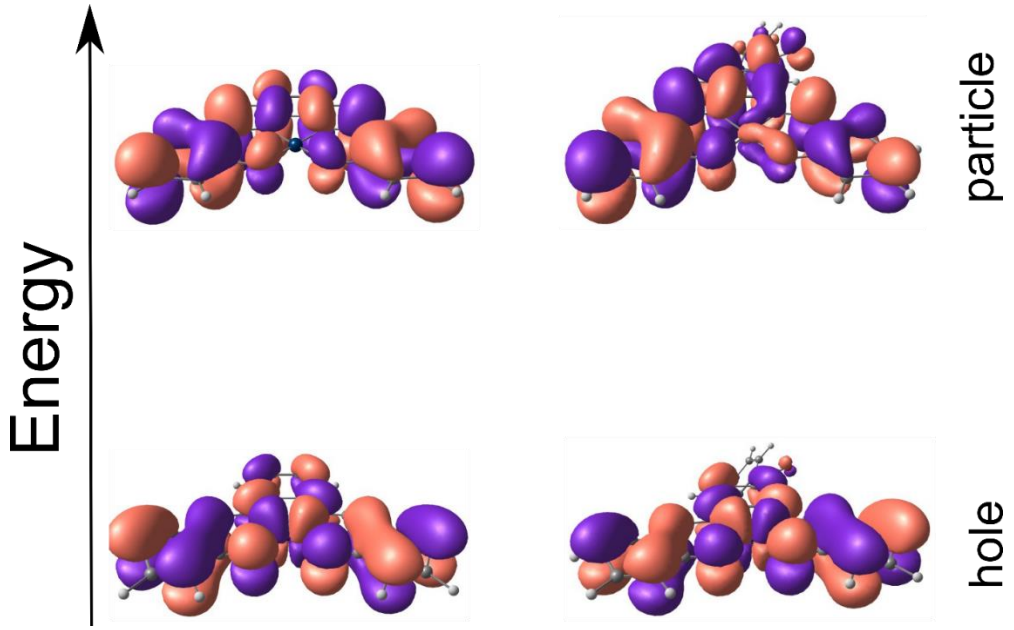

Figure 4. 5. NTOs hole/particle pairs densities for the first singlet excited states of [Pt(salophen)] and [Pt(sal-3,4-ben)] in vacuum at the PBE0/(ZORA-def2-TVZP(C,N,O,H) and SARC-Pt(II) atom) level.

PL spectrum of the [Pt(salophen)] coordination compound (λ_{exc} = 385 nm) measured in THF (Figure 4.5a) (10 μmol L^{-1}) presented that the coordination of the metal atom leads to a considerably spectral red-shift of the emission spectra in comparison to free-salophen ligand, with a well-defined vibronic progression at $\lambda_{0\text{-}0}$ = 575 nm, $\lambda_{0\text{-}1}$ = 621 nm and $\lambda_{0\text{-}2}$ = 663 nm and a Stokes shift of *SS* = 991 cm^{-1} in relation to the zero-phonon emission band with PLQY = 47 % in N_2(g) saturated atmosphere. Its PL spectrum in the DMSO solution (Figure A42) (1 μmol L^{-1}) were observed the presence of the vibronic progression, presenting $\lambda_{0\text{-}0}$ = 560 nm, $\lambda_{0\text{-}1}$ = 613 nm and $\lambda_{0\text{-}2}$ = 630 nm with *SS* = 1227 cm^{-1}, and as consequence of the higher SS in comparison to THF solution, PLQY decreased substantially (PLQY = 13 % N_2(g) saturated atmosphere). Also, the PL spectrum of [Pt(salophen)] in EPA solvent-mixture (Figure 4.6; λ_{exc} = 374 nm; $1x10^{-6}$ mol L^{-1}) showed at T = 298 K (red curve) the maximum emission at $\lambda_{0\text{-}0}$ = 577 nm, $\lambda_{0\text{-}1}$ = 625 nm and $\lambda_{0\text{-}2}$ = 673 nm with *SS* = 1326 cm^{-1} and at T = 77 K (blue curve) was noticed an increase of intensity about 1.36 times and a small blue-shift its 0-1 emission band (621 nm with *SS* = 2554 cm^{-1}). Beside this, the zero-phonon band of [Pt(salophen)] was quenched in over the high probability emission band ($\lambda_{0\text{-}1}$ and $\lambda_{0\text{-}2}$). Also, the calculated energy for the triplet emission ($T_1 \rightarrow S_0$; E = 1.97 eV and λ = 629 nm) match with the experimental data for the three solvent systems, with a small deviation of $\delta \approx 0.20$ eV, in relation to the estimated triplet energy obtained from experimental data (2.17 eV; λ = 571 nm).

As its analogue compound, the PL spectra of the [Pt(sal-3,4-ben)] were recorded in THF, DMSO and EPA solutions in a free-O_2(g) environment (λ_{exc} = 389 nm). PL spectrum in THF (Figure 4.5a) (10 μmol L^{-1}) exhibited the well-defined vibronic transitions with the zero-phonon band centered at $\lambda_{0\text{-}0}$ = 590 nm, the 0-1 band at $\lambda_{0\text{-}1}$ = 637 nm and the 0-2 band at $\lambda_{0\text{-}2}$ = 671 nm and a Stokes shift of *SS* = 537 cm^{-1}, while there was a considerably increase of [Pt(sal-3,4-ben)] phosphorescence quantum yield (PLQY = 76 %) 1.62 times higher than the [Pt(salophen)] at the same experimental conditions. The PL spectrum of the [Pt(sal-3,4-ben)] in DMSO solution (10 μmol L^{-1}) (Figure A42) showed a similar vibronic resolution, however a considerably decrease of the PLQY and increase of the Stokes shifts were noticed. A similar behavior was observed for the sal-3,4-ben Zn(II) coordination compound, which lead us to believe that DMSO has a specific interaction with the benzophenone moiety these of compounds. Also, the effect of the addition of the benzophenone moiety on the Pt(II) coordination compound framework was cleared in the [Pt(sal-3,4-ben) PL spectra in EPA solution (1 μmol L^{-1}; Figure 4.6) at room-temperature (blue curve) and 77 K (red curve): while the PL spectrum at 298 K exhibited the same behavior in the other media, with zero-phonon

band (594 nm) and the 0-1 (640 nm) and 0-2 (681 nm) vibronic progressions, in the PL spectrum at 77 K. There was observed a completely suppression of the 0-0 band and small blue-shift of the 0-1 (634 nm) band, similar to the [Pt(salophen)]. Also, there is a remarkable increase of the phosphorescence intensity (≈ 2.5 times). The calculated energy of the T_1 state emission presented a good agreement to the experimental steady-state PL measurement with a small deviation of d = 0.02 eV, being E_{calc} = 1.91 eV and E_{exp} = 1.93 eV. Thus, the relativistic PBE0/(ZORA-def2-TVZP(C,N,O,H) and SARC-Pt(II) atom) level of theoretical calculations exhibited a very well correlation with the experimental steady-state electronic spectroscopies data in the three solvent media.

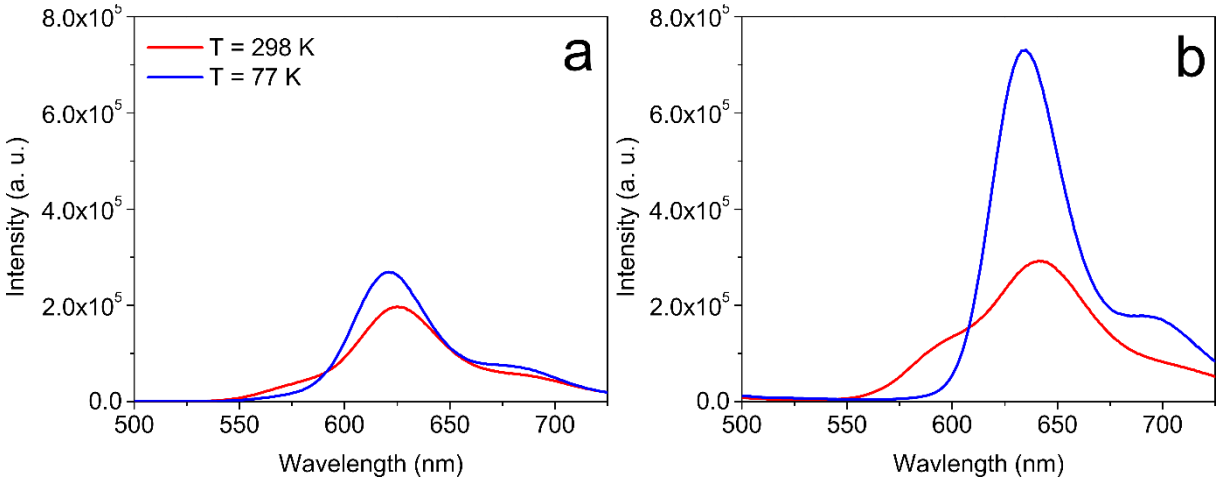

Figure 4. 6. Phosphorescence spectra of [Pt(salophen)] (a; λ_{exc} = 385 nm) and [Pt(sal-3,4-ben)] (b; λ_{exc} = 389 nm) in EPA solutions (1 μmol L^{-1}) at 298 K (red curves) and 77 K (blue curves).

Furthermore, the steady-state phosphorescence spectra of [Pt(salophen)] and [Pt(sal-3,4-ben)] in THF and DMSO (10 μmol L^{-1}) were evaluated in air saturated environment (black curves in the Figure 4.7) in order to evaluate the $^3O_2$(g) suppression of their T_1 state emission via triplet-triplet annihilation (TTA). In the case of DMSO solutions (Figure A43) the effect of the $^3O_2$(g) quenching was very little pronounceable once polar solvents present lower concentrations of dissolved oxygen, while non-polar environments (such as THF) show concentrations of [$^3O_2$(g)] ≈ 10^{-3} mol L^{-1},[239] one hundred times higher than the used concentration for the Pt(salicylidenes) derivatives. PL spectra of [Pt(salophen)] (λ_{exc} = 385 nm) and [Pt(sal-3,4-ben)] (λ_{exc} = 389 nm) in THF solutions (10 μmol L^{-1}) at air saturated condition (black curves in the Figure 4.7) presented a strong quenching process due the presence of $^3O_2$(g) as consequence of the Pt(salicylidenes) phosphorescence emission with a large decrease around ≈ 38 times of their phosphorescence PLQY, being PLQY = 3 and 2 % for [Pt(salophen)] and [Pt(sal-3,4-ben)], respectively.

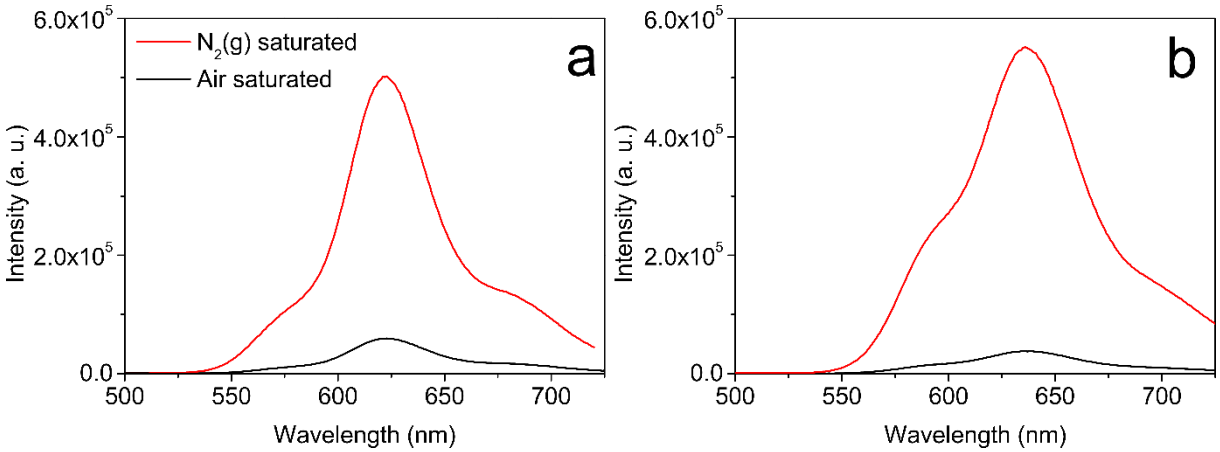

Figure 4. 7. Phosphorescence spectra of [Pt(salophen)] (a; λ_{exc} = 385 nm) and [Pt(sal-3,4-ben)] (b; λ_{exc} = 389 nm) in THF solutions (10 μmol L^{-1}) under N_2(g) and air saturated conditions.

In addition, the phosphorescence dynamics of the Pt(salicylidenes) in THF media (10 μmol L^{-1}) with N_2(g) and/or air saturated environments were studied by TCSPC technique (λ_{exc} = 375 nm) and Table 4.4 summarized the time-resolved photophysical data. In both Pt(II) coordination complexes the N_2(g) saturated solution were observed a monoexponential behavior with a longer phosphorescence lifetime ($\tau_{[Pt(salophen)]}$ = 3.459 ± 0.001 μs; $\tau_{[Pt(sal\text{-}3,4\text{-}ben)]}$ = 2.747 ± 0.006 μs) in comparison to $^3O_2$(g) saturated solution ($\tau_{[Pt(salophen)]}$ = 0.114 ± 0.001 μs; $\tau_{[Pt(sal\text{-}3,4\text{-}ben)]}$ = 0.125 ± 0.001 μs) (Figure 4.8 and Figure 4.9), which is in agreement to their steady-state phosphorescence quantum yields quenching due to the presence of triplet oxygen.

Thus, combining PLQY and transient phosphorescence lifetimes and using the equation 1.13 for excited-state deactivation, the radiative (k_R) and non-radiative (k_{nR}) rates of the Pt(II) coordination compounds were determined, as Table 4.4 summarized. From these experimental data, the quenching rate constants by $^3O_2$(g) in THF solution were determined considering a pseudo-first order approximation ($[^3O_2]_{dissolved}$ >> [Pt(salicylidenes)]) and intersystem crossing quantum yield of 100 %.

Thereby, the rates were obtained as $k_{^3O_2}[^3O_2]$ = 8.356x10^6 s^{-1} and 7.733x10^6 s^{-1} for [Pt(salophen)] and [Pt(sal-3,4-ben)], respectively, sorting out from the sum of the non-radiative processes rate. Presenting values higher than the radiative rates for the two Pt(II) coordination compounds (Table 4.4). Therefore, these Pt(salicylidene) derivatives may be applied as $^3O_2$(g) sensor.

In conclusion [Pt(salophen)] and [Pt(sal-3,4-ben)] exhibit high-intensity phosphorescence emission even at room-temperature and according to our theoretical and experimental results and their emission occurs from the T_1 state ($T_1 \rightarrow S_0$), mainly composed by mixed ^{3}MLCT/^{3}ILCT/^{3}MC character transitions.

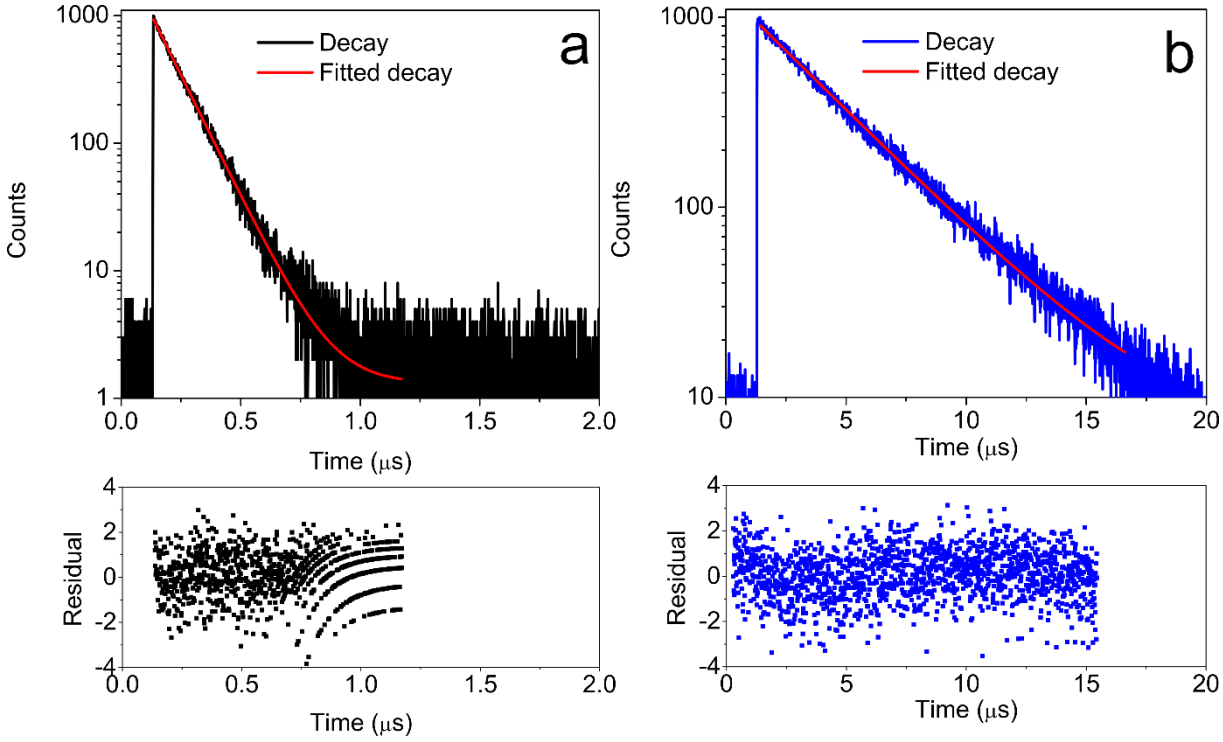

Figure 4. 8. Phosphorescence decays of [Pt(salophen)] (a; λ_{exc} = 375 nm; λ_{PL} = 621 nm) in THF solution (10 μmol L^{-1}) under N_2(g) and air saturated conditions.

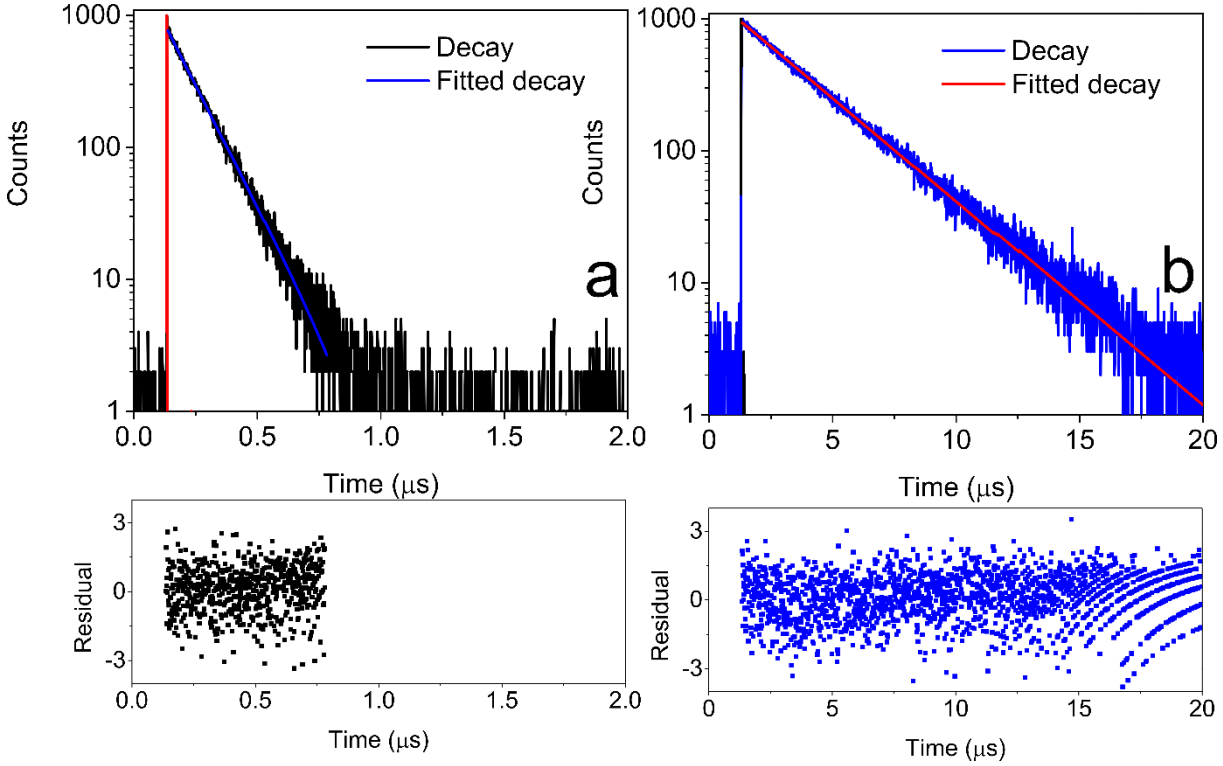

Figure 4. 9. Phosphorescence decays of [Pt(sal-3,4-ben)] (a; λ_{exc} = 375 nm; λ_{PL} = 637 nm) in THF solution (10 μmol L^{-1}) under N_2(g) and air saturated conditions.

Table 4. 4. Photophysical properties of [Pt(salophen)] and [Pt(sal-3,4-ben)] coordination compounds in THF, DMSO and EPA solutions (10 μmol L^{-1}).

	λ_{abs1}/nm (ε/L mol^{-1} cm^{-1})	λ_{abs2}/nm (ε/L mol^{-1} cm^{-1})	λ_{abs3}/nm (ε/L mol^{-1} cm^{-1})	λ_{abs4}/nm (ε/L mol^{-1} cm^{-1})	λ_{abs5}/nm (ε/L mol^{-1} cm^{-1})	λ_{abs6}/nm (ε/L mol^{-1} cm^{-1})	λ_{PL}/nm	PLQY %	τ_{phos}/μs	k_R/s^{-1}	k_{nR}/s^{-1}	*SS*/cm^{-1}
					[Pt(salophen)]							
THF	544 ($1.87x10^4$)	515 ($1.72x10^4$)	462 ($1.81x10^4$)	385 ($7.90x10^4$)	364 ($7.75x10^4$)	316 ($4.70x10^4$)	621	47[a] 3[b]	3.459±0.001[a] 0.114±0.001[b]	$1.36x10^{5}$ [a] $2.63x10^{5}$ [b]	$1.53x10^{5}$ [a] $8.51x10^{6}$ [b]	991
DMSO	524 ($2.12x10^4$)	494 ($1.83x10^4$)	452 ($2.00x10^4$)	380 ($9.03x10^4$)	362 ($9.01x10^4$)	318 ($5.81x10^4$)	613	13[a] 8[b]	0.471±0.001[a] 0.227±0.001[b]	$2.77x10^{5}$ [a] $3.52x10^{5}$ [b]	$1.85x10^{6}$ [a] $4.05x10^{6}$ [b]	1227
EPA	536	512	460	382	364	-	625[c] 621[d]	-	2.768±0.013[c] 4.763±0.020[d]	-	-	2657[c] 2554[d]
					[Pt(sal-3,4-ben)]							
THF	554 ($2.45x10^4$)	524 ($2.11x10^4$)	470 ($1.96x10^4$)	389 ($8.21x10^4$)	374 ($7.68x10^4$)	322 ($6.26x10^4$)	637	76[a] 2[b]	2.747±0.006[a] 0.125±0.001[b]	$2.77x10^{5}$ [a] $1.84x10^{5}$ [b]	$8.74x10^{4}$ [a] $7.82x10^{6}$ [b]	537
DMSO	536 ($2.88x10^4$)	510 ($2.51x10^4$)	460 ($2.29x10^4$)	386 ($1.00x10^5$)	370 ($9.5x10^4$)	322 ($8.01x10^4$)	626	4[a] 3[b]	0.099±0.001[a] 0.085±0.001[b]	$4.02x10^{5}$ [a] $3.86x10^{5}$ [b]	$9.66x10^{6}$ [a] $1.13x10^{7}$ [b]	1386
EPA	552	524	470	388	374	-	641[c] 637[d]	- -	2.544±0.008[c] 4.382±0.016[d]	-	-	2515[c] 2417[d]

[a]N_2(g) saturated solutions; [b]air saturated solutions; [c]298 and [d]77 K in EPA solutions using the 0-1 emission band as reference.

4.3.3 High-Efficiency and Color-Tunable WOLEDs

After careful structural and photophysical characterization of the Pt(salicylidene) derivatives they were used as active layers in two different blue-fluorescent conducting polymers (PVK and PFO) to assemble all solution-processable OLEDs, leading two devices architectures: (**1**) ITO|PEDOT:PSS|PVK:Pt(salicylidene) 2.5 % mol/mol|Ca|Al; and (**2**) ITO|PEDOT:PSS|PVK|PFO:Pt(salicylidene) **X** % mol/mol|Ca|Al, where **X** = 0.1, 0.5, 1.0 and 2.5. In a similar way to their Zn(II) coordination compounds OLEDs.

OLEDs containing only PVK and Pt(salicylidenes) (**1**) were produced in order to evaluate the optical-electronic properties of the Pt(II) coordination compound without the emission of the conducting polymer, as noticed for their Zn(II) analogues. EL spectra of the devices ITO|PEDOT:PSS|PVK:[Pt(salophen)] 2.5 % mol/mol|Ca|Al and ITO|PEDOT:PSS|PVK:[Pt(sal-3,4-ben)] 2.5 % mol/mol|Ca|Al exhibited emission bands close to their PL spectra, also presenting the vibronic-progression centered at $\lambda_{0\text{-}0}$ = 569 and 596 nm, $\lambda_{0\text{-}1}$ = 616 and 636 nm and $\lambda_{0\text{-}2}$ = 648 and 661 nm for the [Pt(salophen)] (black curves in the Figure 4.10) and [Pt(sal-3,4-ben)] (red curves in the Figure 4.10), respectively. Beside this, as for their PL spectra, the addition of the benzophenone moiety disturbs the Pt(II) coordination compounds excited-state electronic, mostly, leading a red-shift of the [Pt(sal-3,4-ben)] EL emission bands in contrast to the [Pt(salophen)] coordination compound device. Also, a red-EL emission was observed for the two OLEDs, however, in their chromaticity diagram CIE 1931 (inset Figure 4.10d) [Pt(sal-3,4-ben)] (b – 0.59, 0.40) showed deepest red EL color emission in comparison to the [Pt(salophen)] (a – 0.55, 0.45), which was in agreement to the EL spectrum of each Pt(II) coordination compound.

The optical-electronic properties of the [Pt(salophen)] and [Pt(sal-3,4-ben)] devices were evaluated in terms of JxV, LxV, η_{curr}xV and η_{P}xV curves (Figure 4.10) and frustrated results were observed. All efficiency parameters of [Pt(salophen)] (V_{on} = 8.0 V, J = 0.058 A cm^{-2}, L_{max} = 48 cd m^{-2}; η_{curr} = 0.004 cd A^{-1} and η_{P} = 0.004 lm W^{-1}) and [Pt(sal-3,4-ben)] (V_{on} = 7.0 V, J = 0.024 A cm^{-2}, L_{max} = 51 cd m^{-2}; η_{curr} = 0.005 cd A^{-1} and η_{P} = 0.009 lm W^{-1}) were worse than the [Zn(salophen)] and [Zn(sal-3,4-ben)] (see Chapter 3). It was expected that Pt(salicylidene) derivatives in PVK would present better performance than the [Zn(salicylidenes)] at the same conditions, because the Pt(II) coordination compounds exhibit intense phosphorescence at room-temperature as it was observed in the photophysics section on this chapter.

Charge mobilities of these devices at drive voltages were obtained from TCLC model according to the equation 1.8. The OLED ITO|PEDOT:PSS|PVK:[Pt(salophen)]|Ca|Al exhibited values of charge mobility of μ_p = 9.858x10^{-5} cm^2 V^{-1} s^{-1} while the device ITO|PEDOT:PSS|PVK:[Pt(sal-3,4-ben)]|Ca|Al was μ_p = 1.954x10^{-5} cm^2 V^{-1} s^{-1} and this last diode presented lowest trap-energy parameter (l = 4.119) in comparison to the [Pt(salophen)] device (l = 6.017), which may be correlated to its better performance and it must be directly related to the active layer organizational (structural and morphological defects) levels.

Thus, in order to investigate how works the mechanism of the [Pt(salophen)] and [Pt(sal-3,4-ben)] electroluminescence and trying to improve their optical-electronic properties, they were dispersed into PFO, forming composites and they were used as active layer in solution-processable OLEDs with the following architecture: ITO|PEDOT:PSS|PVK|PFO:Pt(salicylidene) **X** % mol/mol|Ca|Al, varying the Pt(salicylidene) composition into PFO matrix (**X** = 0.1, 0.5, 1.0 and 2.5).

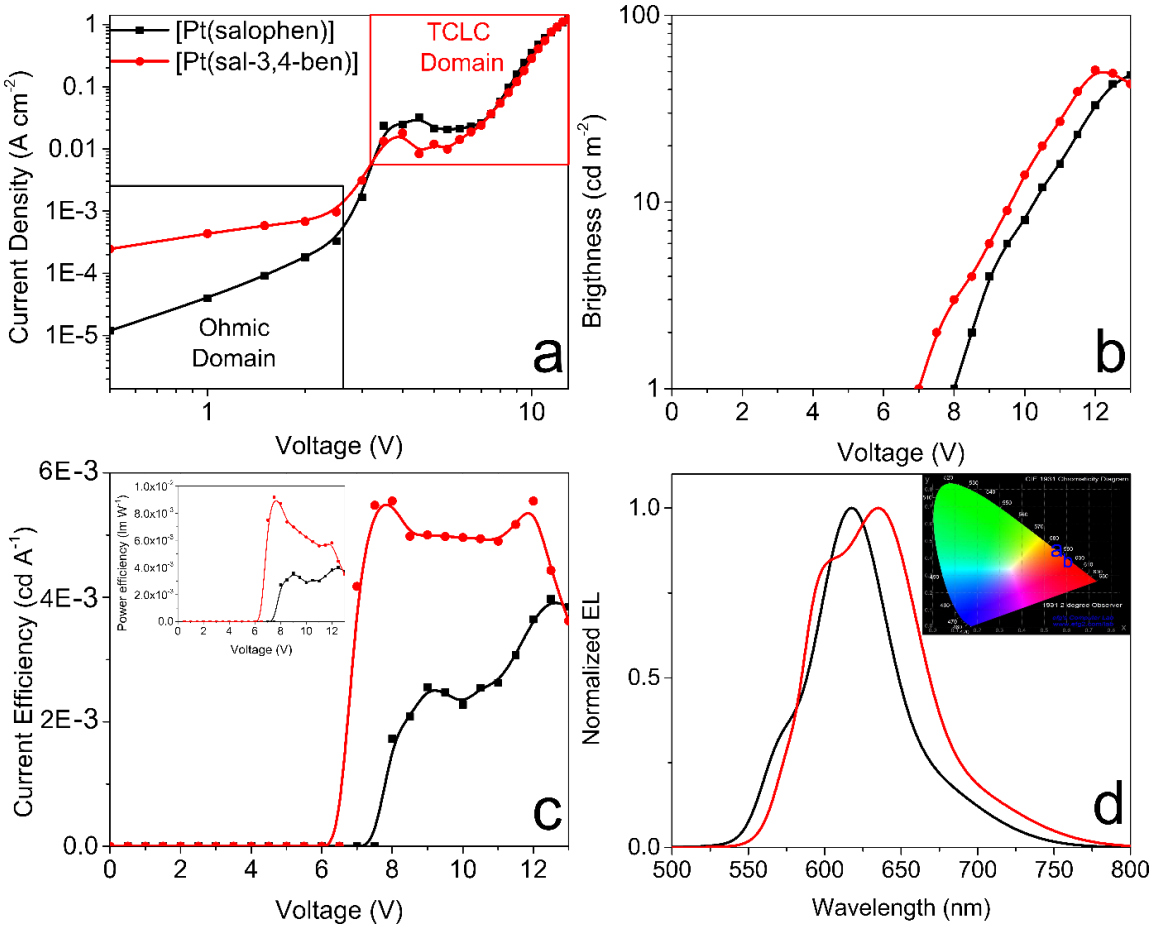

Figure 4. 10. a. log-log Current density vs. voltage; b. brightness vs. voltage; c. current efficiency vs. voltage curves; and d. EL spectra and inset the CIE 1931 of the diodes ITO|PEDOT:PSS|PVK:Pt(salicylidenes)|Ca|Al.

Firstly, the PL spectra of the PFO:Pt(salicylidenes) were done at the same conditions used to assemble the diodes, using λ_{exc} = 375 nm (where PFO is excited preferably), in order to understand the occurrence of non-radiative and/or trivial energy transfer processes from conducting polymer to the Pt(II) coordination compounds. PL spectra of the PFO:[Pt(salophen)] composites in thin-films (Figure 4.12a) showed a commonly improvement of Pt(II) coordination complex emission with its concentration increase and a similar behavior was observed for the PFO:[Pt(sal-3,4-ben)] composites. In the PL spectra of the two coordination compounds composites were observed their well-defined vibronic progression: [Pt(salophen)] – $\lambda_{0\text{-}0}$ = 582 nm, $\lambda_{0\text{-}1}$ = 628 nm and $\lambda_{0\text{-}2}$ = 694 nm; and [Pt(sal-3,4-ben)] – $\lambda_{0\text{-}0}$ = 602 nm, $\lambda_{0\text{-}1}$ = 643 nm and $\lambda_{0\text{-}2}$ = 704 nm. As observed for PL spectra of Pt(salicylidenes) in solution, the emission bands of [Pt(sal-3,4-ben)] red-shifted in comparison to the [Pt(salophen)], due to the electron acceptor effect of the benzophenone moiety on the excited-state (Figure 4.5). Also, in the two composites thin-films were observed an isosbestic point between the PFO and Pt(salicylidenes) emission, centered around λ_{iso} = 560 and 572 nm for the [Pt(salophen)] and [Pt(sal-3,4-ben)] composites, respectively. This iso-emissive effect must be linked to the presence of non-radiative energy transfer processes between the donor (conducting polymer) and acceptor (Pt(II) coordination compounds) molecules, which was proved by the photoluminescence excitation spectra (PLE) of these samples, monitoring the PFO (437 nm), [Pt(salophen)] (628 nm) and [Pt(sal-3,4-ben)] (643 nm) (Figure A49). As expected, monitoring the conducting polymer or the Pt(II) coordination compounds PL band, PLE spectra have exhibited same spectral profile, showing maxima excitation band centered at λ_{exc} = 375 nm (amorphous PFO excitation) with small amounts of crystalline PFO's phase ($\lambda_{exc} \approx$ 430 nm).

Neat PFO thin-film PL spectrum (black curves) has exhibited a mixture of PFO's α ($\lambda_{\alpha\text{-phase}}$ = 425 nm) and β ($\lambda_{\beta\text{-phase}}$ = 437 nm) phases zero-phonon emission bands, as discussed on Chapter 3. However, differently of their Zn(II) derivatives, the addition of the [Pt(salophen)] and [Pt(sal-3,4-ben)] changed the PFO's crystallinity and morphology, consequently, making that in 2.5 % of Pt(II) coordination compound into the PFO matrix is predominantly from α-phase emission, including an iso-emissive point centered at 431 nm for both cases. It is clear when the ratio of the intensities of each PFO's species (I_β/I_α) are done with a $\mathbf{I_\beta/I_\alpha}$ vs. **X** linear trend curve (Figure 4.12): PFO:[Pt(salophen)] = 1.67 (0.0 %), 1.64 (0.1 %), 1.49 (0.5 %), 1.47 (1.0 %) and 0.67 (2.5 %, considering only α-phase $I_{0\text{-}1}/I_{0\text{-}0}$); and PFO:[Pt(sal-3,4-ben)] = 1.67 (0.0 %), 1.41 (0.1 %), 1.39 (0.5 %), 1.14 (1.0) and 0.66 (2.5 % and considering only α-phase $I_{0\text{-}1}/I_{0\text{-}0}$). Thus, the addition of the [Pt(salophen)] into the PFO conducting polymer matrix leads

more pronounceable crystallinity changes than the addition of [Pt(sal-3,4-ben)], which directly impacts in its OLEDs performance. Concluding that the presence of the Pt(II) coordination compounds impacts directly on the morphological and crystallinity properties of the PFO host, including the occurrence of energy transfer processes from the PFO to the [Pt(salophen)] and [Pt(sal-3,4-ben)] molecules.

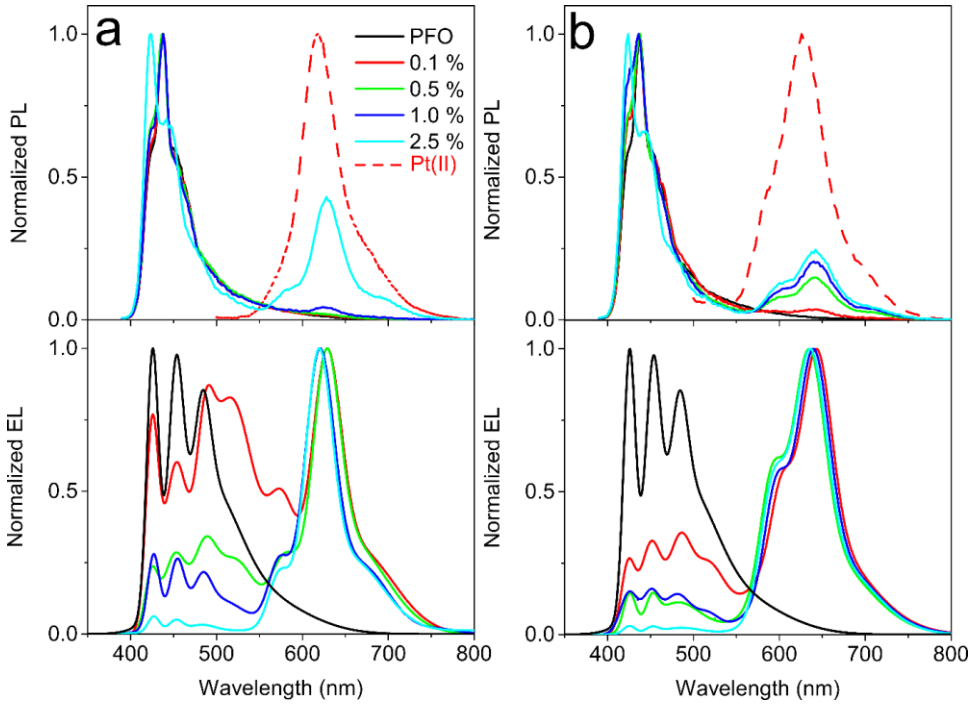

Figure 4. 11. Comparison between normalized PL (λ_{exc} = 375 nm) and EL (at η_{max}) spectra of the ITO|PEDOT:PSS|PVK|PFO:Pt(II) salicylidene|Ca|Al diodes: a. [Pt(salophen)]; and b. [Pt(sal-3,4-ben)].

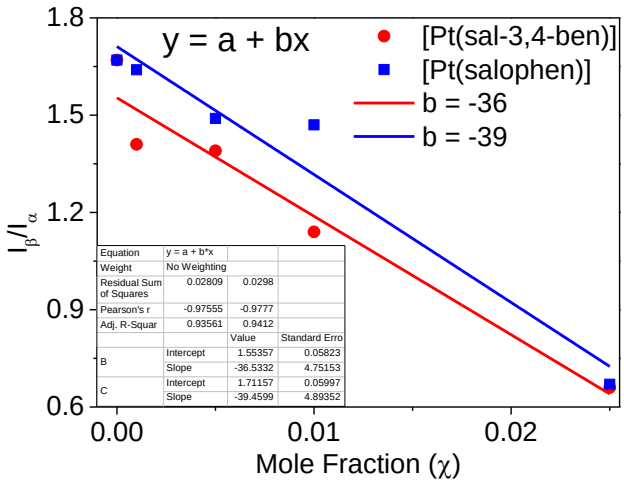

Figure 4. 12. PFO phase changes in PFO:Pt(salicylidene) composites in thin-film according to the PL I_β/I_α vs. χ linear trend curve: [Pt(salophen)] (blue curve) and [Pt(sal-3,4-ben)] (red curve).

After optical characterization of the PFO:Pt(salicylidenes) in thin-films, their electroluminescence devices were obtained at the same conditions and concentration of the [Pt(salophen)] and [Pt(sal-3,4-ben)], and Table 4.5 summarized the OLEDs optical-electronic properties data. EL spectra of the two composites at all molar ratios of the coordination compounds (Figure 4.11) into PFO composites were plotted at the OLEDs maximum efficiencies and all of them exhibited the $PFO_{\alpha\text{-phase}}$ zero-phonon emission band and its well-resolved vibronic progressions centered at λ_{EL} = 425 (0-0), 454 (0-1) and 485 nm with small amounts of PFO aggregates emission (λ_{EL} = 525 nm) for the ITO|PEDOT:PSS|PVK|PFO|Ca|Al device (black curves in the Figure 4.11) and presenting a blue color characteristic of PFO EL emission (CIE 1931 x = 0.17; y = 0.21). Differently of the [Zn(salophen)] and [Zn(sal-3,4-ben)], Pt(salicylidenes) were not able to induce crystallinity on the PFO (β-phase) structure at any used molar ratio of the Pt(II) coordination compounds. In the [Pt(salophen)] and [Pt(sal-3,4-ben)] EL spectra (Figure 4.11) into PFO-host matrix were observed an intense contribution of their red-component emission, including the presence of Pt(salicylidenes) vibronic progression, similar to the solution, thin-films PL and their PVK devices, presenting their EL emission band for each concentration of Pt(II) coordination compounds diodes centered around: ITO|PEDOT:PSS|PVK|PFO:[Pt(salophen)]|Ca|Al – 0.1 and 0.5 % $\lambda_{0\text{-}0}$ = 573 nm, $\lambda_{0\text{-}1}$ = 629 nm and $\lambda_{0\text{-}2}$ = 693 nm, with a blue-shift of 10 nm in the 0-1 and 0-2 EL bands for 1.0 and 2.5 % to $\lambda_{0\text{-}1}$ = 129 nm and $\lambda_{0\text{-}2}$ = 683 nm; ITO|PEDOT:PSS|PVK|PFO:[Pt(sal-3,4-ben)]|Ca|Al – 0.1 % $\lambda_{0\text{-}0}$ = 605 nm, $\lambda_{0\text{-}1}$ = 643 nm and $\lambda_{0\text{-}2}$ = 715 nm, presenting a blue-shift of 4 nm in the 0-0, 0-1 and 0-2 EL bands at each concentration of the [Pt(sal-3,4-ben)]. Thus, combining the amorphous PFO blue-emission and its aggregate greenish-emission ($\lambda_{EL} \approx$ 520 nm) with the red-phosphorescence of the [Pt(salophen)] and [Pt(sal-3,4-ben)] coordination complexes, thereby obtaining white organic light-emitting devices (WOLEDs) (CIE1931 x = 0.33, y = 0.33), principally at the lower concentration (0.1 mol/mol) of Pt(II) complex.

Also, the blue-shifts of the EL emission bands of Pt(salicylidenes) should be attributed to the formation of h-aggregates of the Pt(II) coordination compounds into host-matrix, as noticed by Che and his collaborators in two previous works.[227,230] Beside this, two isosbestic points were observed for the PFO:Pt(salicylidenes) composites diodes around λ_{iso} = 560 and 565 nm for the [Pt(salophen)] and [Pt(sal-3,4-ben)], respectively, indicating the occurrence of non-radiative energy transfer processes (FRET and Dexter) from PFO-host to the Pt(salicylidenes).

WOLEDs have exhibited a strong dependence of the Pt(II) coordination compounds concentration into PFO matrix and principally with the applied electrical field (Figure 4.13). As a general trend Pt(salicylidenes) start their red-EL emission (CIE 1931 x ≈ 0.51, y ≈ 0.40) during low voltages and increasing the applied electrical field, polyfluorene blue-greenish EL (CIE 1931 x ≈ 0.21, y ≈ 0.31) emission goes to emit, leading the true white-light emission according to their chromaticity diagrams (CIE 1931 x = 0.33, y = 0.33) at the drive voltage region (≈ 8 V). This behavior can be obtained for the PFO:[Pt(salophen)] devices at 0.5 and 1.0 %, while only at 0.1 % mol/mol ratios the PFO:[Pt(sal-3,4-ben)] WOLEDs exhibited color tuning from red, achieving true white emission and finishing in blue-greenish EL.

Only the WOLED containing 0.1 % mol/mol of [Pt(salophen)] (Figure 4.13) has shown white-emission with equivalent contributions of PFO and its aggregate and Pt(II) coordination compound in the EL spectrum even at the V_{on} (CIE 1931 x = 0.32, y = 0.35). However, with exception of the 2.5 % devices all OLEDs has exhibited color tuning along the running voltage. Because at high concentrations, Pt(salicylidenes) aggregate into conducting polymer, which does not make white emission devices, presenting only red-emission components, which has compromised the diodes optical-electric performances (Figure 4.15 and Table 4.5).

Furthermore, this behavior is completely supported by the energy level diagram bellow vacuum of the WOLEDs components (Figure 4.14). HOMO and LUMO energy levels of the two Pt(II) coordination compounds have quite similarity, being E_{HOMO} = -5.60 eV and E_{LUMO} = 3.26 eV (E_{gap} = 2.34 eV) and E_{HOMO} = -5.62 eV and E_{LUMO} = -3.29 eV (E_{gap} = 2.33 eV) for [Pt(salophen)] and [Pt(sal-3,4-ben)], respectively. However, EL emission processes on the Pt(salicylidenes) occur via phosphorescence phenomenon ($T_1 \rightarrow S_0$) and their values against E_{HOMO} were obtained from the intersection between PLE and PL spectra, yielding $E_{T_1[Pt(salophen)]}$ = -3.43 eV and $E_{T_1[Pt(sal\text{-}3,4\text{-}ben)]}$ = -3.50 eV. Pt(salicylidenes) have exhibited lower frontier orbitals energy levels values in comparison to the PVK and PFO conducting polymers and energy and charge transfer processes must be happen from the hosts (polymers) from the guests (Pt(II) derivatives). Thus, in the case of the WOLEDs it is clear why [Pt(salophen)] and [Pt(sal-3,4-ben)] have turned on before the PFO, and when the charge carriers in the valence and conduction bands of the coordination compounds have saturated the blue-fluorescent polymer begun to emit, leading a white-light generation device given the applied voltage.

ITO|PEDOT:PSS|PVK|PFO:**[Pt(salophen)]**|Ca|Al

ITO|PEDOT:PSS|PVK|PFO:**[Pt(sal-3,4-ben)]**|Ca|Al

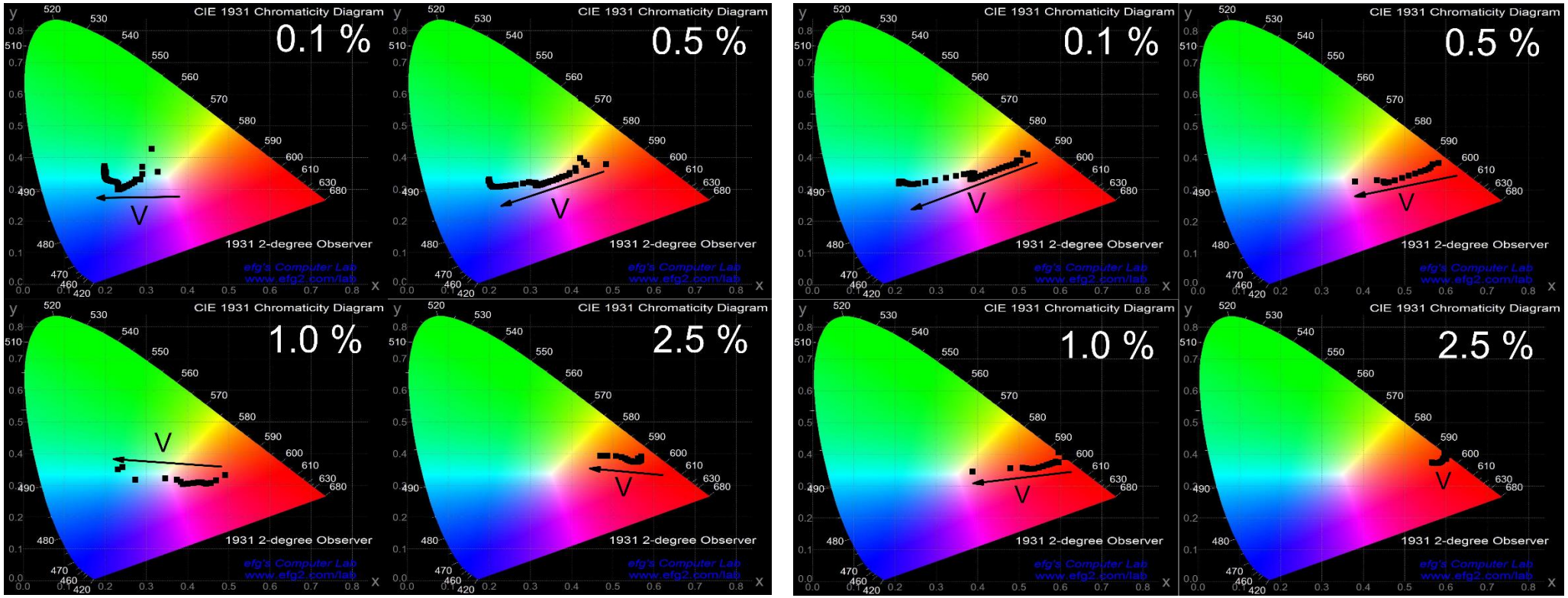

Figure 4. 13. Color tuning according to the CIE 1931 Chromaticity coordinates diagram of the ITO|PEDOT:PSS|PVK|PFO:Pt(salicylidenes)]|Ca|Al diodes with molar ratios 0.1, 0.5, 1.0 and 2.5 % (mol/mol).

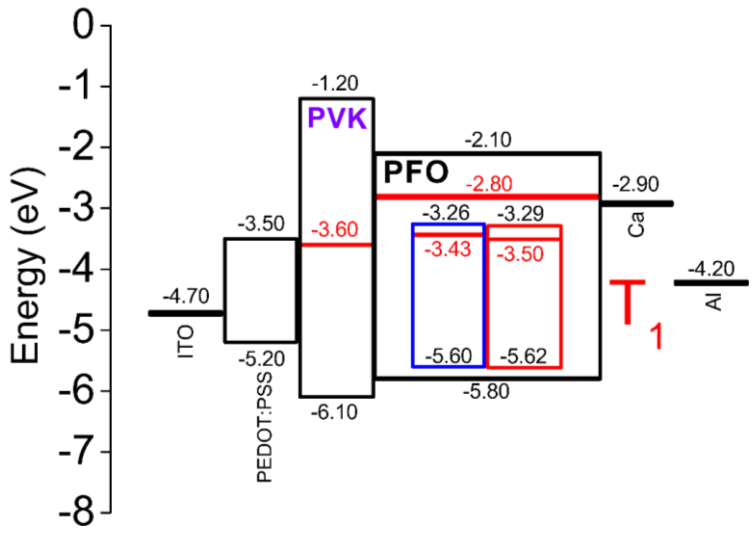

Figure 4. 14. Diagram of HOMO/LUMO frontier orbitals energy level diagram of Al[214], Ca[214], ITO, PEDOT:PSS, PVK, PFO,[196] [Pt(salophen)] and [Pt(sal-3,4-ben)]. *T_1* energies bellow vacuum are marked in red.

Also, the WOLEDs performances were evaluated in terms of optical-electronic properties by current density, brightness, current and power efficiencies *vs.* V curves (Figure 4.15) and all data have summarized on the Table 4.5. As general trend, all ITO|PEDOT:PSS|PVK|PFO:Pt(salicylidenes)|Ca|Al OLEDs had better performances than the pure ITO|PEDOT:PSS|PVK|PFO|Ca|Al and their ITO|PEDOT:PSS|PVK:Pt(salicylidenes)|Ca|Al and its Zn(II) derivatives OLEDs. Comparing the two Pt(II) coordination compounds solution-processable WOLEDs the [Pt(sal-3,4-ben)] diodes have shown much better results in terms of all optical-electronic parameters, principally at 0.1 % mol/mol ratio into PFO matrix which was much better than other WOLEDs have made in this work, exhibiting V_{on} = 3.4 V, maximum luminance of L_{max} = 4000 cd m^{-2} at 9 V with chromaticity of x = 0.38 and y = 0.33 (white-emission region), and maxima current and power efficiencies of η_{curr} = 5.28 cd A^{-1} and η_P = 26.19 lm W^{-1} at 4.4 V in the red-emission region of the x,y CIE 1931 chromaticity diagram and in comparison to the PFO:Zn(salicylidenes), PVK:Pt(salicylidenes) OLEDs and PFO:[Pt(salophen)] WOLEDs at 0.1 % the benzophenone derivative has shown an increase about 6, 100 and 10 times of the device performance, respectively. Also, the increment of the Pt(salicylidene) into polymer host has diminished the WOLEDs performance, strongly, due to the morphological changes into PFO chains as it was observed in their PL and PLE spectra and in the PFO:Zn(salicylidenes) derivatives OLEDs.

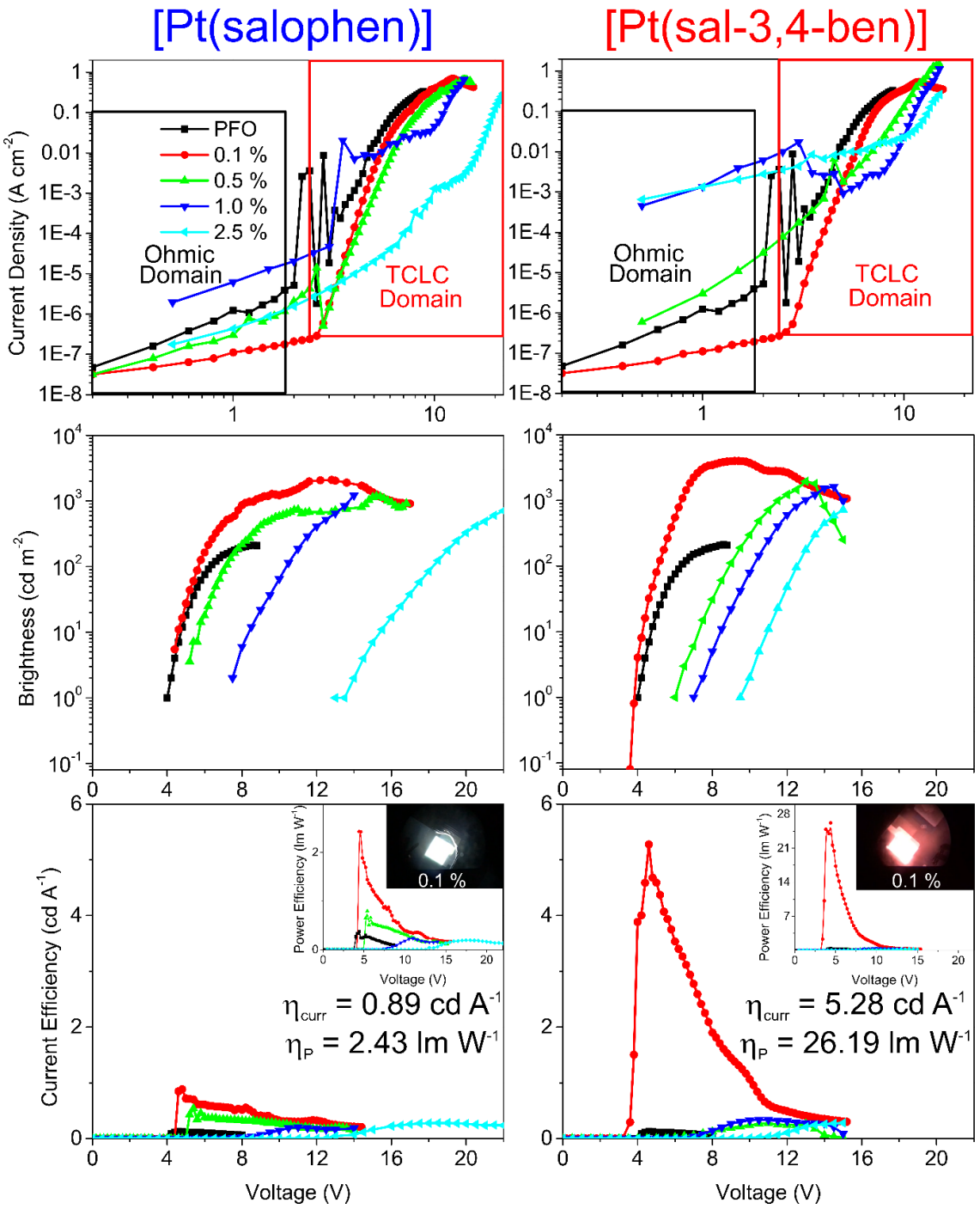

Figure 4. 15. Optical-electronic properties of the diodes ITO|PEDOT:PSS|PVK|PFO:Pt(salicylidenes)|Ca|Al: log-log Current density vs. voltage, brightness vs. voltage, current efficiency vs. voltage curves and power efficiency vs. voltage curves (inset).

Also, ITO|PEDOT:PSS|PVK|PFO:[Pt(sal-3,4-ben)] 0.1 % mol/mol|Ca|Al all solution-processable WOLED has exhibited a satisfactory power efficiency higher than an thermal-evaporated WOLED assembled with another Pt(salicylidene) derivative combined

with the **FIrpic** blue-phosphorescent molecule (η_P = 17 lm W^{-1} and CIE 1931 x = 0.34, y = 0.44)[151].

The HOMO/LUMO energy levels, as well as, the T_1 energy levels of the two Pt(salicylidenes) are quite similar and it was expected their WOLEDs with PFO have shown similar performances. [Pt(sal-3,4-ben)] has presented PLQY two times higher than [Pt(salophen)], which justifies its better performance. However, only this improvement does not able to explain its behavior. Thus, the hole mobilities of the PFO:Pt(salicylidenes) solution-processable WOLEDs have calculated, considering the TCLC model (equation 1.8) in order to clarify and to understand the diodes charge transport and performances, once it was observed a high trap level (m > 2) in these kind of WOLEDs.

The addition of 0.1 % mol/mol of the [Pt(sal-3,4-ben)] into polyfluorene host has increased the diodes hole mobility in two orders of magnitude ($\mu_{p(0.1)}$ = 1.1x10^{-1} cm^2 V^{-1} s^{-1}) in comparison neat PFO's OLED (μ_p = 1.2x10^{-3} cm^2 V^{-1} s^{-1}) and with the increase of the concentration of [Pt(sal-3,4-ben)], the WOLEDs charge carrier mobilities, drive voltage, luminance, and current and power efficiencies have diminished in comparison to the 0.1 % device: $\mu_{p(0.5\ \%)}$ = 9.8x10^{-2}, $\mu_{p(1.0\ \%)}$ = 1.1x10^{-3} and $\mu_{p(2.5\ \%)}$ = 5.8x10^{-5} cm^2 V^{-1} s^{-1}. All obtained values of charges carriers mobilities have decreased in the case of the ITO|PEDOT:PSS|PVK|PFO:[Pt(salophen)]|Ca|Al WOLEDs in contrast to the PFO:[Pt(sal-3,4-ben)] and pure PFO devices, and these observations are completely in agreement to the WOLEDs performances which have obtained from the JxV, LxV and ηxV curves. Beside this, charge carrier transport on the PFO:Pt(salicylidenes) WOLEDs were better than the PFO:Zn(salicylidenes) OLEDs and 2.5 % mol/mol concentration of the Pt(salicylidenes) has presented as a limit to obtain high-efficiency and color-tunable WOLEDs, equally to its Zn(II) derivatives diodes.

Taking into account those experimental and theoretical observations about the PVK:Pt(salicylidenes) OLEDs and PFO:Pt(salicylidenes) WOLEDs, a mechanism based on triplet harvesting phenomenon (Figure 4.16) has proposed in order to explain why the combinations of Pt(II) coordination compounds with polyfluorene conducting polymer exhibit much better performances than their PVK devices. As the coordination compounds are very diluted into polymer hosts, the most part of the charge carriers will be injected and transported by the conducting polymer and then transferred and recombined in the Pt(II) complexes. PVK and PFO host-polymers exhibit an intense fluorescence and the two matrices can undergo non-radiative energy transfer processes to the [Pt(salophen)] and [Pt(sal-3,4-ben)] via Förster

mechanism, which was the principal mechanism to the charge carrier transfer involving the donor and acceptor singlet-states. However, according to the spin-statistics only 25 % of the formed excitons via electrical field are singlets and the rest (75 %) are triplet. In the energy level diagram of the solution-processable OLEDs have presented the T_1 energy levels below vacuum of the active layer components (Figure 4.14) and according to this diagram the PVK T1 energy is smaller than the [Pt(salophen)] and [Pt(sal-3,4-ben)] about ΔE_{T_1} = 0.17 and 0.10 eV, respectively. Already in the PFO case the T_1 energy level is much higher than the T_1 level of the Pt(salicylidenes) and the difference between their T_1 energies are ΔE_{T_1} = -0.63 and 0.70 eV for [Pt(salophen)] and its benzophenone derivative, respectively. Therefore, only singlet excitons formed on the PVK in the ITO|PEDOT:PSS|PVK:Pt(salicylidenes)|Ca|Al OLEDs are transferred to the Pt(II) coordination compounds singlet level via FRET mechanism and the PVK triplet excitons do not transferred to the phosphorescent compounds and moreover the T_1 excitons formed in the [Pt(salophen)] and [Pt(sal-3,4-ben)] by ISC process (k_{ISC}; $S_1 \rightarrow T_1$) or directly injection on their T_1 state should be taken by PVK T_1 level via triplet harvesting mechanism (Dexter), so draining the Pt(salicylidenes) emissive triplet excitons (k_P) to a non-radiative triplet pathway (k_{nR}) and making PVK:Pt(salicylidenes) OLEDs inefficient. However, as PFO and Pt(salicylidenes) S_1 and T_1 levels are in perfect complementarity, all formed excitons into the conducting polymer chain are transferred to the Pt(II) coordination compounds via FRET and Dexter mechanism involving the singlet and triplet (triplet harvesting) states, respectively. Thus, localizing the emissive states on the phosphorescent emitters, and after the saturation of T_1 emissive states due to the limited concentration of the [Pt(salophen)] and [Pt(sal-3,4-ben)] into conducting polymer, PFO radiative singlet states (k_F) start to emit which enables the color tuning from red to blue, passing by the white-light emission region, and allowing us to get the most out of the active layer emissive states. Hence, high-efficient WOLEDs were obtained with PFO as host material, in contrast to PVK polymer, for Pt(salicylidenes) guests.

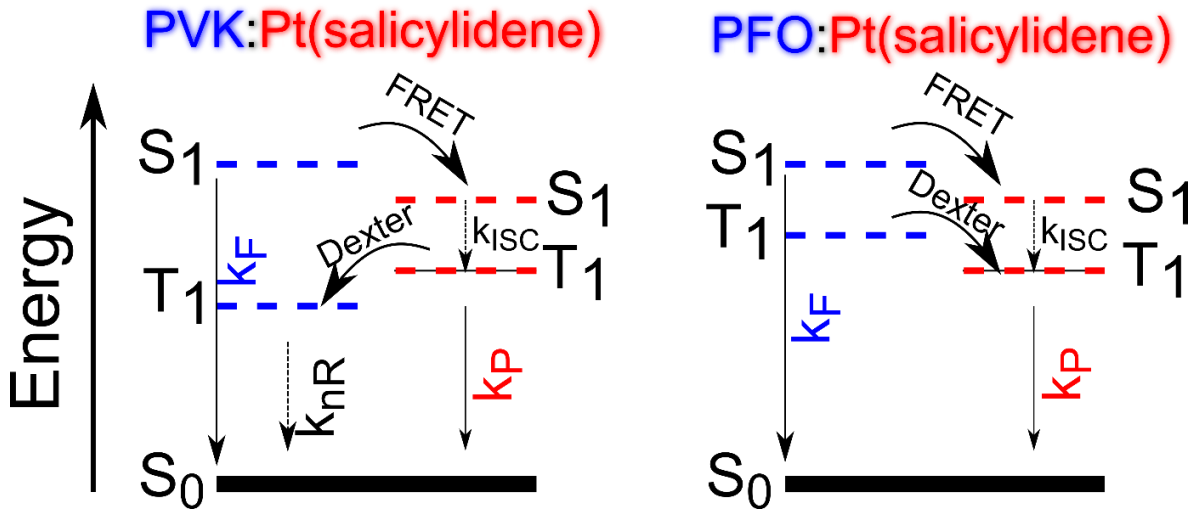

Figure 4. 16. Proposed mechanism for the influence of triplet harvesting processes on the high-efficiency all-solution-processable [Pt(salicylidene) WOLEDs in a simplified Jablonski diagram.

Table 4. 5. Optical-electronic properties of the solution-processed OLEDs of the PFO:Pt(II)salicylidenes composites OLEDs.

	E_H (eV)	E_L (eV)	E_{gap} (eV)	% (mol:mol)	λ_{EL}(nm)[a]	V_{on}	J (A cm^{-2})[a]	μ_p (cm^2 V^{-1} s^{-1})	L_{max} (cd m^{-2})	η_{curr} (cd A^{-1})	η_P (lm W^1)
PFO	-6.10	-2.10	3.42		425	4.0	$3x10^{-3}$	$1.2x10^{-3}$	213	0.13	0.37
[Pt(salophen)]	-5.60	-3.26	2.34	**0.1**	629	4.6	$6.46x10^{-4}$	$4.3x10^{-4}$	2092	0.89	2.43
				0.5	629	5.2	$4.69x10^{-3}$	$2.8x10^{-4}$	1189	0.54	0.80
				1.0	620	7.5	$9.25x10^{-2}$	$5.8x10^{-4}$	1214	0.20	0.23
				2.5	619	13.0	$6.37x10^{-2}$	$2.7x10^{-5}$	710	0.28	0.20
[Pt(sal-3,4-ben)]	-5.62	-3.29	2.33	**0.1**	643	3.4	$3.52x10^{-4}$	$1.0x10^{-1}$	4000	5.28	26.19
				0.5	639	5.5	0.264	$9.8x10^{-2}$	1950	0.27	0.41
				1.0	636	7.0	$4.33x10^{-2}$	$1.1x10^{-3}$	1622	0.33	0.31
				2.5	634	9.5	0.260	$5.8x10^{-5}$	722	0.27	0.24

[a]Values of the λ_{EL} and J were obtained at maximum η_{curr} and η_P.

4.4 Conclusions

This chapter of the Ph.D. thesis, we synthetized and characterized structurally a new phosphorescent Pt(II) coordination compound assembled with salicylidene ligand, the [Pt(sal-3,4-ben)], by ^{1}H and ^{13}C NMR and FT-IR spectra, HRTOF-MS spectrometry, elemental analysis and single-crystal X-ray diffraction and its optical properties were evaluated in comparison to the [Pt(salophen)] coordination complex. These coordination compounds have exhibited a planar square coordination geometry, which will directly impact in their photophysics, due to its great planarity and rigidity on the molecular framework. Steady-state and transient photophysical properties were obtained in terms electronic absorption, photoluminescence and phosphorescence decays and the results have shown an increase of the PLQY and ε after benzophenone insertion on the Pt(II) coordination compound framework, PLQY increases from 47 to 76 %. This improvement of optical properties of the [Pt(sal-3,4-ben)] is connected to the benzophenone electron acceptor effect on the excited-state, which was correlated in agreement to the calculated vertical excitation energies and NTOs under relativistic DFT and TD-DFT framework at PBE0/(ZORA-def2-TVZP(C,N,O,H) and SARC-Pt) level in vacuum, being the electronic transition of the first singlet state (HOMO → LUMO) composed mainly by ILCT/MLCT and ILCT/MLCT/MC for [Pt(salophen)] and [Pt(sal-3,4-ben)], respectively, with contribution of the filled $5d_{x-y}$ Pt(II) orbital on the ground state for the two coordination compounds and the unoccupied $5d_{x^2-y^2}$ orbital as consequence of the benzophenone effect. Also, combining steady-state and the phosphorescence dynamics and using rate equations it was possible to determine the radiative and non-radiative rates pathways, including a qualitative evaluation of $k_{^3O_2}[^3O_2]$ for the Pt(salicylidenes) that presented high sensibility to $^3O_2$ molecules. Thus, these coordination compounds may be applied as $O_2(g)$ sensor and sensitizer.

After careful photophysical characterization, [Pt(salophen)] and [Pt(sal-3,4-ben)] phosphorescent OLEDs were assembled via solution-processable protocols as the following diodes architectures: ITO|PEDOT:PSS|PVK:Pt(salicylidenes) 2.5 % (mol/mol)|Ca|Al; and ITO|PEDOT:PSS|PVK|PFO:Pt(salicylidenes) 0.1, 0.5, 1.0 and 2.5 % (mol/mol)|Ca|Al. First results were obtained from Pt(II) coordination compounds composites with PVK at 2.5 % mol/mol ratios were frustrating and the PVK:[Pt(salophen)] and PVK:[Pt(sal-3,4-ben)] OLEDs have shown performances in terms of optical-electronic properties less than the its Zn(II) analogues due to triplet harvesting processes from the Pt(salicylidenes) T_1 emissive state to the

carbazole conducting polymer T_1 non-emissive state, which leaded to the obtention of poorly electroluminescent devices even using phosphorescent material as active matrix. However, when Pt(salicylidenes) were dispersed into the polyfluorene conducting polymer (PFO) all optical-electronic performances parameters of the [Pt(salophen)] and [Pt(sal-3,4-ben)] have improved in comparison to its PVK OLEDs. These devices exhibited a strong color emission dependence with the applied electrical field, as well as, the concentration of the coordination compounds in the PFO polymer, leading color-tunable WOLEDs from the red EL emission of the coordination complex (low voltages), passing by true white EL (work voltages) and finally blue-greenish EL of the PFO (high voltages). Beside this, the WOLEDs exhibited highest efficiencies in comparison to its PVK and Zn(II)salicylidenes OLEDs, principally the ITO|PEDOT:PSS|PVK|PFO:[Pt(sal-3,4-ben)] 0.1 % (mol/mol)|Ca|Al. A behavior completely in agreement to the [Pt(sal-3,4-ben)] photophysical properties, theoretical calculations and the calculated charge carrier mobilities by TCLC model. Finally, the alignment of the S_1 and T_1 levels of the PFO with the Pt(salicylidenes) derivatives allowed energy and charge transfer (triplet harvesting) from the conducting polymer to the phosphorescent coordination compounds, which enabled the achievement of the high-efficiencies WOLEDs.

CHAPTER 5

FINAL REMARKS

5.1 Final Remarks

Novel and simple strategies for the improvement of some salicylidene derivatives (salophen, sal-3,4-ben and sal-5Cl-py) and their Zn(II) ([Zn(salophen)] and [Zn(sal-3,4-ben)]) and Pt(II) ([Pt(salophen)] and [Pt(sal-3,4-ben)]) coordination compounds in all solution-processed active matrix OLEDs were successfully done by easy chemical modifications on the ligand framework and manipulating the charge carrier mobility and PLQY of the host conducting polymer (PVK and PFO).

Excited state intramolecular proton transfer of the sal-5Cl-py and sal-3,4-ben were evaluated by steady-state (electronic absorption and PL) and transient (femtosecond transient absorption, fluorescence decays and TRES) electronic spectroscopies techniques and they exhibited a very reactive ESIPT process in contrast to salophen, which enabled white-light generation from a single organic chromophore. This phenomenon was directly linked to insertion of the benzophenone and 5-chloro-pyridine substituent into salicylidene framework and it was proven by theoretical predictions according to DFT/TD-DFT ab-initio calculation level. Thus, as proof of concept an electroemissive diode based on PVK:sal-5Cl-py active layer was employed and it was possible to achieve a WOLED. However, its diode exhibited very poor EL properties.

The coordination of Zn(II) cation into salophen and sal-3,4-ben ligands enhanced the salicylidene photophysical properties. An effect completely linked to the planarization of the coordination site due to the insertion of the Zn(II) atom into salicylidene molecules, which increased the charge delocalization along the π framework of the ligand around the coordination site, as the calculated NTOs h^+ and p^- pairs electronic densities exhibited according to TD-DFT excited state calculations at PBE0/6-311++G(d,p) level. The [Zn(salophen)] and [Zn(sal-3,4-ben)] solution-processed OLEDs into PVK matrix have shown better performances in comparison to their free-ligands and the diode ITO|PEDOT:PSS|PVK:[Zn(sal-3,4-ben)] 2.5 % mol/mol|Ca|Al efficiencies comparable of those 8-hydroxyquinolinate derivatives (Alq_3 and Znq_2) devices assembled at the same conditions, as consequence of the Zn(II) coordination, FRET process from PVK to coordination compounds and the increase of the hole mobility on the diode by to the insertion of the benzophenone moiety in the [Zn(salophen)] system. PVK host was substituted by the PFO conducting polymer in order to obtain better optical-electronic properties due to the modification of the charge mobility and photoluminescence quantum yield of host material. Also, the concentration of the Zn(salicylidene) into the PFO matrix (0.1, 0.5,

1.0 and 2.5 % mol/mol) was studied to understand its impact on the device color and performance and to correlate with the morphological changes into active matrix, being 1.0 % mol/mol a concentration threshold. Thereby, an improvement about twenty two times of the Zn(salicylidenes) solution-processable OLEDs performance was obtained in comparison to its PVK devices and pure PFO PLED, highlighted the ITO|PEDOT:PSS|PVK|PFO:[Zn(sal-3,4-ben)] 0.1 % mol/mol|Ca|Al diode performance: V_{on} = 4.0 V, μ_p = 2.5x10^{-2} cm^2 V^{-1} s^{-1}, L_{max} = 748 cd m^{-2}, η_{curr} = 0.52 cd A^{-1} and η_P = 1.16 lm W^{-1}. However, the EL emission of these solution-processed OLEDs were dominated by the Zn(II) coordination compounds emission, leading to the achievement of green-yellowish diodes.

Thus, in order to achieve high-efficient and color-tunable WOLEDs the [Pt(salophen)] and [Pt(sal-3,4-ben)] red-emitters were synthetized, characterized and blended with PVK or PFO blue-fluorescent conducting polymers at 2.5 % and 0.1, 0.5, 1.0 and 2.5 % mol/mol, respectively, to obtain their active layers. According to their photophysical characterization the coordination of Pt(II) provided a phosphorescence emission behavior in the salicylidene molecules due to the spin-orbit coupling, presenting a strong $^3O_2$(g) sensitization. [Pt(sal-3,4-ben)] (PLQY = 76 %) has shown a high PLQY in comparison to the [Pt(salophen)] (PLQY = 47 %) complex by the benzophenone electron acceptor effect on the excited state. A behavior completely in agreement to the theoretical calculation done at relativistic DFT/TD-DFT level (at PBE0/(ZORA-def2-TVZP(C,N,O,H) and SARC-Pt)). Also, their first singlet electronic transition (HOMO $\rightarrow$ LUMO) exhibited a strong mixed ILCT/MLCT and ILCT/MLCT/MC character for the [Pt(salophen)] and [Pt(sal-3,4-ben)], respectively, which allows the $S_1 \rightarrow T_1$ (ISC process) in these coordination compounds, as presented in their NTOs densities. The PVK:[Pt(salophen)] and PVK:[Pt(sal-3,4-ben)] solution-processed OLEDs have shown a high red-color purity. However, PVK:Pt(salicylidene) devices presented frustrating results in terms of their performances even in comparison to PVK:Zn(salicylidene) OLEDs due to the deactivation of the Pt(II) complexes T_1 emissive state by triplet harvesting from coordination compounds to the non-emissive PVK's T_1 state. In contrast to the PVK:Pt(salicylidene) devices the PFO:[Pt(salophen)] and PFO:[Pt(sal-3,4-ben)] solution-processed emissive diodes were exhibited a completely different behavior: due to the S_1 and T_1 energy levels of the PFO have a perfect alignment with the [Pt(salophen)] and [Pt(sal-3,4-ben)] singlet and triplet states, the formed excitons on the active layer were concentrated in the phosphorescent coordination compound by FRET energy transfer and triplet harvesting from the blue-fluorescent conducting polymer to the Pt(salicylidene) derivatives. Furthermore, the

addition of the [Pt(sal-3,4-ben)] into the PFO matrix considerably increased the devices hole mobilities in comparison to [Pt(salophen)] and [Zn(sal-3,4-ben)] at the same conditions, which were obtained from TCLC model. Thus, color-tunable and high-efficient WOLEDs were obtained, highlighting the ITO|PEDOT:PSS|PVK|PFO:[Pt(sal-3,4-ben)] 0.1 % mol/mol|Ca|Al device: V_{on} = 3.4 V, μ_p = 1.0x10^{-1} cm^2 V^{-1} s^{-1}, L_{max} = 4000 cd m^{-2}, η_{curr} = 5.28 cd A^{-1}, η_P = 26.19 lm W^{-1} and CIE 1931 x = 0.33, y =0.33.

Therefore, with a small and ease molecular modification and combining an accurate blue-fluorescent conducting polymer (PFO) with a red-phosphorescent Pt(II) coordination compound has been possible to make a high-efficiency and color-tunable WOLEDs with a low-cost and environmental-friendly deposition technique (solution-processable), in contrast to common paper thermal-evaporated WOLEDs.

6. REFERENCES

(1) Akcelrud, L. Electroluminescent Polymers. *Prog. Polym. Sci.* **2003**, *28* (6), 875–962.

(2) Kim, F. S.; Ren, G.; Jenekhe, S. a. One-Dimensional Nanostructures of π-Conjugated Molecular Systems: Assembly, Properties, and Applications from Photovoltaics, Sensors, and Nanophotonics to Nanoelectronics. *Chem. Mater.* **2011**, *23* (3), 682–732.

(3) Casalini, S.; Bortolotti, C. A.; Leonardi, F.; Biscarini, F.; Dimitrakopoulos, C. D.; Malenfant, P. R. L.; Whitesides, G. M.; Grzybowski, B.; Zhang, S.; Bigelow, W. C.; et al. Self-Assembled Monolayers in Organic Electronics. *Chem. Soc. Rev.* **2016**, *14*, 99–117.

(4) Bright, A. A.; Cohen, M. J.; Garito, A. F.; Heeger, A. J.; Mikulski, C. M.; MacDiarmid, A. G. Epitaxial Crystalline Films of the Metallic Polymer (SN)X. *Appl. Phys. Lett.* **1975**, *26* (11), 612–615.

(5) Ito, T.; Shirakawa, H.; Ikeda, S. Simultaneous Polymerization and Formation of Polyacetylene Film on the Surface of Concentrated Soluble Ziegler-Type Catalyst Solution. *J. Polym. Sci. Part A Polym. Chem.* **1996**, *34* (13), 2533–2542.

(6) Irimia-Vladu, M. "Green" Electronics: Biodegradable and Biocompatible Materials and Devices for Sustainable Future. *Chem. Soc. Rev.* **2014**, *43* (2), 588–610.

(7) Li, P.; Zheng, Y.; Li, M.; Fan, W.; Shi, T.; Wang, Y.; Zhang, A.; Wang, J. Enhanced Flame-Retardant Property of Epoxy Composites Filled with Solvent-Free and Liquid-like Graphene Organic Hybrid Material Decorated by Zinc Hydroxystannate Boxes. *Compos. Part A Appl. Sci. Manuf.* **2016**, *81*, 172–181.

(8) Parrenin, L.; Brochon, C.; Hadziioannou, G.; Cloutet, E. Low Bandgap Semiconducting Copolymer Nanoparticles by Suzuki Cross-Coupling Polymerization in Alcoholic Dispersed Media. *Macromol. Rapid Commun.* **2015**, *36* (20), 1816–1821.

(9) Farinola, G. M.; Ragni, R. Electroluminescent Materials for White Organic Light Emitting Diodes. *Chem. Soc. Rev.* **2011**, *40* (7), 3467–3482.

(10) Web of Science [v.5.27] - Organic Light-Emitting Diodes - Todas as bases de dados - Relatório de citações http://apps.webofknowledge.com/CitationReport.do?product=UA&search_mode=CitationReport&SID=8AseeyYGBZCXflJbe2G&page=1&cr_pqid=1&viewType=summary (accessed Jan 31, 2018).

(11) Kim, S.; Kwon, H. J.; Lee, S.; Shim, H.; Chun, Y.; Choi, W.; Kwack, J.; Han, D.; Song,

M.; Mohammadi, S.; et al. Low-Power Flexible Organic Light-Emitting Diode Display Device. *Adv. Mater.* **2011**, *23* (31), 3511–3516.

(12) Pope, M.; Kallmann, H. P.; Magnante, P. Electroluminescence in Organic Crystals. *J. Chem. Phys.* **1963**, *38* (8), 2042.

(13) Kelley, T. W.; Baude, P. F.; Gerlach, C.; Ender, D. E.; Muyres, D.; Haase, M. A.; Vogel, D. E.; Theiss, S. D. Recent Progress in Organic Electronics: Materials, Devices, and Processes. *Chemistry of Materials*. American Chemical Society 2004, pp 4413–4422.

(14) Zhao, F.; Ma, D. Approaches to High Performance White Organic Light-Emitting Diodes for General Lighting. *Mater. Chem. Front.* **2017**.

(15) Höfle, S.; Schienle, A.; Bernhard, C.; Bruns, M.; Lemmer, U.; Colsmann, A. Solution Processed, White Emitting Tandem Organic Light-Emitting Diodes with Inverted Device Architecture. *Adv. Mater.* **2014**, *26* (30), 5155–5159.

(16) de Azevedo, D.; Freitas, J. N.; Domingues, R. A.; Faleiros, M. M.; de Almeida Santos, T. E. E.; Atvars, T. D. Z. Tuning the Emission Color of a Single-Layer Polymer Light-Emitting Diode with a Solution-Processed External Layer. *Synth. Met.* **2016**, *222*, 205–210.

(17) Pope, M.; Kallmann, H. P.; Magnante, P. Electroluminescence in Organic Crystals. *J. Chem. Phys.* **1963**, *38* (8), 2042–2043.

(18) Partridge, R. H. Electroluminescence from Polyvinylcarbazole Films: 1. Carbazole Cations. *Polymer (Guildf).* **1983**, *24* (6), 733–738.

(19) Partridge, R. H. Electroluminescence from Polyvinylcarbazole Films: 2. Polyvinylcarbazole Films Containing Antimony Pentachloride. *Polymer (Guildf).* **1983**, *24* (6), 739–747.

(20) Partridge, R. H. Electroluminescence from Polyvinylcarbazole Films: 3. Electroluminescent Devices. *Polymer (Guildf).* **1983**, *24* (6), 748–754.

(21) Partridge, R. H. Electroluminescence from Polyvinylcarbazole Films: 4. Electroluminescence Using Higher Work Function Cathodes. *Polymer (Guildf).* **1983**, *24* (6), 755–762.

(22) Tang, C. W.; Vanslyke, S. A. Organic Electroluminescent Diodes. *Appl. Phys. Lett.* **1987**, *51* (12), 913–915.

(23) Web of Science [v.5.29] - Todas as bases de dados Análise de resultados http://wcs.webofknowledge.com/RA/analyze.do (accessed May 28, 2018).

(24) Evans, R. C.; Douglas, P.; Winscom, C. J. Coordination Complexes Exhibiting Room-

Temperature Phosphorescence: Evaluation of Their Suitability as Triplet Emitters in Organic Light Emitting Diodes. *Coord. Chem. Rev.* **2006**, *250* (15–16), 2093–2126.

(25) Xu, H.; Chen, R.; Sun, Q.; Lai, W.; Su, Q.; Huang, W.; Liu, X. Recent Progress in Metal-Organic Complexes for Optoelectronic Applications. *Chem. Soc. Rev.* **2014**, *43* (10), 3259–3302.

(26) Zheng, S.-L.; Chen, X.-M. Recent Advances in Luminescent Monomeric, Multinuclear, and Polymeric Zn(II) and Cd(II) Coordination Complexes. *Aust. J. Chem.* **2004**, *57* (8), 703.

(27) Vivas, M. G.; Germino, J. C.; Barboza, C. A.; Vazquez, P. A. M. M.; De Boni, L.; Atvars, T. D. Z. Z.; Mendonça, C. R. Excited-State and Two-Photon Absorption in Salicylidene Molecules: The Role of Zn(II) Planarization. *J. Phys. Chem. C* **2016**, *120* (7), 4032–4039.

(28) Germino, J. C.; de Freitas, J. N.; Domingues, R. A.; Quites, F. J.; Feleiros, M. M.; Atvars, T. D. Z. Organic Light-Emitting Diodes Based on PVK and Zn(II) Salicylidene Composites. *Synth. Met.* **2018**, *241*, 7–16.

(29) Nakanotani, H.; Higuchi, T.; Furukawa, T.; Masui, K.; Morimoto, K.; Numata, M.; Tanaka, H.; Sagara, Y.; Yasuda, T.; Adachi, C. High-Efficiency Organic Light-Emitting Diodes with Fluorescent Emitters. *Nat. Commun.* **2014**, *5* (May), 4016.

(30) Sun, J. W.; Lee, J.; Moon, C.; Kim, K.; Shin, H.; Kim, J. A Fluorescent Organic Light-Emitting Diode with 30 % External Quantum Effi Ciency. *Adv. Mater.* **2014**, *26*, 5684–5688.

(31) Lee, S. E.; Lee, H. W.; Lee, D. H.; Yang, H. J.; Lee, S. J.; Koo, J.-R.; Kim, H. J.; Yoon, S. S.; Kim, Y. K. Enhanced Hybrid Blue Organic Light Emitting Diodes with a Multi-Emitting Layer Using Fluorescent and Phosphorescent Emitters. *Mol. Cryst. Liq. Cryst.* **2014**, *601* (1), 223–230.

(32) Bullock, J. D.; Salehi, A.; Zeman, C. J.; Abboud, K. A.; So, F.; Schanze, K. S. In Search of Deeper Blues: Trans-N-Heterocyclic Carbene Platinum Phenylacetylide as a Dopant for Phosphorescent OLEDs. *ACS Appl. Mater. Interfaces* **2017**, *9* (47), 41111–41114.

(33) Baldo, M. A.; Thompson, M. E.; Forrest, S. R. Phosphorescent Materials for Application to Organic Light Emitting Devices. *Pure Appl. Chem.* **1999**, *71* (11), 2095–2106.

(34) Reineke, S.; Thomschke, M.; Lüssem, B.; Leo, K. White Organic Light-Emitting Diodes: Status and Perspective. *Rev. Mod. Phys.* **2013**, *85* (3), 1245–1293.

(35) Im, Y.; Byun, S. Y.; Kim, J. H.; Lee, D. R.; Oh, C. S.; Yook, K. S.; Lee, J. Y. Recent

Progress in High-Efficiency Blue-Light-Emitting Materials for Organic Light-Emitting Diodes. *Adv. Funct. Mater.* **2017**, *27* (13), 1603007.

(36) Müller, C.; Salzmann, I. MRS Fall 2017 Symposium: Organic Semiconductors—Surface, Interface, Bulk Doping, and Charge Transport. *Chem. Mater.* **2018**, *30* (10), 3151–3154.

(37) Wong, M. Y.; Zysman-Colman, E. Purely Organic Thermally Activated Delayed Fluorescence Materials for Organic Light-Emitting Diodes. *Adv. Mater.* **2017**, *29* (22), 1605444.

(38) Du, B. S.; Liao, J. L.; Huang, M. H.; Lin, C. H.; Lin, H. W.; Chi, Y.; Pan, H. A.; Fan, G. L.; Wong, K. T.; Lee, G. H.; et al. Os(II) Based Green to Red Phosphors: A Great Prospect for Solution-Processed, Highly Efficient Organic Light-Emitting Diodes. *Adv. Funct. Mater.* **2012**, *22* (16), 3491–3499.

(39) Oner, I.; Sahin, C.; Varlikli, C. Electroluminescence from Two New Ruthenium(II) Complexes as Phosphorescent Dopant: Positive Effect of Swallow-Tail Bipyridyl Ligand. *Dye. Pigment.* **2012**, *95* (1), 23–32.

(40) Barron, J. A.; Bernhard, S.; Houston, P. L.; Abruña, H. D.; Ruglovsky, J. L.; Malliaras, G. G. Electroluminescence in Ruthenium(II) Dendrimers. *J. Phys. Chem. A* **2003**, *107* (40), 8130–8133.

(41) Mizoguchi, S. K.; Santos, G.; Andrade, A. M.; Fonseca, F. J.; Pereira, L.; Murakami Iha, N. Y. Luminous Efficiency Enhancement of PVK Based OLEDs with Fac-[ClRe(CO) 3(Bpy)]. *Synth. Met.* **2011**, *161* (17–18), 1972–1975.

(42) Lepnev, L.; Vaschenko, A.; Vitukhnovsky, A.; Eliseeva, S.; Kotova, O.; Kuzmina, N. OLEDs Based on Some Mixed-Ligand Terbium Carboxylates and Zinc Complexes with Tetradentate Schiff Bases: Mechanisms of Electroluminescence Degradation. *Synth. Met.* **2009**, *159* (7–8), 625–631.

(43) Turchetti, DA1,5; Domingues, R.; ; Freitas, J.; ; Azevedo, D.; ; Duarte, L.; ; Germino, J.; ; Atvars, T.; ; Akcelrud, L.; 1. Photo- and Electroluminescence Behavior of a Polyfluorene Derivative Containing Complexed Europium Ions. *J. Lumin.* **2018**, *201*, 290–297.

(44) Tang, M. C.; Tsang, D. P. K.; Wong, Y. C.; Chan, M. Y.; Wong, K. M. C.; Yam, V. W. W. Bipolar Gold(III) Complexes for Solution-Processable Organic Light-Emitting Devices with a Small Efficiency Roll-Off. *J. Am. Chem. Soc.* **2014**, *136* (51), 17861–17868.

(45) Zhang, J.; Duan, C.; Han, C.; Yang, H.; Wei, Y.; Xu, H. Balanced Dual Emissions from Tridentate Phosphine-Coordinate Copper(I) Complexes toward Highly Efficient Yellow OLEDs. *Adv. Mater.* **2016**, *28* (28), 5975–5979.

(46) Choy, W. C. H.; Chan, W. K.; Yuan, Y. Recent Advances in Transition Metal Complexes and Light-Management Engineering in Organic Optoelectronic Devices. *Adv. Mater.* **2014**, *26* (31), 5368–5399.

(47) Gather, M. C.; Köhnen, A.; Meerholz, K. White Organic Light-Emitting Diodes. *Adv. Mater.* **2011**, *23* (2), 233–248.

(48) Mukherjee, S.; Thilagar, P. Organic White-Light Emitting Materials. *Dye. Pigment.* **2014**, *110*, 2–27.

(49) Sun, D.; Ren, Z.; Yan, S. Efficient Triplet Utilization in Conventional Solution-Processed Phosphorescent Organic Light Emitting Diodes Using a Thermal Activated Delayed Fluorescence Polymer as an Assistant Host. *J. Mater. Chem. C* **2018**, *6* (17), 4800–4806.

(50) Yang, X.; Yao, C.; Zhou, G. Highly Efficient Phosphorescent Materials Based on Platinum Complexes and Their Devices (OLEDs). *Platin. Met. Rev.* **2013**, *57* (1), 2–16.

(51) Kalinowski, J.; Fattori, V.; Cocchi, M.; Williams, J. A. G. Light-Emitting Devices Based on Organometallic Platinum Complexes as Emitters. *Coord. Chem. Rev.* **2011**, *255* (21–22), 2401–2425.

(52) Aizawa, N.; Pu, Y.-J.; Watanabe, M.; Chiba, T.; Ideta, K.; Toyota, N.; Igarashi, M.; Suzuri, Y.; Sasabe, H.; Kido, J.; et al. Solution-Processed Multilayer Small-Molecule Light-Emitting Devices with High-Efficiency White-Light Emission. *Nat. Commun.* **2014**, *5*, 5756.

(53) Fu, H.; Cheng, Y.-M.; Chou, P.-T.; Chi, Y. Feeling Blue? Blue Phosphors for OLEDs. *Mater. Today* **2011**, *14* (10), 472–479.

(54) Erickson, N. C.; Holmes, R. J. Highly Efficient, Single-Layer Organic Light-Emitting Devices Based on a Graded-Composition Emissive Layer. *Appl. Phys. Lett.* **2010**, *97* (8), 083308.

(55) Chou, H. H.; Cheng, C. H. A Highly Efficient Universal Bipolar Host for Blue, Green, and Red Phosphorescent OLEDs. *Adv. Mater.* **2010**, *22* (22), 2468–2471.

(56) Kondakova, M. E.; Deaton, J. C.; Pawlik, T. D.; Giesen, D. J.; Kondakov, D. Y.; Young, R. H.; Royster, T. L.; Comfort, D. L.; Shore, J. D. Highly Efficient Fluorescent-Phosphorescent Triplet-Harvesting Hybrid Organic Light-Emitting Diodes. *J. Appl.*

Phys. **2010**, *107* (1), 014515.

(57) Yam, V. W.-W.; Au, V. K.-M.; Leung, S. Y.-L. Light-Emitting Self-Assembled Materials Based on d ^{8} and d ^{10} Transition Metal Complexes. *Chem. Rev.* **2015**, *115* (15), 7589–7728.

(58) Bolink, H. J.; De Angelis, F.; Baranoff, E.; Klein, C.; Fantacci, S.; Coronado, E.; Sessolo, M.; Kalyanasundaram, K.; Grätzel, M.; Nazeeruddin, M. K. White-Light Phosphorescence Emission from a Single Molecule: Application to OLED. *Chem. Commun.* **2009**, *0* (31), 4672.

(59) Kulkarni, A. P.; Tonzola, C. J.; Babel, A.; Jenekhe, S. a. Electron Transport Materials for Organic Light-Emitting Diodes. *Chem. Mater.* **2004**, *16* (23), 4556–4573.

(60) Shinar, J. *Organic Light-Emitting Devices : A Survey*; Springer, 2004.

(61) Hopkins, T. A.; Meerholz, K.; Shaheen, S.; Anderson, M. L.; Schmidt, A.; Kippelen, B.; Padias, A. B.; Hall, H. K.; Peyghambarian, N.; Armstrong, N. R. Substituted Aluminum and Zinc Quinolates with Blue-Shifted Absorbance/Luminescence Bands: Synthesis and Spectroscopic, Photoluminescence, and Electroluminescence Characterization. *Chem. Mater.* **1996**, *8* (2), 344–351.

(62) Taiju Tsuboi1, Yosuke Nakai, Y. T. Photoluminescence of Bis(8-Hydroxyquinoline) Zinc (Znq2) and Magnesium (Mgq2). *Cent. Eur. J. Phys. @BULLET* **2012**, *10* (2), 524–528.

(63) Tachibana, H.; Aizawa, N.; Hidaka, Y.; Yasuda, T. Tunable Full-Color Electroluminescence from All-Organic Optical Upconversion Devices by Near-Infrared Sensing. *ACS Photonics* **2017**, *4* (2), 223–227.

(64) Wang, H.; Xu, B.; Liu, X.; Zhou, H.; Hao, Y.; Xu, H.; Chen, L. A Novel Blue-Light Organic Electroluminescence Material Derived from 8-Hydroxyquinoline Lithium. *Org. Electron.* **2009**, *10* (5), 918–924.

(65) Dodabalapur, A. Organic Light Emitting Diodes. *Solid State Commun.* **1997**, *102* (2–3), 259–267.

(66) Zhang, R.; Li, Y.; Duan, L.; Zhang, D.; Qiu, Y. Efficient Organic Light-Emitting Diode Using Lithium Tetra-(8-Hydroxy-Quinolinato) Boron as the Electron Injection Layer. *Acta Phys. - Chim. Sin.* **2007**, *23* (4), 455–458.

(67) Tao, X. T.; Suzuki, H.; Wada, T.; Miyata, S.; Sasabe, H. Highly Efficient Blue Electroluminescence of Lithium Tetra-(2-Methyl-8- Hydroxy-Quinolinato) Boron [1]. *Journal of the American Chemical Society*. American Chemical Society 1999, pp 9447–

9448.

(68) Wang, R.; Deng, L.; Fu, M.; Cheng, J.; Li, J. Novel ZnII Complexes of 2-(2-Hydroxyphenyl)Benzothiazoles Ligands: Electroluminescence and Application as Host Materials for Phosphorescent Organic Light-Emitting Diodes. *J. Mater. Chem.* **2012**, *22* (44), 23454.

(69) Dumur, F.; Beouch, L.; Tehfe, M.-A.; Contal, E.; Lepeltier, M.; Wantz, G.; Graff, B.; Goubard, F.; Mayer, C. R.; Lalevée, J.; et al. Low-Cost Zinc Complexes for White Organic Light-Emitting Devices. *Thin Solid Films* **2014**, *564*, 351–360.

(70) Li, Z.; Dellali, A.; Malik, J.; Motevalli, M.; Nix, R. M.; Olukoya, T.; Peng, Y.; Ye, H.; Gillin, W. P.; Hernández, I.; et al. Luminescent Zinc(II) Complexes of Fluorinated Benzothiazol-2-Yl Substituted Phenoxide and Enolate Ligands. *Inorg. Chem.* **2013**, *52* (3), 1379–1387.

(71) Yuan, G.; Huo, Y.; Nie, X.; Jiang, H.; Liu, B.; Fang, X.; Zhao, F. Controllable Supramolecular Structures and Luminescent Properties of Unique Trimeric Zn(Ii) 8-Hydroxyquinolinates Tuned by Functional Substituents. *Dalt. Trans.* **2013**, *42* (8), 2921–2929.

(72) Ho, K.-Y.; Yu, W.-Y.; Cheung, K.-K.; Che, C.-M. Blue Luminescent Zinc(II) Complexes with Polypyridylamine Ligands: Crystal Structures and Luminescence Properties. *J. Chem. Soc. Dalt. Trans.* **1999**, *0* (10), 1581–1586.

(73) Yeh, A. Synthesis and Electroluminescent Property of Bis (2-(Benzimidazol-2-Yl) Quinolinato) Zinc. *Mater. Lett.* **2005**, *59* (14–15), 1811–1814.

(74) Xu, X.; Liao, Y.; Yu, G.; You, H.; Di, C.; Su, Z.; Ma, D.; Wang, Q.; Li, S.; Wang, S.; et al. Charge Carrier Transporting, Photoluminescent, and Electroluminescent Properties of Zinc(II)-2-(2-Hydroxyphenyl)Benzothiazolate Complex. *Chem. Mater.* **2007**, *19* (7), 1740–1748.

(75) Mirabella, S.; Oliveri, I. P.; Ruffino, F.; Maccarrone, G.; Di Bella, S. Low-Cost Chemiresistive Sensor for Volatile Amines Based on a 2D Network of a Zinc(II) Schiff-Base Complex. *Appl. Phys. Lett.* **2016**, *109* (14), 143108.

(76) Irimia-Vladu, M.; Głowacki, E. D.; Voss, G.; Bauer, S.; Sariciftci, N. S. Green and Biodegradable Electronics. *Mater. Today* **2012**, *15* (7–8), 340–346.

(77) Toolan, D. T. W.; Howse, J. R. Development of in Situ Studies of Spin Coated Polymer Films. *J. Mater. Chem. C* **2013**, *1* (4), 603–616.

(78) Kraft, A.; Grimsdale, A. C.; Holmes, A. B. Electroluminescent Conjugated Polymers—

Seeing Polymers in a New Light. *Angew. Chemie Int. Ed.* **1998**, *37* (4), 402–428.

(79) Bradley, D. D. C.; Brown, A. R.; Burn, P. L.; Burroughes, J. H.; Friend, R. H.; Holmes, A. B.; Mackay, K. D.; Marks, R. N. Light Emission from Poly(p-Phenylene Vinylene): A Comparison between Photo- and Electro-Luminescence. *Synth. Met.* **1991**, *43* (1–2), 3135–3141.

(80) Burn, P. L.; Holmes, A. B.; Kraft, A.; Bradley, D. D. C.; Brown, A. R.; Friend, R. H. Synthesis of a Segmented Conjugated Polymer-Chain Giving a Blue-Shifted Electroluminescence and Improved Efficiency. *J. Chem. Soc. Commun.* **1992**, *0* (1), 32–34.

(81) Burn, P. L.; Holmes, A. B.; Kraft, A.; Bradley, D. D. C.; Brown, A. R.; Friend, R. H.; Gymer, R. W. Chemical Tuning of Electroluminescent Copolymers to Improve Emission Efficiencies and Allow Patterning. *Nature* **1992**, *356* (6364), 47.

(82) Swanson, L. S.; Shinar, J.; Burn, P. L.; Kraft, A.; Holmes, A. B. Ames Laboratory - USDOE and Physics Department, Iowa State University, Ames, IA 50011. *Energy* **1993**, *57* (1), 241–248.

(83) Kraft, A.; Burn, P. L.; Holmes, A. B.; Bradley, D. D. C.; Brown, A. R.; Friend, R. H.; Gymer, R. W. Chemical Control of Colour and Electroluminescent Device Efficiency in Copolymeric Poly(Arylenevylenes). *Synth. Met.* **1993**, *55* (2–3), 936–941.

(84) Greenham, N. C.; Moratti, S. C.; Bradley, D. D. C.; Friend, R. H.; Holmes, A. B. Efficient Light-Emitting Diodes Based on Polymers with High Electron Affinities. *Nature* **1993**, *365* (6447), 628–630.

(85) Burn, P. L.; Kraft, A.; Holmes, A. B.; Jackson, R. W.; Baigent, D. R.; Bradley, D. D. C.; Brown, A. R.; Friend, R. H.; Gymer, R. W. Chemical Tuning of the Electronic Properties of Poly(p-Phenylenevinylene)-Based Copolymers. *J. Am. Chem. Soc.* **1993**, *115* (22), 10117–10124.

(86) MacDiarmid, A. G. "Synthetic Metals": A Novel Role for Organic Polymers (Nobel Lecture). *Angewandte Chemie - International Edition*. Wiley-Blackwell July 16, 2001, pp 2581–2590.

(87) Janietz, S.; Bradley, D. D. C.; Grell, M.; Giebeler, C.; Inbasekaran, M.; Woo, E. P. Electrochemical Determination of the Ionization Potential and Electron Affinity of Poly(9,9-Dioctylfluorene). *Appl. Phys. Lett.* **1998**, *73* (17), 2453–2455.

(88) Quites, F. J.; Faria, G. C.; Germino, J. C.; Atvars, T. D. Z. Tuning Emission Colors from Blue to Green in Polymeric Light- Emitting Diodes Fabricated Using Poly Fl Uorene

Blends. *J. Phys. Chem. A* **2014**, *118* (45), 10380–10390.

(89) Lane, P. A.; Palilis, L. C.; O'Brien, D. F.; Giebeler, C.; Cadby, A. J.; Lidzey, D. G.; Campbell, A. J.; Blau, W.; Bradley, D. D. C. Origin of Electrophosphorescence from a Doped Polymer Light Emitting Diode. *Phys. Rev. B* **2001**, *63* (23), 235206.

(90) Redecker, M.; Bradley, D. D. C.; Inbasekaran, M.; Woo, E. P. Nondispersive Hole Transport in an Electroluminescent Polyfluorene. *Appl. Phys. Lett.* **1998**, *73* (11), 1565–1567.

(91) Redecker, M.; Bradley, D. D. C.; Inbasekaran, M.; Woo, E. P. Mobility Enhancement through Homogeneous Nematic Alignment of a Liquid-Crystalline Polyfluorene. *Appl. Phys. Lett.* **1999**, *74* (10), 1400–1402.

(92) Yang, C. M.; Liao, H. H.; Horng, S. F.; Meng, H. F.; Tseng, S. R.; Hsu, C. S. Electron Mobility and Electroluminescence Efficiency of Blue Conjugated Polymers. *Synth. Met.* **2008**, *158* (1–2), 25–28.

(93) Yu, M. N.; Soleimaninejad, H.; Lin, J. Y.; Zuo, Z. Y.; Liu, B.; Bo, Y. F.; Bai, L. B.; Han, Y. M.; Smith, T. A.; Xu, M.; et al. Photophysical and Fluorescence Anisotropic Behavior of Polyfluorene β-Conformation Films. *J. Phys. Chem. Lett.* **2018**, *9* (2), 364–372.

(94) Lane, P. A. Polyfluorene Electroluminescence. In *Organic Light-Emitting Devices*; Springer New York: New York, NY, 2004; pp 265–301.

(95) Bonon, B. M. A.; Atvars, T. D. Z. Energy Transfer from Poly(Vinyl Carbazole) to a Fluorene-Vinylene Copolymer in Solution and in the Solid State. *Photochem. Photobiol.* **2012**, *88* (4), 801–809.

(96) Halls, J. J. M.; Arias, A. C.; MacKenzie, J. D.; Wu, W.; Inbasekaran, M.; Woo, E. P.; Friend, R. H. Photodiodes Based on Polyfluorene Composites: Influence of Morphology. *Adv. Mater.* **2000**, *12* (7), 498–502.

(97) Herguth, P.; Jiang, X.; Liu, M. S.; Jen, A. K. Y. Highly Efficient Fluorene- and Benzothiadiazole-Based Conjugated Copolymers for Polymer Light-Emitting Diodes. *Macromolecules* **2002**, *35* (16), 6094–6100.

(98) Kim, Y.; Cook, S.; Choulis, S. A.; Nelson, J.; Durrant, J. R.; Bradley, D. D. C. Organic Photovoltaic Devices Based on Blends of Regioregular Poly(3-Hexylthiophene) and Poly(9,9-Dioctylfluorene-Co-Benzothiadiazole). *Chem. Mater.* **2004**, *16* (23), 4812–4818.

(99) Pope, M.; Swenberg, C. E. *Electronic Processes in Organic Crystals and Polymers*; Oxford University Press, 1999.

(100) Kwon, J.-H.; Pode, R. High Efficiency Red Phosphorescent Organic Light-Emitting Diodes with Simple Structure. In *Organic Light Emitting Diode - Material, Process and Devices*; 2011; Vol. 3.

(101) Huang, J.; Pfeiffer, M.; Werner, A.; Blochwitz, J.; Leo, K.; Liu, S. Low-Voltage Organic Electroluminescent Devices Using Pin Structures. *Appl. Phys. Lett.* **2002**, *80* (1), 139–141.

(102) You, J.; Dou, L.; Yoshimura, K.; Kato, T.; Ohya, K.; Moriarty, T.; Emery, K.; Chen, C.-C.; Gao, J.; Li, G.; et al. A Polymer Tandem Solar Cell with 10.6% Power Conversion Efficiency. *Nat. Commun.* **2013**, *4*, 1446.

(103) Lampert, M. A.; Mark, P. *Current Injection in Solids*; Academic Press, 1970.

(104) Campbell, A. J.; Bradley, D. D. C.; Lidzey, D. G. Space-Charge Limited Conduction with Traps in Poly(Phenylene Vinylene) Light Emitting Diodes. *J. Appl. Phys.* **1997**, *82* (12), 6326–6342.

(105) Stallinga, P. *Electrical Characterization of Organic Electronic Materials and Devices*; John Wiley & Sons, Ltd: Chichester, UK, 2009.

(106) Mark, P.; Helfrich, W. Space-Charge-Limited Currents in Organic Crystals. *J. Appl. Phys.* **1962**, *33*.

(107) Li, B.; Chen, J.; Yang, D.; Ma, D. A Comparative Investigation of Trap-Limited Hole Transport Properties in Organic Bulk Heterojunctions. *Semicond. Sci. Technol. Semicond. Sci. Technol* **2011**, *26* (26), 115006–5.

(108) Kim, G. W.; Son, Y. H.; Yang, H. I.; Park, J. H.; Ko, I. J.; Lampande, R.; Sakong, J.; Maeng, M. J.; Hong, J. A.; Lee, J. Y.; et al. Diphenanthroline Electron Transport Materials for the Efficient Charge Generation Unit in Tandem Organic Light-Emitting Diodes. *Chem. Mater.* **2017**, *29* (19), 8299–8312.

(109) Stallinga, P. *Electrical Characterization of Organic Electronic Materials and Devices*; John Wiley & Sons, 2009.

(110) Kalinowski, J. *Organic Light-Emitting Diodes*; Optical Science and Engineering; CRC Press, 2004; Vol. 92.

(111) Schubert, E. F. *Light-Emitting Diodes*; Cambridge University Press, 2006.

(112) Dumur, F. Zinc Complexes in OLEDs: An Overview. *Synthetic Metals*. 2014, pp 241–251.

(113) Wu, Z.; Ma, D. Recent Advances in White Organic Light-Emitting Diodes. *Materials Science and Engineering R: Reports*. Elsevier September 1, 2016, pp 1–42.

(114) Valeur, B. Molecular Fluorescence Principles and Applications; Wiley-VCH Verlag GmbH, 2002; pp 20–33.

(115) Rohatgi-Mukherjee, K. K. *Fundamentals of Photochemistry*; New Age International, 1978.

(116) Birks, J. B. *Photophysics of Aromatic Molecules*, 1st ed.; John Wiley & Sons Ltda, 1970.

(117) McQuarrie, D. A.; Simon, J. D. *Physical Chemistry: A Molecular Approach* ,; University Science Books, 1997.

(118) Lakowicz, J. R. *Principles of Fluorescence Spectroscopy*; Lakowicz, J. R., Ed.; Springer US: Boston, MA, 2006.

(119) Laquai, F.; Park, Y.-S.; Kim, J.-J.; Basché, T. Excitation Energy Transfer in Organic Materials: From Fundamentals to Optoelectronic Devices. *Macromol. Rapid Commun.* **2009**, *30* (14), 1203–1231.

(120) Luhman, W. A.; Holmes, R. J. Investigation of Energy Transfer in Organic Photovoltaic Cells and Impact on Exciton Diffusion Length Measurements. *Adv. Funct. Mater.* **2011**, *21* (4), 764–771.

(121) Valeur, B.; Berberan-Santos, M. N. *Molecular Fluorescence : Principles and Applications*; Wiley-VCH, 2013.

(122) Förster, T. Fluoreszenzspektrum Und Wasserstoffionen-Konzentration. *Naturwissenschaften* **1949**, *36* (6), 186–187.

(123) Förster, T. 10th Spiers Memorial Lecture. Transfer Mechanisms of Electronic Excitation. *Discuss. Faraday Soc.* **1959**, *27* (10), 7.

(124) Dexter, D. L. A Theory of Sensitized Luminescence in Solids. *J. Chem. Phys.* **1953**, *21* (5), 836.

(125) Turchetti, D. A.; Domingues, R. A.; Zanlorenzi, C.; Nowacki, B.; Atvars, T. D. Z.; Akcelrud, L. C. A Photophysical Interpretation of the Thermochromism of a Poly Fl Uorene Derivative − Europium Complex. *J. Phys. Chem. C* **2014**, *118*, 30079–30086.

(126) Rogach, A. L.; Klar, T. A.; Lupton, J. M.; Meijerink, A.; Feldmann, J. Energy Transfer with Semiconductor Nanocrystals. *J. Mater. Chem.* **2009**, *19* (9), 1208–1221.

(127) Turro, N. J.; Mcvey, J.; Ramamurthy, V.; Lechtken, P. Adiabatic Photoreactions of Organic Molecules. *Angew. Chemie Int. Ed.* **1979**, *18*, 572–586.

(128) Nome, R. A.; De Oliveira, H. P. M.; Akcelrud, L.; Atvars, T. D. Z. Electronic Energy Transfer between Poly(9,9-Dihexylfluorene-2,2-Dyil) and MEH-PPV: A Photophysical Study in Solutions and in the Solid State. *Synth. Met.* **2011**, *161* (19–20), 2154–2161.

(129) De Azevedo, D.; Freitas, J. N.; Domingues, R. A.; Faleiros, M. M.; Dib, T.; Atvars, Z. Correlation between the PL and EL Emissions of Polyfluorene-Based Diodes Using Bilayers or Polymer Blends. **2017**.

(130) Ye, T.; Chen, J.; Ma, D. Electroluminescence of Poly(N-Vinylcarbazole) Films: Fluorescence, Phosphorescence and Electromers. *Phys. Chem. Chem. Phys.* **2010**, *12* (47), 15410–15413.

(131) Persano, L.; Camposeo, A.; Pisignano, D. Active Polymer Nanofibers for Photonics, Electronics, Energy Generation and Micromechanics. *Prog. Polym. Sci.* **2014**, *43*, 48–95.

(132) Vivas, M. G.; Silva, D. L.; Malinge, J.; Boujtita, M.; Zaleśny, R.; Bartkowiak, W.; Agren, H.; Canuto, S.; De Boni, L.; Ishow, E.; et al. Molecular Structure - Optical Property Relationships for a Series of Non-Centrosymmetric Two-Photon Absorbing Push-Pull Triarylamine Molecules. *Sci. Rep.* **2014**, *4*, 4447.

(133) Gündüz, B. Sensing and Surface Morphological Properties of a Poly[(9,9-Dioctylfluorenyl-2,7-Diyl)-Co-Bithiophene] Liquid-Crystalline Polymer for Optoelectronic Applications. *J. Appl. Polym. Sci.* **2014**, *41659*, n/a-n/a.

(134) Vieira, N. C. S.; Figueiredo, A.; Fernandes, E. G. R.; Guimarães, F. E. G.; Zucolotto, V. Nanostructured Polyaniline Thin Films as Urea-Sensing Membranes in Field-Effect Devices. *Synth. Met.* **2013**, *175*, 108–111.

(135) Man, J. X.; Luo, D. Y.; Yu, L. M.; Wang, D. K.; Liu, Z.; Lu, Z. H. Ultrathin Optical Design for Organic Photovoltaic Cells. *Opt. Commun.* **2015**, *342*, 184–188.

(136) Freitas, J. N.; Gonçalves, A. S.; Nogueira, A. F. A Comprehensive Review of the Application of Chalcogenide Nanoparticles in Polymer Solar Cells. *Nanoscale* **2014**, *6* (12), 6371–6397.

(137) Quites, F. J. J.; Faria, G. C. G. C.; Germino, J. C. J.; Atvars, T. D. Z.; Dib, T.; Atvars, Z. Tuning Emission Colors from Blue to Green in Polymeric Light-Emitting Diodes Fabricated Using Polyfluorene Blends. *J. Phys. Chem. A* **2014**, *118* (45), 10380–10390.

(138) Franks, A. T.; Peng, D.; Yang, W.; Franz, K. J. Characterization of a Photoswitching Chelator with Light-Modulated Geometric, Electronic, and Metal-Binding Properties. *Inorg. Chem.* **2014**, *53* (3), 1397–1405.

(139) Na, Y.-J.; Song, W.; Lee, J. Y.; Hwang, S.-H. Synthesis of Dibenzothiophene-Based Host Materials and Their Blue Phosphorescent Device Performances. *Org. Electron.* **2015**, *22*, 92–97.

(140) Yardan, A.; Hopa, C.; Yahsi, Y.; Karahan, A.; Kara, H.; Kurtaran, R. Two New Heterodinuclear Schiff Base Complexes: Synthesis, Crystal Structure and Thermal Studies. *Spectrochim. Acta Part A Mol. Biomol. Spectrosc.* **2015**, *137*, 351–356.

(141) Prakash, G.; Nirmala, M.; Ramachandran, R.; Viswanathamurthi, P.; Malecki, J. G.; Sanmartin, J. Heteroleptic Binuclear Copper(I) Complexes Bearing Bis(Salicylidene)Hydrazone Ligands: Synthesis, Crystal Structure and Application in Catalytic N-Alkylation of Amines. *Polyhedron* **2015**, *89*, 62–69.

(142) Gulino, A.; Fragalà, I. L.; Lupo, F.; Malandrino, G.; Motta, A.; Colombo, A.; Dragonetti, C.; Righetto, S.; Roberto, D.; Ugo, R.; et al. Fascinating Role of the Number of f Electrons in Dipolar and Octupolar Contributions to Quadratic Hyperpolarizability of Trinuclear Lanthanides-Biscopper Schiff Base Complexes. *Inorg. Chem.* **2013**, *52* (13), 7550–7556.

(143) Kleij, A. W. New Templating Strategies with Salen Scaffolds (Salen=N, N???Bis(Salieylidene)Ethylenediamine Dianion). *Chem. - A Eur. J.* **2008**, *14* (34), 10520–10529.

(144) Martín, C.; Whiteoak, C. J.; Martin, E.; Martínez Belmonte, M.; Escudero-Adán, E. C.; Kleij, a. W. Easily Accessible Bifunctional Zn(Salpyr) Catalysts for the Formation of Organic Carbonates. *Catal. Sci. Technol.* **2014**, *4* (6), 1615.

(145) Kleij, A. W.; Kuil, M.; Tooke, D. M.; Lutz, M.; Spek, A. L.; Reek, J. N. H. ZnII-Salphen Complexes as Versatile Building Blocks for the Construction of Supramolecular Box Assemblies. *Chem. - A Eur. J.* **2005**, *11* (16), 4743–4750.

(146) Martin, E.; Martínez Belmonte, M.; Escudero-Adán, E. C.; Kleij, A. W. Exploring the Building-Block Potential of Readily Accessible Chiral [Zn(Salen)] Complexes. *Eur. J. Inorg. Chem.* **2014**, *2014* (27), 4632–4641.

(147) Cheng, J.; Ma, X.; Zhang, Y.; Liu, J.; Zhou, X.; Xiang, H. Optical Chemosensors Based on Transmetalation of Salen-Based Schiff Base Complexes. *Inorg. Chem.* **2014**, *53* (6), 3210–3219.

(148) Bhattacharjee, C. R.; Das, G.; Mondal, P.; Prasad, S. K.; Rao, D. S. S. Novel Green Light Emitting Nondiscoid Liquid Crystalline Zinc(II) Schiff-Base Complexes. *Eur. J. Inorg. Chem.* **2011**, *2011* (9), 1418–1424.

(149) Zhao, L.; Sui, D.; Chai, J.; Wang, Y.; Jiang, S. Digital Logic Circuit Based on a Single Molecular System of Salicylidene Schiff Base. *J. Phys. Chem. B* **2006**, *110* (48), 24299–24304.

(150) Beraeu, V.; Duhayon, C.; Sournia-Saquet, A.; Sutter, J. Tuning of the Emission Efficiency and HOMO − LUMO Band Gap for Ester-Functionalized {Al(Salophen)(H2O)2}+ Blue Luminophors. *Inorg. Chem.* 2012, pp 1309–1318.

(151) Zhang, J.; Zhao, F.; Zhu, X.; Wong, W.-Y. W.-K.; Ma, D.; Wong, W.-Y. W.-K. New Phosphorescent Platinum(Ii) Schiff Base Complexes for PHOLED Applications. *J. Mater. Chem.* **2012**, *22* (32), 16448.

(152) Barboza, C. A.; Germino, J. C.; Santana, A. M.; Quites, F. J.; Vazquez, P. A. M.; Atvars, T. D. Z. Structural Correlations between Luminescent Properties and Excited State Internal Proton Transfer in Some Zinc(II) N,N ’-Bis(Salicylidenes). *J. Phys. Chem. C* **2015**, *119* (11), 6152–6163.

(153) Maher, K. A.; Mohammed, S. R. METAL COMPLEXES OF SCHIFF BASE DERIVED FROM SALICYLALDEHYDE – A REVIEW. **2015**, *7* (2), 6–16.

(154) Soliman, A. a.; Linert, W. Structural Features of ONS-Donor Salicylidene Schiff Base Complexes. *Monatshefte fur Chemie* **2007**, *138* (3), 175–189.

(155) Brissos, R.; Ramos, D.; Lima, J. C.; Yafteh Mihan, F.; Borras, M.; de Lapuente, J.; Dalla Cort, A.; Rodriquez, L. Luminescent Zinc Salophen Derivatives: Cytoxicity Assessment and Action Mechanism Studies. *New J. Chem.* **2013**, 1046–1055.

(156) Xie, D.; Jing, J.; Cai, Y.-B.; Tang, J.; Chen, J.-J.; Zhang, J.-L. Construction of an Orthogonal ZnSalen/Salophen Library as a Colour Palette for One- and Two-Photon Live Cell Imaging. *Chem. Sci.* **2014**, *5* (6), 2318.

(157) Trujillo, A.; Fuentealba, M.; Carrillo, D.; Manzur, C.; Ledoux-Rak, I.; Hamon, J.-R.; Saillard, J.-Y.; Bretagne, D.; La, B. Synthesis, Spectral, Structural, Second-Order Nonlinear Optical Properties and Theoretical Studies on New Organometallic Donor-Acceptor Substituted Nickel(II) and Copper(II) Unsymmetrical Schiff-Base Complexes. *Acs Symp. Ser.* **2010**, *49* (II), 2750–2764.

(158) Ordronneau, L.; Nitadori, H.; Ledoux, I.; Singh, A.; Williams, J. a G.; Akita, M.; Guerchais, V.; Le Bozec, H. Photochromic Metal Complexes: Photoregulation of Both the Nonlinear Optical and Luminescent Properties. *Inorg. Chem.* **2012**, *51* (10), 5627–5636.

(159) Fukumoto, H.; Yamane, K.; Kase, Y.; Yamamoto, T. π-Conjugated Poly(Aryleneethynylene)s Consisting of Salophen and Ni−Salophen Units in the π-Conjugated Main Chain: Preparation and Chemical Properties. *Macromolecules* **2010**, *43* (24), 10366–10375.

(160) Ghosh, S.; Biswas, S.; Bauzá, A.; Barceló-Oliver, M.; Frontera, A.; Ghosh, A. Use of Metalloligands [CuL] (H2L = Salen Type Di-Schiff Bases) in the Formation of Heterobimetallic Copper(II)-Uranyl Complexes: Photophysical Investigations, Structural Variations, and Theoretical Calculations. *Inorg. Chem.* **2013**, *52* (13), 7508–7523.

(161) Hazari, A.; Ghosh, A. Trinuclear Complexes of [CuL] (H2L=N,N′-Bis(Salicylidene)-1,4-Butanediamine) with HgX2 (X−=N3− and NCO−): Facile Crystallization with Z′=1 and Z′=0.5 for Both Complexes. *Polyhedron* **2015**, *87*, 403–410.

(162) Kumar, V.; Kumar, A.; Diwan, U.; Shweta; Ramesh; Srivastava, S. K.; Upadhyay, K. K. Salicylideneimines as Efficient Dual Channel Emissive Probes for Al3+: Harnessing ESIPT and ICT Processes. *Sensors Actuators B Chem.* **2015**, *207*, 650–657.

(163) Zhao, J.; Ji, S.; Chen, Y.; Guo, H.; Yang, P. Excited State Intramolecular Proton Transfer (ESIPT): From Principal Photophysics to the Development of New Chromophores and Applications in Fluorescent Molecular Probes and Luminescent Materials. *Phys. Chem. Chem. Phys.* **2012**, *14* (25), 8803.

(164) Kim, C. H.; Park, J.; Seo, J.; Park, S. Y.; Joo, T. Excited State Intramolecular Proton Transfer and Charge Transfer Dynamics of a 2- (2 ′ -Hydroxyphenyl) Benzoxazole Derivative in Solution. *J. Phys. Chem. A* **2010**, *114* (18), 5618–5629.

(165) Wnuk, P.; Burdziński, G.; Sliwa, M.; Kijak, M.; Grabowska, A.; Sepioł, J.; Kubicki, J. From Ultrafast Events to Equilibrium--Uncovering the Unusual Dynamics of ESIPT Reaction: The Case of Dually Fluorescent Diethyl-2,5-(Dibenzoxazolyl)-Hydroquinone. *Phys. Chem. Chem. Phys.* **2014**, *16* (6), 2542–2552.

(166) Park, S.; Kwon, J. E.; Kim, S. H.; Seo, J.; Chung, K.; Park, S.-Y.; Jang, D.-J.; Milián Medina, B.; Gierschner, J.; Park, S. Y. A White-Light-Emitting Molecule: Frustrated Energy Transfer between Constituent Emitting Centers. *J. Am. Chem. Soc.* **2009**, *131* (39), 14043–14049.

(167) Tang, K.; Chang, M.; Lin, T.; Pan, H.; Fang, T.; Chen, K.; Hung, W.; Hsu, Y.; Chou, P. Fine Tuning the Energetics of Excited-State Intramolecular Proton Transfer (ESIPT): White Light Generation in A Single ESIPT System. **2011**, 17738–17745.

(168) Bruker. Bruker AXS Inc. Madison, Winsconsin, USA 2010.

(169) Sheldrick, G. M. A Short History of SHELX. *Acta Crystallogr. Sect. A Found. Crystallogr.* **2007**, *64* (1), 112–122.

(170) Sheldrick, G. M. Shelx 2013: Program for the Solution of Crystal Structures. 2013.

(171) Macrae, C. F.; Edgington, P. R.; McCabe, P.; Pidcock, E.; Shields, G. P.; Taylor, R.; Towler, M.; Van De Streek, J. Mercury: Visualization and Analysis of Crystal Structures. *J. Appl. Crystallogr.* **2006**, *39* (3), 453–457.

(172) Quites, F. J.; Domingues, R. A.; Ferbonink, G. F.; Nome, R. A.; Atvars, T. D. Z. Facile Control of System-Bath Interactions and the Formation of Crystalline Phases of Poly[(9,9-Dioctylfluorenyl-2,7-Diyl)-Alt-Co-(9,9-Di-{5′-Pentanyl}-Fluorenyl-2,7-Diyl)] in Silicone-Based Polymer Hosts. *Eur. Polym. J.* **2013**, *49* (3), 693–705.

(173) Barboza, C. A.; Germino, J. C.; Santana, A. M.; Quites, F. J.; Vazquez, P. A. M. A. M.; Atvars, T. D. Z. Structural Correlations between Luminescent Properties and Excited State Internal Proton Transfer in Some Zinc(II) N,N ′-Bis(Salicylidenes). *J. Phys. Chem. C* **2015**, *119* (11), 6152–6163.

(174) Liang, W.; Xu, L.; Sun, S.; Lan, L.; Qiu, X.; Chen, R.; Li, Y. Polystyrenesulfonate Dispersed Dopamine with Unexpected Stable Semiquinone Radical and Electrochemical Behavior: A Potential Alternative to PEDOT:PSS. *ACS Sustain. Chem. Eng.* **2017**, *5* (1), 460–468.

(175) Jia, L.; Jin, L.; Yuan, K.; Chen, L.; Yuan, J.; Xu, S.; Lv, W.; Chen, R. High-Performance Exciplex-Type Host for Multicolor Phosphorescent Organic Light-Emitting Diodes with Low Turn-On Voltages. *ACS Sustain. Chem. Eng.* **2018**, acssuschemeng.8b01155.

(176) Kuo, K.; Huang, C.; Lin, Y. Synthesis and Photophysical Properties of Multinuclear Zinc-Salophen Complexes: Enhancement of Fluorescence by Fluorene Termini. *Dalton Trans.* **2008**, No. 29, 3889–3898.

(177) Burgess, J.; Prince, R. H. Zinc: Inorganic & Coordination ChemistryBased in Part on the Article Zinc: Inorganic & Coordination Chemistry by Reg H. Prince Which Appeared in the Encyclopedia of Inorganic Chemistry, First Edition . In *Encyclopedia of Inorganic and Bioinorganic Chemistry*; John Wiley & Sons, Ltd: Chichester, UK, 2011.

(178) United States Geological Survey, U.; Haxel, G. B.; Hedrick, J. B.; Orris, G. J. Rare Earth Elements—Critical Resources for High Technology | USGS Fact Sheet 087-02 https://pubs.usgs.gov/fs/2002/fs087-02/ (accessed May 23, 2018).

(179) Frassinetti, S.; Bronzetti, G. L.; Caltavuturo, L.; Cini, M.; Croce, C. Della. The Role of Zinc in Life: A Review. *J. Environ. Pathol. Toxicol. Oncol.* **2006**, *25* (3), 597–610.

(180) Barboza, C. A.; Germino, J. C.; Santana, A. M.; Quites, F. J.; Vazquez, P. A. M.; Atvars, T. D. Z. Structural Correlations between Luminescent Properties and Excited State Internal Proton Transfer in Some Zinc(II) N,N ’-Bis(Salicylidenes). *J. Phys. Chem. C*

2015, *119* (11), 6152–6163.

(181) Akasaki, I.; Amano, H. Stimulated Emission by Current Injection from an AlGaN / GaN / GaInN Quantum Well Device. *Jpn. J. Appl. Phys.* **1995**, *34*, L1517.

(182) Nakamura, S.; Mukai, T.; Senoh, M. Candela-Class High-Brightness InGaN/AlGaN Double-Heterostructure Blue-Light-Emitting Diodes. *Appl. Phys. Lett.* **1994**, *64* (13), 1687–1689.

(183) Chen, Y.; Xia, Y.; Smith, G. M.; Sun, H.; Yang, D.; Ma, D.; Li, Y.; Huang, W.; Carroll, D. L. Solution-Processable Hole-Generation Layer and Electron-Transporting Layer: Towards High-Performance, Alternating-Current-Driven, Field-Induced Polymer Electroluminescent Devices. *Adv. Funct. Mater.* **2014**, *24* (18), 2677–2688.

(184) Liu, L.; Chen, F.; Xu, B.; Dong, Y.; Zhao, Z.; Tian, W.; Ping, L. Solution-Processed White Organic Light-Emitting Diode Based on a Single-Emitting Small Molecule. *Synth. Met.* **2010**, *160* (17–18), 1968–1972.

(185) Tang, C.; Liu, X. D.; Liu, F.; Wang, X. L.; Xu, H.; Huang, W. Recent Progress in Polymer White Light-Emitting Materials and Devices. *Macromol. Chem. Phys.* **2013**, *214* (3), 314–342.

(186) Zhang, L.; Zu, F. S.; Deng, Y. L.; Igbari, F.; Wang, Z. K.; Liao, L. S. Origin of Enhanced Hole Injection in Organic Light-Emitting Diodes with an Electron-Acceptor Doping Layer: P-Type Doping or Interfacial Diffusion? *ACS Appl. Mater. Interfaces* **2015**, *7* (22), 11965–11971.

(187) Fathollahi, M.; Ameri, M.; Mohajerani, E.; Mehrparvar, E.; Babaei, M. Organic/Organic Heterointerface Engineering to Boost Carrier Injection in OLEDs. *Sci. Rep.* **2017**, *7*, 42787.

(188) Earmme, T.; Jenekhe, S. A. Solution-Processed, Alkali Metal-Salt-Doped, Electron-Transport Layers for High-Performance Phosphorescent Organic Light-Emitting Diodes. *Adv. Funct. Mater.* **2012**, *22* (24), 5126–5136.

(189) Shinar, J.; Savvateev, V. Introduction to Organic Light-Emitting Devices. In *Organic Light-Emitting Devices*; Springer New York: New York, NY, 2004; pp 1–41.

(190) Kao, K.-C.; Hwang, W. *Electrical Transport in Solids : With Particular Reference to Organic Semiconductors*, 1st ed.; Pergamon Press, 1981.

(191) Würth, C.; Grabolle, M.; Pauli, J.; Spieles, M.; Resch-Genger, U. Comparison of Methods and Achievable Uncertainties for the Relative and Absolute Measurement of Photoluminescence Quantum Yields. *Anal. Chem.* **2011**, *83* (9), 3431–3439.

(192) Würth, C.; Grabolle, M.; Pauli, J.; Spieles, M.; Resch-Genger, U. Relative and Absolute Determination of Fluorescence Quantum Yields of Transparent Samples. *Nat. Protoc.* **2013**, *8* (8), 1535–1550.

(193) Brouwer, A. M. Standards for Photoluminescence Quantum Yield Measurements in Solution (IUPAC Technical Report). *Pure Appl. Chem.* **2011**, *83* (12), 2213–2228.

(194) de Mello, J. C.; Wittmann, H. F.; Friend, R. H. An Improved Experimental Determination of External Photoluminescence Quantum Efficiency. *Adv. Mater.* **1997**, *9* (3), 230–232.

(195) Cardona, C. M.; Li, W.; Kaifer, A. E.; Stockdale, D.; Bazan, G. C. Electrochemical Considerations for Determining Absolute Frontier Orbital Energy Levels of Conjugated Polymers for Solar Cell Applications. *Adv. Mater.* **2011**, *23* (20), 2367–2371.

(196) Germino, J. C.; Quites, F. J.; Faria, G. C; Ramos, R. J; Atvars, T. D. Z. Improving the Electroluminescence of [Zn(Salophen)(OH 2)] in Polyfluorene-Based Light-Emitting Diode: The Role of Energy Transfer and Charge Recombination. *J. Braz. Chem. Soc.* **2016**, *27* (2), 295–302.

(197) Germino, J. C.; Barboza, C. A.; Junior Quites, F.; Muniz Vazquez, P. A.; Zambon Atvars, T. D. Dual Emissions of Salicylidene-5-Chloroaminepyridine Due to Excited State Intramolecular Proton Transfer: Dynamic Photophysical and Theoretical Studies. *J. Phys. Chem. C* **2015**, *119* (49), 27666–27675.

(198) Vivas, M. G.; Germino, J. C.; Barboza, C. A.; Simoni, D. D. A.; Vazquez, P. A. M.; De Boni, L.; Atvars, T. D. Z.; Mendonça, C. R. Revealing the Dynamic of Excited State Proton Transfer of a π-Conjugated Salicylidene Compound: An Experimental and Theoretical Study. *J. Phys. Chem. C* **2017**, *121* (2), 1283–1290.

(199) Barboza, C. A.; Germino, J. C.; Duarte, L. G. T. A.; Quites, F. J.; Vazquez, P. A. M.; Atvars, T. D. Z. Photoacidity of the N-Salicylidene-5-Chloroaminopyridine. *J. Lumin.* **2017**, *184*, 268–272.

(200) Adamo, C.; Barone, V. Toward Reliable Density Functional Methods without Adjustable Parameters: The PBE0 Model. *J. Chem. Phys.* **1999**, *110* (13), 6158–6170.

(201) Krishnan, R.; Binkley, J. S.; Seeger, R.; Pople, J. A. Self-consistent Molecular Orbital Methods. XX. A Basis Set for Correlated Wave Functions. *J. Chem. Phys.* **1980**, *72* (1), 650–654.

(202) Raghavachari, K.; Trucks, G. W. Highly Correlated Systems. Ionization Energies of First Row Transition Metals Sc-Zn. *J. Chem. Phys.* **1989**, *91* (4), 2457.

(203) Sinnecker, S.; Rajendran, A.; Klamt, A.; Diedenhofen, M.; Neese, F. Calculation of Solvent Shifts on Electronic G-Tensors with the Conductor-like Screening Model (COSMO) and Its Self-Consistent Generalization to Real Solvents (Direct COSMO-RS). *J. Phys. Chem. A* **2006**, *110* (6), 2235–2245.

(204) Campoy-Quiles, M.; Heliotis, G.; Xia, R.; Ariu, M.; Pintani, M.; Etchegoin, P.; Bradley, D. D. C. Ellipsometric Characterization of the Optical Constants of Polyfluorene Gain Media. *Adv. Funct. Mater.* **2005**, *15* (6), 925–933.

(205) Frisch; Trucks, G.; Schlegel, H.; Scuseria, G.; Robb, M.; Cheeseman, J.; Scalmani, G.; Barone, V.; Mennucci, B.; Petersson, G.; et al. Gaussian 09, Revision B.01. *Gaussian 09, Revis. B.01, Gaussian, Inc., Wallingford CT* **2009**.

(206) Barboza, C. A.; Germino, J. C.; Santana, A. M.; Quites, F. J.; Vazquez, P. A. M.; Atvars, T. D. Z. Structural Correlations between Luminescent Properties and Excited State Internal Proton Transfer in Some Zinc(II) N,N ’-Bis(Salicylidenes). *J. Phys. Chem. C* **2015**, *119* (11), 6152–6163.

(207) Vivas, M. G.; Germino, J. C.; Barboza, C. A.; Simoni, D. de A.; Vazquez, P. A. M. M.; De Boni, L.; Atvars, T. D. Z. Z.; Mendonça, C. R. Revealing the Dynamic of Excited State Proton Transfer of a π-Conjugated Salicylidene Compound: An Experimental and Theoretical Study. *J. Phys. Chem. C* **2017**, *121* (2), 1283–1290.

(208) Pérez-Bolívar, C.; Takizawa, S. Y.; Nishimura, G.; Montes, V. A.; Anzenbacher, P. High-Efficiency Tris(8-Hydroxyquinoline)Aluminum (Alq3) Complexes for Organic White-Light-Emitting Diodes and Solid-State Lighting. *Chem. - A Eur. J.* **2011**, *17* (33), 9076–9082.

(209) Khan, T.; Vaidya, S.; Mhatre, D. S.; Datta, A. The Prospect of Salophen in Fluorescence Lifetime Sensing of Al^{3+}. *J. Phys. Chem. B* **2016**, *120* (39), 10319–10326.

(210) Germino, J. C., Baboza, C. A., Atvars, T. D. Z. Salophen – Regarding the Phopoluminescence Spectra Dependence with the Solvents and Concentration of Solutions. *Prep.* **2017**.

(211) Itaya, A.; Sakai, H.; Masuhara, H. Excimer Dynamics of Poly(n-Vinylcarbazole) Films Revealed by Time-Correlated Single Photon Counting Measurements. *Chem. Phys. Lett.* **1987**, *138* (2–3), 231–236.

(212) Sillen, A.; Engelborghs, Y. The Correct Use of “Average” Fluorescence Parameters. *Photochem. Photobiol.* **1998**, *67* (5), 475–486.

(213) Zhang, Y.; Hu, Y.; Chen, J.; Zhou, Q.; Ma, D. Charge Carrier Injection and Transport in

PVK : Alq $_3$ Blend Films. *J. Phys. D. Appl. Phys.* **2003**, *36* (16), 2006–2009.

(214) Skriver, H. L.; Rosengaard, N. M. Surface-Energy and Work Function of Elemental Metals. *Phys. Rev. B* **1992**, *46* (11), 7157–7168.

(215) Hagen, J. a.; Li, W.; Steckl, A. J.; Grote, J. G. Enhanced Emission Efficiency in Organic Light-Emitting Diodes Using Deoxyribonucleic Acid Complex as an Electron Blocking Layer. *Appl. Phys. Lett.* **2006**, *88* (17), 2004–2007.

(216) Yu, W. L.; Pei, J.; Cao, Y.; Huang, W. Hole-Injection Enhancement by Copper Phthalocyanine (CuPc) in Blue Polymer Light-Emitting Diodes. *J. Appl. Phys.* **2001**, *89* (4), 2343–2350.

(217) Murata, H.; Merritt, C. D.; Kafafi, Z. H. Emission Mechanism in Rubrene-Doped Molecular Organic Light-Emitting Diodes: Direct Carrier Recombination at Luminescent Centers. *IEEE J. Sel. Top. Quantum Electron.* **1998**, *4* (1), 119–124.

(218) Khalifa, M. Ben; Vaufrey, D.; Bouazizi, A.; Tardy, J.; Maaref, H. Hole Injection and Transport in ITO/PEDOT/PVK/Al Diodes. *Mater. Sci. Eng. C* **2002**, *21* (1–2), 277–282.

(219) Xu, T.; Zhou, J. G.; Huang, C. C.; Zhang, L.; Fung, M. K.; Murtaza, I.; Meng, H.; Liao, L. S. Highly Simplified Tandem Organic Light-Emitting Devices Incorporating a Green Phosphorescence Ultrathin Emitter within a Novel Interface Exciplex for High Efficiency. *ACS Appl. Mater. Interfaces* **2017**, *9* (12), 10955–10962.

(220) Huang, W.-K.; Wu, H.-P.; Lin, P.-L.; Lee, Y.-P.; Diau, E. W.-G. Design and Characterization of Heteroleptic Ruthenium Complexes Containing Benzimidazole Ligands for Dye-Sensitized Solar Cells: The Effect of Fluorine Substituents on Photovoltaic Performance. *J. Phys. Chem. Lett.* **2012**, *3* (13), 1830–1835.

(221) Qin, Y.; Lu, J.; Li, S.; Li, Z.; Zheng, S. Phosphorescent Sensor Based on Iridium Complex/Poly(Vinylcarbazole) Orderly Assembled with Layered Double Hydroxide Nanosheets: Two-Dimensional Föster Resonance Energy Transfer and Reversible Luminescence Response for VOCs. *J. Phys. Chem. C* **2014**, *118* (35), 20538–20544.

(222) Li, K.; Ming Tong, G. S.; Wan, Q.; Cheng, G.; Tong, W. Y.; Ang, W. H.; Kwong, W. L.; Che, C. M. Highly Phosphorescent Platinum(Ii) Emitters: Photophysics, Materials and Biological Applications. *Chemical Science*. 2016, pp 1653–1673.

(223) Reineke, S.; Baldo, M. A. Recent Progress in the Understanding of Exciton Dynamics within Phosphorescent OLEDs. *Phys. Status Solidi* **2012**, *209* (12), 2341–2353.

(224) Zhang, Y.; Yin, Z.; Meng, F.; Yu, J.; You, C.; Yang, S.; Tan, H.; Zhu, W.; Su, S. Tetradentate Pt(II) 3,6-Substitued Salophen Complexes: Synthesis and Tuning Emission

from Deep-Red to near Infrared by Appending Donor-Acceptor Framework. *Org. Electron.* **2017**, *50*, 317–324.

(225) Achira, H.; Hoga, Y.; Yoshikawa, I.; Mutai, T.; Matsumura, K.; Houjou, H. Effects of a Semiflexible Linker on the Mechanochromic Photoluminescence of Bis(Pt-Salen) Complex. *Polyhedron* **2016**, *113*, 123–131.

(226) Germino, J. C.; de Freitas, J. N.; Domingues, R. A.; Quites, F. J.; Feleiros, M. M.; Atvars, T. D. Z. Organic Light-Emitting Diodes Based on PVK and Zn(II) Salicylidene Composites. *Synth. Met.* **2018**, *241*, 7–16.

(227) Che, C. M.; Kwok, C. C.; Lai, S. W.; Rausch, A. F.; Finkenzeller, W. J.; Zhu, N.; Yersin, H. Photophysical Properties and OLED Applications of Phosphorescent Platinum(II) Schiff Base Complexes. *Chem. - A Eur. J.* **2010**, *16* (1), 233–247.

(228) Zhang, J.; Dai, G.; Wu, F.; Li, D.; Gao, D.; Jin, H.; Chen, S.; Zhu, X.; Huang, C.; Han, D. Efficient and Tunable Phosphorescence of New Platinum(II) Complexes Based on the Donor–π–acceptor Schiff Bases. *J. Photochem. Photobiol. A Chem.* **2016**, *316*, 12–18.

(229) Che, C.-M.; Chan, S.-C.; Xiang, H.-F.; Chan, M. C. W.; Liu, Y.; Wang, Y. Tetradentate Schiff Base Platinum(II) Complexes as New Class of Phosphorescent Materials for High-Efficiency and White-Light Electroluminescent Devices. *Chem. Commun.* **2004**, No. 13, 1484–1485.

(230) Zhou, L.; Kwong, C. L.; Kwok, C. C.; Cheng, G.; Zhang, H.; Che, C. M. Efficient Red Electroluminescent Devices with Sterically Hindered Phosphorescent Platinum(II) Schiff Base Complexes and Iridium Complex Codopant. *Chem. - An Asian J.* **2014**, *9* (10), 2984–2994.

(231) Schwartz, G.; Reineke, S.; Rosenow, T. C.; Walzer, K.; Leo, K. Triplet Harvesting in Hybrid White Organic Light-Emitting Diodes. *Adv. Funct. Mater.* **2009**, *19* (9), 1319–1333.

(232) Chen, J.; Zhao, F.; Ma, D. Hybrid White OLEDs with Fluorophors and Phosphors. *Mater. Today* **2014**, *17* (4), 175–183.

(233) Du, X.; Zhao, J.; Yuan, S.; Zheng, C.; Lin, H.; Tao, S.; Lee, C. S. High-Performance Fluorescent/Phosphorescent (F/P) Hybrid White OLEDs Consisting of a Yellowish-Green Phosphorescent Emitter. *J. Mater. Chem. C* **2016**, *4* (25), 5907–5913.

(234) Kim, T.-H.; Lee, H. K.; Park, O. O.; Chin, B. D.; Lee, S.-H.; Kim, J. K. White-Light-Emitting Diodes Based on Iridium Complexes via Efficient Energy Transfer from a

Conjugated Polymer. *Adv. Funct. Mater.* **2006**, *16* (5), 611–617.

(235) Weigend, F.; Ahlrichs, R. Balanced Basis Sets of Split Valence, Triple Zeta Valence and Quadruple Zeta Valence Quality for H to Rn: Design and Assessment of Accuracy. *Phys. Chem. Chem. Phys.* **2005**, *7* (18), 3297–3305.

(236) Bühl, M.; Reimann, C.; Pantazis, D. A.; Bredow, T.; Neese, F. Geometries of Third-Row Transition-Metal Complexes from Density-Functional Theory. *J. Chem. Theory Comput.* **2008**, *4* (9), 1449–1459.

(237) Pantazis, D. A.; Chen, X. Y.; Landis, C. R.; Neese, F. All-Electron Scalar Relativistic Basis Sets for Third-Row Transition Metal Atoms. *J. Chem. Theory Comput.* **2008**, *4* (6), 908–919.

(238) Neese, F. Software Update: The ORCA Program System, Version 4.0. *Wiley Interdiscip. Rev. Comput. Mol. Sci.* **2018**, *8* (1), 1–6.

(239) Birks, J. B. *Photophysics of Aromatic Molecules*, 1st ed.; John Wiley & Sons Ltda, 1970.

7. APPENDIX

Structural characterization of salicylidene derivatives

Sal-3,4-ben

^{1}H and ^{13}C 1D NMR

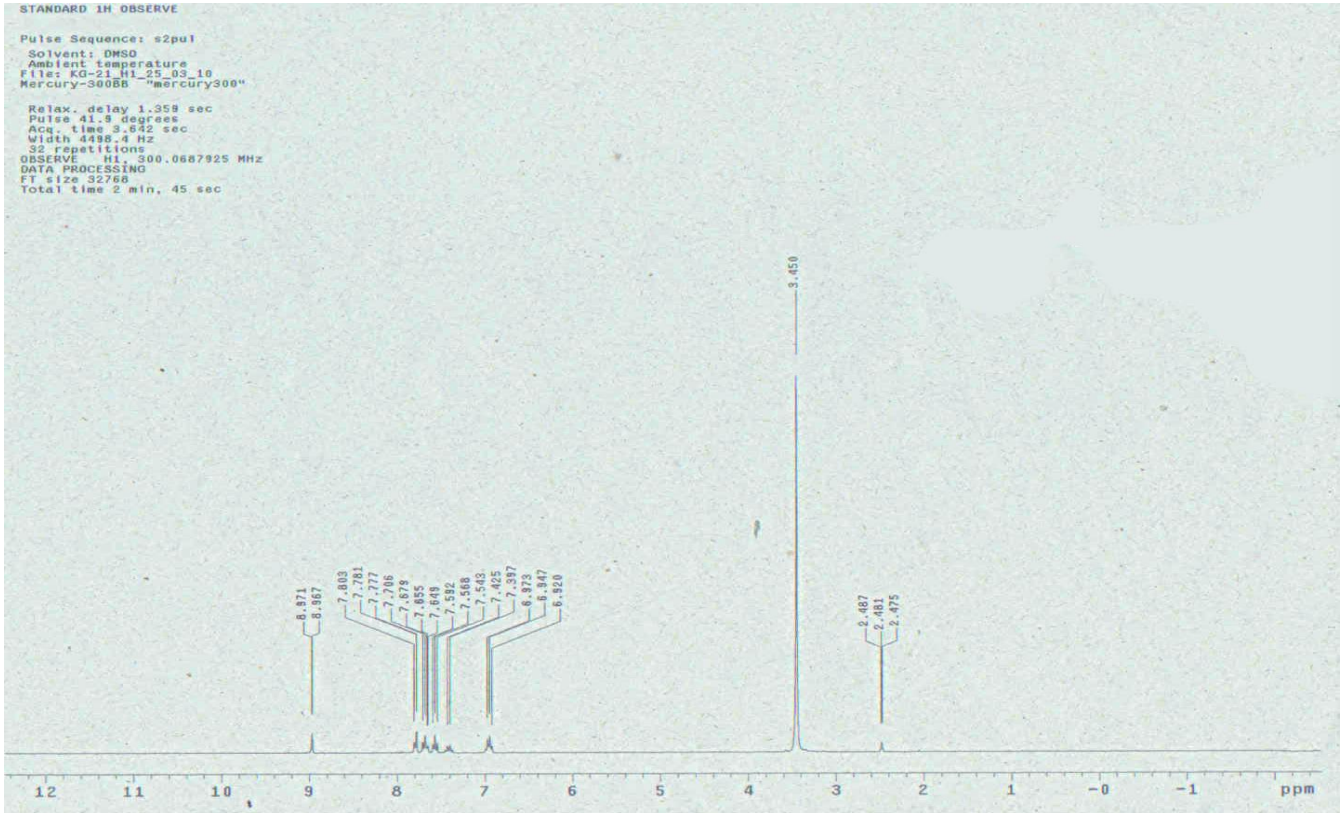

Figure A1. ^{1}H NMR spectrum of sal-3,4-ben solution in DMSO-d_6 (33 mg mL^{-1}).

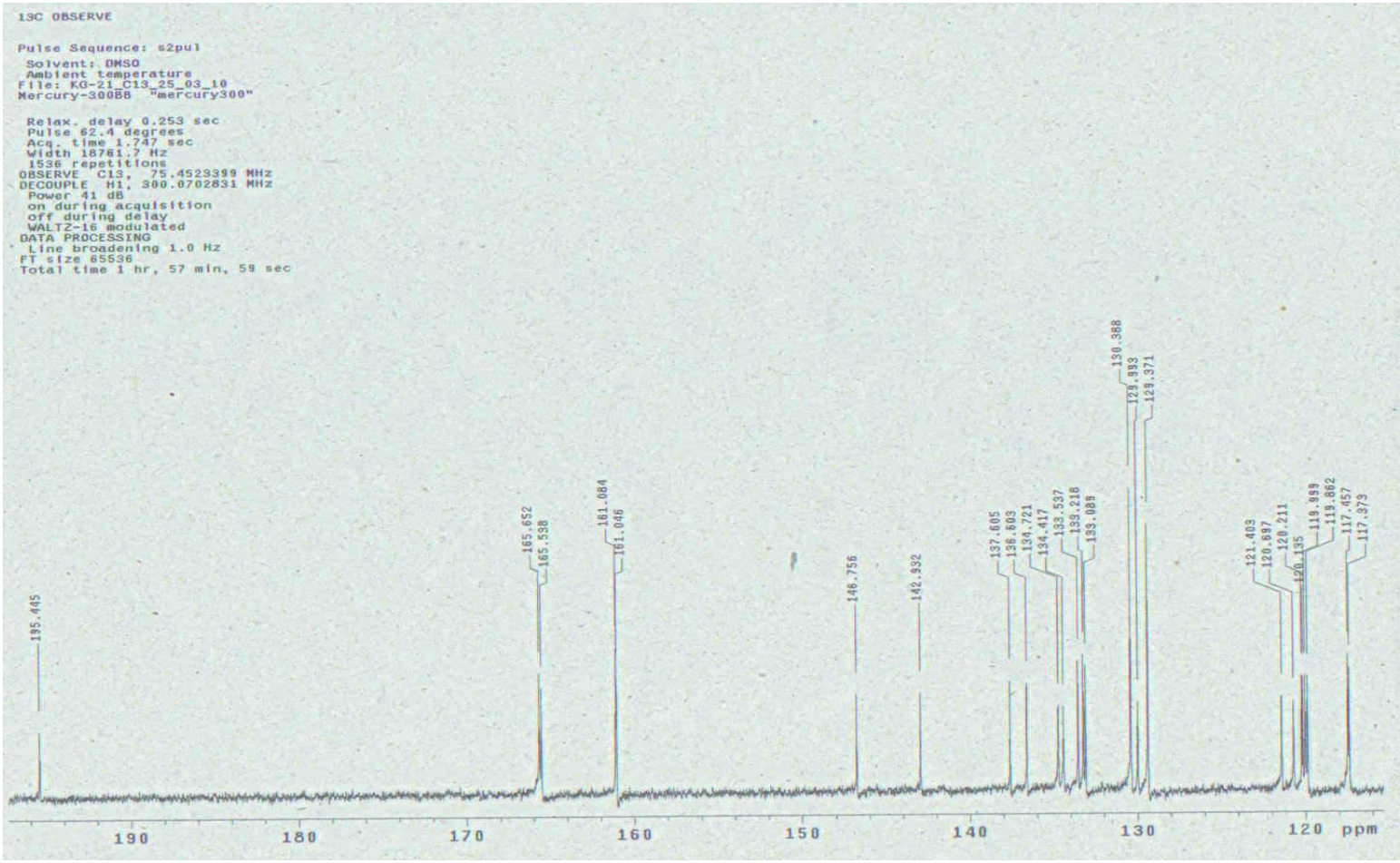

Figure A2. ^{13}C NMR spectrum of sal-3,4-ben solution in DMSO-d_6 (33 mg mL^{-1}).

FT-IR

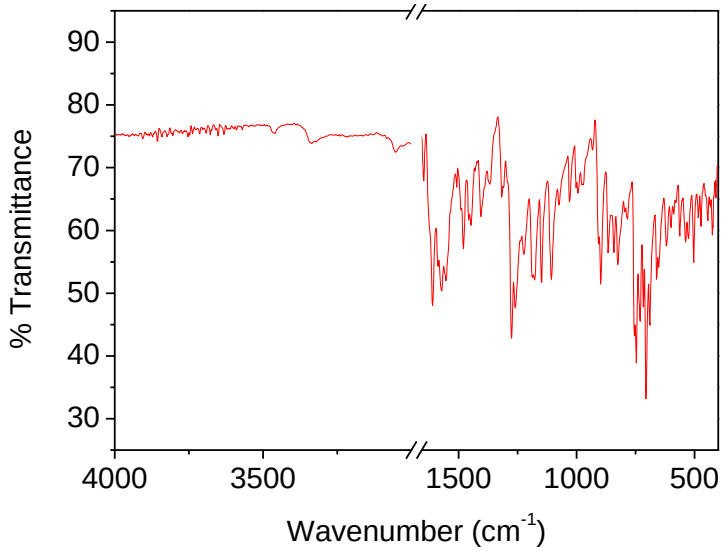

Figure A3. FT-IR spectra of sal-3,4-ben measured at ATR mode.

Mass Spectrometry

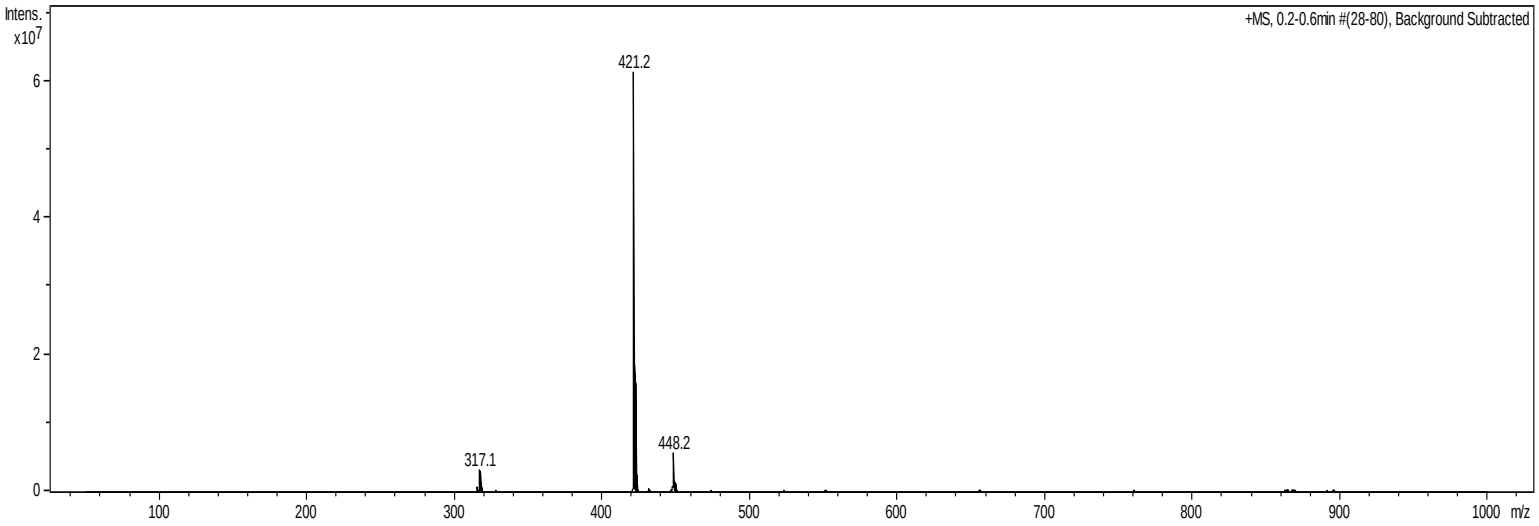

Figure A4. Sal-3,4-ben ESI-MS spectrometry at positive mode.

Table A1. Crystal data of the sal-3,4-ben.

$C_{27}H_{20}N_2O_3$	Sal-3,4-ben
M_r = 420.45	D_x = 1.371 Mg m^{-3}
Monoclinic, *C*2/*c*	Melting point: ? K
Hall symbol: ?	Mo *K*α radiation, λ = 0.71073 Å

a = 30.328 (8) Å	Cell parameters from Full-matrixleast-squares-on-F2 reflections
b = 5.8792 (15) Å	θ = 1.4–25.9°
c = 24.113 (6) Å	μ = 0.09 mm^{-1}
β = 108.640 (4)°	*T* = 296 K
V = 4073.9 (18) $Å^3$	?, yellow
Z = 8	0.26 × 0.09 × 0.07 mm
F(000) = 1760	

Data collection

BRUKER APEX CCD DETECTOR DIFFRACTOMETER diffractometer	3692 independent reflections	BRUKER APEX CCD DETECTOR DIFFRACTOMETER diffractometer	3692 independent reflections
Radiation source: FINE-FOCUS SEALED TUBE, Mo Kα (λ = 0.71073 Å)	3509 reflections with *I* > 2σ(*I*)	Radiation source: FINE-FOCUS SEALED TUBE, Mo Kα (λ = 0.71073 Å)	3509 reflections with *I* > 2σ(*I*)
CCD DETECTOR monochromator	R_{int} = 0.039	CCD DETECTOR monochromator	R_{int} = 0.039
Detector resolution: 8.3333 pixels mm^{-1}	θ_{max} = 27.9°, θ_{min} = 1.7°	Detector resolution: 8.3333 pixels mm^{-1}	θ_{max} = 27.9°, θ_{min} = 1.7°
Phi and ω Scans scans	*h* = −6 6	Phi and ω Scans scans	*h* = −6 6
Absorption correction: multi-scan *SADABS2014*/5 (Bruker,2014/5) was used for absorption correction. wR2(int) was 0.0860 before and 0.0587 after correction. The Ratio of minimum to maximum transmission is 0.7762. The λ/2 correction factor is 0.00150.	*k* = −22 22	Absorption correction: multi-scan *SADABS2014*/5 (Bruker,2014/5) was used for absorption correction. wR2(int) was 0.0860 before and 0.0587 after correction. The Ratio of minimum to maximum transmission is 0.7762. The λ/2 correction factor is 0.00150.	*k* = −22 22

T_{min} = 0.579, T_{max} = 0.746	l = −22 23
18211 measured reflections	
BRUKER APEX CCD DETECTOR DIFFRACTOMETER diffractometer	3692 independent reflections
Radiation source: FINE-FOCUS SEALED TUBE, Mo Kα (λ = 0.71073 Å)	3509 reflections with $I > 2\sigma(I)$
CCD DETECTOR monochromator	R_{int} = 0.039
Detector resolution: 8.3333 pixels mm^{-1}	θ_{max} = 27.9°, θ_{min} = 1.7°
Phi and ω Scans scans	h = −6 6
Absorption correction: multi-scan *SADABS2014*/5 (Bruker,2014/5) was used for absorption correction. wR2(int) was 0.0860 before and 0.0587 after correction. The Ratio of minimum to maximum transmission is 0.7762. The λ/2 correction factor is 0.00150.	k = −22 22
T_{min} = 0.579, T_{max} = 0.746	l = −22 23
18211 measured reflections	

T_{min} = 0.579, T_{max} = 0.746	l = −22 23
18211 measured reflections	
BRUKER APEX CCD DETECTOR DIFFRACTOMETER diffractometer	3692 independent reflections
Radiation source: FINE-FOCUS SEALED TUBE, Mo Kα (λ = 0.71073 Å)	3509 reflections with $I > 2\sigma(I)$
CCD DETECTOR monochromator	R_{int} = 0.039
Detector resolution: 8.3333 pixels mm^{-1}	θ_{max} = 27.9°, θ_{min} = 1.7°
Phi and ω Scans scans	h = −6 6
Absorption correction: multi-scan *SADABS2014*/5 (Bruker,2014/5) was used for absorption correction. wR2(int) was 0.0860 before and 0.0587 after correction. The Ratio of minimum to maximum transmission is 0.7762. The λ/2 correction factor is 0.00150.	k = −22 22
T_{min} = 0.579, T_{max} = 0.746	l = −22 23
18211 measured reflections	

BRUKER APEX CCD DETECTOR	3692 independent reflections

BRUKER APEX CCD DETECTOR	3692 independent reflections

DIFFRACTOMETER diffractometer	
Radiation source: FINE-FOCUS SEALED TUBE, Mo Kα (λ = 0.71073 Å)	3509 reflections with $I > 2\sigma(I)$
CCD DETECTOR monochromator	R_{int} = 0.039
Detector resolution: 8.3333 pixels mm^{-1}	θ_{max} = 27.9°, θ_{min} = 1.7°
Phi and ω Scans scans	h = −6 6
Absorption correction: multi-scan *SADABS2014*/5 (Bruker,2014/5) was used for absorption correction. wR2(int) was 0.0860 before and 0.0587 after correction. The Ratio of minimum to maximum transmission is 0.7762. The λ/2 correction factor is 0.00150.	k = −22 22
T_{min} = 0.579, T_{max} = 0.746	l = −22 23
18211 measured reflections	

DIFFRACTOMETER diffractometer	
Radiation source: FINE-FOCUS SEALED TUBE, Mo Kα (λ = 0.71073 Å)	3509 reflections with $I > 2\sigma(I)$
CCD DETECTOR monochromator	R_{int} = 0.039
Detector resolution: 8.3333 pixels mm^{-1}	θ_{max} = 27.9°, θ_{min} = 1.7°
Phi and ω Scans scans	h = −6 6
Absorption correction: multi-scan *SADABS2014*/5 (Bruker,2014/5) was used for absorption correction. wR2(int) was 0.0860 before and 0.0587 after correction. The Ratio of minimum to maximum transmission is 0.7762. The λ/2 correction factor is 0.00150.	k = −22 22
T_{min} = 0.579, T_{max} = 0.746	l = −22 23
18211 measured reflections	

BRUKER APEX CCD DETECTOR DIFFRACTOMETER diffractometer	3692 independent reflections
Radiation source: FINE-FOCUS SEALED TUBE, Mo Kα (λ = 0.71073 Å)	3509 reflections with $I > 2\sigma(I)$
CCD DETECTOR monochromator	R_{int} = 0.039

BRUKER APEX CCD DETECTOR DIFFRACTOMETER diffractometer	3692 independent reflections
Radiation source: FINE-FOCUS SEALED TUBE, Mo Kα (λ = 0.71073 Å)	3509 reflections with $I > 2\sigma(I)$
CCD DETECTOR monochromator	R_{int} = 0.039

Detector resolution: 8.3333 pixels mm^{-1}	θ_{max} = 27.9°, θ_{min} = 1.7°	Detector resolution: 8.3333 pixels mm^{-1}	θ_{max} = 27.9°, θ_{min} = 1.7°
Phi and ω Scans scans	h = −6 6	Phi and ω Scans scans	h = −6 6
Absorption correction: multi-scan *SADABS2014*/5 (Bruker,2014/5) was used for absorption correction. wR2(int) was 0.0860 before and 0.0587 after correction. The Ratio of minimum to maximum transmission is 0.7762. The λ/2 correction factor is 0.00150.	k = −22 22	Absorption correction: multi-scan *SADABS2014*/5 (Bruker,2014/5) was used for absorption correction. wR2(int) was 0.0860 before and 0.0587 after correction. The Ratio of minimum to maximum transmission is 0.7762. The λ/2 correction factor is 0.00150.	k = −22 22
T_{min} = 0.579, T_{max} = 0.746	l = −22 23	T_{min} = 0.579, T_{max} = 0.746	l = −22 23
18211 measured reflections		18211 measured reflections	
BRUKER APEX CCD DETECTOR DIFFRACTOMETER diffractometer	3692 independent reflections	BRUKER APEX CCD DETECTOR DIFFRACTOMETER diffractometer	3692 independent reflections
Radiation source: FINE-FOCUS SEALED TUBE, Mo Kα (λ = 0.71073 Å)	3509 reflections with $I > 2\sigma(I)$	Radiation source: FINE-FOCUS SEALED TUBE, Mo Kα (λ = 0.71073 Å)	3509 reflections with $I > 2\sigma(I)$
CCD DETECTOR monochromator	R_{int} = 0.039	CCD DETECTOR monochromator	R_{int} = 0.039
Detector resolution: 8.3333 pixels mm^{-1}	θ_{max} = 27.9°, θ_{min} = 1.7°	Detector resolution: 8.3333 pixels mm^{-1}	θ_{max} = 27.9°, θ_{min} = 1.7°
Phi and ω Scans scans	h = −6 6	Phi and ω Scans scans	h = −6 6
Absorption correction: multi-scan *SADABS2014*/5 (Bruker,2014/5) was	k = −22 22	Absorption correction: multi-scan *SADABS2014*/5 (Bruker,2014/5) was	k = −22 22

used for absorption correction. wR2(int) was 0.0860 before and 0.0587 after correction. The Ratio of minimum to maximum transmission is 0.7762. The λ/2 correction factor is 0.00150.	
T_{min} = 0.579, T_{max} = 0.746	l = −22 23
18211 measured reflections	
BRUKER APEX CCD DETECTOR DIFFRACTOMETER diffractometer	3692 independent reflections
Radiation source: FINE-FOCUS SEALED TUBE, Mo Kα (λ = 0.71073 Å)	3509 reflections with $I > 2\sigma(I)$
CCD DETECTOR monochromator	R_{int} = 0.039
Detector resolution: 8.3333 pixels mm^{-1}	θ_{max} = 27.9°, θ_{min} = 1.7°
Phi and ω Scans scans	h = −6 6
Absorption correction: multi-scan *SADABS2014*/5 (Bruker,2014/5) was used for absorption correction. wR2(int) was 0.0860 before and 0.0587 after correction. The Ratio of minimum to maximum transmission is 0.7762. The λ/2	k = −22 22

used for absorption correction. wR2(int) was 0.0860 before and 0.0587 after correction. The Ratio of minimum to maximum transmission is 0.7762. The λ/2 correction factor is 0.00150.	
T_{min} = 0.579, T_{max} = 0.746	l = −22 23
18211 measured reflections	
BRUKER APEX CCD DETECTOR DIFFRACTOMETER diffractometer	3692 independent reflections
Radiation source: FINE-FOCUS SEALED TUBE, Mo Kα (λ = 0.71073 Å)	3509 reflections with $I > 2\sigma(I)$
CCD DETECTOR monochromator	R_{int} = 0.039
Detector resolution: 8.3333 pixels mm^{-1}	θ_{max} = 27.9°, θ_{min} = 1.7°
Phi and ω Scans scans	h = −6 6
Absorption correction: multi-scan *SADABS2014*/5 (Bruker,2014/5) was used for absorption correction. wR2(int) was 0.0860 before and 0.0587 after correction. The Ratio of minimum to maximum transmission is 0.7762. The λ/2	k = −22 22

correction factor is 0.00150.	
T_{min} = 0.579, T_{max} = 0.746	l = −22 23
18211 measured reflections	
BRUKER APEX CCD DETECTOR DIFFRACTOMETER diffractometer	3692 independent reflections
Radiation source: FINE-FOCUS SEALED TUBE, Mo Kα (λ = 0.71073 Å)	3509 reflections with $I > 2\sigma(I)$
CCD DETECTOR monochromator	R_{int} = 0.039
Detector resolution: 8.3333 pixels mm^{-1}	θ_{max} = 27.9°, θ_{min} = 1.7°
Phi and ω Scans scans	h = −6 6
Absorption correction: multi-scan *SADABS2014*/5 (Bruker,2014/5) was used for absorption correction. wR2(int) was 0.0860 before and 0.0587 after correction. The Ratio of minimum to maximum transmission is 0.7762. The λ/2 correction factor is 0.00150.	k = −22 22
T_{min} = 0.579, T_{max} = 0.746	l = −22 23
18211 measured reflections	

correction factor is 0.00150.	
T_{min} = 0.579, T_{max} = 0.746	l = −22 23
18211 measured reflections	
BRUKER APEX CCD DETECTOR DIFFRACTOMETER diffractometer	3692 independent reflections
Radiation source: FINE-FOCUS SEALED TUBE, Mo Kα (λ = 0.71073 Å)	3509 reflections with $I > 2\sigma(I)$
CCD DETECTOR monochromator	R_{int} = 0.039
Detector resolution: 8.3333 pixels mm^{-1}	θ_{max} = 27.9°, θ_{min} = 1.7°
Phi and ω Scans scans	h = −6 6
Absorption correction: multi-scan *SADABS2014*/5 (Bruker,2014/5) was used for absorption correction. wR2(int) was 0.0860 before and 0.0587 after correction. The Ratio of minimum to maximum transmission is 0.7762. The λ/2 correction factor is 0.00150.	k = −22 22
T_{min} = 0.579, T_{max} = 0.746	l = −22 23
18211 measured reflections	

Refinement

Refinement on F^2	Secondary atom site location: ?
Least-squares matrix: full	Hydrogen site location: inferred from neighbouring sites
$R[F^2 > 2\sigma(F^2)] = 0.049$	H-atom parameters constrained
$wR(F^2) = 0.118$	$w = 1/[\sigma^2(F_o^2) + (0.0573P)^2]$ where $P = (F_o^2 + 2F_c^2)/3$
$S = 1.02$	$(\Delta/\sigma)_{max} < 0.001$
3952 reflections	$\Delta\rho_{max} = 0.23$ e Å^{-3}
291 parameters	$\Delta\rho_{min} = -0.25$ e Å^{-3}
0 restraints	Extinction correction: none
? constraints	Extinction coefficient: ?
Primary atom site location: ?	

Fractional atomic coordinates and isotropic or equivalent isotropic displacement parameters (Å^2)

	x	*y*	*z*	U_{iso}*/U_{eq}
O1	0.01226 (5)	−0.0186 (3)	0.19619 (6)	0.0225 (4)
H1	0.0312	0.0267	0.2267	0.034*
O2	0.12047 (5)	−0.1459 (3)	0.22107 (6)	0.0239 (4)
H2	0.1203	−0.0497	0.2456	0.036*
O3	0.22464 (5)	0.5174 (3)	0.51217 (7)	0.0274 (4)
N1	0.06892 (5)	0.2810 (3)	0.26744 (7)	0.0188 (4)
N2	0.14733 (6)	0.0536 (3)	0.32007 (7)	0.0194 (4)
C1	−0.03053 (7)	0.2539 (4)	0.05432 (9)	0.0255 (6)
H1A	−0.0495	0.2183	0.0167	0.031*
C2	−0.01049 (7)	0.4686 (4)	0.06593 (9)	0.0237 (5)
H2A	−0.0160	0.5770	0.0364	0.028*
C3	0.01769 (7)	0.5184 (4)	0.12175 (9)	0.0213 (5)
H3	0.0313	0.6615	0.1296	0.026*
C4	0.02634 (6)	0.3597 (4)	0.16694 (9)	0.0176 (5)
C5	0.05602 (6)	0.4234 (4)	0.22479 (9)	0.0185 (5)

H5	0.0662	0.5733	0.2314	0.022*
C6	0.09772 (7)	0.3624 (4)	0.32243 (8)	0.0177 (5)
C7	0.08670 (7)	0.5568 (4)	0.34754 (9)	0.0199 (5)
H7	0.0605	0.6410	0.3276	0.024*
C8	0.11470 (7)	0.6259 (4)	0.40228 (9)	0.0206 (5)
H8	0.1071	0.7567	0.4189	0.025*
C9	0.15403 (7)	0.5021 (4)	0.43275 (9)	0.0204 (5)
C10	0.18464 (7)	0.5818 (4)	0.49140 (9)	0.0210 (5)
C11	0.16390 (7)	0.7448 (4)	0.52397 (9)	0.0199 (5)
C12	0.12370 (7)	0.6876 (4)	0.53713 (9)	0.0227 (5)
H12	0.1086	0.5508	0.5239	0.027*
C13	0.10632 (7)	0.8343 (4)	0.56988 (9)	0.0253 (5)
H13	0.0800	0.7942	0.5795	0.030*
C14	0.12794 (7)	1.0404 (4)	0.58834 (9)	0.0260 (5)
H14	0.1161	1.1393	0.6102	0.031*
C15	0.00573 (7)	0.1434 (4)	0.15448 (9)	0.0189 (5)
C16	−0.02258 (7)	0.0932 (4)	0.09807 (9)	0.0232 (5)
H16	−0.0363	−0.0497	0.0897	0.028*
C17	0.16619 (7)	0.3102 (4)	0.40681 (9)	0.0197 (5)
H17	0.1932	0.2304	0.4264	0.024*
C18	0.13825 (7)	0.2374 (4)	0.35181 (9)	0.0182 (5)
C19	0.18204 (7)	−0.0823 (4)	0.33826 (9)	0.0212 (5)
H19	0.2036	−0.0632	0.3753	0.025*
C20	0.18736 (7)	−0.2651 (4)	0.30091 (9)	0.0209 (5)
C21	0.15583 (7)	−0.2911 (4)	0.24369 (9)	0.0199 (5)
C22	0.16045 (7)	−0.4767 (4)	0.20978 (10)	0.0254 (5)
H22	0.1393	−0.4964	0.1725	0.031*
C23	0.19582 (7)	−0.6294 (4)	0.23099 (11)	0.0294 (6)
H23	0.1984	−0.7525	0.2080	0.035*
C24	0.22798 (8)	−0.6032 (4)	0.28652 (11)	0.0292 (6)

H24	0.2524	−0.7059	0.3004	0.035*
C25	0.22324 (7)	−0.4230 (4)	0.32075 (10)	0.0266 (5)
H25	0.2445	−0.4063	0.3581	0.032*
C26	0.16706 (7)	1.0992 (4)	0.57442 (9)	0.0269 (5)
H26	0.1812	1.2392	0.5863	0.032*
C27	0.18552 (7)	0.9518 (4)	0.54292 (9)	0.0230 (5)
H27	0.2124	0.9913	0.5344	0.028*

Atomic displacement parameters (Å^2)

	U^{11}	U^{22}	U^{33}	U^{12}	U^{13}	U^{23}
O1	0.0249 (9)	0.0175 (9)	0.0219 (8)	−0.0015 (6)	0.0030 (6)	−0.0003 (7)
O2	0.0272 (9)	0.0176 (9)	0.0250 (8)	0.0020 (7)	0.0058 (7)	−0.0032 (7)
O3	0.0187 (8)	0.0293 (10)	0.0311 (9)	0.0022 (7)	0.0036 (6)	−0.0047 (8)
N1	0.0170 (9)	0.0178 (11)	0.0203 (9)	0.0007 (8)	0.0040 (7)	−0.0012 (8)
N2	0.0198 (9)	0.0148 (10)	0.0231 (9)	0.0004 (8)	0.0064 (7)	0.0001 (8)
C1	0.0224 (12)	0.0281 (15)	0.0211 (12)	0.0053 (10)	0.0000 (9)	−0.0032 (11)
C2	0.0273 (12)	0.0225 (14)	0.0203 (11)	0.0083 (10)	0.0061 (9)	0.0032 (10)
C3	0.0215 (12)	0.0176 (13)	0.0253 (12)	0.0033 (9)	0.0082 (9)	−0.0011 (10)
C4	0.0139 (11)	0.0171 (12)	0.0211 (11)	0.0022 (9)	0.0047 (8)	−0.0007 (10)
C5	0.0154 (11)	0.0148 (12)	0.0249 (11)	0.0005 (9)	0.0060 (9)	−0.0013 (10)
C6	0.0171 (11)	0.0167 (13)	0.0191 (11)	−0.0036 (9)	0.0054 (9)	0.0004 (10)
C7	0.0189 (11)	0.0194 (13)	0.0211 (11)	0.0010 (9)	0.0058 (9)	0.0023 (10)
C8	0.0205 (11)	0.0196 (13)	0.0228 (11)	−0.0008 (9)	0.0084 (9)	−0.0017 (10)

C9	0.0182 (11)	0.0211 (13)	0.0233 (11)	−0.0031 (9)	0.0083 (9)	−0.0003 (10)
C10	0.0202 (12)	0.0190 (13)	0.0241 (11)	−0.0024 (9)	0.0075 (9)	0.0004 (10)
C11	0.0187 (11)	0.0206 (13)	0.0166 (11)	0.0021 (9)	0.0002 (8)	0.0012 (10)
C12	0.0216 (12)	0.0234 (14)	0.0225 (11)	−0.0015 (10)	0.0063 (9)	−0.0016 (10)
C13	0.0221 (12)	0.0303 (15)	0.0256 (12)	0.0037 (10)	0.0105 (9)	0.0050 (11)
C14	0.0290 (13)	0.0258 (14)	0.0218 (11)	0.0077 (11)	0.0060 (9)	−0.0034 (11)
C15	0.0171 (11)	0.0180 (13)	0.0216 (11)	0.0042 (9)	0.0060 (9)	0.0003 (10)
C16	0.0198 (11)	0.0191 (13)	0.0277 (12)	0.0009 (9)	0.0032 (9)	−0.0042 (11)
C17	0.0167 (11)	0.0190 (13)	0.0221 (11)	0.0000 (9)	0.0044 (9)	0.0012 (10)
C18	0.0198 (11)	0.0140 (12)	0.0219 (11)	−0.0017 (9)	0.0083 (9)	0.0022 (10)
C19	0.0174 (11)	0.0222 (13)	0.0230 (11)	−0.0037 (10)	0.0049 (9)	0.0002 (10)
C20	0.0180 (11)	0.0173 (13)	0.0288 (12)	−0.0013 (9)	0.0097 (9)	0.0030 (10)
C21	0.0206 (11)	0.0146 (12)	0.0268 (12)	−0.0015 (9)	0.0109 (9)	0.0008 (10)
C22	0.0262 (12)	0.0229 (14)	0.0293 (12)	−0.0036 (10)	0.0119 (10)	−0.0034 (11)
C23	0.0297 (13)	0.0197 (14)	0.0452 (15)	−0.0034 (11)	0.0210 (11)	−0.0053 (12)
C24	0.0232 (12)	0.0197 (14)	0.0495 (15)	0.0053 (10)	0.0182 (11)	0.0035 (12)
C25	0.0202 (12)	0.0232 (14)	0.0368 (13)	−0.0001 (10)	0.0098 (10)	0.0029 (12)
C26	0.0268 (13)	0.0223 (14)	0.0268 (12)	−0.0011 (10)	0.0019 (10)	−0.0037 (11)

C27	0.0207 (12)	0.0251 (14)	0.0222 (11)	−0.0013 (10)	0.0055 (9)	0.0001 (10)

Geometric parameters (Å, °)

O1—C15	1.353 (2)	C11—C27	1.389 (3)
O1—H1	0.8200	C11—C12	1.396 (3)
O2—C21	1.343 (2)	C12—C13	1.383 (3)
O2—H2	0.8200	C12—H12	0.9300
O3—C10	1.215 (2)	C13—C14	1.382 (3)
N1—C5	1.286 (3)	C13—H13	0.9300
N1—C6	1.417 (3)	C14—C26	1.376 (3)
N2—C19	1.282 (3)	C14—H14	0.9300
N2—C18	1.402 (3)	C15—C16	1.388 (3)
C1—C16	1.379 (3)	C16—H16	0.9300
C1—C2	1.390 (3)	C17—C18	1.393 (3)
C1—H1A	0.9300	C17—H17	0.9300
C2—C3	1.376 (3)	C19—C20	1.444 (3)
C2—H2A	0.9300	C19—H19	0.9300
C3—C4	1.394 (3)	C20—C25	1.393 (3)
C3—H3	0.9300	C20—C21	1.413 (3)
C4—C15	1.406 (3)	C21—C22	1.397 (3)
C4—C5	1.447 (3)	C22—C23	1.367 (3)
C5—H5	0.9300	C22—H22	0.9300
C6—C7	1.383 (3)	C23—C24	1.390 (3)
C6—C18	1.413 (3)	C23—H23	0.9300
C7—C8	1.383 (3)	C24—C25	1.379 (3)
C7—H7	0.9300	C24—H24	0.9300
C8—C9	1.390 (3)	C25—H25	0.9300
C8—H8	0.9300	C26—C27	1.383 (3)
C9—C17	1.396 (3)	C26—H26	0.9300
C9—C10	1.497 (3)	C27—H27	0.9300

C10—C11	1.499 (3)		
C15—O1—H1	109.5	C26—C14—C13	119.9 (2)
C21—O2—H2	109.5	C26—C14—H14	120.0
C5—N1—C6	117.85 (19)	C13—C14—H14	120.0
C19—N2—C18	125.22 (18)	O1—C15—C16	118.48 (19)
C16—C1—C2	120.7 (2)	O1—C15—C4	121.87 (18)
C16—C1—H1A	119.7	C16—C15—C4	119.7 (2)
C2—C1—H1A	119.7	C1—C16—C15	120.4 (2)
C3—C2—C1	119.0 (2)	C1—C16—H16	119.8
C3—C2—H2A	120.5	C15—C16—H16	119.8
C1—C2—H2A	120.5	C18—C17—C9	120.5 (2)
C2—C3—C4	121.7 (2)	C18—C17—H17	119.8
C2—C3—H3	119.2	C9—C17—H17	119.8
C4—C3—H3	119.2	C17—C18—N2	126.21 (19)
C3—C4—C15	118.58 (19)	C17—C18—C6	119.0 (2)
C3—C4—C5	118.9 (2)	N2—C18—C6	114.72 (18)
C15—C4—C5	122.50 (19)	N2—C19—C20	119.58 (19)
N1—C5—C4	122.6 (2)	N2—C19—H19	120.2
N1—C5—H5	118.7	C20—C19—H19	120.2
C4—C5—H5	118.7	C25—C20—C21	118.3 (2)
C7—C6—C18	120.21 (18)	C25—C20—C19	120.8 (2)
C7—C6—N1	121.70 (18)	C21—C20—C19	120.92 (19)
C18—C6—N1	118.09 (19)	O2—C21—C22	118.38 (19)
C8—C7—C6	120.0 (2)	O2—C21—C20	122.06 (19)
C8—C7—H7	120.0	C22—C21—C20	119.5 (2)
C6—C7—H7	120.0	C23—C22—C21	120.5 (2)
C7—C8—C9	120.8 (2)	C23—C22—H22	119.8
C7—C8—H8	119.6	C21—C22—H22	119.8
C9—C8—H8	119.6	C22—C23—C24	120.8 (2)
C8—C9—C17	119.42 (19)	C22—C23—H23	119.6

C8—C9—C10	120.3 (2)	C24—C23—H23	119.6
C17—C9—C10	120.21 (19)	C25—C24—C23	119.1 (2)
O3—C10—C9	121.85 (19)	C25—C24—H24	120.4
O3—C10—C11	120.93 (19)	C23—C24—H24	120.4
C9—C10—C11	117.22 (18)	C24—C25—C20	121.7 (2)
C27—C11—C12	119.4 (2)	C24—C25—H25	119.1
C27—C11—C10	119.97 (19)	C20—C25—H25	119.1
C12—C11—C10	120.6 (2)	C14—C26—C27	120.6 (2)
C13—C12—C11	120.0 (2)	C14—C26—H26	119.7
C13—C12—H12	120.0	C27—C26—H26	119.7
C11—C12—H12	120.0	C26—C27—C11	119.9 (2)
C14—C13—C12	120.2 (2)	C26—C27—H27	120.1
C14—C13—H13	119.9	C11—C27—H27	120.1
C12—C13—H13	119.9		

All esds (except the esd in the dihedral angle between two l.s. planes) are estimated using the full covariance matrix. The cell esds are taken into account individually in the estimation of esds in distances, angles and torsion angles; correlations between esds in cell parameters are only used when they are defined by crystal symmetry. An approximate (isotropic) treatment of cell esds is used for estimating esds involving l.s. planes.

Sal-5Cl-py

^{1}H and ^{13}C 1D NMR spectra

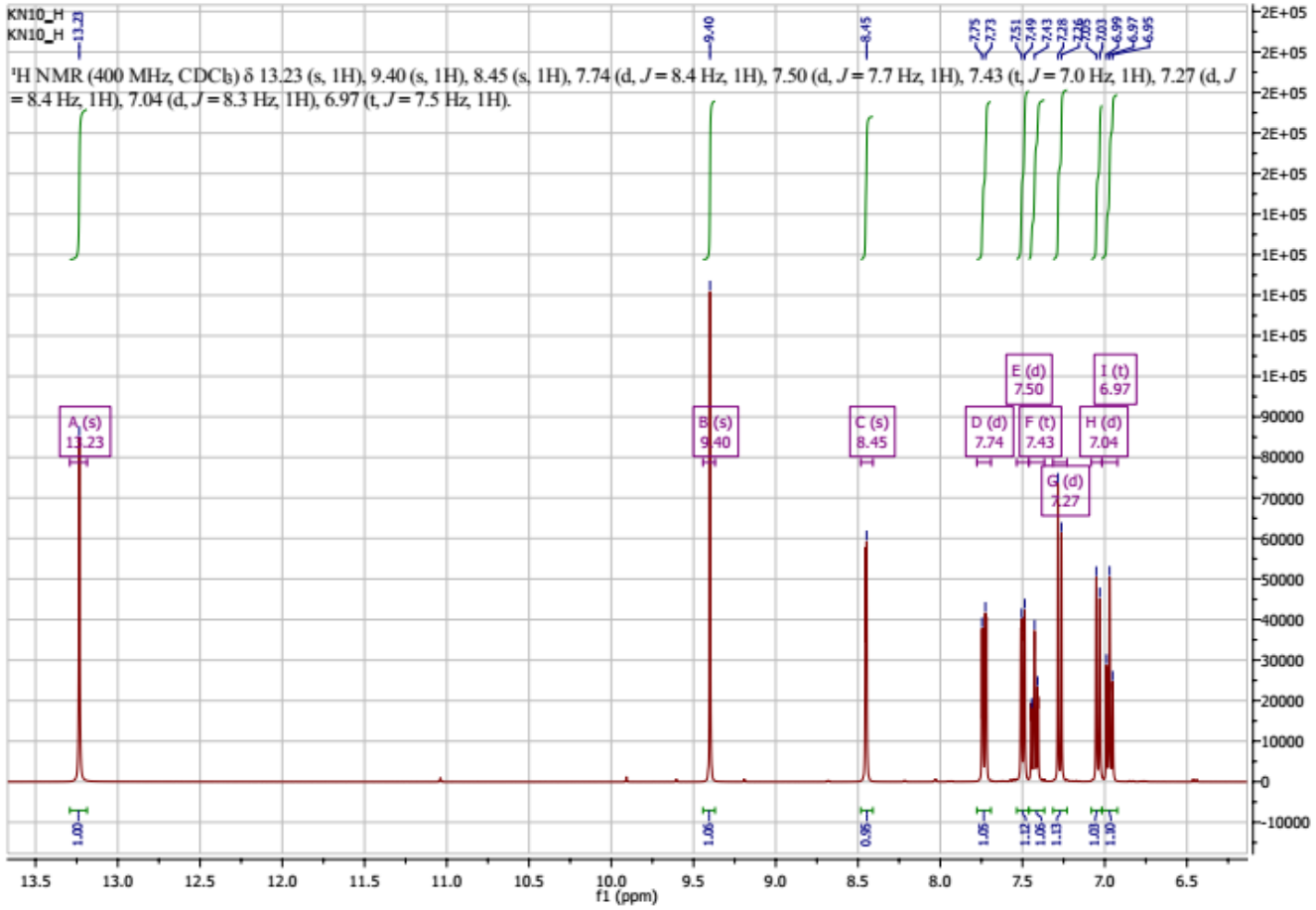

Figure A5. ^{1}H NMR spectrum of sal-5Cl-py solution in $CDCl_3$ (33 mg mL^{-1}).

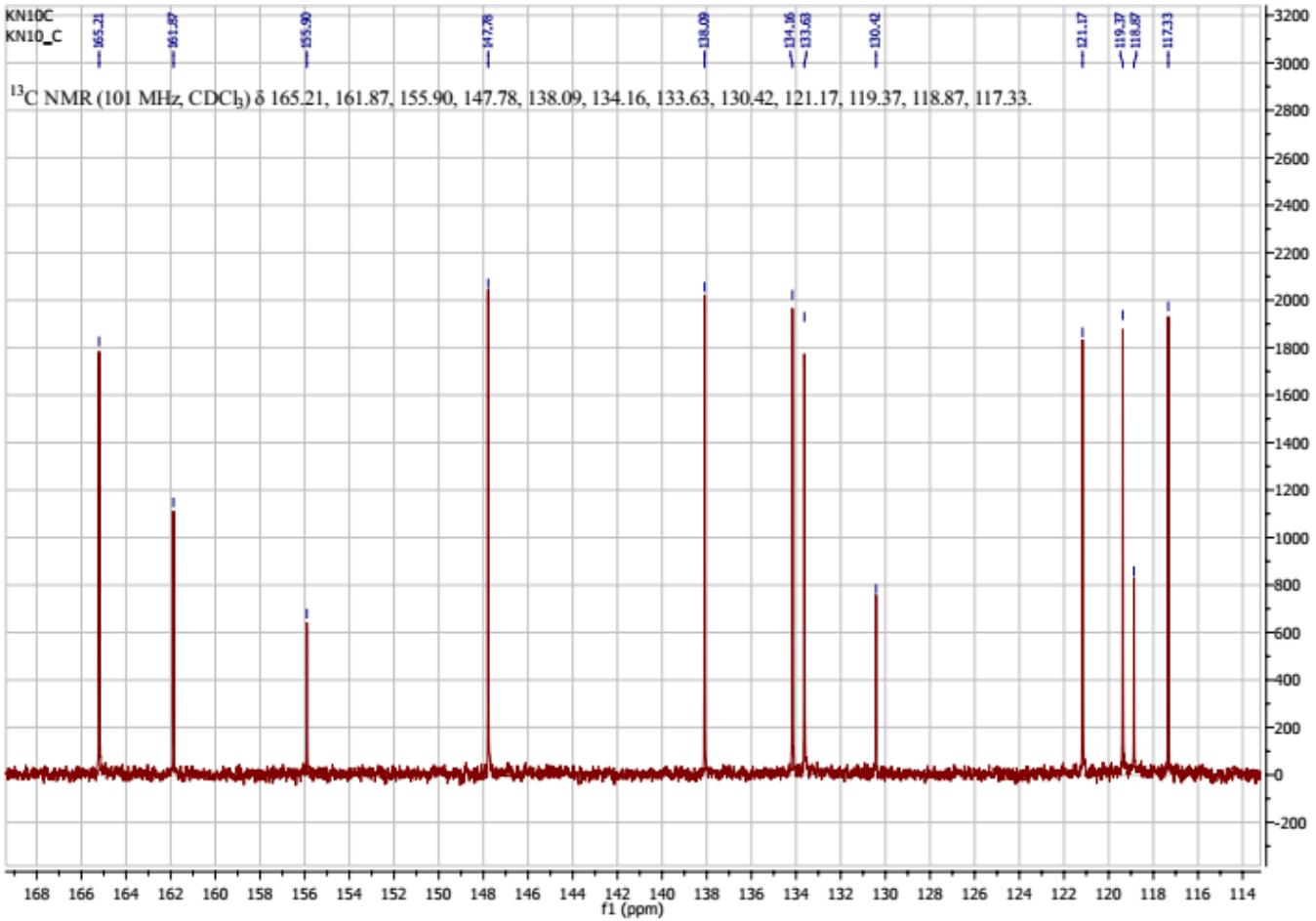

Figure A6. ^{13}C NMR spectrum of sal-5Cl-py solution in $CDCl_3$ (33 mg mL^{-1}).

FTIR

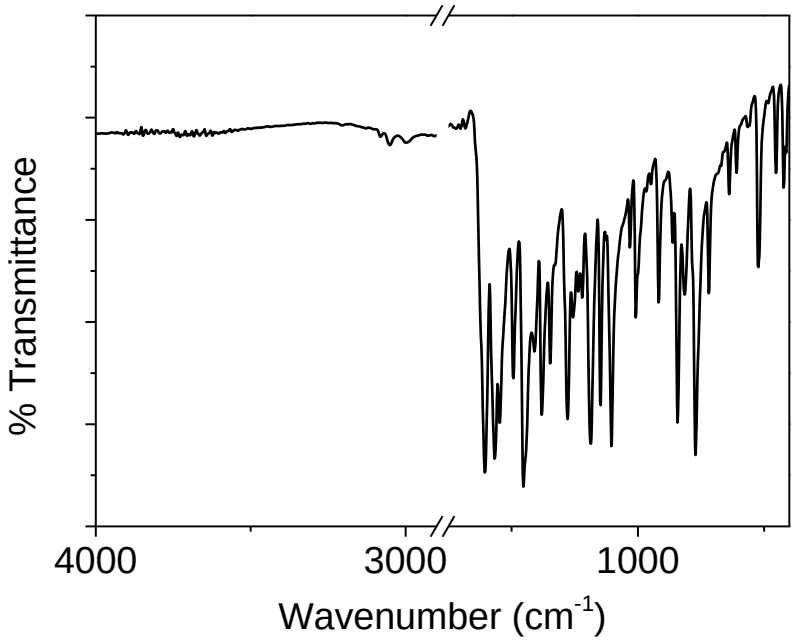

Figure A7. FT-IR spectra of sal-5Cl-py measured in ATR mode.

Mass spectrometry

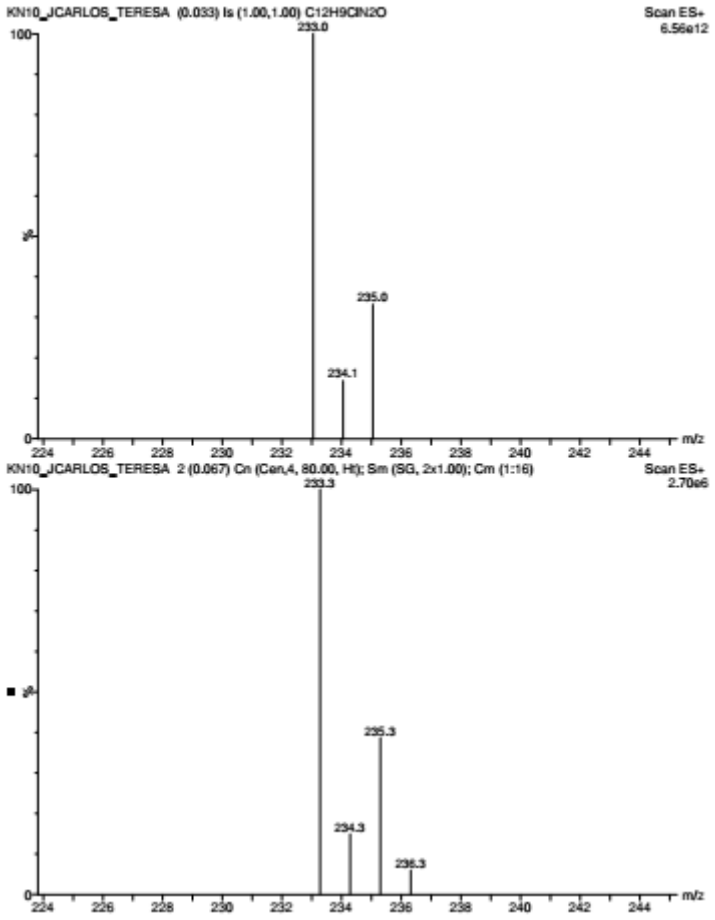

Figure A8. Sal-5Cl-py ESI-MS spectrometry at positive mode.

Cyclic Voltammogram of sal-5Cl-py

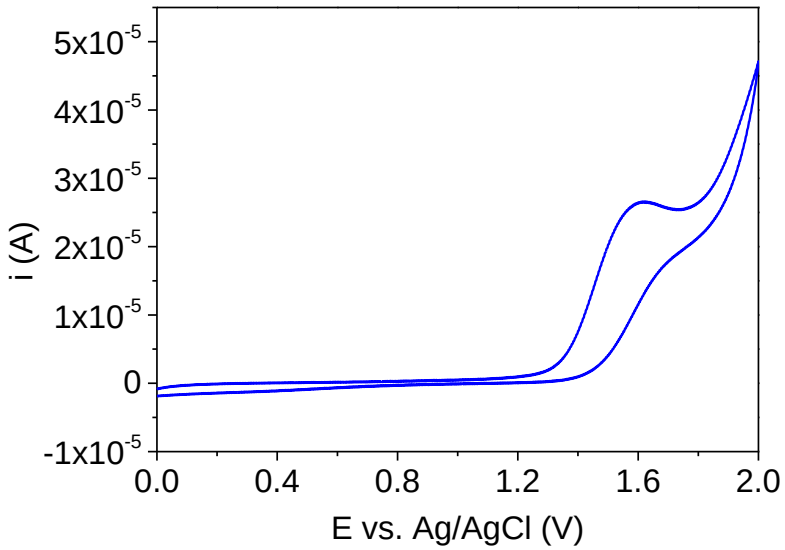

Figure A9. Sal-5Cl-py voltammogram measured in acetonitrile ($1x10^{-3}$ mol L^{-1}).

Additional optical characterization

Electronic absorption spectra and determination of the molar absorptivity coefficient in DMSO and MeOH dilute solutions of sal-5Cl-py.

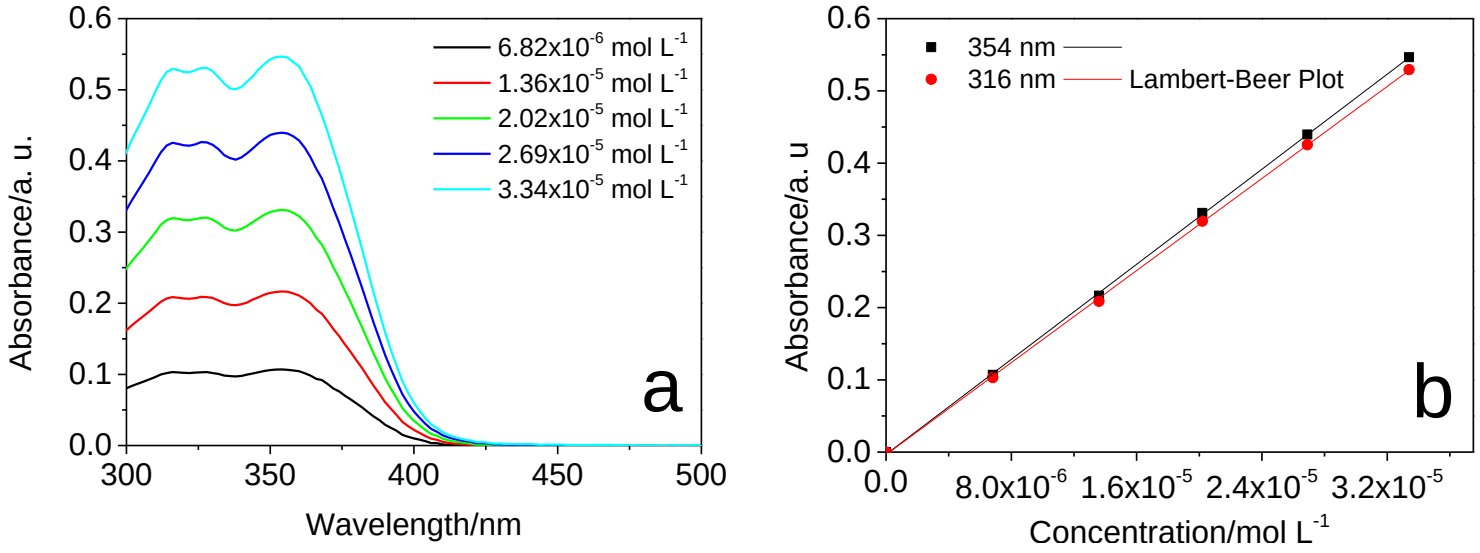

Figure A10. a. Electronic absorption spectra of sal-5Cl-py in DMSO dilute solutions: $6.82x10^{-6}$, $1.36x10^{-5}$, $2.02x10^{-5}$, $2.69x10^{-5}$ and $3.35x10^{-5}$mol L^{-1}; b. determination of the molar absorptivity coefficient.

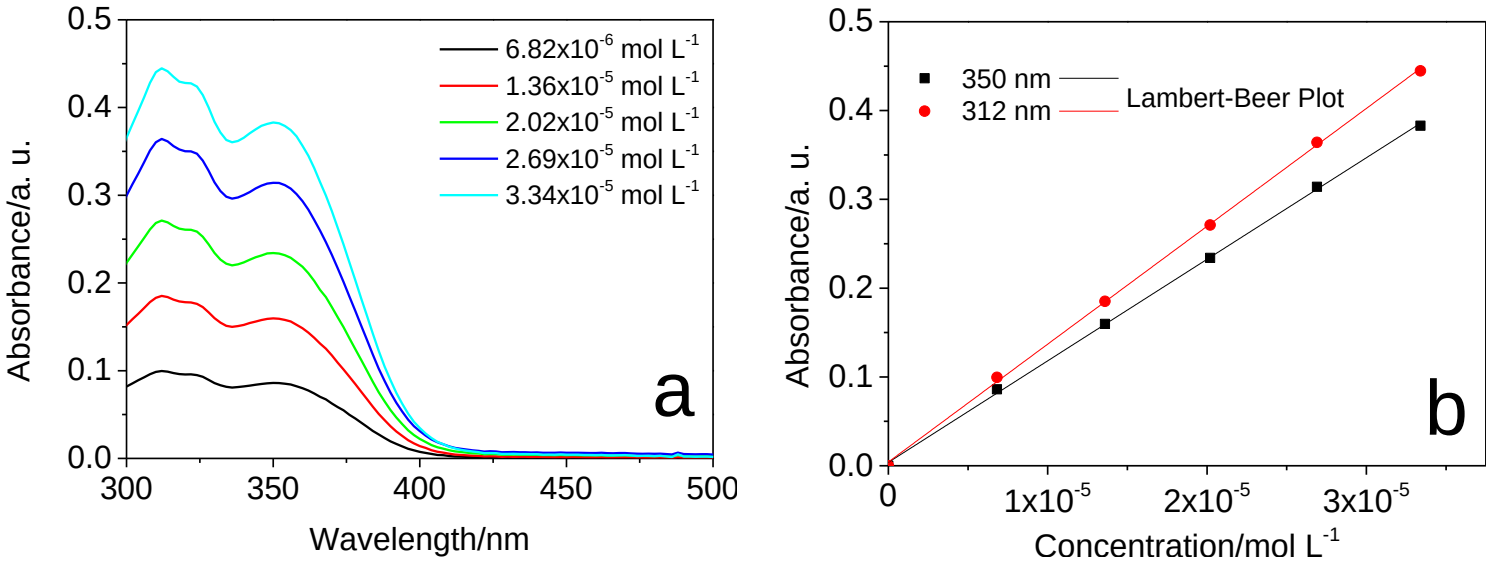

Figure A11. a. Electronic absorption spectra of sal-5Cl-py in MeOH dilute solutions: $6.82x10^{-6}$, $1.36x10^{-5}$, $2.02x10^{-5}$, $2.69x10^{-5}$ and $3.35x10^{-5}$mol L^{-1}; b. determination of the molar absorptivity coefficient.

Electronic absorption and emission spectra of sal-5Cl-py in solid-state.

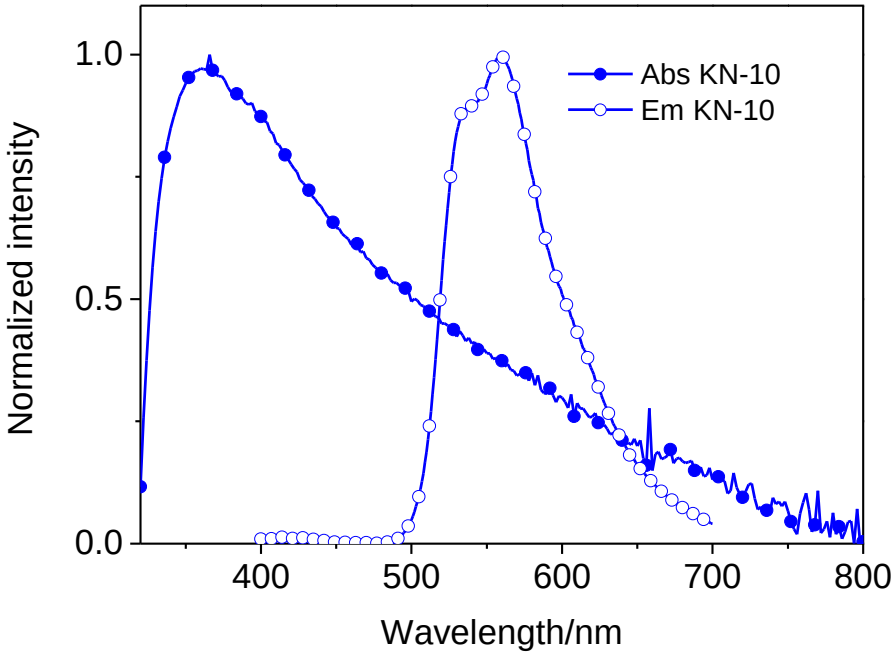

Figure A12. Normalized electronic absorption and photoluminescence spectra of sal-5Cl-py in solid-state.

Time-resolved emission spectra (TRES) of sal-5Cl-py MeOH and MeOH + CF_3COOH solutions

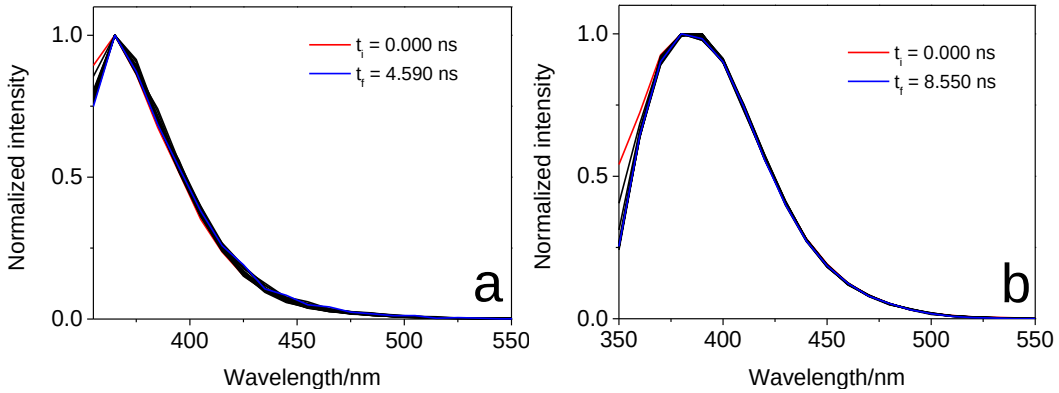

Figure A13. Normalized TRES of sal-5Cl-py in MeOH (a) and MeOH + CF_3COOH (b) solutions; λ_{exc} = 335 nm. Concentration: 10 μmol L^{-1}.

Table A2. Crystal data of the sal-5Cl-py.

$C_{12}H_9ClN_2O$	Monoclinic
M_r = 232.66	D_x = 1.483 Mg m^{-3}
Monoclinic, $P2_1/c$	Melting point: ? K

Hall symbol: ?	Mo *Kα* radiation, λ = 0.71073 Å
a = 5.8492 (15) Å	Cell parameters from 2272 reflections
b = 8.032 (2) Å	θ = 3.5–26.6°
c = 22.211 (6) Å	μ = 0.34 mm^{-1}
β = 92.990 (5)°	*T* = 100 K
V = 1042.1 (5) $Å^3$	Needle, metallic yellow
Z = 4	0.2 × 0.14 × 0.08 mm
F(000) = 480	

Data collection

Bruker SMART APEX2 area detector diffractometer	2229 independent reflections
Radiation source: microfocus sealed X-ray tube, Incoatec Iμs	1758 reflections with $I > 2\sigma(I)$
Mirror optics monochromator	R_{int} = 0.039
Detector resolution: 7.9 pixels mm^{-1}	θ_{max} = 26.8°, θ_{min} = 1.8°
ω and φ scans	*h* = −7 6
Absorption correction: multi-scan *SADABS2008*/1 (Bruker,2008) was used for absorption correction. wR2(int) was 0.0536 before and 0.0442 after correction. The Ratio of minimum to maximum transmission is 0.8880. The λ/2 correction factor is 0.0015.	*k* = −8 10
T_{min} = 0.662, T_{max} = 0.745	*l* = −28 25
9700 measured reflections	

Refinement

Refinement on F^2	Secondary atom site location: ?
Least-squares matrix: full	Hydrogen site location: inferred from neighbouring sites
$R[F^2 > 2\sigma(F^2)]$ = 0.037	H-atom parameters constrained

$wR(F^2)$ = 0.087	$w = 1/[\sigma^2(F_o^2) + (0.0382P)^2 + 0.4299P]$ where $P = (F_o^2 + 2F_c^2)/3$
S = 1.03	$(\Delta/\sigma)_{max}$ = 0.001
2229 reflections	$\Delta\rho_{max}$ = 0.22 e Å^{-3}
146 parameters	$\Delta\rho_{min}$ = −0.27 e Å^{-3}
0 restraints	Extinction correction: none
? constraints	Extinction coefficient: ?
Primary atom site location: dual	

Fractional atomic coordinates and isotropic or equivalent isotropic displacement parameters (Å^2)

	x	y	z	U_{iso}*/U_{eq}
Cl01	0.19027 (8)	0.90953 (6)	0.60377 (2)	0.02186 (14)
O002	1.0480 (2)	0.46832 (17)	0.36544 (6)	0.0216 (3)
H002	0.9736	0.5194	0.3910	0.032*
N003	0.7000 (2)	0.62487 (18)	0.40837 (7)	0.0169 (3)
N004	0.3770 (3)	0.7692 (2)	0.44265 (7)	0.0188 (3)
C005	0.5796 (3)	0.6965 (2)	0.45563 (8)	0.0163 (4)
C006	0.7030 (3)	0.5322 (2)	0.30599 (8)	0.0158 (4)
C007	0.9234 (3)	0.4612 (2)	0.31251 (8)	0.0164 (4)
C008	0.5939 (3)	0.6064 (2)	0.35632 (8)	0.0171 (4)
H008	0.4396	0.6428	0.3510	0.020*
C009	0.5872 (3)	0.5284 (2)	0.24879 (8)	0.0181 (4)
H009	0.4400	0.5779	0.2436	0.022*
C00A	0.2654 (3)	0.8324 (2)	0.48824 (8)	0.0195 (4)
H00A	0.1215	0.8845	0.4797	0.023*
C00B	0.6833 (3)	0.4543 (2)	0.20039 (8)	0.0198 (4)
H00B	0.6046	0.4543	0.1619	0.024*
C00C	0.5605 (3)	0.7523 (2)	0.56109 (8)	0.0195 (4)
H00C	0.6229	0.7472	0.6014	0.023*
C00D	0.6771 (3)	0.6869 (2)	0.51403 (8)	0.0184 (4)

H00D	0.8223	0.6358	0.5215	0.022*
C00E	0.3505 (3)	0.8253 (2)	0.54764 (8)	0.0177 (4)
C00F	0.8976 (3)	0.3792 (2)	0.20843 (8)	0.0204 (4)
H00F	0.9629	0.3255	0.1753	0.024*
C00G	1.0168 (3)	0.3816 (2)	0.26401 (8)	0.0196 (4)
H00G	1.1620	0.3289	0.2689	0.024*

Atomic displacement parameters (Å^2)

	U^{11}	U^{22}	U^{33}	U^{12}	U^{13}	U^{23}
Cl01	0.0215 (2)	0.0266 (3)	0.0177 (2)	0.0002 (2)	0.00313 (17)	−0.0025 (2)
O002	0.0186 (7)	0.0261 (8)	0.0196 (7)	0.0044 (6)	−0.0043 (5)	−0.0023 (6)
N003	0.0190 (8)	0.0158 (8)	0.0160 (7)	0.0004 (6)	0.0011 (6)	0.0004 (6)
N004	0.0181 (8)	0.0205 (8)	0.0178 (8)	0.0017 (7)	−0.0004 (6)	−0.0008 (7)
C005	0.0165 (9)	0.0139 (9)	0.0185 (9)	−0.0015 (7)	0.0010 (7)	0.0010 (8)
C006	0.0149 (8)	0.0140 (9)	0.0186 (9)	−0.0024 (7)	0.0006 (7)	0.0015 (7)
C007	0.0176 (9)	0.0137 (9)	0.0178 (9)	−0.0013 (7)	−0.0014 (7)	0.0025 (7)
C008	0.0154 (8)	0.0133 (9)	0.0223 (9)	0.0001 (7)	0.0000 (7)	0.0027 (8)
C009	0.0153 (9)	0.0171 (9)	0.0217 (9)	−0.0009 (7)	−0.0024 (7)	0.0012 (8)
C00A	0.0178 (9)	0.0197 (10)	0.0209 (9)	0.0006 (8)	−0.0002 (7)	0.0010 (8)
C00B	0.0238 (10)	0.0181 (10)	0.0172 (9)	−0.0032 (8)	−0.0020 (7)	0.0004 (8)
C00C	0.0212 (9)	0.0196 (10)	0.0173 (9)	−0.0022 (8)	−0.0024 (7)	0.0016 (8)
C00D	0.0168 (9)	0.0177 (10)	0.0204 (9)	0.0009 (8)	−0.0015 (7)	0.0015 (8)

C00E	0.0202 (9)	0.0158 (9)	0.0174 (9)	−0.0034 (8)	0.0033 (7)	−0.0022 (8)
C00F	0.0245 (10)	0.0167 (10)	0.0205 (9)	−0.0007 (8)	0.0067 (8)	−0.0010 (8)
C00G	0.0163 (9)	0.0181 (10)	0.0245 (10)	0.0020 (8)	0.0014 (8)	0.0016 (8)

Geometric parameters (Å, °)

Cl01—C00E	1.7356 (18)	C006—C009	1.409 (2)
O002—C007	1.352 (2)	C007—C00G	1.389 (3)
N003—C005	1.416 (2)	C009—C00B	1.374 (3)
N003—C008	1.292 (2)	C00A—C00E	1.387 (3)
N004—C005	1.339 (2)	C00B—C00F	1.394 (3)
N004—C00A	1.334 (2)	C00C—C00D	1.381 (3)
C005—C00D	1.391 (2)	C00C—C00E	1.379 (3)
C006—C007	1.410 (2)	C00F—C00G	1.386 (3)
C006—C008	1.445 (2)		
C008—N003—C005	118.41 (15)	N003—C008—C006	121.93 (16)
C00A—N004—C005	117.73 (15)	C00B—C009—C006	121.20 (17)
N004—C005—N003	119.09 (15)	N004—C00A—C00E	122.75 (17)
N004—C005—C00D	122.67 (16)	C009—C00B—C00F	119.27 (17)
C00D—C005—N003	118.24 (16)	C00E—C00C—C00D	117.84 (17)
C007—C006—C008	121.73 (16)	C00C—C00D—C005	119.33 (17)
C009—C006—C007	118.53 (16)	C00A—C00E—Cl01	119.12 (14)
C009—C006—C008	119.74 (16)	C00C—C00E—Cl01	121.21 (14)
O002—C007—C006	121.38 (16)	C00C—C00E—C00A	119.67 (17)
O002—C007—C00G	118.55 (16)	C00G—C00F—C00B	121.00 (17)
C00G—C007—C006	120.07 (16)	C00F—C00G—C007	119.82 (17)

All e.s.d.'s (except the e.s.d. in the dihedral angle between two l.s. planes) are estimated using the full covariance matrix. The cell e.s.d.'s are taken into account individually in the estimation of e.s.d.'s in distances, angles and torsion angles; correlations between e.s.d.'s in cell parameters are only used when they are defined by crystal symmetry. An approximate (isotropic) treatment of cell e.s.d.'s is used for estimating e.s.d.'s involving l.s. planes.

Zn(II)Salicylidenes in PVK – OLEDs and Optical characterization
[Zn(sal-3,4-ben)]
^{1}H and ^{13}C 1D NMR

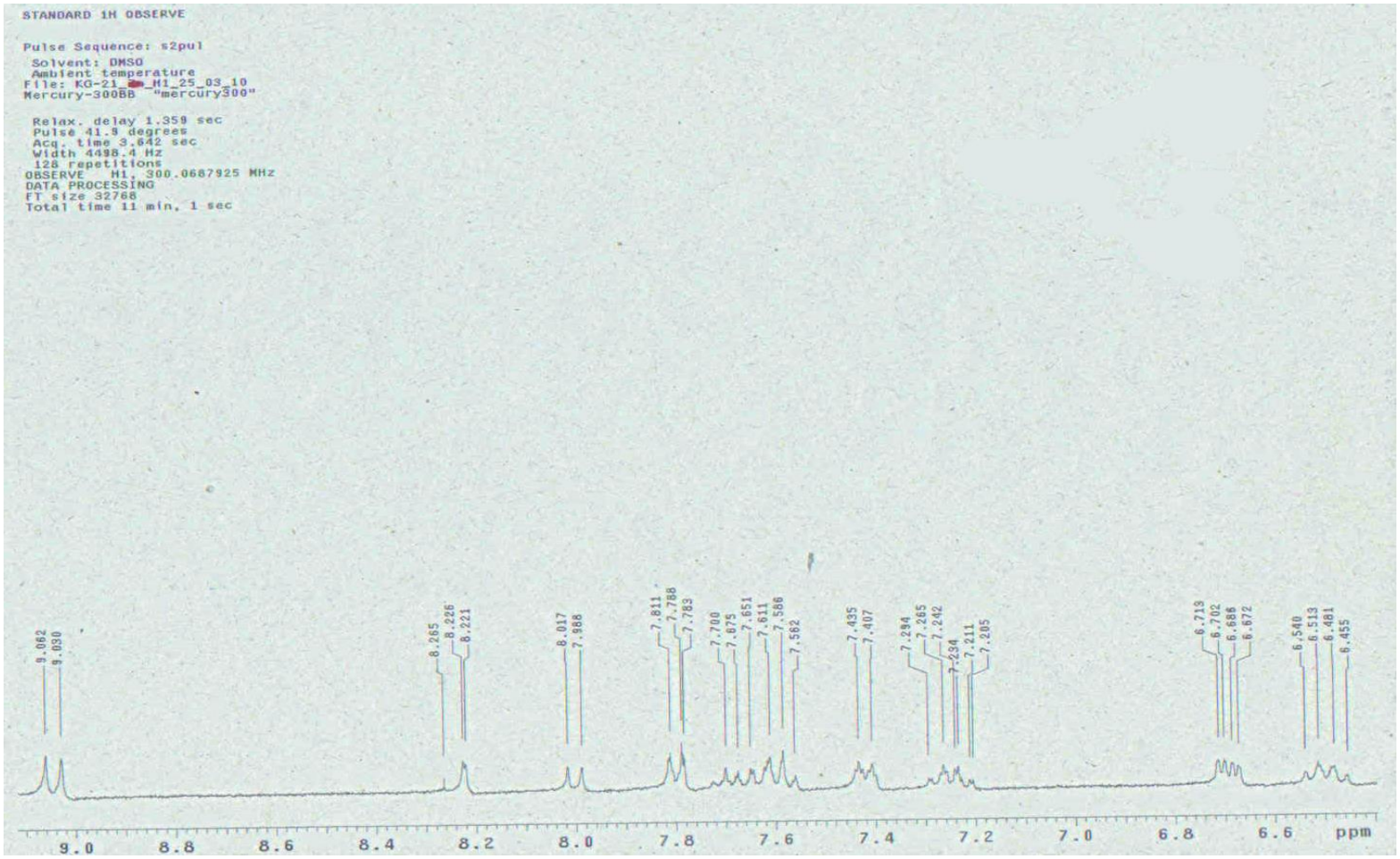

Figure A14. ^{1}H NMR spectrum of [Zn(sal-3,4-ben)] solution in DMSO-d_6 (33 mg mL^{-1}).

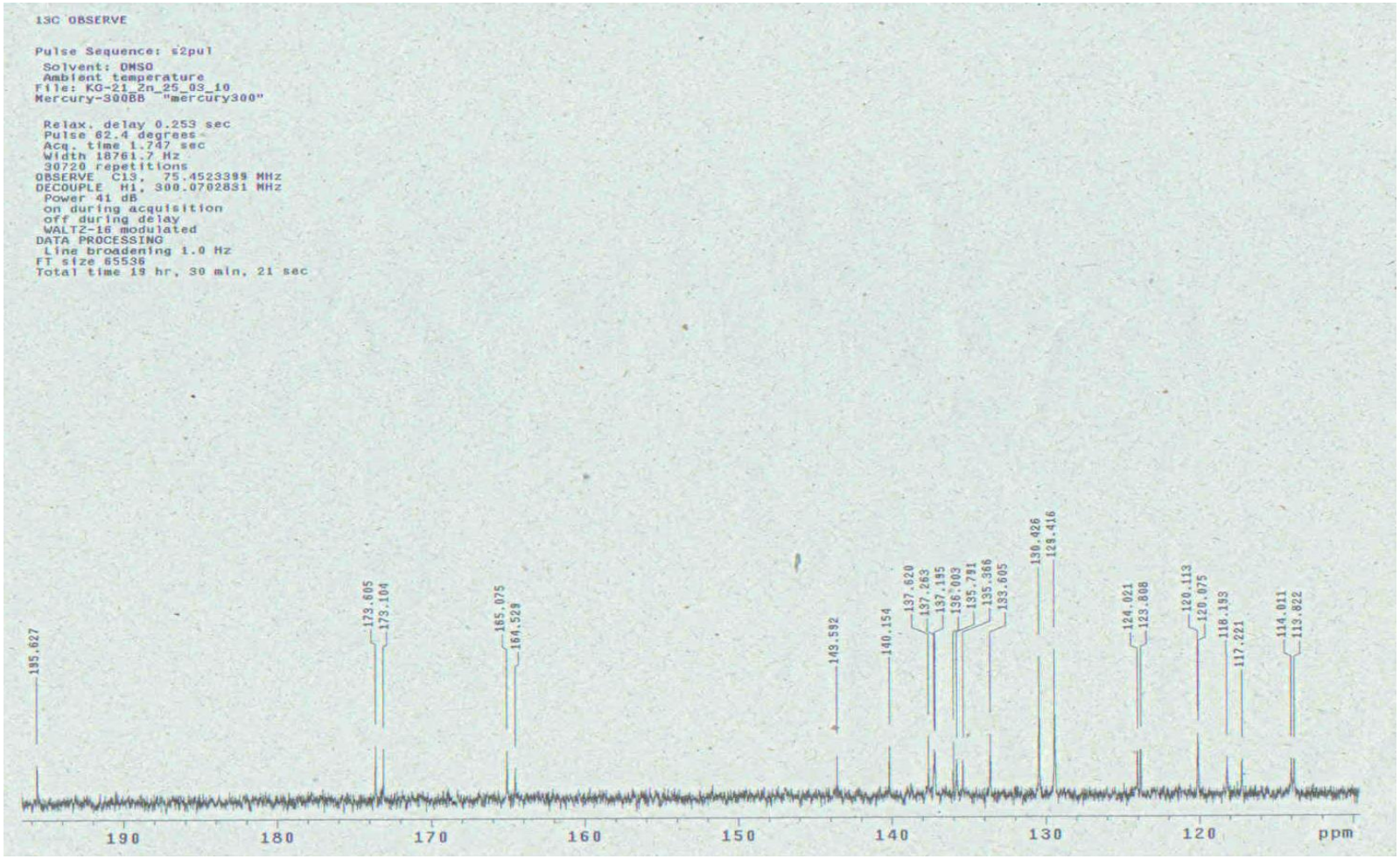

Figure A15. ^{13}C NMR spectrum of [Zn(sal-3,4-ben)] solution in DMSO-d_6 (33 mg mL^{-1}).

FT-IR

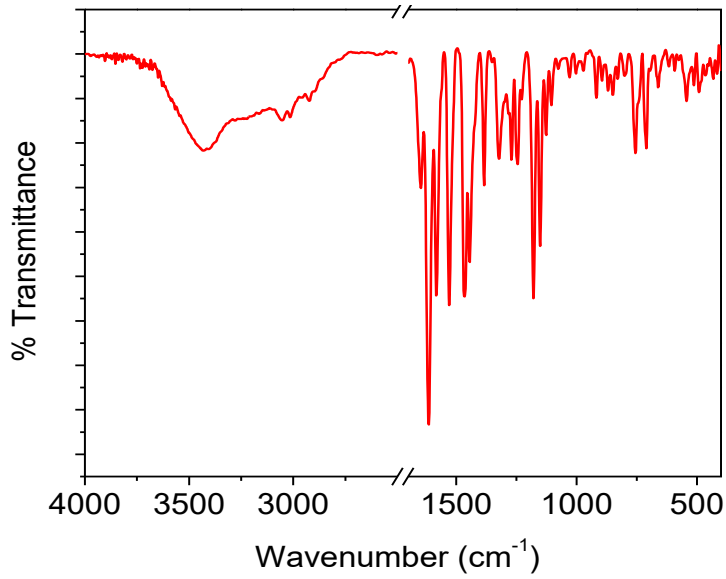

Figure A16. FT-IR spectra of [Zn(sal-3,4-ben)] measured at ATR mode.

TGA-DTA Curves

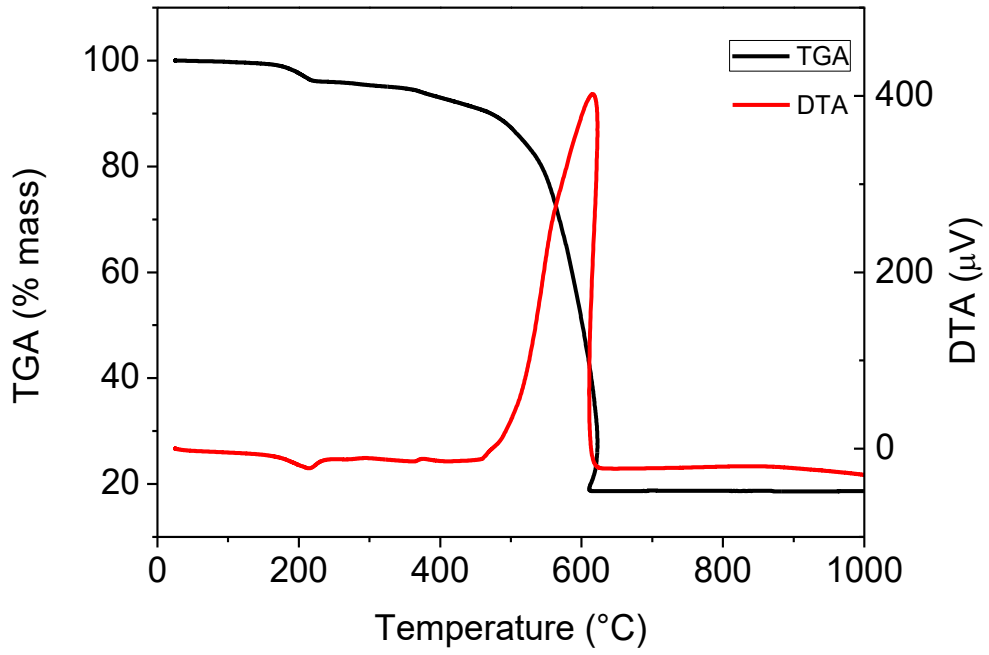

Figure A17. Thermo-gravimetric analyses (TGA) and differential thermal analyses (DTA) of [Zn(sal-3,4-ben)].

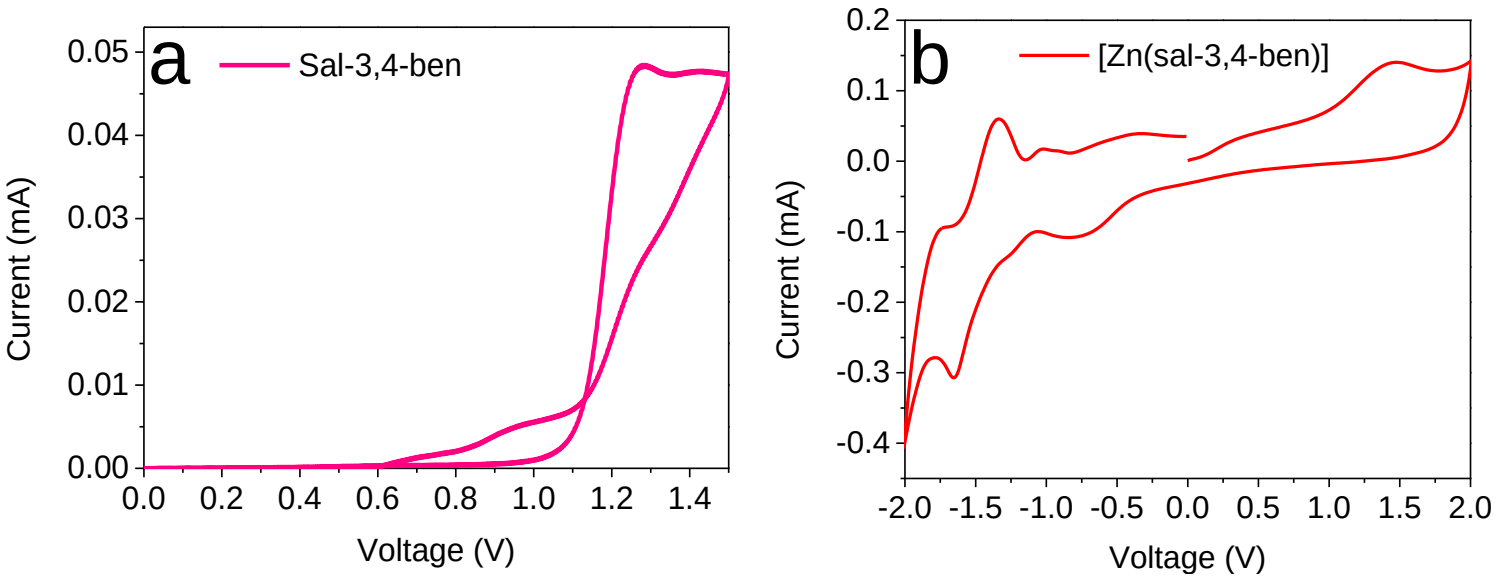

Figure A18. Cyclic voltammogram of sal-3,4-ben (a) and [Zn(sal-3,4-ben)] (b) measured in acetonitrile ($1.0x10^{-4}$ mol L^{-1}).

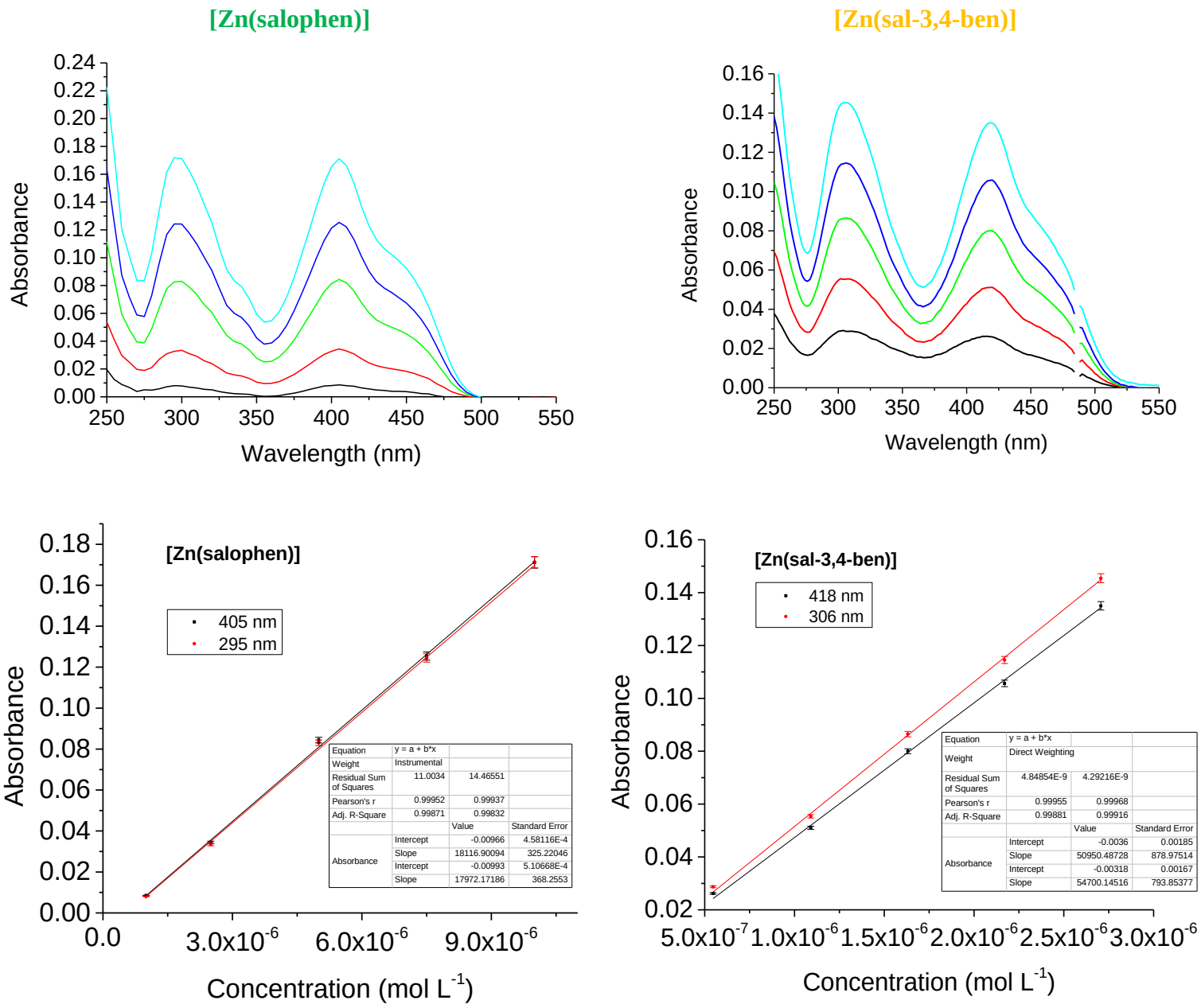

Figure A19. [Zn(salophen)] and [Zn(sal-3,4-ben)] electronic absorption spectra and Lambert-Beer fits in THF solution.

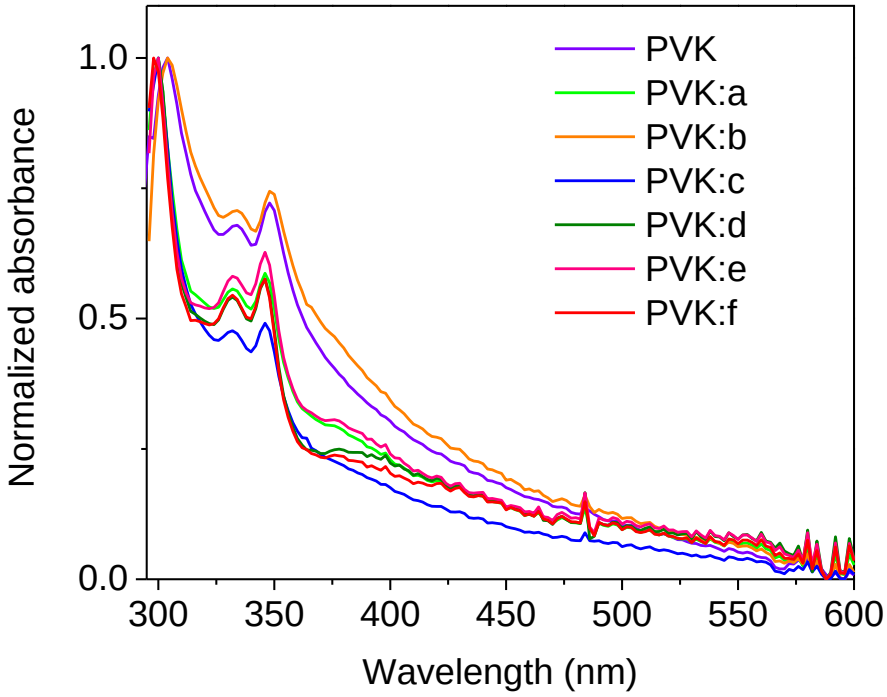

Figure A20. Normalized electronic absorption spectra of the PVK:X (2.5 % mol/mol) solution-processed diodes where X = a) Alq_3, b) Znq_2, c) salophen, d) [Zn(salophen)], e) sal-3,4-ben and f) [Zn(sal-3,4-ben)].

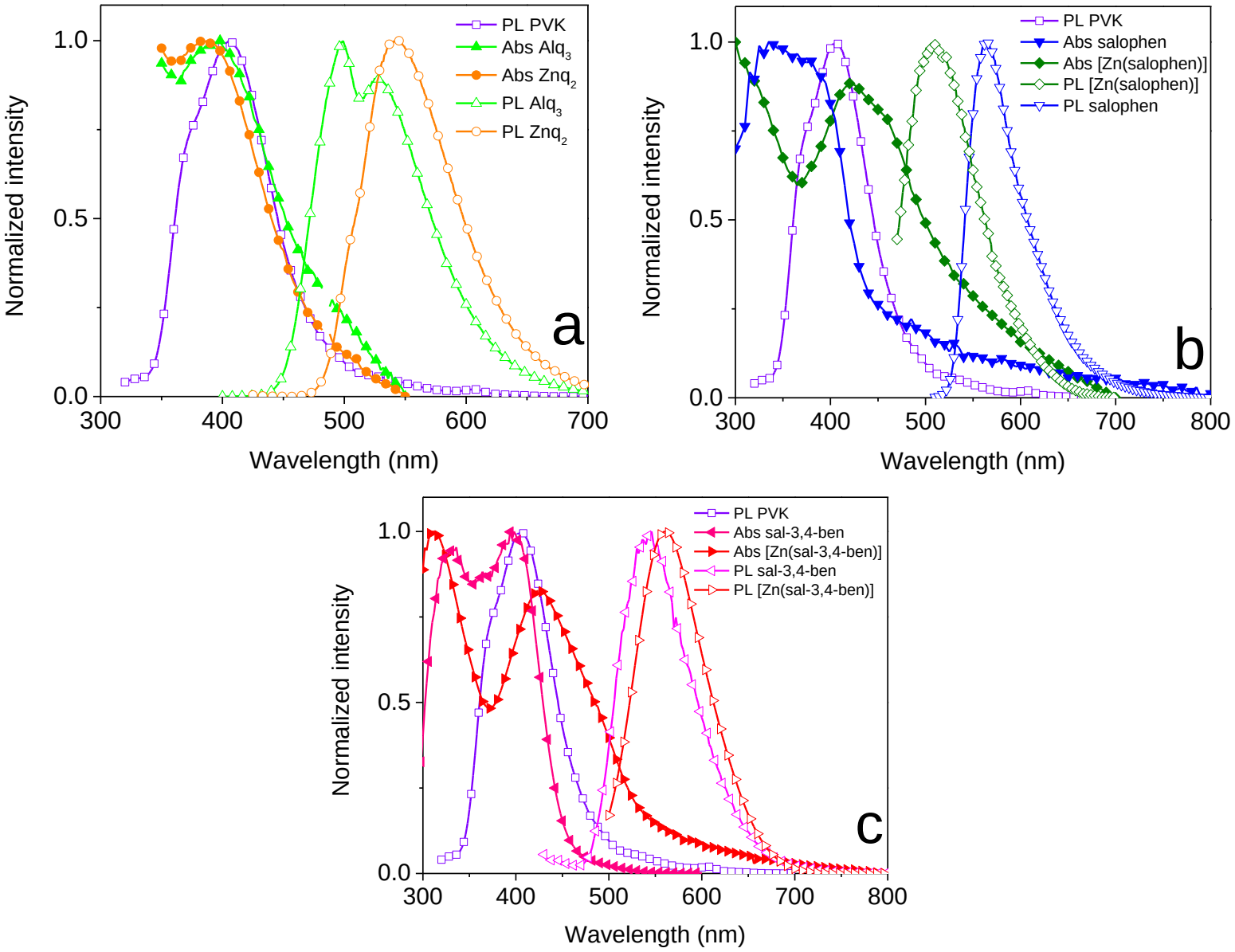

Figure A21. Spectral overlap between the PL emission of the PVK and the electronic absorption and PL spectra of the compounds at solid-state: a. Alq_3 and Znq_2, b. salophen and [Zn(salophen)], c. sal-3,4-ben and [Zn(sal-3,4-ben)].

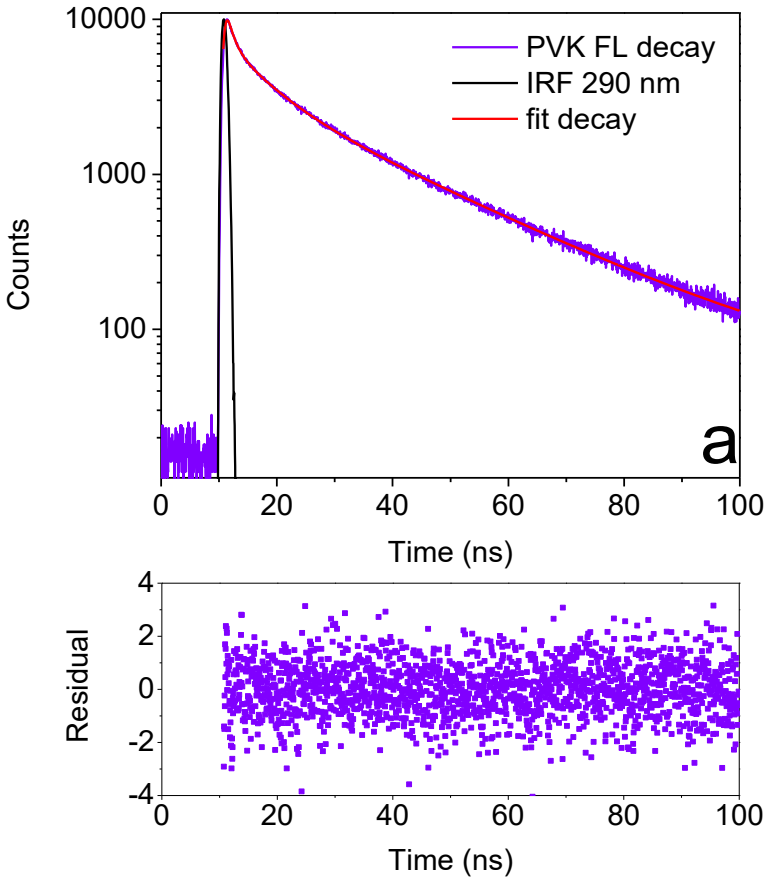

	Fix	Value / ns	Std. Dev / ns		Fix	Value	Std. Dev	Rel %
τ_1		1.0765	0.03321	B1		0.029	0.0005	6.00
τ_2		6.5244	0.16576	B2		0.017	0.0002	20.45
τ_3		24.2563	0.24592	B3		0.016	0.0002	73.55
τ_4				B4				
ϑ		0.1896	0.0060	A		35.918		

χ^2 : 1.036

Figure A22a. Fluorescence decays, residuals from the fitting the decay curves, results of the fitting (Table) - PVK (λ_{exc} = 290 nm; λ_{PL} = 405 nm).

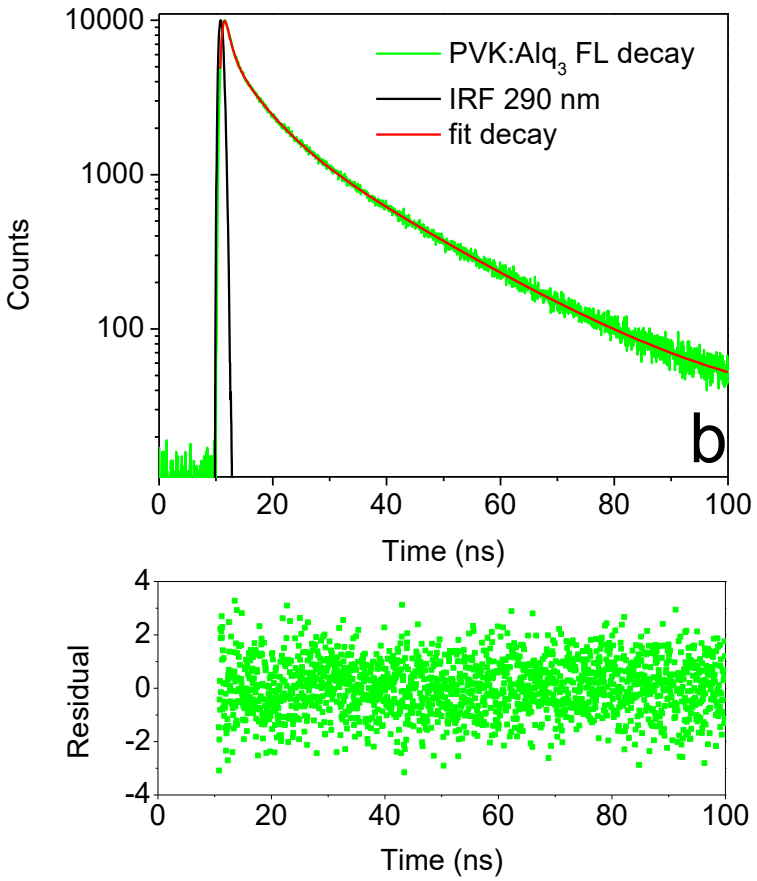

	Fix	Value / ns	Std. Dev / ns		Fix	Value	Std. Dev	Rel %
τ_1	☐	0.9883	0.02350	B1	☐	0.038	0.0004	10.56
τ_2	☐	5.3889	0.10259	B2	☐	0.019	0.0002	28.94
τ_3	☐	19.6318	0.17300	B3	☐	0.011	0.0002	60.49
τ_4	☐			B4	☐			
δ	☐	0.0092	0.0043	A	☐	23.860		

χ^2 : 1.062

Figure A22b. Fluorescence decays, residuals from the fitting the decay curves, results of the fitting (Table) - PVK:Alq_3 composite (λ_{exc} = 290 nm; λ_{PL} = 405 nm).

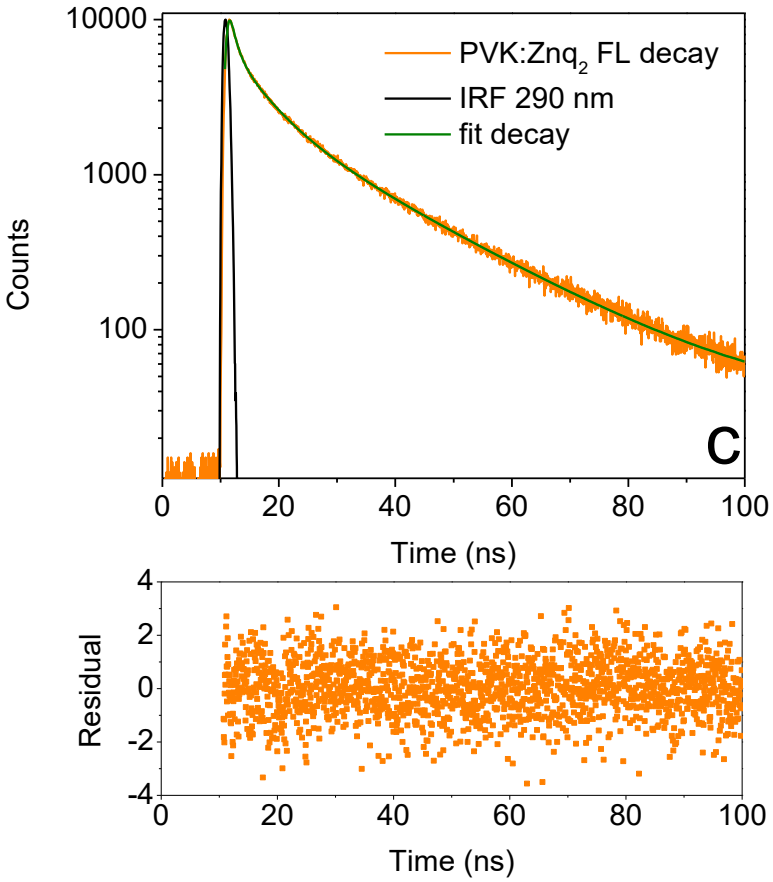

	Fix	Value / ns	Std. Dev / ns		Fix	Value	Std. Dev	Rel %
τ_1		1.0513	0.02635	B1		0.035	0.0004	9.68
τ_2		5.5734	0.11425	B2		0.019	0.0002	27.48
τ_3		20.2930	0.18341	B3		0.012	0.0002	62.84
τ_4				B4				
δ		0.0138	0.0043	A		26.803		

χ^2 : 1.086

Figure A22c. Fluorescence decays, residuals from the fitting the decay curves, results of the fitting (Table) - PVK:Znq$_2$ composite (λ_{exc} = 290 nm; λ_{PL} = 405 nm).

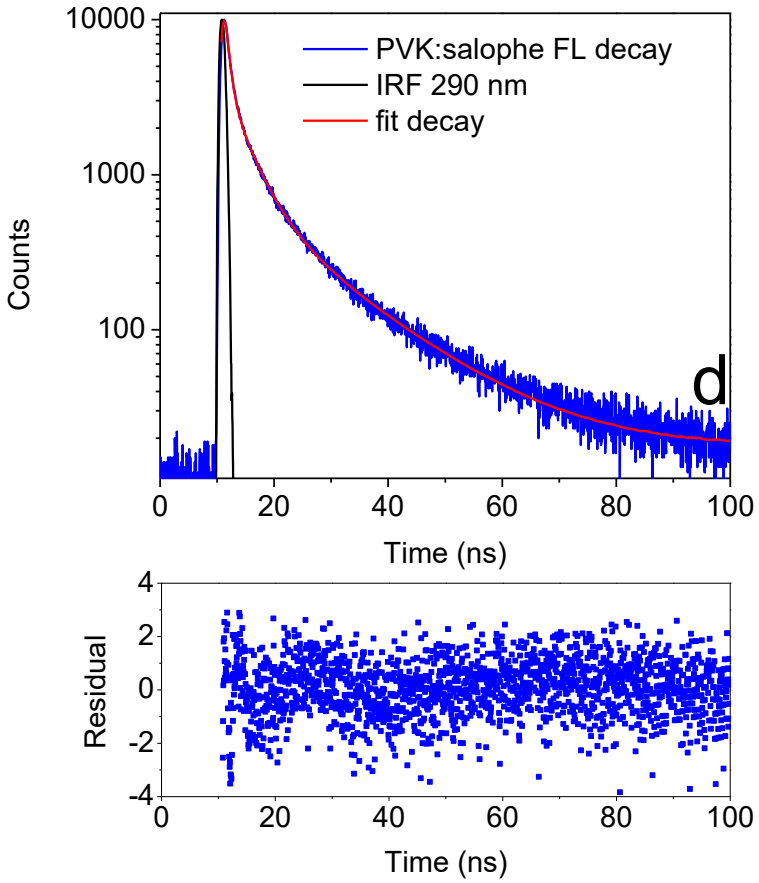

	Fix	Value / ns	Std. Dev / ns		Fix	Value	Std. Dev	Rel %
τ_1		0.6575	0.01144	B1		0.073	0.0007	31.05
τ_2		3.6435	0.05483	B2		0.016	0.0002	37.42
τ_3		14.7497	0.16858	B3		0.003	0.0001	31.53
τ_4				B4				
δ		0.1363	0.0054	A		16.534		

χ^2 : 1.173

Figure A22d. Fluorescence decays, residuals from the fitting the decay curves, results of the fitting (Table) - PVK:salophen (λ_{exc} = 290 nm; λ_{PL} = 405 nm).

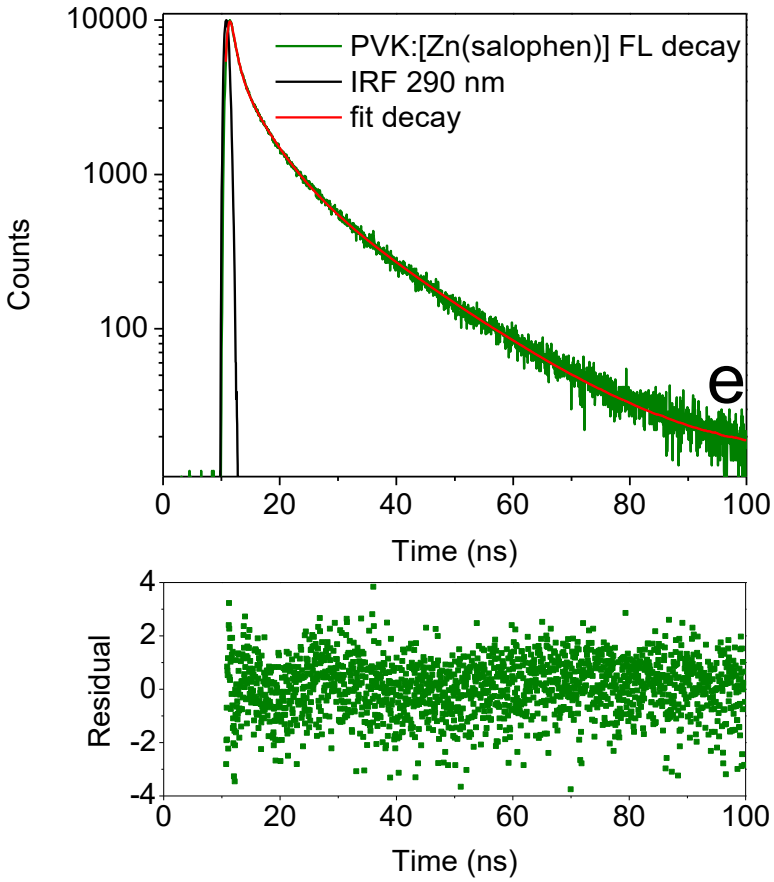

	Fix	Value / ns	Std. Dev / ns		Fix	Value	Std. Dev	Rel %
τ_1		0.9395	0.01866	B1		0.047	0.0004	18.74
τ_2		4.6115	0.08034	B2		0.019	0.0003	36.25
τ_3		15.9422	0.14974	B3		0.007	0.0001	45.02
τ_4				B4				
δ		0.0393	0.0044	A		11.907		

χ^2 : 1.154

Figure A22e. Fluorescence decays, residuals from the fitting the decay curves, results of the fitting (Table) - PVK:[Zn(salophen)] (λ_{exc} = 290 nm; λ_{PL} = 405 nm).

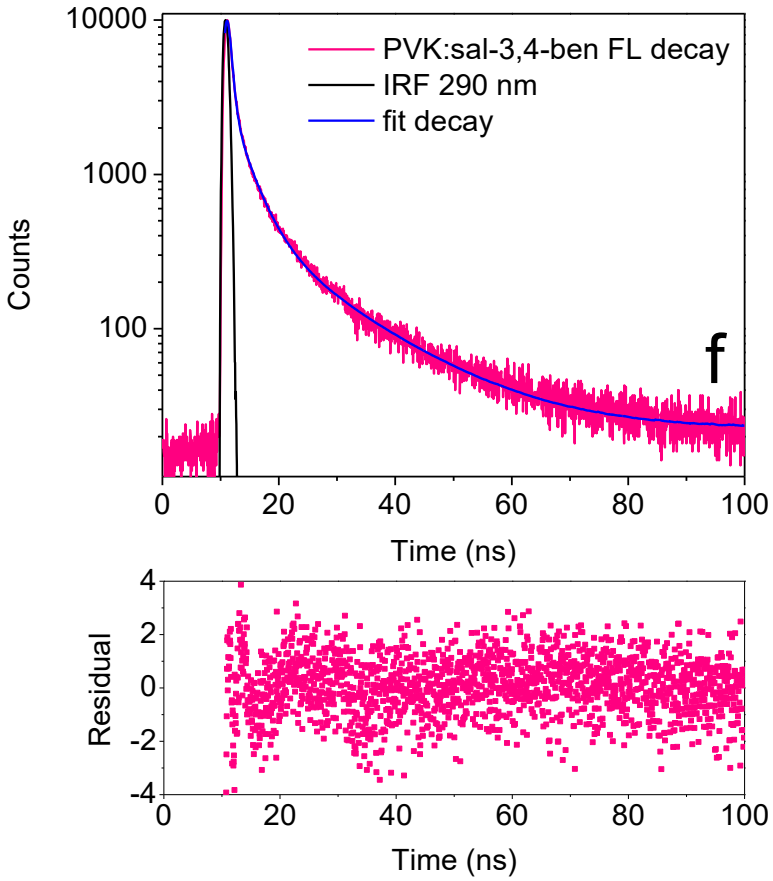

	Fix	Value / ns	Std. Dev / ns		Fix	Value	Std. Dev	Rel %
τ_1		0.5380	0.00934	B1		0.093	0.0010	40.97
τ_2		3.1615	0.05012	B2		0.013	0.0002	33.11
τ_3		14.9356	0.20469	B3		0.002	0.0000	25.92
τ_4				B4				
δ		0.1958	0.0061	A		21.597		

χ^2 : 1.250

Figure A22f. Fluorescence decays, residuals from the fitting the decay curves, results of the fitting (Table) - PVK:sal-3,4-ben (λ_{exc} = 290 nm; λ_{PL} = 405 nm).

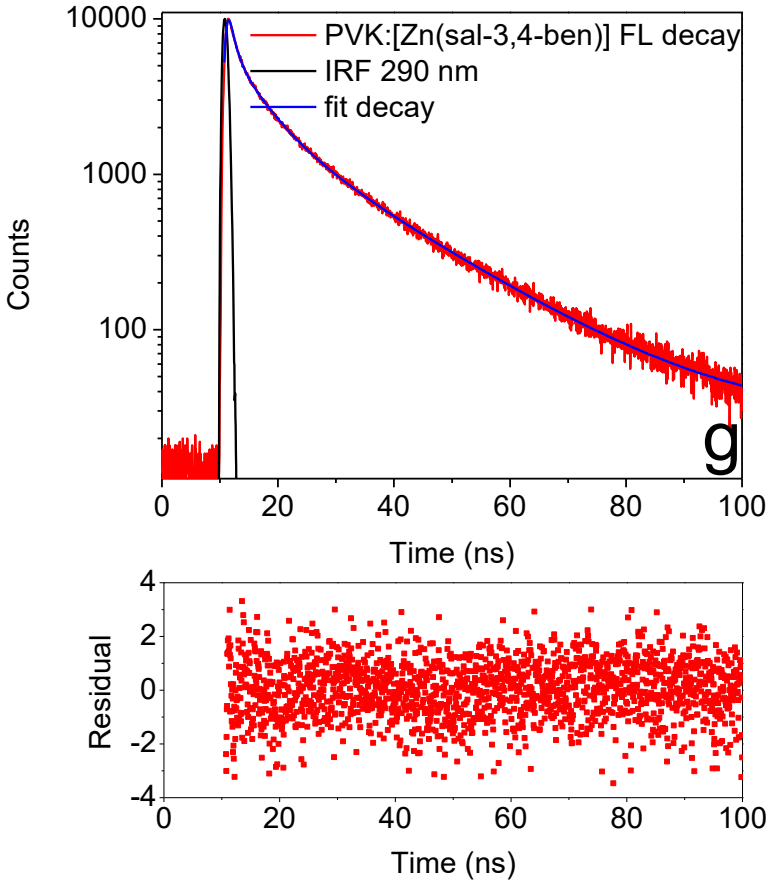

	Fix	Value / ns	Std. Dev / ns		Fix	Value	Std. Dev	Rel %
τ_1	☐	0.9913	0.02446	B1	☐	0.037	0.0004	11.12
τ_2	☐	5.1760	0.09832	B2	☐	0.019	0.0003	30.42
τ_3	☐	18.3585	0.15688	B3	☐	0.010	0.0002	58.46
τ_4	☐			B4	☐			
δ	☐	0.0507	0.0047	A	☐	23.061		

χ^2 : 1.172

Figure A22g. Fluorescence decays, residuals from the fitting the decay curves, results of the fitting (Table) - PVK:[Zn(sal-3,4-ben)] (λ_{exc} = 290 nm; λ_{PL} = 405 nm).

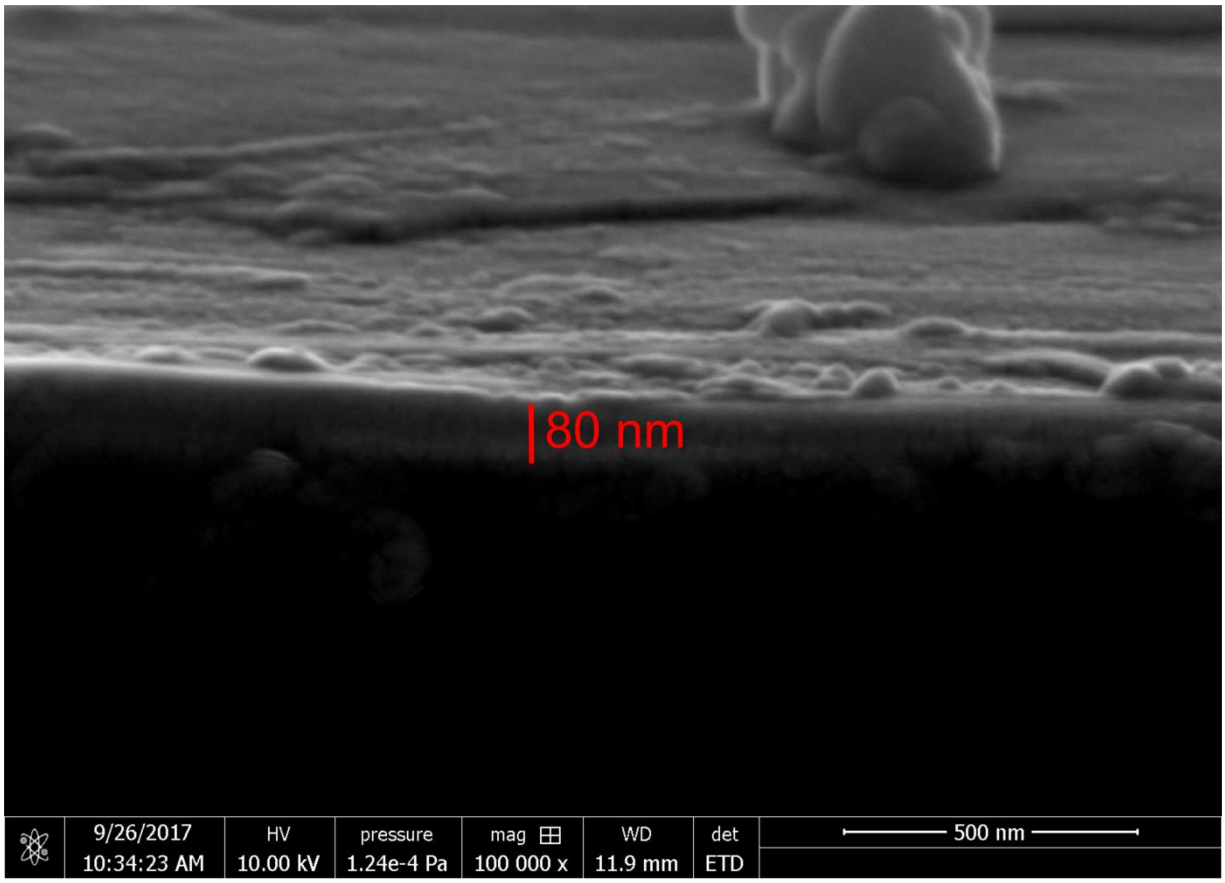

Figure A23. FEG-SEM cross-section image of the solution-processed PVK thin film (L ≈ 80 nm).

Zn(II)Salicylidenes in PFO – OLEDs and Optical characterization

Electronic Absorption and Photoluminescence Excitation Spectroscopies

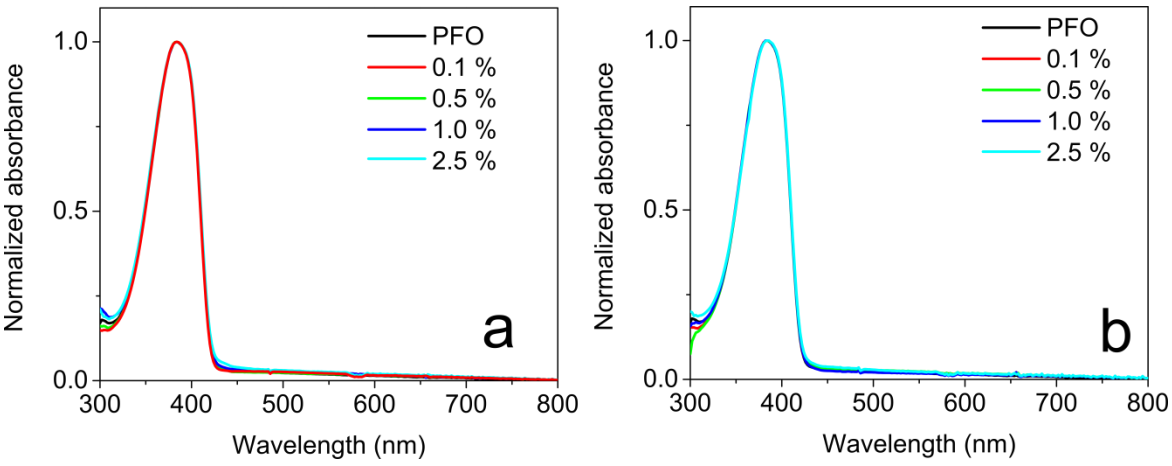

Figure A24. Normalized electronic absorption spectra of the PVK|PFO:Zn(salicylidene) composites thin films: a) PFO:[Zn(salophen)]; and b) PFO:[Zn(sal-3,4-ben)].

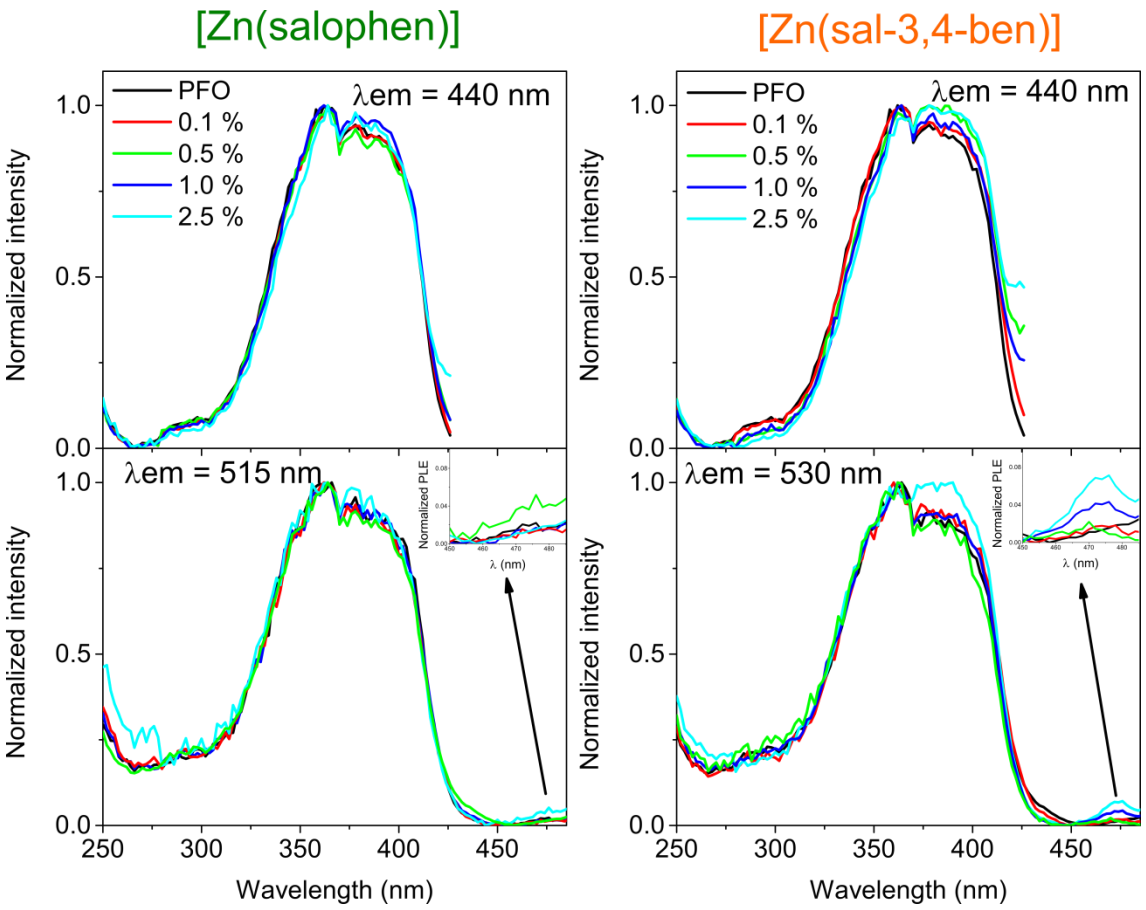

Figure A25. Normalized PLE spectra of the PVK|PFO:Zn(salicylidene) composites thin films (PFO:[Zn(salophen)] – left, λ_{em1} = 440 nm and λ_{em2} = 515 nm; PFO:[Zn(sal-3,4-ben)] – right, λ_{em1} = 440 nm and λ_{em2} = 530 nm).

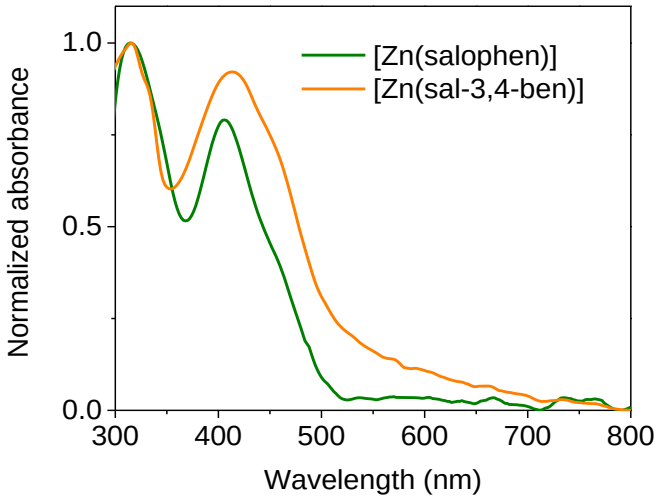

Figure A26. Normalized electronic absorption spectra of the [Zn(salophen)] (green) and [Zn(sal-3,4-ben)] (orange curve) PFO composites (2.5 % mol/mol) using PVK:PFO thin-film as baseline.

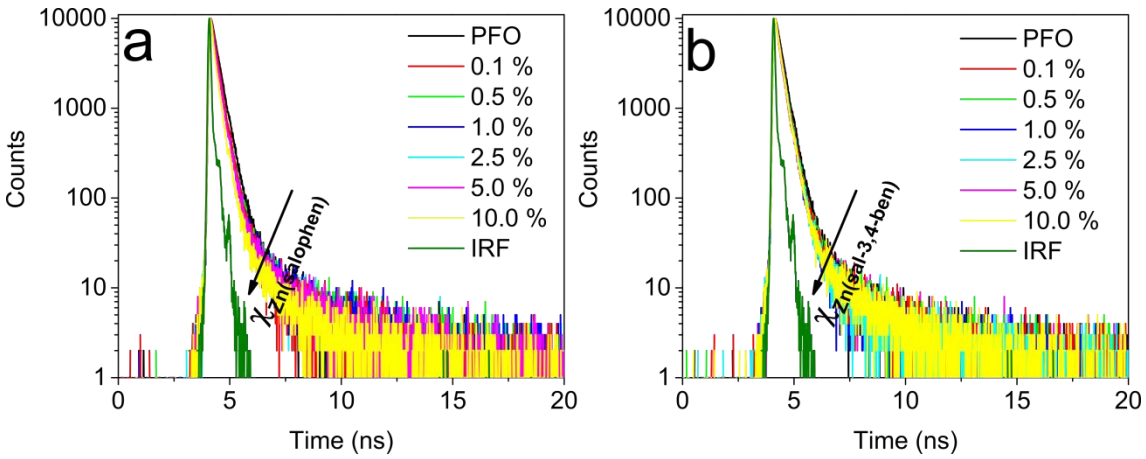

Figure A27. Fluorescence decays of the PFO:Zn(salicylidenes) composites (λ_{exc} = 370 nm, λ_{PL} = 425 nm): a) PFO:[Zn(salophen)]; and b) PFO:[Zn(sal-3,4-ben)].

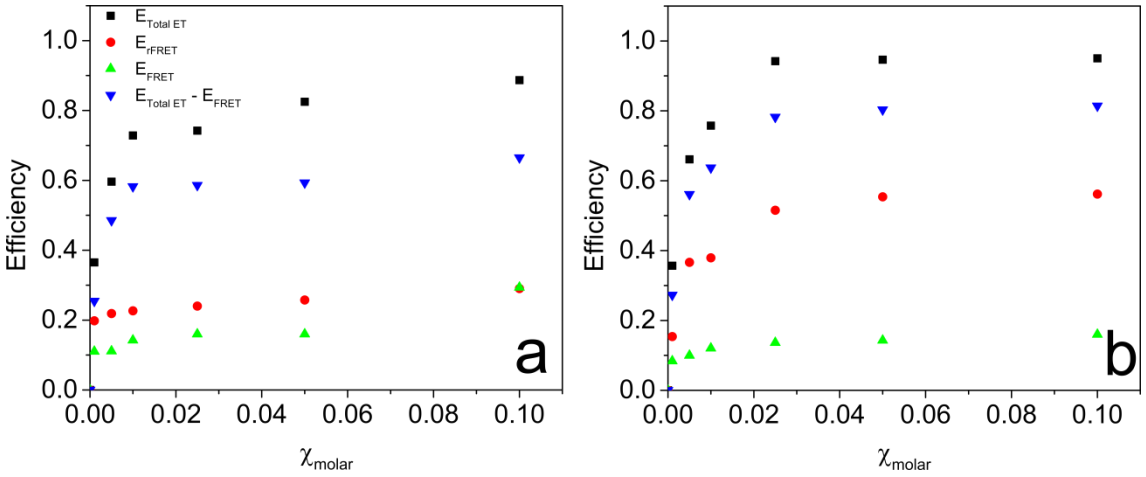

Figure A28. Total energy transfer (black squares), relative FRET (red circles), average FRET (green triangles) and Total ET - E_{aFRET} (blue nablas) efficiencies calculations for PFO:Zn(salicylidenes) composites: a) PFO:[Zn(salophen)]; and b) PFO:[Zn(sal-3,4-ben)].

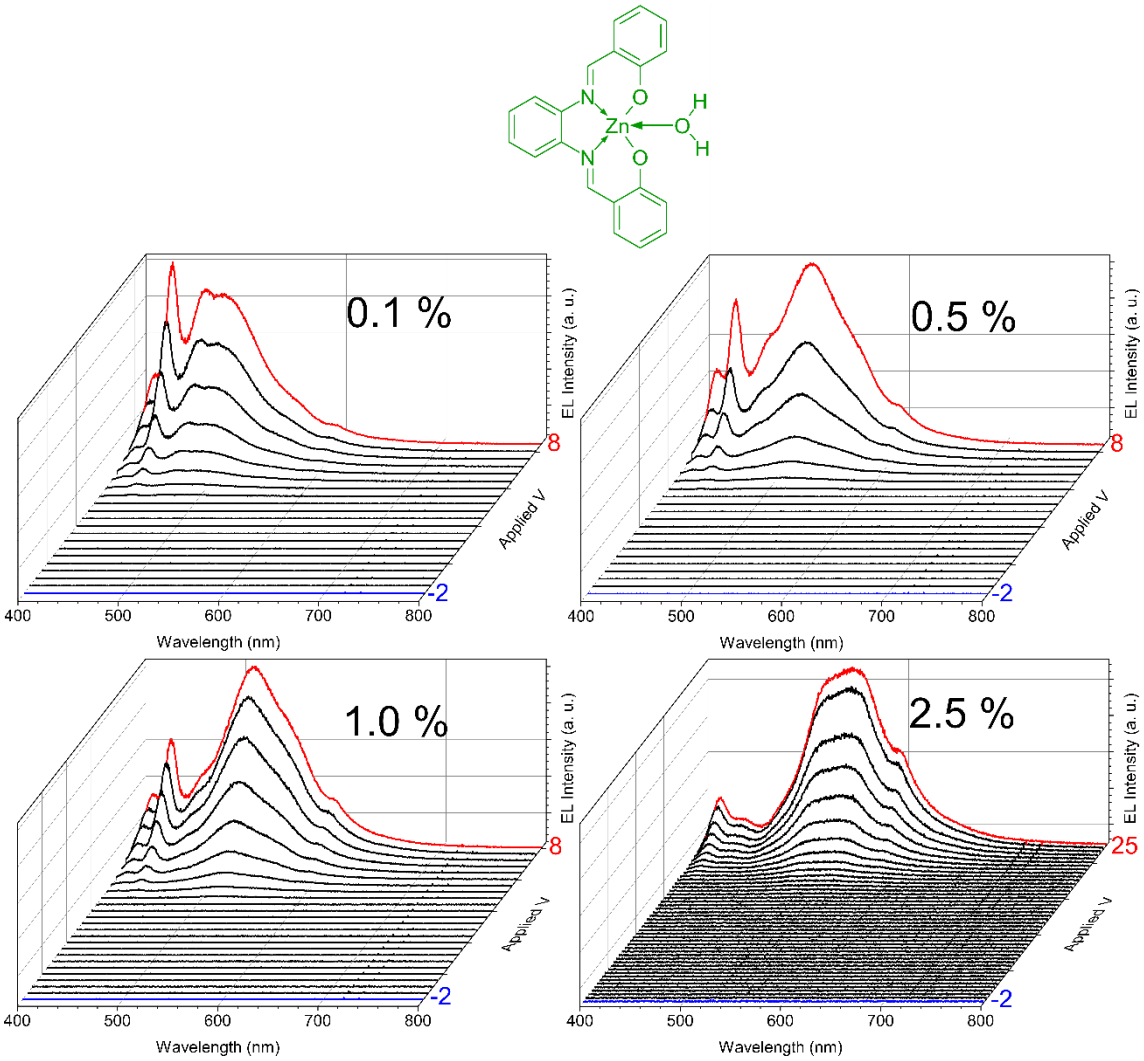

Figure A29. Dependence of the ITO|PEDOT:PSS|PVK|PFO:[Zn(salophen)] *X* % (mol/mol)|Ca|Al OLEDs electroluminescence spectra with the applied field**.**

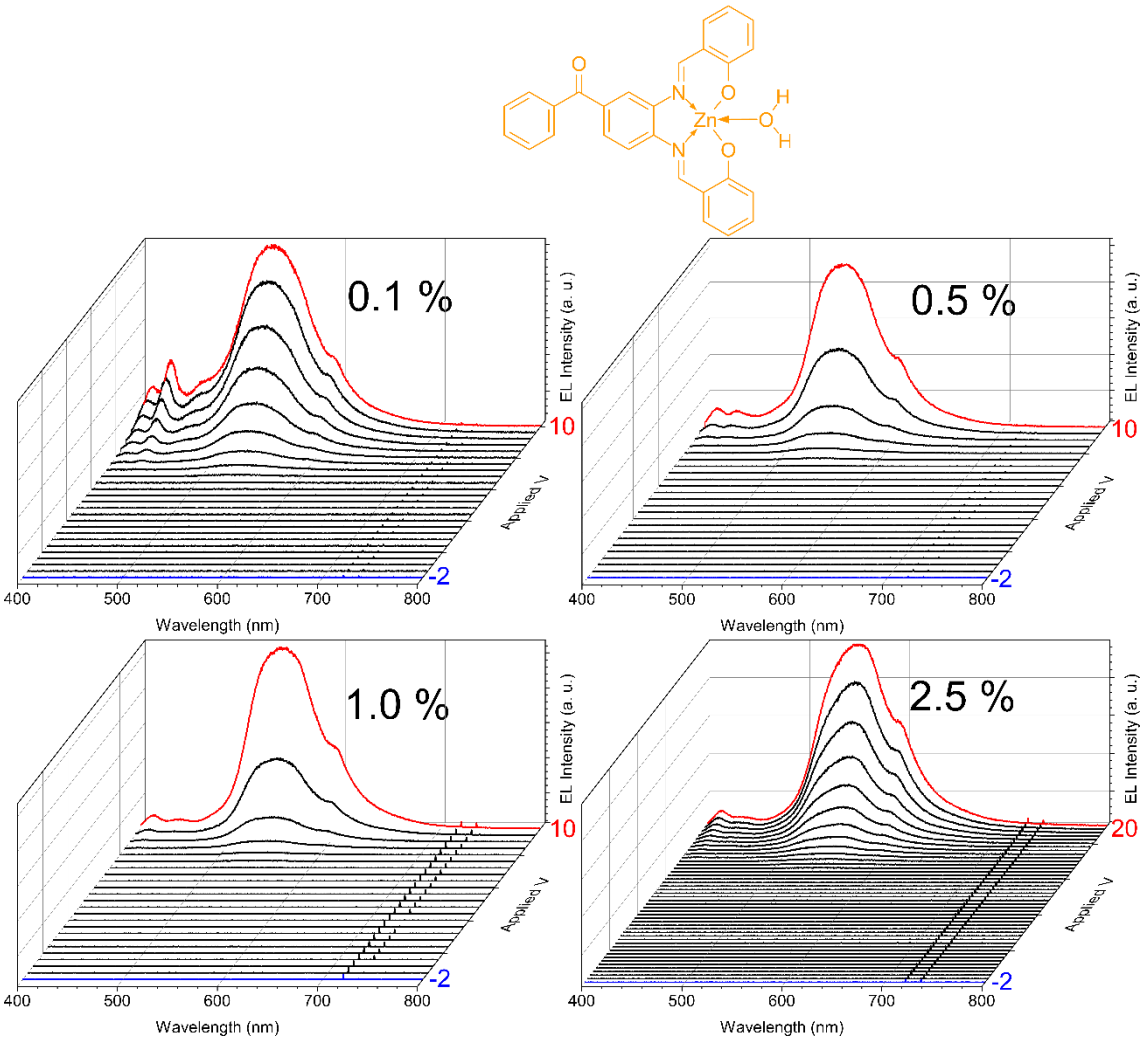

Figure A30. Dependence of the ITO|PEDOT:PSS|PVK|PFO:[Zn(sal-3,4-ben)] *X* % (mol/mol)|Ca|Al OLEDs electroluminescence spectra with the applied field.

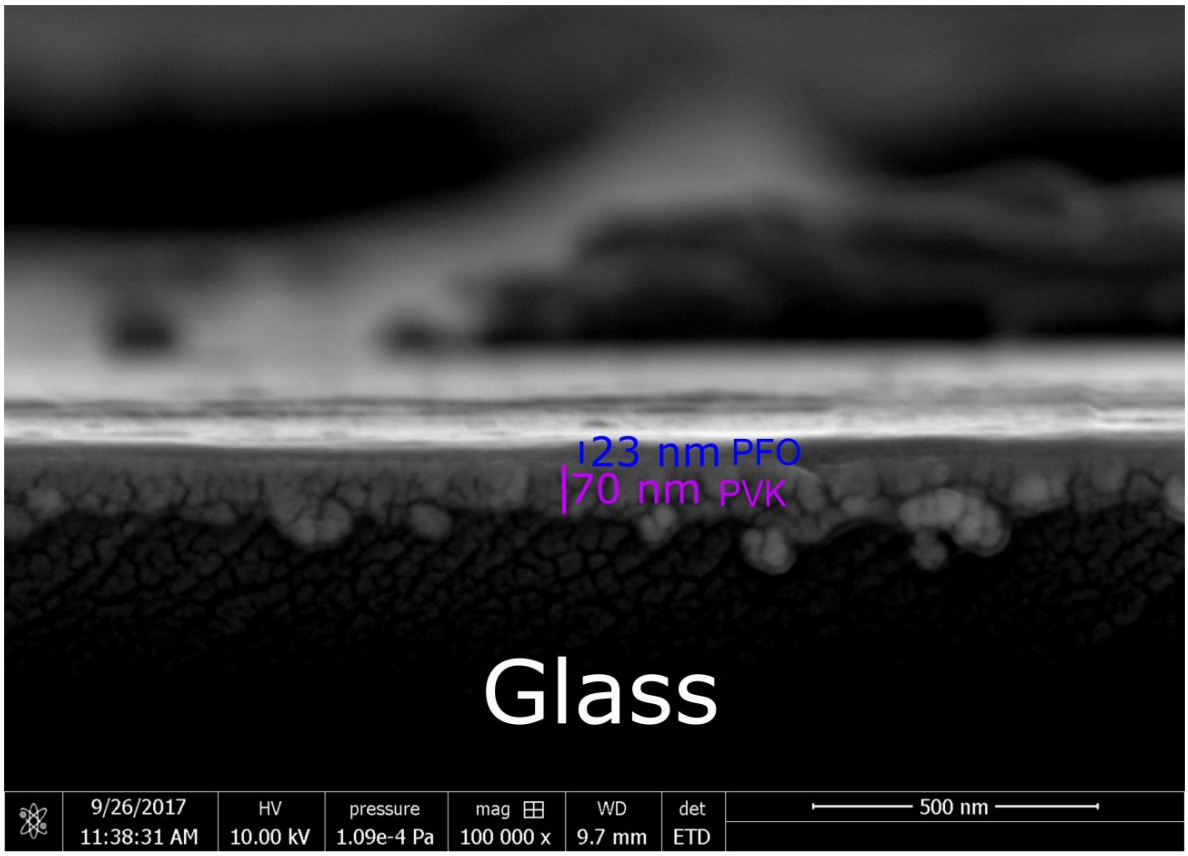

Figure A31. FEG-SEM cross-section image of the solution-processed PVK|PFO thin film ($L_{PVK} \approx 70$ nm and PFO ≈ 23 nm).

[Pt(salicylidenes)]

^{1}H and ^{13}C NMR spectra

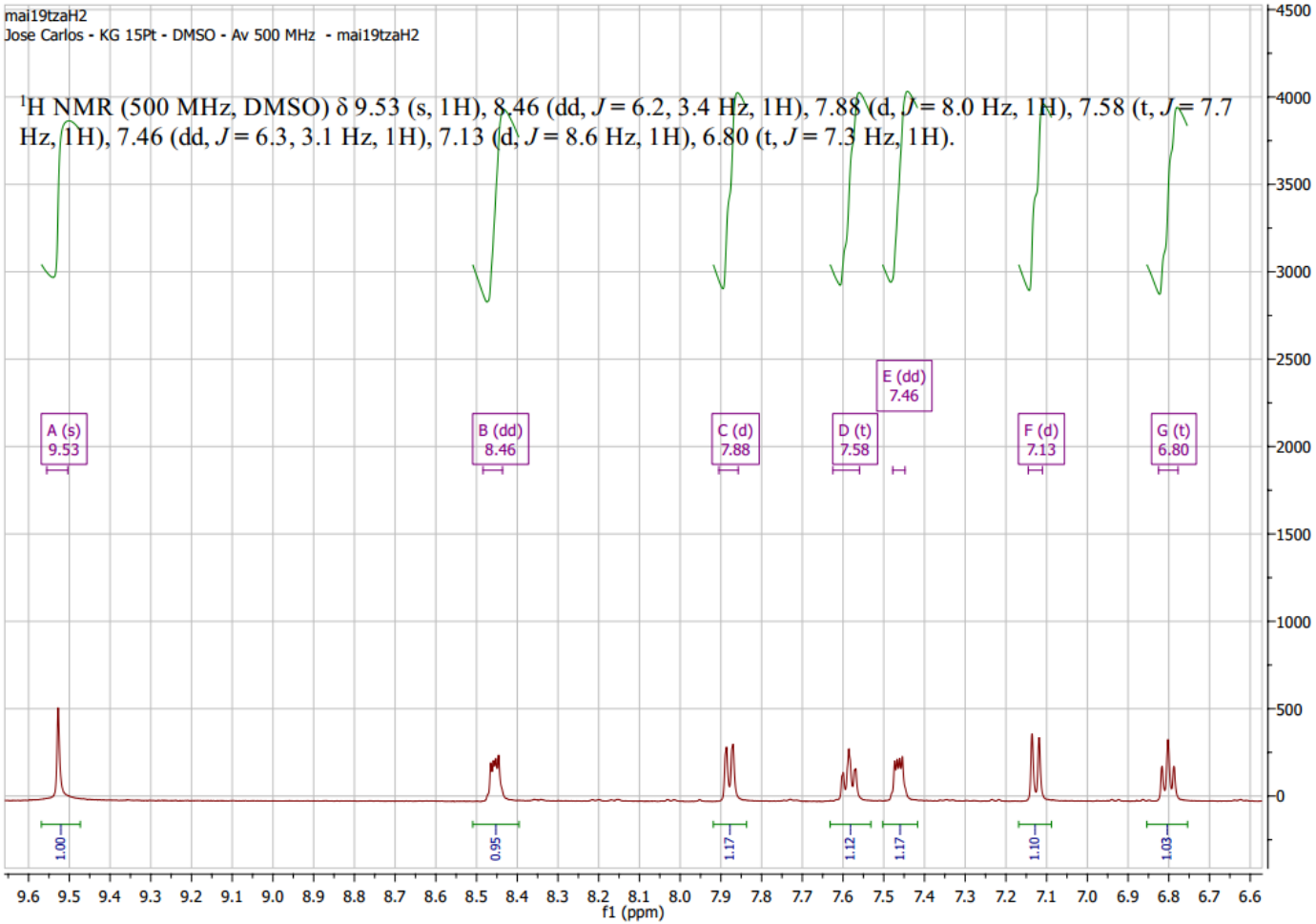

Figure A32. ^{1}H NMR spectrum of [Pt(salophen)] solution in DMSO-d_6.

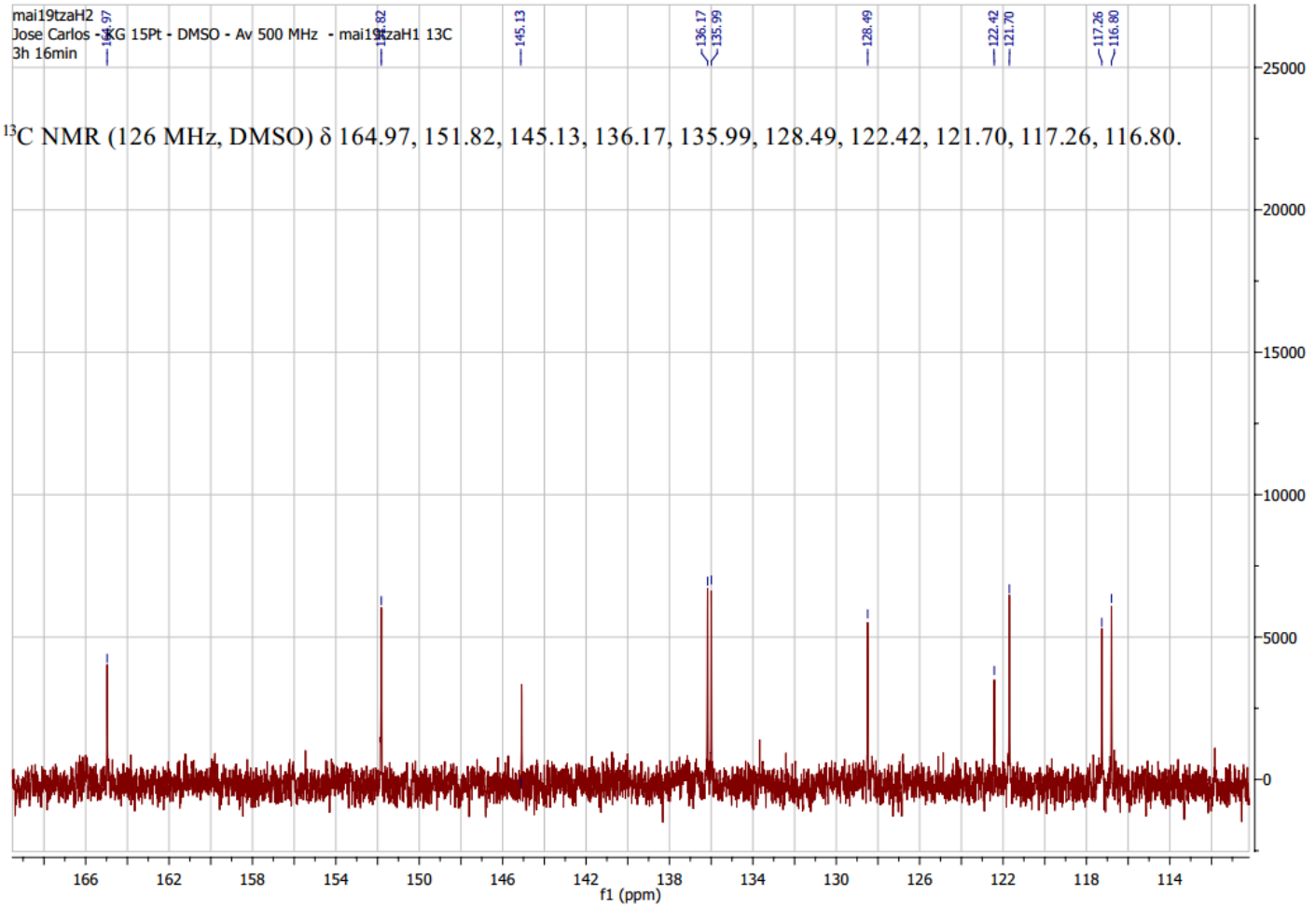

Figure A33. ^{13}C NMR spectrum of [Pt(salophen)] solution in DMSO-d_6.

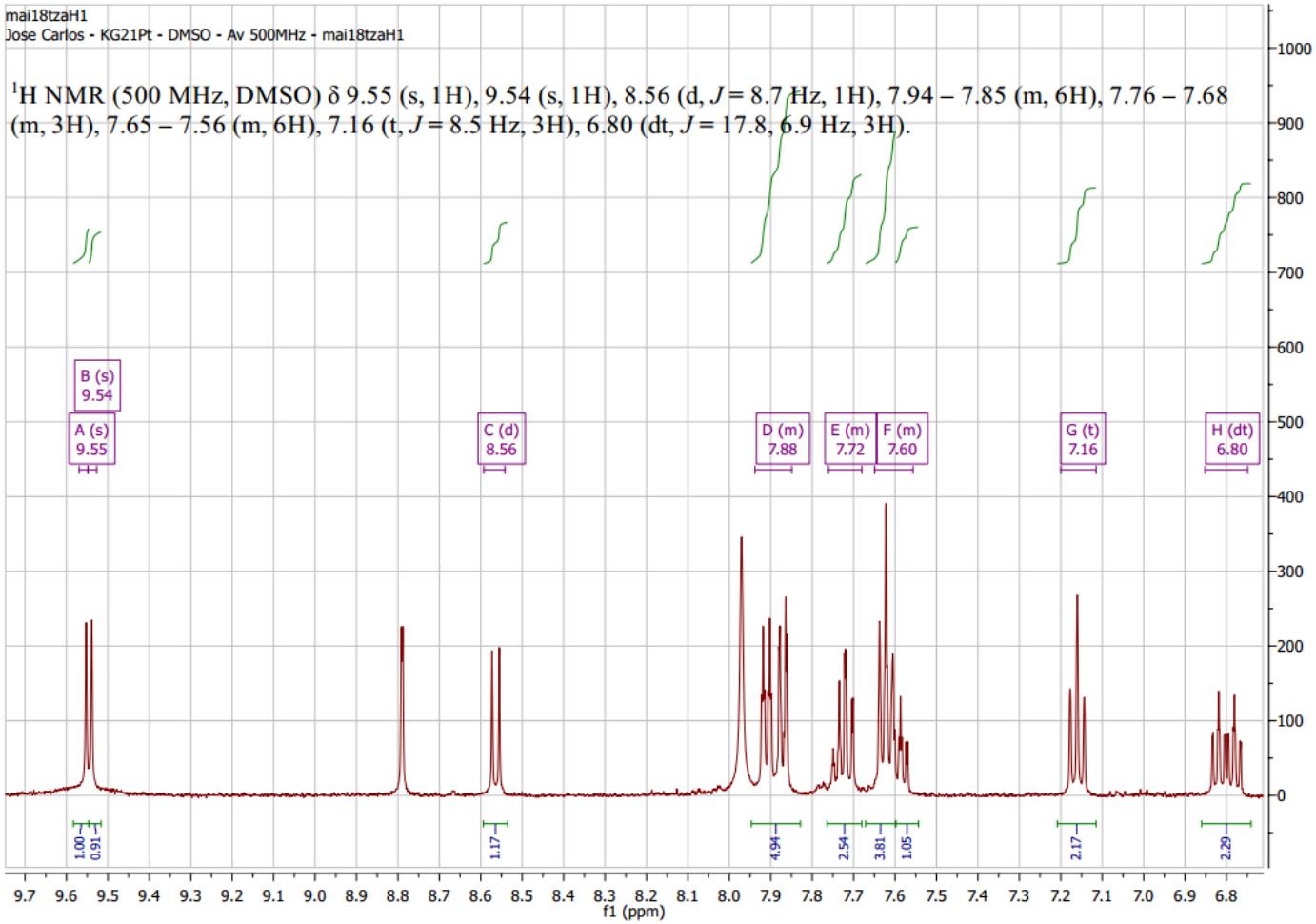

Figure A34. ^{1}H NMR spectrum of [Pt(sal-3,4-ben)] solution in DMSO-d_6.

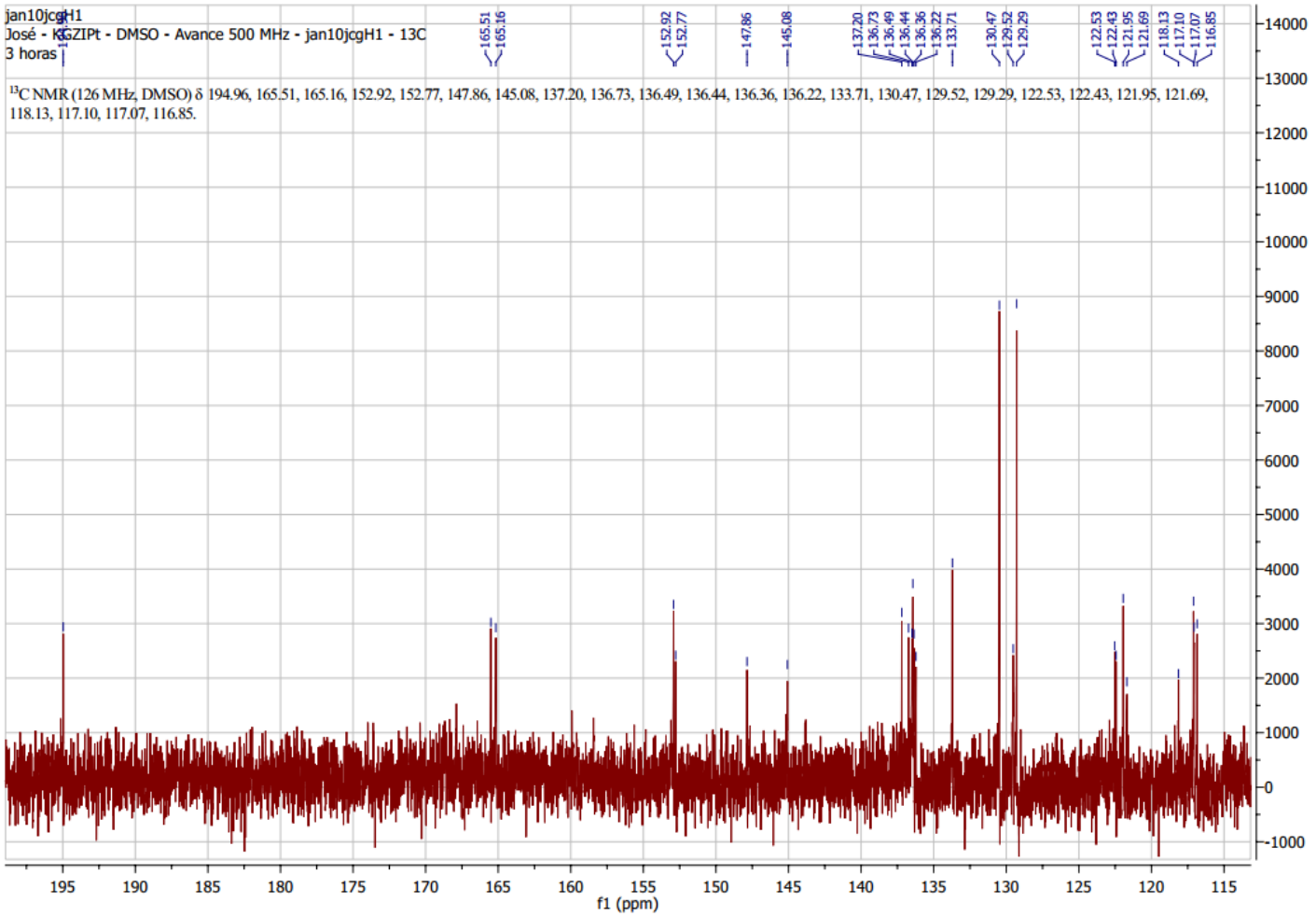

Figure A35. ^{13}C NMR spectrum of [Pt(sal-3,4-ben)] solution in DMSO-d_6.

Time-of-Flight Mass Spectrometry

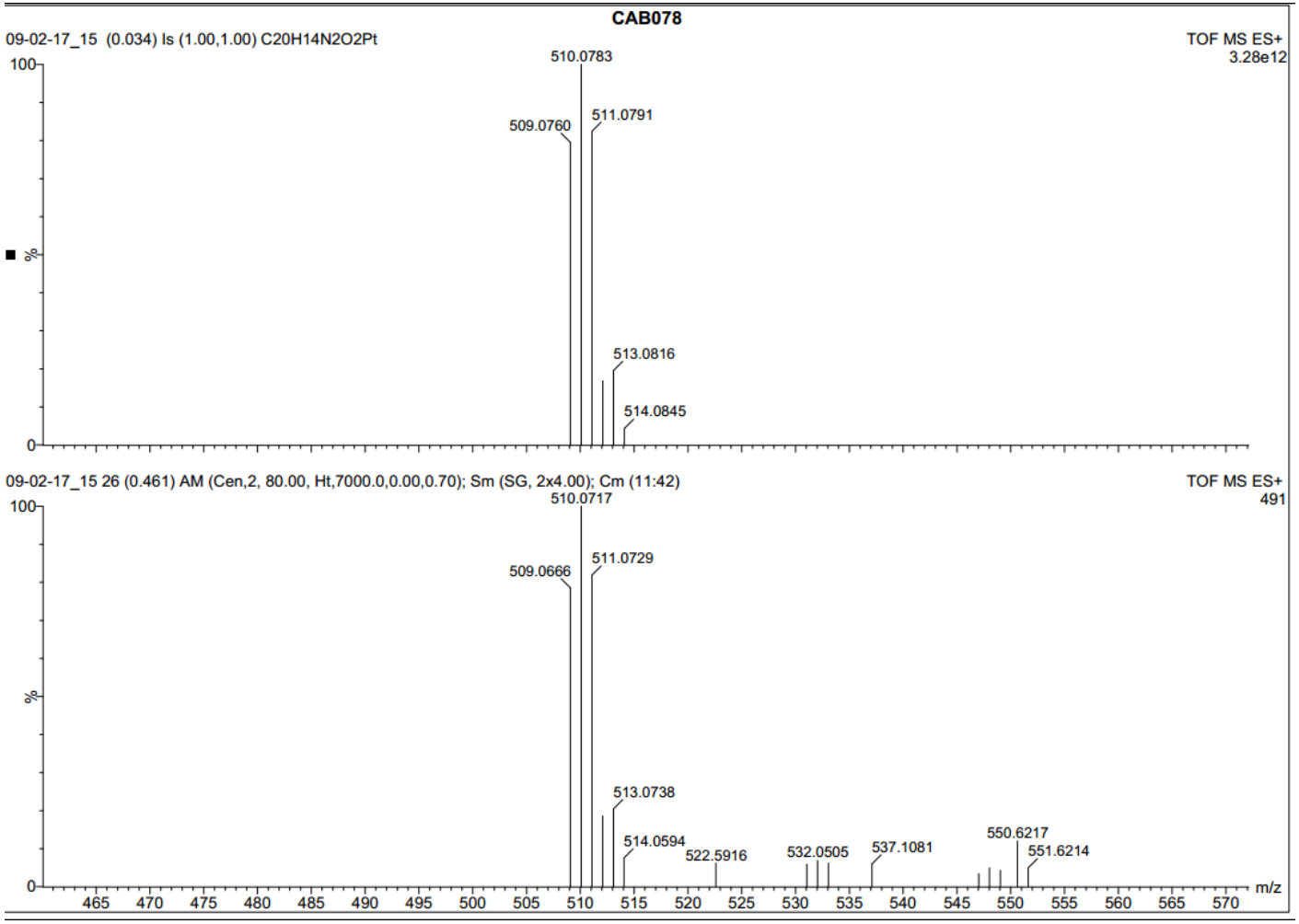

Figure A36. [Pt(salophen)] TOF-MS spectrometry at positive mode.

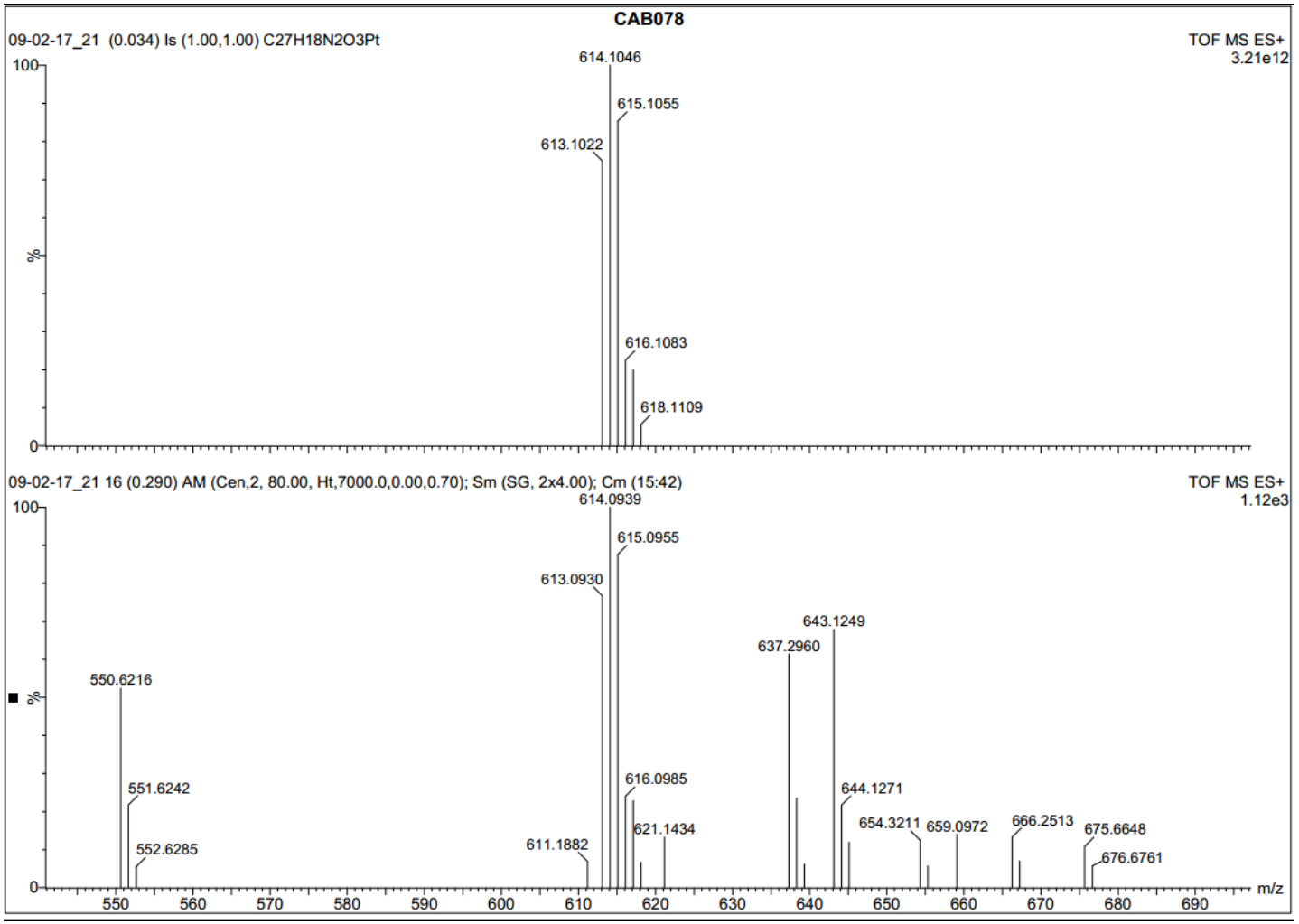

Figure A37. [Pt(sal-3,4-ben)] TOF-MS at positive mode.

Fourier-transform infrared spectra

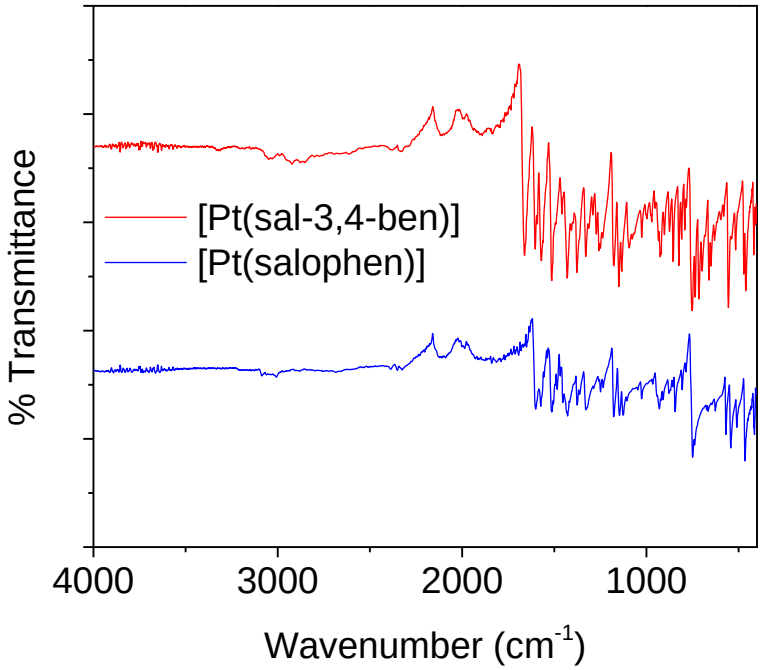

Figure A38. FT-IR spectra of [Pt(salophen)] (blue curve) [Pt(sal-3,4-ben)] (red curve) in ATR mode.

Crystallographic Data

[Pt(salophen)]

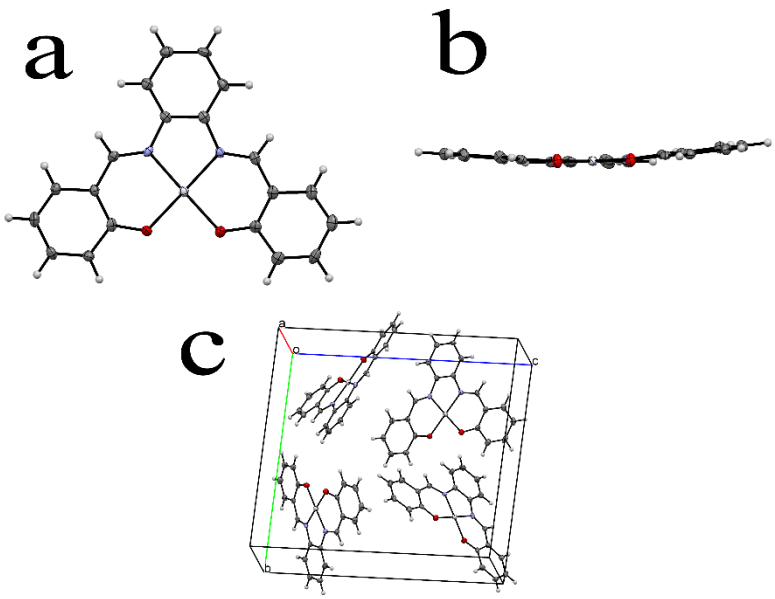

Figure A39. Crystal structure in the plane (a), out of plane (b) and cell packing of the [Pt(salophen)] (c) ellipsoids with 50 % probability.

Table A3. Crystal data of the [Pt(salophen)].

$C_{20}H_{14}N_2O_2Pt$	
M_r = 509.42	D_x = 2.172 Mg m^{-3}
Orthorhombic	
Hall symbol: $P2_12_12_1$	Mo $K\alpha$ radiation, λ = 0.71073 Å
a = 5.2794 (3) Å	Cell parameters from 9937 reflections
b = 16.8189 (9) Å	θ = 2.6–28.3°
c = 17.5444 (9) Å	μ = 9.02 mm^{-1}
V = 1557.83 (15) Å^3	T = 150 K
Z = 4	Needle, red
F(000) = 968	0.24 × 0.07 × 0.03 mm

Data collection

BRUKER APEX CCD DETECTOR DIFFRACTOMETER diffractometer	3692 independent reflections
Radiation source: FINE-FOCUS SEALED TUBE, Mo Kα (λ = 0.71073 Å)	3509 reflections with $I > 2\sigma(I)$
CCD DETECTOR monochromator	R_{int} = 0.039
Detector resolution: 8.3333 pixels mm^{-1}	θ_{max} = 27.9°, θ_{min} = 1.7°
Phi and ω Scans scans	h = −6 6
Absorption correction: multi-scan *SADABS2014*/5 (Bruker,2014/5) was used for absorption correction. wR2(int) was 0.0860 before and 0.0587 after correction. The Ratio of minimum to maximum transmission is 0.7762. The λ/2 correction factor is 0.00150.	k = −22 22
T_{min} = 0.579, T_{max} = 0.746	l = −22 23
18211 measured reflections	

Refinement

Refinement on F^2	Hydrogen site location: inferred from neighbouring sites
Least-squares matrix: full	H-atom parameters constrained
$R[F^2 > 2\sigma(F^2)] = 0.020$	$w = 1/[\sigma^2(F_o^2) + (0.0159P)^2]$ where $P = (F_o^2 + 2F_c^2)/3$
$wR(F^2) = 0.041$	$(\Delta/\sigma)_{max} = 0.002$
$S = 1.00$	$\Delta\rho_{max} = 0.90$ e Å^{-3}
3692 reflections	$\Delta\rho_{min} = -0.65$ e Å^{-3}
226 parameters	Extinction correction: none
0 restraints	
	Absolute structure: Flack x determined using 1431 quotients [(I+)-(I-)]/[(I+)+(I-)] (Parsons, Flack and Wagner, Acta Cryst. B69 (2013) 249-259).
Primary atom site location: dual	Absolute structure parameter: −0.002 (7)

Fractional atomic coordinates and isotropic or equivalent isotropic displacement parameters (Å^2)

	x	*y*	*z*	U_{iso}*/U_{eq}
Pt01	0.34259 (4)	0.28306 (2)	0.69175 (2)	0.01433 (6)
O002	0.3515 (8)	0.3876 (2)	0.6395 (2)	0.0189 (8)
O003	0.0437 (8)	0.3266 (2)	0.7469 (2)	0.0191 (9)
N004	0.6391 (9)	0.2390 (3)	0.6389 (2)	0.0151 (9)
N005	0.3447 (10)	0.1809 (3)	0.7449 (2)	0.0143 (9)
C006	0.7757 (9)	0.2796 (4)	0.5913 (3)	0.0163 (11)
H006	0.920202	0.253539	0.570876	0.020*
C007	0.1976 (9)	0.1642 (3)	0.8026 (3)	0.0174 (11)
H007	0.223149	0.114430	0.826892	0.021*
C008	−0.0645 (9)	0.2901 (4)	0.8041 (3)	0.0174 (10)
C009	−0.2703 (11)	0.3299 (4)	0.8397 (3)	0.0212 (13)
H009	−0.320933	0.380494	0.821113	0.025*
C00A	0.6946 (10)	0.1601 (3)	0.6621 (3)	0.0165 (12)

C00B	0.0029 (10)	0.2136 (4)	0.8324 (3)	0.0177 (11)
C00C	0.7323 (10)	0.3591 (4)	0.5664 (3)	0.0159 (12)
C00D	0.6968 (11)	0.5148 (4)	0.5129 (3)	0.0212 (13)
H00D	0.683458	0.567882	0.494862	0.025*
C00E	−0.3305 (11)	0.2228 (4)	0.9287 (3)	0.0245 (12)
H00E	−0.419626	0.200447	0.970573	0.029*
C00F	0.8972 (11)	0.4676 (4)	0.4883 (3)	0.0225 (14)
H00F	1.020102	0.487721	0.453821	0.027*
C00G	0.5288 (11)	0.4081 (4)	0.5915 (3)	0.0180 (12)
C00H	0.8942 (10)	0.1148 (4)	0.6339 (3)	0.0184 (12)
H00H	1.003124	0.135988	0.595832	0.022*
C00I	0.5749 (12)	0.0515 (4)	0.7443 (3)	0.0217 (13)
H00I	0.464068	0.029322	0.781232	0.026*
C00J	0.9126 (10)	0.3914 (4)	0.5152 (3)	0.0185 (13)
H00J	1.049320	0.358831	0.498862	0.022*
C00K	−0.1351 (12)	0.1830 (4)	0.8955 (3)	0.0230 (13)
H00K	−0.088844	0.132467	0.915319	0.028*
C00L	0.9328 (11)	0.0391 (4)	0.6615 (3)	0.0217 (13)
H00L	1.070122	0.008373	0.642569	0.026*
C00M	0.5356 (11)	0.1282 (4)	0.7185 (3)	0.0171 (12)
C00N	0.5192 (11)	0.4863 (4)	0.5623 (3)	0.0193 (12)
H00N	0.384615	0.520245	0.577585	0.023*
C00O	0.7743 (12)	0.0071 (4)	0.7165 (3)	0.0244 (14)
H00O	0.802846	−0.045259	0.735029	0.029*
C00P	−0.3968 (10)	0.2974 (4)	0.8997 (3)	0.0235 (15)
H00P	−0.532659	0.325977	0.922332	0.028*

Atomic displacement parameters (Å^2)

	U^{11}	U^{22}	U^{33}	U^{12}	U^{13}	U^{23}
Pt01	0.01666 (9)	0.01422 (9)	0.01212 (9)	−0.00161 (10)	0.00070 (9)	−0.00030 (9)
O002	0.0225 (19)	0.014 (2)	0.0200 (19)	0.002 (2)	0.006 (2)	0.0024 (15)
O003	0.021 (2)	0.018 (2)	0.019 (2)	0.0003 (17)	0.0051 (17)	0.0008 (16)
N004	0.015 (2)	0.020 (3)	0.0098 (19)	0.002 (2)	0.002 (2)	−0.0022 (17)
N005	0.018 (2)	0.011 (2)	0.014 (2)	−0.003 (2)	0.001 (2)	−0.0001 (16)
C006	0.016 (2)	0.018 (3)	0.014 (2)	−0.001 (3)	−0.0001 (18)	−0.004 (3)
C007	0.020 (3)	0.019 (3)	0.013 (2)	−0.006 (2)	−0.004 (2)	0.002 (2)
C008	0.019 (2)	0.017 (3)	0.016 (2)	−0.005 (2)	−0.002 (2)	−0.005 (3)
C009	0.021 (3)	0.024 (4)	0.019 (3)	−0.003 (2)	−0.002 (2)	−0.005 (3)
C00A	0.020 (3)	0.016 (3)	0.013 (2)	−0.002 (2)	−0.005 (2)	0.001 (2)
C00B	0.018 (2)	0.021 (3)	0.015 (2)	−0.007 (3)	−0.001 (2)	−0.003 (2)
C00C	0.018 (2)	0.018 (3)	0.012 (3)	−0.001 (2)	0.000 (2)	0.001 (2)
C00D	0.029 (3)	0.016 (3)	0.019 (3)	−0.006 (3)	0.001 (3)	0.003 (2)
C00E	0.024 (2)	0.035 (3)	0.015 (2)	−0.007 (4)	−0.001 (2)	0.000 (3)
C00F	0.022 (3)	0.028 (4)	0.017 (3)	−0.006 (3)	0.003 (2)	0.003 (3)
C00G	0.022 (3)	0.022 (3)	0.009 (2)	−0.005 (3)	−0.001 (2)	−0.002 (2)
C00H	0.020 (3)	0.020 (3)	0.016 (3)	0.000 (2)	−0.002 (2)	0.000 (2)
C00I	0.030 (3)	0.020 (3)	0.015 (3)	−0.002 (3)	−0.001 (2)	0.004 (2)
C00J	0.020 (3)	0.021 (3)	0.015 (3)	−0.002 (2)	0.002 (2)	0.000 (2)
C00K	0.021 (3)	0.029 (3)	0.019 (3)	−0.005 (3)	0.000 (3)	0.003 (2)
C00L	0.025 (3)	0.021 (3)	0.018 (3)	0.004 (3)	−0.002 (2)	−0.003 (2)
C00M	0.021 (3)	0.019 (3)	0.012 (2)	−0.003 (2)	−0.005 (2)	0.000 (2)
C00N	0.022 (3)	0.017 (3)	0.019 (3)	0.003 (2)	0.000 (2)	0.001 (2)
C00O	0.038 (4)	0.013 (3)	0.022 (3)	0.008 (3)	−0.002 (3)	0.001 (2)

C00P	0.017 (3)	0.033 (4)	0.020 (3)	−0.004 (2)	0.005 (2)	−0.009 (3)

Geometric parameters (Å, °)

Pt01—O002	1.983 (4)	C00C—C00J	1.417 (7)
Pt01—O003	1.991 (4)	C00D—H00D	0.9500
Pt01—N004	1.965 (5)	C00D—C00F	1.391 (8)
Pt01—N005	1.955 (4)	C00D—C00N	1.364 (8)
O002—C00G	1.306 (7)	C00E—H00E	0.9500
O003—C008	1.306 (7)	C00E—C00K	1.361 (8)
N004—C006	1.298 (7)	C00E—C00P	1.399 (9)
N004—C00A	1.419 (7)	C00F—H00F	0.9500
N005—C007	1.306 (7)	C00F—C00J	1.368 (8)
N005—C00M	1.420 (7)	C00G—C00N	1.413 (8)
C006—H006	0.9500	C00H—H00H	0.9500
C006—C00C	1.426 (9)	C00H—C00L	1.378 (8)
C007—H007	0.9500	C00I—H00I	0.9500
C007—C00B	1.422 (8)	C00I—C00M	1.382 (8)
C008—C009	1.421 (8)	C00I—C00O	1.380 (8)
C008—C00B	1.424 (9)	C00J—H00J	0.9500
C009—H009	0.9500	C00K—H00K	0.9500
C009—C00P	1.361 (8)	C00L—H00L	0.9500
C00A—C00H	1.391 (8)	C00L—C00O	1.386 (8)
C00A—C00M	1.405 (8)	C00N—H00N	0.9500
C00B—C00K	1.422 (8)	C00O—H00O	0.9500
C00C—C00G	1.423 (8)	C00P—H00P	0.9500
O002—Pt01—O003	85.28 (17)	C00N—C00D—C00F	121.3 (6)
N004—Pt01—O002	95.60 (17)	C00K—C00E—H00E	120.8
N004—Pt01—O003	178.98 (18)	C00K—C00E—C00P	118.4 (5)
N005—Pt01—O002	178.1 (2)	C00P—C00E—H00E	120.8
N005—Pt01—O003	95.49 (18)	C00D—C00F—H00F	120.9
N005—Pt01—N004	83.62 (19)	C00J—C00F—C00D	118.3 (5)

C00G—O002—Pt01	123.3 (4)	C00J—C00F—H00F	120.9
C008—O003—Pt01	123.2 (4)	O002—C00G—C00C	126.0 (5)
C006—N004—Pt01	123.2 (4)	O002—C00G—C00N	117.0 (5)
C006—N004—C00A	124.2 (5)	C00N—C00G—C00C	116.9 (5)
C00A—N004—Pt01	112.5 (4)	C00A—C00H—H00H	120.2
C007—N005—Pt01	123.7 (4)	C00L—C00H—C00A	119.5 (5)
C007—N005—C00M	122.8 (5)	C00L—C00H—H00H	120.2
C00M—N005—Pt01	113.4 (3)	C00M—C00I—H00I	119.8
N004—C006—H006	116.5	C00O—C00I—H00I	119.8
N004—C006—C00C	127.0 (5)	C00O—C00I—C00M	120.3 (6)
C00C—C006—H006	116.5	C00C—C00J—H00J	118.8
N005—C007—H007	116.9	C00F—C00J—C00C	122.5 (5)
N005—C007—C00B	126.2 (5)	C00F—C00J—H00J	118.8
C00B—C007—H007	116.9	C00B—C00K—H00K	118.5
O003—C008—C009	116.8 (5)	C00E—C00K—C00B	122.9 (6)
O003—C008—C00B	125.6 (5)	C00E—C00K—H00K	118.5
C009—C008—C00B	117.6 (5)	C00H—C00L—H00L	119.5
C008—C009—H009	119.1	C00H—C00L—C00O	121.0 (6)
C00P—C009—C008	121.8 (6)	C00O—C00L—H00L	119.5
C00P—C009—H009	119.1	C00A—C00M—N005	114.6 (5)
C00H—C00A—N004	124.5 (5)	C00I—C00M—N005	125.6 (5)
C00H—C00A—C00M	119.7 (5)	C00I—C00M—C00A	119.8 (5)
C00M—C00A—N004	115.8 (5)	C00D—C00N—C00G	122.2 (6)
C007—C00B—C008	125.4 (5)	C00D—C00N—H00N	118.9
C00K—C00B—C007	116.4 (6)	C00G—C00N—H00N	118.9
C00K—C00B—C008	118.1 (5)	C00I—C00O—C00L	119.7 (6)
C00G—C00C—C006	124.7 (5)	C00I—C00O—H00O	120.1
C00J—C00C—C006	116.4 (5)	C00L—C00O—H00O	120.1
C00J—C00C—C00G	118.8 (5)	C009—C00P—C00E	121.2 (6)
C00F—C00D—H00D	119.4	C009—C00P—H00P	119.4

C00N—C00D—H00D	119.4	C00E—C00P—H00P	119.4

[Pt(sal-3,4-ben)]

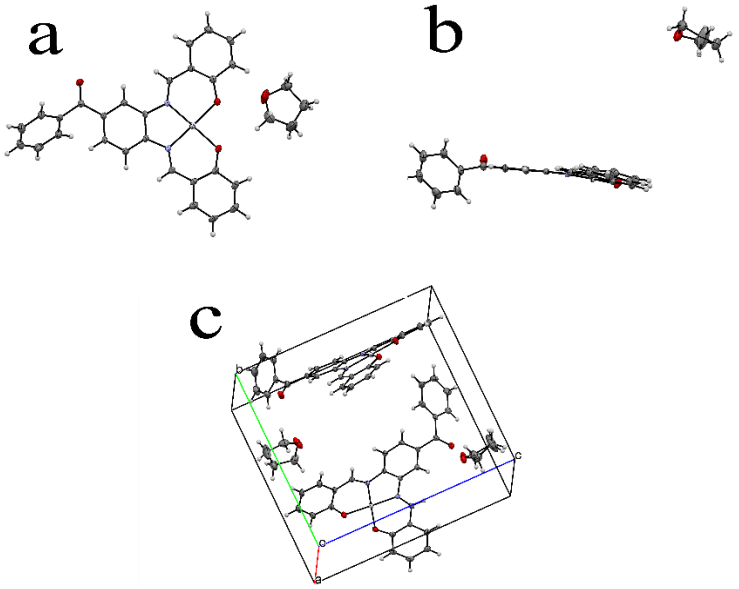

Figure A40. Crystal structure in the plane (a), out of plane (b) and cell packing of the [Pt(sal-3,4-ben)] (c) with THF solvent ellipsoids with 50 % probability.

Table A4. Crystal data of the [Pt(sal-3,4-ben)]

$C_{31}H_{26}N_2O_4Pt$	[Pt(sal-3,4-ben)]
M_r = 685.63	D_x = 1.834 Mg m^{-3}
Monoclinic	
Hall symbol: $P2_1$	Mo $K\alpha$ radiation, λ = 0.71073 Å
a = 5.8808 (10) Å	Cell parameters from 12558 reflections
b = 14.243 (2) Å	θ = 1.4°
c = 14.957 (3) Å	μ = 5.69 mm^{-1}
β = 97.564 (3)°	T = 150 K
V = 1241.9 (4) Å^3	Block, dark red
Z = 2	0.21 × 0.15 × 0.13 mm
F(000) = 672	

Data collection

Bruker APEX CCD detector diffractometer	6421 independent reflections
Radiation source: fine-focus sealed tube	6137 reflections with $I > 2\sigma(I)$
monochromator	R_{int} = 0.019
Detector resolution: 8.3333 pixels mm^{-1}	θ_{max} = 29.1°, θ_{min} = 1.4°
phi and ω scans	h = −8 7
Absorption correction: multi-scan *SADABS* (Bruker, 2010)	k = −19 19
T_{min} = 0.636, T_{max} = 0.746	l = −20 20
18856 measured reflections	

Refinement

Refinement on F^2	Hydrogen site location: inferred from neighbouring sites
Least-squares matrix: full	H-atom parameters constrained
$R[F^2 > 2\sigma(F^2)]$ = 0.015	$w = 1/[\sigma^2(F_o^2)]$ where $P = (F_o^2 + 2F_c^2)/3$
$wR(F^2)$ = 0.030	$(\Delta/\sigma)_{max}$ = 0.002
S = 0.96	$\Delta\rho_{max}$ = 0.81 e Å^{-3}
6421 reflections	$\Delta\rho_{min}$ = −0.40 e Å^{-3}
344 parameters	Extinction correction: none
1 restraint	
	Absolute structure: Refined as an inversion twin.
	Absolute structure parameter: 0.013 (7)

Refined as a 2-component inversion twin.

Fractional atomic coordinates and isotropic or equivalent isotropic displacement parameters (Å^2)

	x	y	z	U_{iso}*/U_{eq}
Pt1	−0.15330 (2)	0.77547 (2)	0.59169 (2)	0.01362 (3)
O2	−0.1503 (4)	0.7888 (2)	0.72457 (15)	0.0213 (8)

N1	−0.1513 (4)	0.7629 (3)	0.46139 (16)	0.0125 (7)
C4	−0.8015 (7)	0.5577 (2)	0.3824 (3)	0.0244 (8)
H4	−0.8849	0.5236	0.3361	0.029*
C7	−0.2916 (6)	0.7116 (2)	0.4090 (2)	0.0169 (7)
H7	−0.2691	0.7081	0.3487	0.020*
C6	−0.4789 (6)	0.6596 (2)	0.4359 (2)	0.0166 (6)
C1	−0.5451 (6)	0.6587 (2)	0.5241 (2)	0.0163 (6)
O1	−0.4382 (4)	0.70176 (15)	0.59538 (16)	0.0183 (5)
C5	−0.6116 (9)	0.6072 (3)	0.3671 (3)	0.0208 (10)
H5	−0.5677	0.6066	0.3096	0.025*
C8	0.0203 (6)	0.8261 (2)	0.7770 (2)	0.0185 (7)
C13	0.2257 (6)	0.8638 (2)	0.7487 (2)	0.0167 (6)
C20	0.3728 (6)	0.9068 (2)	0.4761 (2)	0.0173 (7)
H20	0.4761	0.9339	0.5212	0.021*
C19	0.4029 (8)	0.9172 (3)	0.3868 (3)	0.0172 (9)
H19	0.5278	0.9511	0.3719	0.021*
C18	0.2481 (6)	0.8773 (2)	0.3181 (2)	0.0172 (7)
C21	0.2847 (6)	0.8867 (2)	0.2217 (2)	0.0209 (7)
O3	0.1919 (5)	0.83302 (18)	0.16470 (17)	0.0289 (6)
C15	0.1876 (6)	0.85590 (19)	0.4980 (2)	0.0138 (6)
C9	0.0030 (7)	0.8276 (2)	0.8706 (2)	0.0226 (7)
H9	−0.1307	0.8059	0.8905	0.027*
C10	0.1772 (7)	0.8601 (2)	0.9325 (2)	0.0269 (8)
H10	0.1608	0.8591	0.9935	0.032*
C28	0.4378 (8)	0.1594 (3)	0.8858 (4)	0.0431 (11)
H28A	0.5471	0.2094	0.8801	0.052*
H28B	0.5187	0.0999	0.8907	0.052*
C31	0.0640 (8)	0.1201 (3)	0.8410 (3)	0.0357 (10)
H31A	0.0529	0.0536	0.8270	0.043*
H31B	−0.0725	0.1511	0.8116	0.043*

C30	0.0875 (9)	0.1351 (4)	0.9409 (3)	0.0443 (11)
H30A	−0.0295	0.1780	0.9564	0.053*
H30B	0.0734	0.0761	0.9721	0.053*
C29	0.3154 (11)	0.1751 (6)	0.9652 (4)	0.092 (3)
H29A	0.3946	0.1441	1.0181	0.110*
H29B	0.3053	0.2417	0.9779	0.110*
O4	0.2637 (6)	0.1590 (3)	0.8113 (2)	0.0497 (9)
N10	0.1332 (5)	0.84343 (17)	0.58692 (18)	0.0138 (5)
C16	0.0328 (5)	0.8142 (2)	0.4298 (2)	0.0140 (6)
C11	0.3800 (7)	0.8950 (3)	0.9052 (2)	0.0265 (8)
H11	0.4978	0.9171	0.9476	0.032*
C17	0.0624 (6)	0.8253 (2)	0.3401 (2)	0.0172 (6)
H17	−0.0407	0.7982	0.2949	0.021*
C14	0.2708 (6)	0.8703 (2)	0.6581 (2)	0.0164 (6)
H14	0.4108	0.8960	0.6484	0.020*
C12	0.4022 (8)	0.8961 (3)	0.8155 (3)	0.0242 (9)
H12	0.5374	0.9189	0.7976	0.029*
C22	0.4462 (7)	0.9613 (2)	0.1976 (2)	0.0223 (7)
C27	0.4281 (7)	1.0541 (2)	0.2257 (3)	0.0279 (8)
H27	0.3134	1.0715	0.2597	0.034*
C23	0.6168 (7)	0.9356 (3)	0.1471 (3)	0.0287 (9)
H23	0.6273	0.8739	0.1277	0.034*
C25	0.7579 (8)	1.0937 (3)	0.1537 (3)	0.0379 (10)
H25	0.8649	1.1377	0.1402	0.046*
C26	0.5836 (10)	1.1201 (3)	0.2023 (3)	0.0354 (13)
H26	0.5706	1.1825	0.2193	0.042*
C2	−0.7444 (6)	0.6075 (2)	0.5378 (2)	0.0196 (7)
H2	−0.7915	0.6068	0.5948	0.024*
C3	−0.8690 (6)	0.5590 (2)	0.4690 (3)	0.0220 (7)
H3	−0.9999	0.5266	0.4798	0.026*

C24	0.7727 (8)	1.0026 (3)	0.1255 (3)	0.0356 (10)
H24	0.8879	0.9855	0.0916	0.043*

Atomic displacement parameters (Å^2)

	U^{11}	U^{22}	U^{33}	U^{12}	U^{13}	U^{23}
Pt1	0.01496 (5)	0.01466 (4)	0.01170 (5)	0.00051 (10)	0.00340 (3)	0.00046 (9)
O2	0.0231 (11)	0.027 (2)	0.0148 (10)	−0.0009 (11)	0.0054 (9)	−0.0001 (10)
N1	0.0147 (10)	0.0092 (19)	0.0133 (10)	0.0015 (12)	0.0013 (9)	0.0003 (11)
C4	0.0250 (19)	0.0187 (15)	0.028 (2)	−0.0027 (14)	−0.0023 (16)	0.0011 (13)
C7	0.0175 (16)	0.0178 (13)	0.0158 (16)	0.0026 (12)	0.0037 (14)	0.0013 (12)
C6	0.0176 (16)	0.0159 (13)	0.0159 (16)	0.0002 (13)	0.0007 (14)	−0.0001 (12)
C1	0.0159 (17)	0.0133 (13)	0.0197 (18)	0.0042 (12)	0.0020 (14)	0.0034 (12)
O1	0.0180 (12)	0.0215 (10)	0.0161 (12)	−0.0021 (9)	0.0046 (10)	0.0012 (9)
C5	0.025 (2)	0.0186 (19)	0.018 (2)	−0.0017 (17)	0.0025 (17)	−0.0012 (15)
C8	0.0237 (18)	0.0160 (13)	0.0156 (16)	0.0037 (13)	0.0018 (14)	0.0007 (12)
C13	0.0202 (17)	0.0164 (13)	0.0131 (16)	0.0048 (12)	0.0008 (13)	−0.0013 (11)
C20	0.0186 (17)	0.0176 (14)	0.0152 (17)	−0.0018 (13)	−0.0002 (15)	0.0003 (12)
C19	0.020 (2)	0.0160 (18)	0.017 (2)	−0.0043 (16)	0.0079 (18)	0.0005 (15)
C18	0.0227 (18)	0.0172 (13)	0.0125 (15)	−0.0022 (13)	0.0051 (14)	0.0001 (12)
C21	0.0249 (19)	0.0215 (14)	0.0171 (17)	−0.0054 (14)	0.0052 (15)	0.0005 (13)

O3	0.0390 (16)	0.0317 (12)	0.0169 (13)	−0.0133 (12)	0.0075 (12)	−0.0054 (10)
C15	0.0159 (16)	0.0132 (12)	0.0124 (15)	0.0022 (11)	0.0020 (13)	0.0006 (11)
C9	0.030 (2)	0.0233 (15)	0.0158 (17)	0.0037 (14)	0.0066 (15)	0.0022 (13)
C10	0.039 (2)	0.0287 (16)	0.0132 (16)	0.0092 (16)	0.0036 (16)	0.0003 (13)
C28	0.033 (3)	0.036 (2)	0.061 (3)	−0.003 (2)	0.011 (2)	0.004 (2)
C31	0.031 (2)	0.041 (2)	0.034 (2)	0.0054 (18)	−0.0029 (19)	−0.0069 (18)
C30	0.046 (3)	0.057 (3)	0.033 (2)	−0.001 (2)	0.016 (2)	−0.003 (2)
C29	0.073 (5)	0.171 (7)	0.034 (3)	−0.053 (5)	0.013 (3)	−0.031 (4)
O4	0.0419 (19)	0.083 (2)	0.0273 (17)	0.0144 (18)	0.0151 (15)	0.0166 (16)
N10	0.0163 (14)	0.0134 (11)	0.0121 (13)	0.0014 (10)	0.0027 (11)	−0.0003 (9)
C16	0.0133 (15)	0.0134 (11)	0.0160 (16)	0.0016 (11)	0.0045 (13)	0.0010 (11)
C11	0.034 (2)	0.0302 (17)	0.0138 (17)	0.0022 (16)	−0.0032 (16)	−0.0032 (14)
C17	0.0198 (17)	0.0172 (14)	0.0145 (16)	−0.0015 (12)	0.0016 (13)	−0.0014 (11)
C14	0.0179 (17)	0.0165 (13)	0.0148 (16)	0.0013 (12)	0.0019 (13)	−0.0003 (11)
C12	0.028 (2)	0.024 (2)	0.019 (2)	0.0032 (18)	−0.0012 (17)	−0.0005 (16)
C22	0.0277 (19)	0.0263 (15)	0.0131 (16)	−0.0061 (15)	0.0033 (15)	0.0009 (12)
C27	0.039 (2)	0.0267 (16)	0.0191 (18)	−0.0046 (17)	0.0080 (17)	0.0020 (14)
C23	0.036 (2)	0.0281 (18)	0.024 (2)	−0.0070 (17)	0.0113 (18)	−0.0022 (16)
C25	0.049 (3)	0.035 (2)	0.031 (2)	−0.021 (2)	0.008 (2)	0.0051 (17)
C26	0.059 (3)	0.022 (2)	0.024 (2)	−0.009 (2)	0.002 (2)	−0.0018 (17)

C2	0.0187 (17)	0.0164 (13)	0.0244 (18)	0.0015 (13)	0.0052 (14)	0.0052 (12)
C3	0.0172 (17)	0.0169 (14)	0.032 (2)	−0.0004 (13)	0.0028 (15)	0.0054 (13)
C24	0.037 (2)	0.043 (2)	0.030 (2)	−0.0118 (19)	0.013 (2)	0.0013 (17)

Geometric parameters (Å, °)

Pt1—N10	1.953 (3)	C10—H10	0.9300
Pt1—N1	1.959 (2)	C28—O4	1.410 (6)
Pt1—O1	1.984 (2)	C28—C29	1.485 (7)
Pt1—O2	1.994 (2)	C28—H28A	0.9700
O2—C8	1.302 (4)	C28—H28B	0.9700
N1—C7	1.287 (5)	C31—O4	1.421 (5)
N1—C16	1.437 (4)	C31—C30	1.499 (6)
C4—C5	1.366 (6)	C31—H31A	0.9700
C4—C3	1.404 (5)	C31—H31B	0.9700
C4—H4	0.9300	C30—C29	1.457 (8)
C7—C6	1.428 (5)	C30—H30A	0.9700
C7—H7	0.9300	C30—H30B	0.9700
C6—C5	1.419 (5)	C29—H29A	0.9700
C6—C1	1.425 (5)	C29—H29B	0.9700
C1—O1	1.316 (4)	N10—C14	1.306 (4)
C1—C2	1.418 (5)	C16—C17	1.385 (4)
C5—H5	0.9300	C11—C12	1.365 (6)
C8—C9	1.417 (5)	C11—H11	0.9300
C8—C13	1.435 (5)	C17—H17	0.9300
C13—C14	1.418 (4)	C14—H14	0.9300
C13—C12	1.420 (6)	C12—H12	0.9300
C20—C19	1.378 (6)	C22—C23	1.383 (5)
C20—C15	1.384 (4)	C22—C27	1.395 (5)
C20—H20	0.9300	C27—C26	1.389 (6)

C19—C18	1.400 (6)	C27—H27	0.9300
C19—H19	0.9300	C23—C24	1.391 (5)
C18—C17	1.394 (4)	C23—H23	0.9300
C18—C21	1.491 (5)	C25—C24	1.370 (6)
C21—O3	1.219 (4)	C25—C26	1.384 (7)
C21—C22	1.501 (5)	C25—H25	0.9300
C15—C16	1.406 (4)	C26—H26	0.9300
C15—N10	1.419 (4)	C2—C3	1.368 (5)
C9—C10	1.368 (5)	C2—H2	0.9300
C9—H9	0.9300	C3—H3	0.9300
C10—C11	1.402 (6)	C24—H24	0.9300
N10—Pt1—N1	83.74 (12)	O4—C31—H31A	110.4
N10—Pt1—O1	177.73 (10)	C30—C31—H31A	110.4
N1—Pt1—O1	95.44 (11)	O4—C31—H31B	110.4
N10—Pt1—O2	95.43 (11)	C30—C31—H31B	110.4
N1—Pt1—O2	179.13 (11)	H31A—C31—H31B	108.6
O1—Pt1—O2	85.38 (10)	C29—C30—C31	105.4 (4)
C8—O2—Pt1	122.9 (2)	C29—C30—H30A	110.7
C7—N1—C16	122.6 (3)	C31—C30—H30A	110.7
C7—N1—Pt1	124.8 (2)	C29—C30—H30B	110.7
C16—N1—Pt1	112.6 (2)	C31—C30—H30B	110.7
C5—C4—C3	118.9 (4)	H30A—C30—H30B	108.8
C5—C4—H4	120.5	C30—C29—C28	105.6 (4)
C3—C4—H4	120.5	C30—C29—H29A	110.6
N1—C7—C6	125.4 (3)	C28—C29—H29A	110.6
N1—C7—H7	117.3	C30—C29—H29B	110.6
C6—C7—H7	117.3	C28—C29—H29B	110.6
C5—C6—C1	118.4 (3)	H29A—C29—H29B	108.8
C5—C6—C7	116.1 (3)	C28—O4—C31	107.4 (3)
C1—C6—C7	125.5 (3)	C14—N10—C15	122.3 (3)

O1—C1—C2	116.1 (3)	C14—N10—Pt1	124.1 (2)
O1—C1—C6	125.9 (3)	C15—N10—Pt1	113.5 (2)
C2—C1—C6	118.1 (3)	C17—C16—C15	120.2 (3)
C1—O1—Pt1	122.7 (2)	C17—C16—N1	124.9 (3)
C4—C5—C6	122.3 (4)	C15—C16—N1	114.9 (3)
C4—C5—H5	118.8	C12—C11—C10	119.0 (4)
C6—C5—H5	118.8	C12—C11—H11	120.5
O2—C8—C9	116.8 (3)	C10—C11—H11	120.5
O2—C8—C13	125.9 (3)	C16—C17—C18	119.4 (3)
C9—C8—C13	117.3 (3)	C16—C17—H17	120.3
C14—C13—C12	116.1 (3)	C18—C17—H17	120.3
C14—C13—C8	125.2 (3)	N10—C14—C13	125.9 (3)
C12—C13—C8	118.6 (3)	N10—C14—H14	117.1
C19—C20—C15	119.5 (3)	C13—C14—H14	117.1
C19—C20—H20	120.3	C11—C12—C13	122.2 (4)
C15—C20—H20	120.3	C11—C12—H12	118.9
C20—C19—C18	120.9 (4)	C13—C12—H12	118.9
C20—C19—H19	119.6	C23—C22—C27	120.3 (3)
C18—C19—H19	119.6	C23—C22—C21	118.1 (3)
C17—C18—C19	119.8 (3)	C27—C22—C21	121.5 (3)
C17—C18—C21	119.5 (3)	C26—C27—C22	119.2 (4)
C19—C18—C21	120.7 (3)	C26—C27—H27	120.4
O3—C21—C18	120.8 (3)	C22—C27—H27	120.4
O3—C21—C22	121.0 (3)	C22—C23—C24	119.6 (4)
C18—C21—C22	118.2 (3)	C22—C23—H23	120.2
C20—C15—C16	120.2 (3)	C24—C23—H23	120.2
C20—C15—N10	124.7 (3)	C24—C25—C26	120.1 (4)
C16—C15—N10	115.0 (3)	C24—C25—H25	120.0
C10—C9—C8	121.9 (4)	C26—C25—H25	120.0
C10—C9—H9	119.0	C25—C26—C27	120.4 (4)

C8—C9—H9	119.0	C25—C26—H26	119.8
C9—C10—C11	120.9 (3)	C27—C26—H26	119.8
C9—C10—H10	119.6	C3—C2—C1	121.5 (3)
C11—C10—H10	119.6	C3—C2—H2	119.3
O4—C28—C29	104.8 (4)	C1—C2—H2	119.3
O4—C28—H28A	110.8	C2—C3—C4	120.8 (3)
C29—C28—H28A	110.8	C2—C3—H3	119.6
O4—C28—H28B	110.8	C4—C3—H3	119.6
C29—C28—H28B	110.8	C25—C24—C23	120.5 (4)
H28A—C28—H28B	108.9	C25—C24—H24	119.8
O4—C31—C30	106.5 (4)	C23—C24—H24	119.8

All esds (except the esd in the dihedral angle between two l.s. planes) are estimated using the full covariance matrix. The cell esds are taken into account individually in the estimation of esds in distances, angles and torsion angles; correlations between esds in cell parameters are only used when they are defined by crystal symmetry. An approximate (isotropic) treatment of cell esds is used for estimating esds involving l.s. planes.

Cyclic Voltammetry

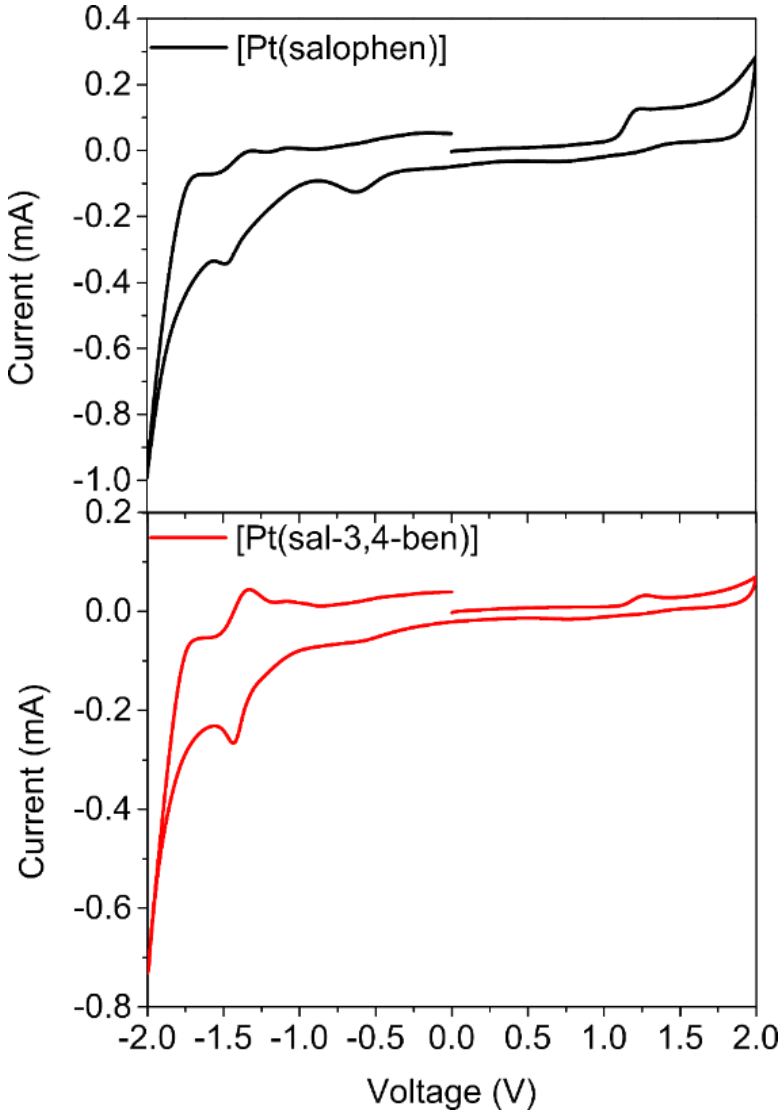

Figure A41. Cyclic voltammogram of [Pt(salophen)] (black curves) and [Pt(sal-3,4-ben)] (red curves) measured in acetonitrile (1.0×10^{-4} mol L^{-1}).

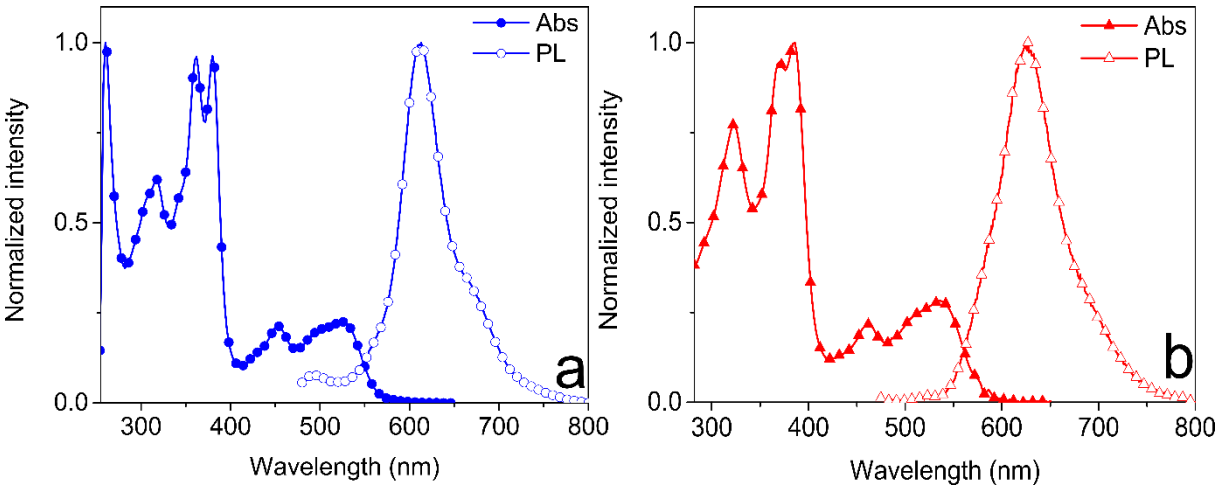

Figure A42. Normalized electronic absorption and phosphorescence spectra of [Pt(salophen)] (a; λ_{exc} = 375 nm) and [Pt(sal-3,4-ben)] (b; λ_{exc} = 385 nm) in THF solutions (10 μmol L^{-1}).

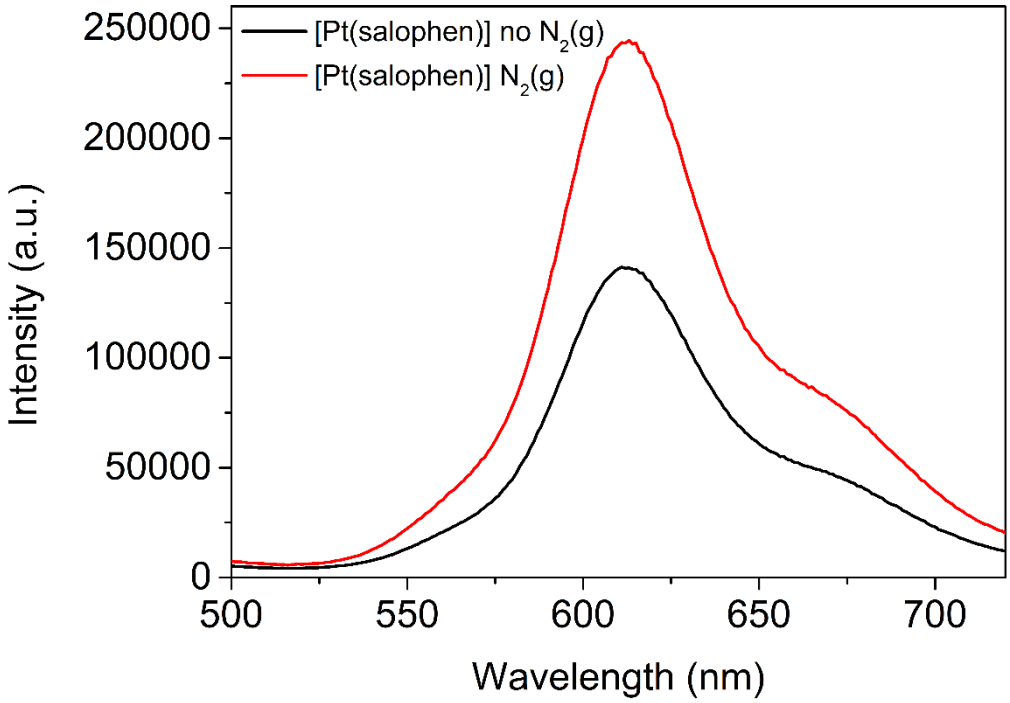

Figure A43. Photoluminescence spectra of [Pt(salophen)] in DMSO solution (λ_{exc} = 380 nm; $1x10^{-5}$ mol L^{-1}) saturated with N_2(g) (red spectra) and without N_2(g) (black spectra).

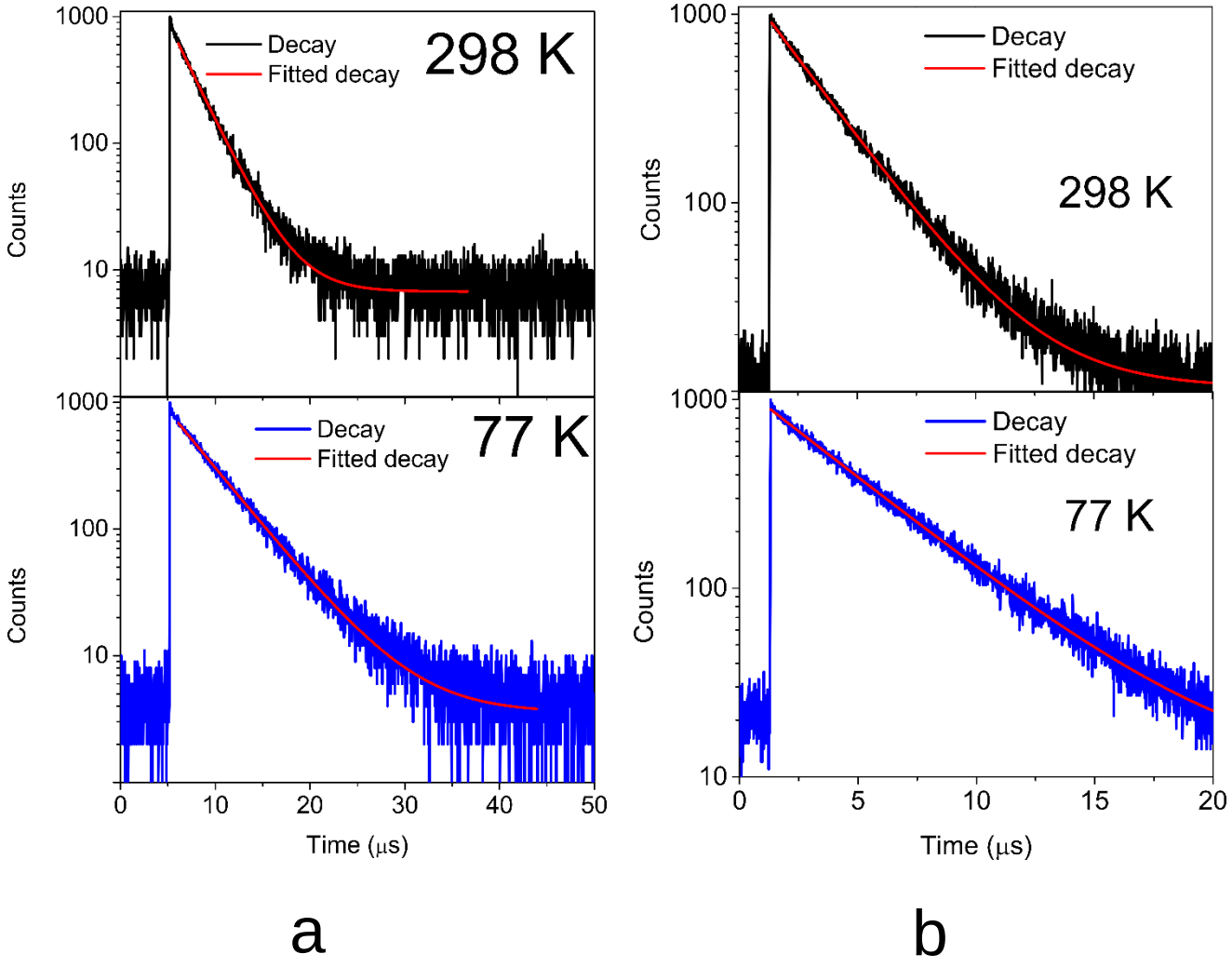

Figure A44. Phosphorescence decays (λ_{exc} = 375 nm) of [Pt(salophen)] (a. λ_{PL} = 621 nm) and [Pt(sal-3,4-ben)] (b; λ_{PL} = 641 nm) in EPA solutions (1 μmol L^{-1}) at 298 K (black decays) and 77 K (blue decays).

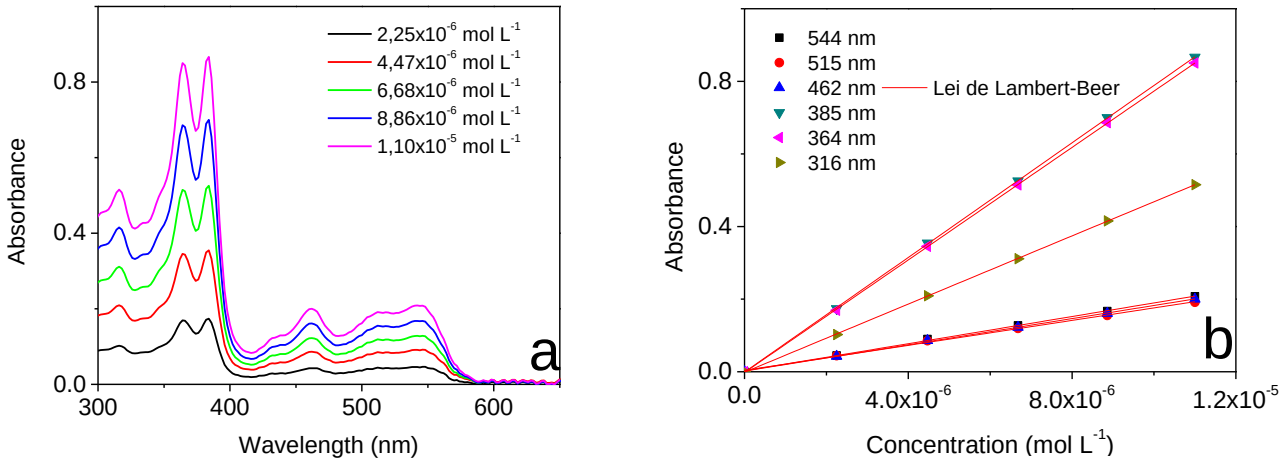

Figura A45. a. Electronic absorption spectra of [Pt(salophen)] in THF dilute solutions; and b. Molar absorption coefficient determination.

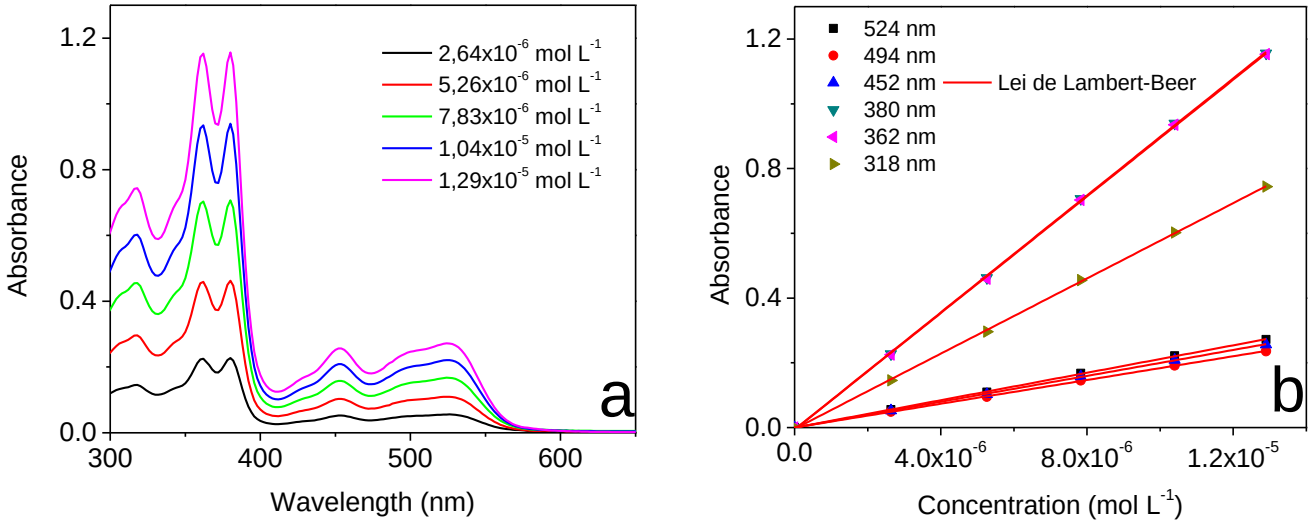

Figura A46. a. Electronic absorption spectra of [Pt(salophen)] in DMSO dilute solutions; and b. Molar absorption coefficient determination.

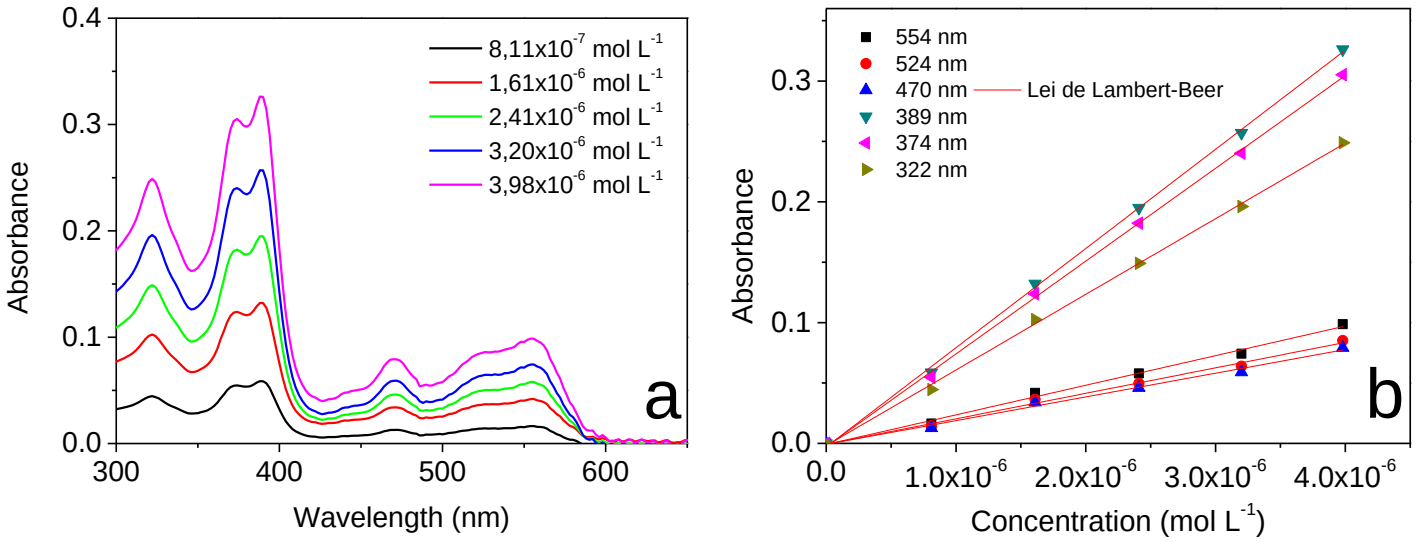

FiguraA47. a. Electronic absorption spectra of [Pt(sal-3,4-ben)] in THF dilute solutions; and b. Molar absorption coefficient determination.

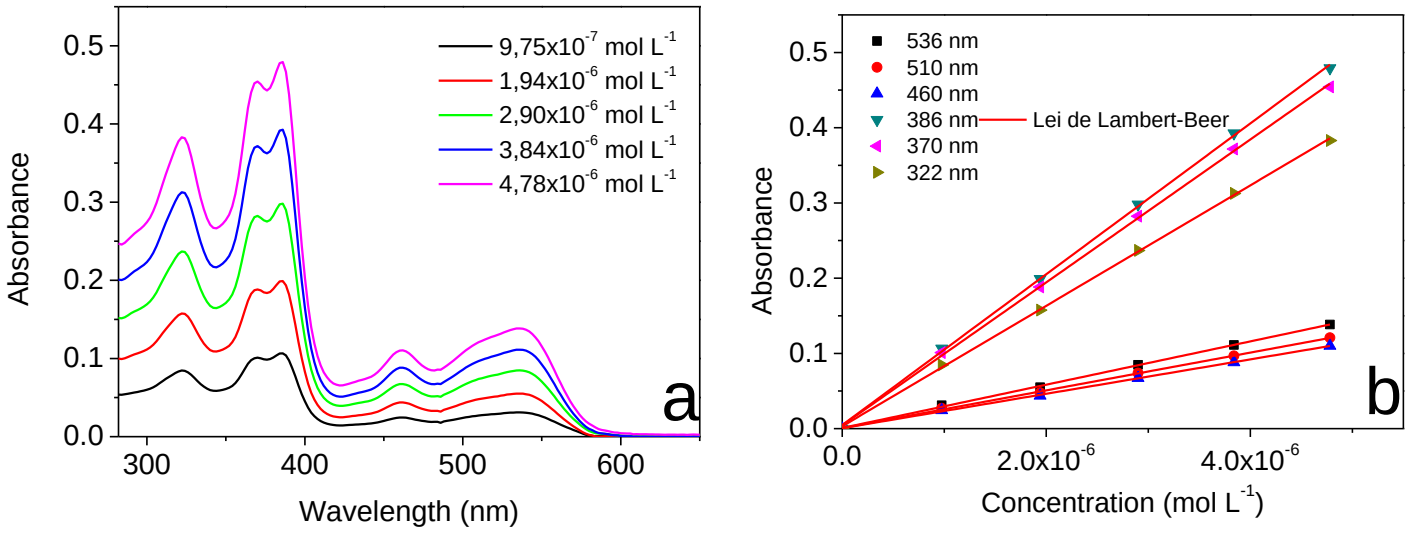

Figure A48. a. Electronic absorption spectra of [Pt(sal-3,4-ben)] in DMSO dilute solutions; and b. Molar absorption coefficient determination.

Electronic Absorption and Photoluminescence Excitation Spectroscopies

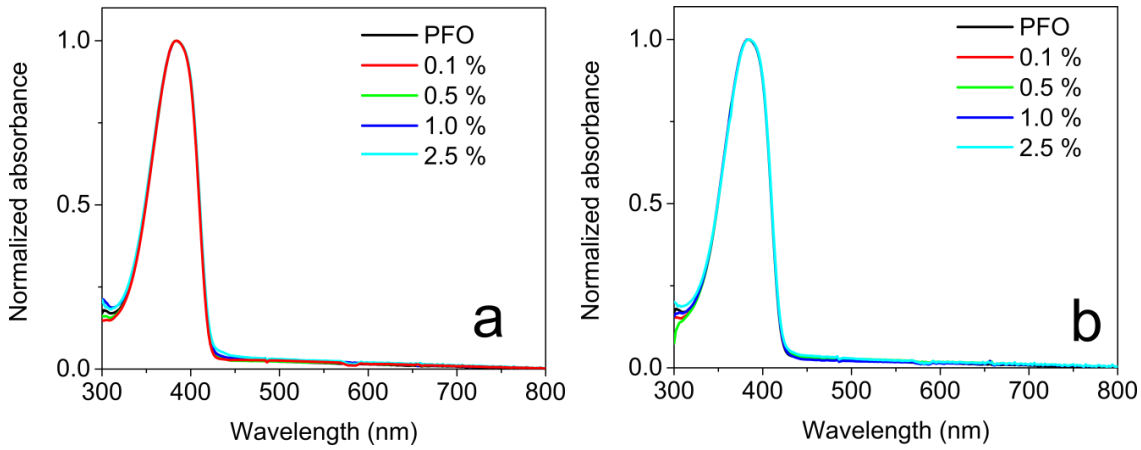

Figure A49. Normalized electronic absorption spectra of the PVK|PFO:Pt(salicylidene) composites thin films: a) PFO:[Pt(salophen)]; and b) PFO:[Pt(sal-3,4-ben)].